

AFIT/DS/ENG/96-06

Electromagnetic Scattering from Semi-Infinite Planar Arrays

DISSERTATION

Peter J. Collins  
Captain, USAF

AFIT/DS/ENG/96-06

**DTIC QUALITY INSPECTED 2**

Approved for public release; distribution unlimited

19970501166

AFIT/DS/ENG/96-06

Electromagnetic Scattering from Semi-Infinite Planar Arrays

DISSERTATION

Presented to the Faculty of the School of Engineering  
of the Air Force Institute of Technology

Air University

In Partial Fulfillment of the  
Requirements for the Degree of  
Doctor of Philosophy

Peter J. Collins, B.A., B.S.E.E., M.S.E.E.

Captain, USAF

September, 1996

Approved for public release; distribution unlimited

19970501166

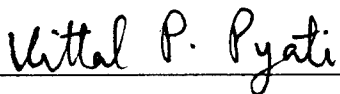
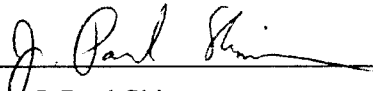
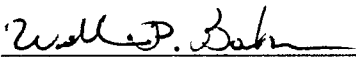
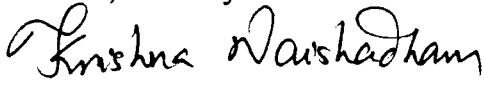
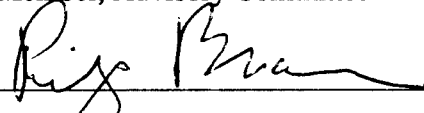
AFIT/DS/ENG/96-06

Electromagnetic Scattering from Semi-Infinite Planar Arrays

Peter J. Collins, B.A., B.S.E.E., M.S.E.E.

Captain, USAF

Approved:

 _____	<u>9 Sep 96</u>
Dr. Vittal Pyati Chairman, Advisory Committee	Date
 _____	<u>3 Sep 96</u>
Dr. J. Paul Skinner Member, Advisory Committee	Date
 _____	<u>4 Sep 96</u>
Dr. William Baker Member, Advisory Committee	Date
 _____	<u>4 Sep. 96</u>
Dr. Krishna Naishadham Member, Advisory Committee	Date
 _____	<u>5 Sep 96</u>
Dr. Philip Beran Dean's Representative	Date

Accepted:

  
\_\_\_\_\_

Robert A. Calico, Jr.  
Dean, Graduate School of Engineering

## *Dedication*

To my Lord Jesus Christ, the source of all knowledge and inspiration; to my loving wife, Cheryl, who's infinite strength, patience, and wisdom in raising our three children and supporting an "absentee" husband over the last three years deserves a doctorate degree, Summa Cum Laude; and to my daughters, Lydia, Rachel, and Hannah, who always showed daddy the truly important things in life, especially when he became too engrossed in writing his "book," this dissertation is humbly and lovingly dedicated.

## *Acknowledgements*

One always takes a risk in writing acknowledgments, because invariably an individual who contributed to the work is left out. So right up front, I say thanks to all, mentioned and unmentioned, who helped make this work possible. Your support is gratefully acknowledged.

I would first like to thank Dr. Paul Skinner, my advisor for the majority of the time, for his many invaluable contributions. Indeed, there should be one big citation at the end of this dissertation acknowledging Dr. Skinner's guidance, both technical and otherwise, throughout this experience. Paul, you truly are an idea man!

I would also like to thank my doctoral committee, Dr. Vittal Pyati, Dr. Krishna Naishadham, and Dr. William Baker for not only critiquing this material, but also providing invaluable technical inputs.

To Bill Wood, fellow sojourner along this doctoral journey, I say thanks for being a sounding board for all my crack-pot ideas. It was great to have an office-mate who actually talked EMAG!

Finally, I would like to give a note of thanks to the folks at the Wright Laboratory Signature Technology Office for all their support with the measurement aspects of this research. Also, thanks to Dr. Errol English at Mission Research Corporation of Dayton for providing the radome samples as well as helpful technical advice.

Peter J. Collins

## *Table of Contents*

	Page
Dedication . . . . .	iii
Acknowledgements . . . . .	iv
List of Figures . . . . .	viii
List of Tables . . . . .	xv
Abstract . . . . .	xvi
I. Introduction . . . . .	1
1.1 Problem Statement . . . . .	4
1.2 Solution Approach . . . . .	5
1.3 Dissertation Summary . . . . .	11
II. Two-Dimensional Semi-Infinite Wire Array . . . . .	12
2.1 Coupling Matrix . . . . .	12
2.1.1 Physical Basis Function . . . . .	13
2.1.2 Edge Element Basis Function . . . . .	33
2.1.3 Test Function Location Convention . . . . .	36
2.2 Excitation Vector . . . . .	37
2.3 Solution Vector and Far-Field Radiation . . . . .	39
III. Three-Dimensional Semi-Infinite Slot Array . . . . .	43
3.1 Coupling Matrix . . . . .	45
3.1.1 Physical Basis Function . . . . .	46
3.1.2 Edge Element Basis Function . . . . .	59

	Page
3.1.3 Edge Element Loading . . . . .	61
3.2 Excitation Vector . . . . .	65
3.3 Solution Vector and Far-Field Radiation . . . . .	66
IV. Validation . . . . .	70
4.1 Reference Code Comparison . . . . .	70
4.1.1 Wire Array in a Homogeneous Media . . . . .	71
4.1.2 Wire Array in a Stratified Media . . . . .	81
4.1.3 Slot Array in a Homogeneous Media . . . . .	90
4.1.4 Slot Array in a Stratified Media . . . . .	96
4.1.5 Slot Array with Loaded Edge Elements . . . . .	100
4.2 Measurement Comparison . . . . .	104
4.2.1 Dielectric Backed Metal Radome . . . . .	112
4.2.2 Dielectric Backed Metal Radome with R-Card Edge Treatment .	116
4.2.3 Metal Radome in Homogeneous Media . . . . .	119
4.2.4 Metal Radome in Homogeneous Media with R-Card Edge Treat- ment . . . . .	125
4.3 Array Size Scaling . . . . .	130
V. Conclusion . . . . .	132
Appendix A. One-Sided Poisson Sum Formula . . . . .	134
Appendix B. Summation Acceleration Algorithms . . . . .	139
B.1 $\epsilon$ -Algorithm . . . . .	139
B.2 Circle-Fit Algorithm . . . . .	140
B.3 $\rho$ -Algorithm . . . . .	144
Appendix C. Continuous Spectrum Integral: Uniform Asymptotic Expansion . . . . .	147

	Page
Appendix D.     Array Scanning Method . . . . .	153
Appendix E.     Physical Basis Function (PBF) in the Excitation Vector . . . . .	156
Bibliography . . . . .	161
Vita . . . . .	164



## *List of Figures*

Figure		Page
1.	Typical FSS Geometry . . . . .	2
2.	Semi-Infinite Wire Array . . . . .	7
3.	Equivalent Geometry . . . . .	8
4.	Semi-Infinite Wire Array Geometry . . . . .	12
5.	PBF Radiating to Test Function Location in Homogeneous Media . . . . .	14
6.	Angular Spectral Integral Contour . . . . .	17
7.	Alternate Cylindrical Coordinate System . . . . .	18
8.	Semi-Infinite Wire Array Green's Function . . . . .	21
9.	Number of Terms Required for Convergence . . . . .	22
10.	Complex Spectra . . . . .	23
11.	PBF Radiating to Test Function Location in Stratified Media . . . . .	24
12.	Plane Wave Polarization Decomposition . . . . .	25
13.	Decomposition of the Plane Waves Internally Reflected in the Dielectric Slab . . . . .	26
14.	T-factor Singularity in a $\epsilon_2 = 2\epsilon_o, 0.2\lambda_o$ Thick Slab with a 0.1 Loss . . . . .	29
15.	T-factor Singularity in a $\epsilon_2 = 2\epsilon_o, 0.2\lambda_o$ Thick Slab with a 0.01 Loss . . . . .	30
16.	T-factor Singularity in a $\epsilon_2 = 2\epsilon_o, 0.2\lambda_o$ Thick Slab with a 0.001 Loss . . . . .	31
17.	PBF Radiation in the Presence of a Dielectric Slab of Various Relative Permittivities . . . . .	32
18.	PBF Radiation for Various Scan Path Elevations above the Array Plane . . . . .	33
19.	Edge Element Radiation in the Presence of a Dielectric Slab of Various Relative Permittivities . . . . .	37
20.	Basis and Testing Function Locations for Semi-Infinite Wire Array . . . . .	38
21.	Large Finite Wire Array . . . . .	40
22.	Complementary Semi-Infinite Array Problem for the Large Finite Array Right Edge . . . . .	41
23.	Semi-Infinite Slot Array Geometry . . . . .	43
24.	Equivalent Slot Array Geometry . . . . .	44

Figure	Page
25. Hertzian Dipole PBF Radiating to Test Location in Homogeneous Media . . . . .	47
26. Geometry for PBF One-sided Admittance Problem . . . . .	55
27. Distributed to Lumped Loading Conversion . . . . .	62
28. Alternate Basis and Testing Function Locations . . . . .	63
29. Plane Wave Illumination of Slot Column . . . . .	65
30. 600 Element Wire Array in Homogeneous Media Illuminated by Plane Wave at an Arbitrary Incident Angle . . . . .	71
31. Induced Current Magnitude on Left 50 Elements of Wire Array with Normal Illumination . . . . .	74
32. Induced Current Phase on Left 50 Elements of Wire Array with Normal Illumination	74
33. Induced Current Magnitude on Left 50 Elements of Wire Array with 5° off Normal Illumination . . . . .	75
34. Induced Current Phase on Left 50 Elements of Wire Array with 5° off Normal Illumination . . . . .	75
35. Induced Current Magnitude on Right 50 Elements of Wire Array with 5° off Normal Illumination . . . . .	76
36. Induced Current Phase on Right 50 Elements of Wire Array with 5° off Normal Illumination . . . . .	76
37. Induced Current Magnitude on Left 50 Elements of Wire Array with 45° off Normal Illumination . . . . .	77
38. Induced Current Phase on Left 50 Elements of Wire Array with 45° off Normal Illumination . . . . .	77
39. Induced Current Magnitude on Right 50 Elements of Wire Array with 45° off Normal Illumination . . . . .	78
40. Induced Current Phase on Right 50 Elements of Wire Array with 45° off Normal Illumination . . . . .	78
41. Induced Current Magnitude on Left 150 Elements of Wire Array with 85° off Normal Illumination . . . . .	79
42. Induced Current Phase on Left 150 Elements of Wire Array with 85° off Normal Illumination . . . . .	79

Figure	Page
43. Induced Current Magnitude on Right 50 Elements of Wire Array with 85° off Normal Illumination . . . . .	80
44. Induced Current Phase on Right 50 Elements of Wire Array with 85° off Normal Illumination . . . . .	80
45. 600 Element Wire Array in a Dielectric Slab Illuminated by Plane Wave at an Arbitrary Incident Angle . . . . .	81
46. Induced Current Magnitude on Left 50 Elements of Wire Array in Slab with Normal Illumination . . . . .	83
47. Induced Current Phase on Left 50 Elements of Wire Array in Slab with Normal Illumination . . . . .	83
48. Induced Current Magnitude on Left 70 Elements of Wire Array in Slab with 5° off Normal Illumination . . . . .	84
49. Induced Current Phase on Left 70 Elements of Wire Array in Slab with 5° off Normal Illumination . . . . .	84
50. Induced Current Magnitude on Right 50 Elements of Wire Array in Slab with 5° off Normal Illumination . . . . .	85
51. Induced Current Phase on Right 50 Elements of Wire Array in Slab with 5° off Normal Illumination . . . . .	85
52. Induced Current Magnitude on Left 150 Elements of Wire Array in Slab with 45° off Normal Illumination . . . . .	86
53. Induced Current Phase on Left 150 Elements of Wire Array in Slab with 45° off Normal Illumination . . . . .	86
54. Induced Current Magnitude on Right 50 Elements of Wire Array in Slab with 45° off Normal Illumination . . . . .	87
55. Induced Current Phase on Right 50 Elements of Wire Array in Slab with 45° off Normal Illumination . . . . .	87
56. Induced Current Magnitude on Left 250 Elements of Wire Array in Slab with 85° off Normal Illumination . . . . .	88
57. Induced Current Phase on Left 250 Elements of Wire Array in Slab with 85° off Normal Illumination . . . . .	88

Figure	Page
58. Induced Current Magnitude on Right 50 Elements of Wire Array in Slab with 85° off Normal Illumination . . . . .	89
59. Induced Current Phase on Right 50 Elements of Wire Array in Slab with 85° off Normal Illumination . . . . .	89
60. Induced Current Magnitude on 100 Element Slot Array with 5° off Normal Illumination	92
61. Induced Current Phase on 100 Element Slot Array with 5° off Normal Illumination .	92
62. Induced Current Magnitude on 100 Element Slot Array with 45° off Normal Illumination . . . . .	93
63. Induced Current Phase on 100 Element Slot Array with 45° off Normal Illumination	93
64. Induced Current Magnitude on 100 Element Slot Array with 85° off Normal Illumination . . . . .	94
65. Induced Current Phase on 100 Element Slot Array with 85° off Normal Illumination	94
66. REA pattern at 15 GHz for 100 Column Slot Array in Homogeneous Media . . . .	95
67. Induced Current Magnitude on 100 Element Slot Array in Stratified Media with 5° off Normal Illumination . . . . .	97
68. Induced Current Phase on 100 Element Slot Array in Stratified Media with 5° off Normal Illumination . . . . .	97
69. Induced Current Magnitude on 100 Element Slot Array in Stratified Media with 45° off Normal Illumination . . . . .	98
70. Induced Current Phase on 100 Element Slot Array in Stratified Media with 45° off Normal Illumination . . . . .	98
71. Induced Current Magnitude on 100 Element Slot Array in Stratified Media with 85° off Normal Illumination . . . . .	99
72. Induced Current Phase on 100 Element Slot Array in Stratified Media with 85° off Normal Illumination . . . . .	99
73. Induced Current Magnitude on 100 Element Loaded Slot Array with 5° off Normal Illumination . . . . .	101
74. Induced Current Phase on 100 Element Loaded Slot Array with 5° off Normal Illumination . . . . .	101

Figure	Page
75. Induced Current Magnitude on 100 Element Loaded Slot Array with 45° off Normal Illumination . . . . .	102
76. Induced Current Phase on 100 Element Loaded Slot Array with 45° off Normal Illumination . . . . .	102
77. Induced Current Magnitude on 100 Element Loaded Slot Array with 85° off Normal Illumination . . . . .	103
78. Induced Current Phase on 100 Element Loaded Slot Array with 85° off Normal Illumination . . . . .	103
79. Radome Measurement Test Fixture . . . . .	105
80. Metal Radome Transmission for Three Angles of Incidence . . . . .	106
81. Dielectric Backed Radome Transmission for Three Angles of Incidence . . . . .	106
82. Radome Mounted in Test Fixture . . . . .	107
83. Test Fixture Cavity Treatment . . . . .	107
84. R-Card Application . . . . .	108
85. Frequency versus Angle Plot for Radome Configuration Number 1 . . . . .	110
86. Frequency versus Angle Plot for Radome Configuration Number 2 . . . . .	110
87. Frequency versus Angle Plot for Radome Configuration Number 3 . . . . .	111
88. Frequency versus Angle Plot for Radome Configuration Number 4 . . . . .	111
89. REA pattern at 13 GHz for Metal Radome in Stratified Media . . . . .	112
90. REA pattern at 15 GHz for Metal Radome in Stratified Media . . . . .	113
91. REA pattern at 17 GHz for Metal Radome in Stratified Media . . . . .	114
92. Induced Currents on Metal Radome in Stratified Media at 15 GHz . . . . .	115
93. Hybrid PMM/MM Approximation to Induced Currents on Metal Radome in Stratified Media at 15 GHz . . . . .	115
94. REA pattern at 13 GHz for R-Card Treated Metal Radome in Stratified Media . . . . .	116
95. REA pattern at 15 GHz for R-Card Treated Metal Radome in Stratified Media . . . . .	117
96. REA pattern at 17 GHz for R-Card Treated Metal Radome in Stratified Media . . . . .	117
97. Induced Currents on R-Card Treated Metal Radome in Stratified Media at 15 GHz . . . . .	118

Figure	Page
98. Hybrid PMM/MM Approximation to Induced Currents on R-Card Treated Metal Radome in Stratified Media at 15 GHz . . . . .	118
99. REA pattern at 13 GHz for Metal Radome in Homogeneous Media . . . . .	120
100. REA pattern at 15 GHz for Metal Radome in Homogeneous Media . . . . .	120
101. REA pattern at 17 GHz for Metal Radome in Homogeneous Media . . . . .	121
102. Induced Currents on Metal Radome in Homogeneous Media at 13 GHz . . . . .	122
103. Hybrid PMM/MM Approximation to Induced Currents on Metal Radome in Homogeneous Media at 13 GHz . . . . .	122
104. Induced Currents on Metal Radome in Homogeneous Media at 15 GHz . . . . .	123
105. Hybrid PMM/MM Approximation to Induced Currents on Metal Radome in Homogeneous Media at 15 GHz . . . . .	123
106. Induced Currents on Metal Radome in Homogeneous Media at 17 GHz . . . . .	124
107. Hybrid PMM/MM Approximation to Induced Currents on Metal Radome in Homogeneous Media at 17 GHz . . . . .	124
108. REA pattern at 13 GHz for R-Card Treated Metal Radome in Homogeneous Media .	125
109. REA pattern at 15 GHz for R-Card Treated Metal Radome in Homogeneous Media .	126
110. REA pattern at 17 GHz for R-Card Treated Metal Radome in Homogeneous Media .	126
111. Induced Currents on R-Card Treated Metal Radome in Homogeneous Media at 13 GHz	127
112. Hybrid PMM/MM Approximation to Induced Currents on R-Card Treated Metal Radome in Homogeneous Media at 13 GHz . . . . .	127
113. Induced Currents on R-Card Treated Metal Radome in Homogeneous Media at 15 GHz	128
114. Hybrid PMM/MM Approximation to Induced Currents on R-Card Treated Metal Radome in Homogeneous Media at 15 GHz . . . . .	128
115. Induced Currents on R-Card Treated Metal Radome in Homogeneous Media at 17 GHz	129
116. Hybrid PMM/MM Approximation to Induced Currents on R-Card Treated Metal Radome in Homogeneous Media at 17 GHz . . . . .	129
117. Circle-fit Algorithm for Two-dimensional Free-space Periodic Green's Function . .	142
118. Angular Spectral Integral Steepest Descent Path . . . . .	150
119. Numerical versus Asymptotic Integral Evaluation Error . . . . .	152

Figure	Page
120. Single Wire in a Dielectric Slab . . . . .	153
121. 600 Element Wire Array in Homogeneous Media . . . . .	156
122. Left 110 Elements Based on First Formulation (Leading Edge of Array is Element 1)	159
123. Right 110 Elements Based on First Formulation (Trailing Edge of Array is Element 600) . . . . .	159
124. Left 110 Elements Based on Second Formulation (Leading Edge of Array is Element 1) . . . . .	160
125. Right 110 Elements Based on Second Formulation (Trailing Edge of Array is Element 600) . . . . .	160

*List of Tables*

Table	Page
1. Wire Array in Homogeneous Media Reference MM Code versus Hybrid PMM/MM Code Time Comparison . . . . .	73
2. Wire Array in Slab Reference MM Code versus Hybrid PMM/MM Code Time Comparison . . . . .	82
3. Radome Measurement Matrix . . . . .	109
4. Slot Array in Homogeneous Media Reference MM Code versus Hybrid PMM/MM Code Time Comparison . . . . .	131
5. Sequence of Partial Sums for the RHS . . . . .	138
6. Circle-fit and $\epsilon$ Algorithms Applied to Equation (193) . . . . .	144
7. $\epsilon$ and $\rho$ Algorithms Applied to Equation (202) . . . . .	145
8. $\epsilon$ and $\rho$ Algorithms Applied to Equation (203) . . . . .	146
9. Asymptotic and Numerical Integral Evaluation Time Comparison . . . . .	152



*Abstract*

A hybrid method of moments (MM) based numerical model for the electromagnetic scattering from large finite by infinite planar slot arrays is developed. The method incorporates the novel concept of a physical basis function (PBF) to dramatically reduce the number of required unknowns. The model can represent a finite number of slot columns with slots oriented along the infinite axis, surrounded by an arbitrary number of coplanar dielectric slabs. Each slot column can be loaded with a complex impedance, allowing one to tailor the edge currents to provide a desired echo width pattern.

The surface equivalence theorem is used to convert the original slotted ground plane geometry to an equivalent unbroken ground plane with magnetic surface currents. An integral equation based on these magnetic scattering currents is solved via the MM. The magnetic currents are approximated by a set of basis functions composed of periodic basis functions representing the edge slot columns and a single PBF representing the interior slot columns. In particular, the PBF captures the behavior of the central portion of the array where the perturbations from the edges have become negligible. Based on Floquet's theorem, the PBF is able to represent an arbitrarily large number of slot columns with just one unknown. The array scanning method (ASM) provides the contributions from the individual edge columns. Finally, a newly developed one-sided Poisson sum formulation provides an efficient means to account for the stratified dielectric media via a spectral domain conversion.

The hybrid method is validated using both MM reference codes and measured data. The results clearly demonstrate the method's accuracy as well as its ability to handle array problems too large for traditional MM solutions.

# Electromagnetic Scattering from Semi-Infinite Planar Arrays

## *I. Introduction*

Most of the fundamental ideas of science are essentially simple, and may, as a rule, be expressed in a language comprehensible to everyone.

- *Albert Einstein*

Periodic screens have long been of interest to the scientific and engineering communities. Commonly called frequency surfaces (FSS) for their frequency filtering properties, they find application over a large range of the electromagnetic spectrum. They hold particular interest to the Air Force as antenna radomes and dichroic antenna feed systems.

FSS typically consist of regular arrays of either conducting patch elements deposited on a dielectric substrate or apertures in a conducting surface. Figure 1 depicts an example FSS geometry. Arrays of this type exhibit total reflection (patches) or transmission (apertures) near the resonance of the individual elements. In studying the electromagnetic scattering from these structures, most authors use an integral equation formulation which connects the currents induced on the periodic elements to the fields scattered from the FSS. To keep the problem tractable, they approximate the actual curved finite array with a flat infinite array and use Floquet analysis to reduce the infinite domain problem to one involving a representative cell. The Method of Moments (MM) is then used to convert the integral equation into a system of linear equations suitable for numerical solution.

Traditionally the actual implementation of the MM in infinite array analysis has taken two different tracks. The first, pioneered by Munk and others at The Ohio State University [26, 28], approximates the induced currents as filamentary currents. The authors use a plane wave expansion method to derive very efficient expressions for the radiated fields. The Periodic Moment Method (PMM) code written by Henderson [19] is an excellent example of the use of this technique.

The second implementation, developed by Mittra and others at the University of Illinois [23], favors more complex basis functions to better model the actual element currents. In this case the

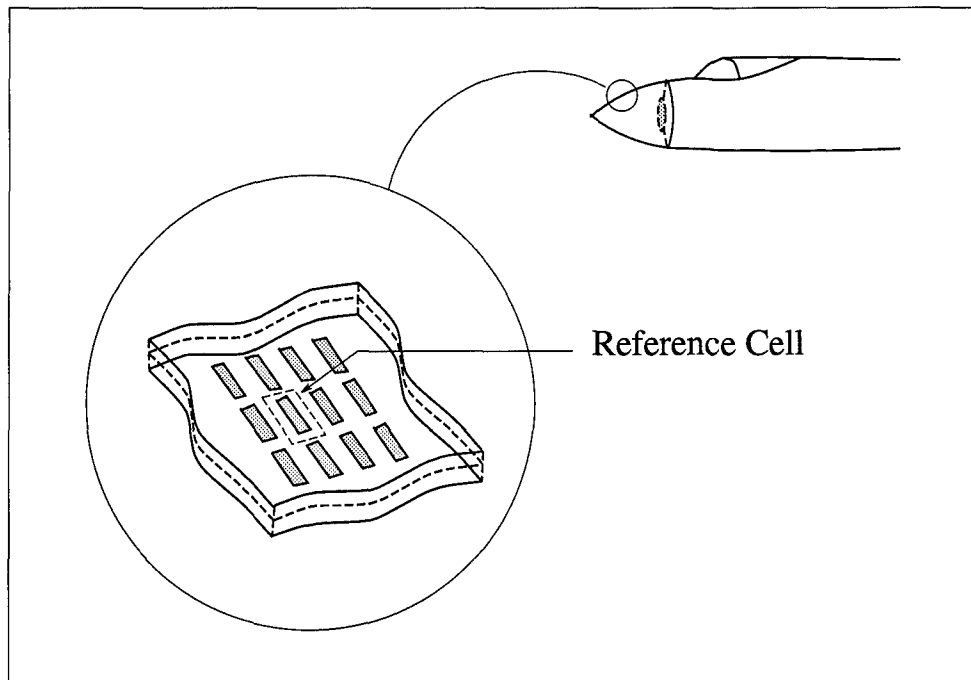


Figure 1. Typical FSS Geometry

authors transform the integral equation to the spectral domain where they use a conjugate gradient technique to solve the system. Although generally more accurate for a given number of basis functions, codes based on this approach tend to be less efficient.

Regardless of the solution method, all of the infinite array techniques fail to account for the edge diffraction or curvature effects present in real world arrays. A knowledge of these effects is critical to advanced radome and antenna design. Consequently, recent research efforts have focused on finite array analysis methods.

Due to their finite nature, Floquet theory does not strictly apply to these arrays. The current on each of the array elements must be treated as an independent quantity. Most of the research in this area falls into one of two categories; studying the effects of termination using relatively small finite-by-infinite or finite-by-finite arrays or finding efficient ways to compute element currents in an effort to handle large array sizes. In both cases, the general approach begins with the development of an integral equation involving unknown element currents. Some authors choose to represent the

integral equation kernel in the spatial domain where others prefer the spectral domain. Next, one approximates the currents using sub-domain or entire domain basis functions. With an appropriately defined inner product, one can convert the integral equation to a matrix equation which can then be solved using either Gaussian elimination or iterative techniques.

Examples of this general approach include Kastner and Mittra's [20] paper based on the spectral iteration and conjugate gradient iteration techniques applied to finite-by-finite planar patch arrays, Grounds and Webb's [14] attack of the finite-by-infinite problem using a spectral domain Green's function formulation, and Skinner, Munk, and Barré's [34, 2] work based on the array scanning method (ASM) applied to the finite-by-infinite problem in a layered dielectric media. All of these approaches are able to explicitly model the edge termination effects characteristic of finite arrays. Unfortunately, their strength is also the source of their weakness. Since the current on each array element in the finite dimension is an unknown quantity, these methods are limited to relatively small arrays by available computer resources. Many authors have proposed various schemes to alleviate this fundamental problem [4, 6, 7, 15, 22, 36, 37], but the literature is devoid of calculated results for finite arrays larger than tens or hundreds of elements.

The limitations of these finite and infinite array methods suggest a hybrid approach for the large array problem. Surprisingly, only a small number of papers on such techniques have been published. Researchers at the University of Illinois [8] have investigated truncated and curved strip arrays via a technique which approximates the induced current on each element as if it were a member of an infinite array. The authors then replace the edge element currents by those calculated for a much smaller array. Unfortunately, this method gives poor results for incidence angles near grazing where the coupling between the edge elements and those interior to the array becomes significant. In addition, the authors make no attempt to model the dielectric coatings common in radome applications.

Felsen and Carin have recently investigated finite wire arrays using a Floquet current approximation on two semi-infinite<sup>1</sup> sub-arrays [10, 12]. They combined the two sub-arrays such that

---

<sup>1</sup>The term "semi-infinite," in the context of this dissertation, will always refer to an array with only one edge analogous to a half-plane. (*i.e.* Along the semi-infinite axis, the elements go on "forever" in one direction, but terminate at some point in the opposite direction.) This definition contrasts with one commonly used in the literature to refer to an array which has a finite number of elements in one direction and an infinite number of elements in the orthogonal direction.

the composite currents are that of the desired finite wire array. Several assumptions constrain their analysis. Namely, they assume all propagation is ray optical. Also they ignore any deviation in the edge element currents as well as multiple scattering between array elements. As a result, their formulation gives poor results near the grazing incident angles common for forward aspect illumination of radomes.

Finally, in his 1973 paper, Wasyliwskyj [40] examines the mutual coupling effects in semi-infinite antenna arrays. His analysis is based on a Wiener-Hopf solution technique for an infinite order difference equation modeling the antenna element port currents. Wasyliwskyj's transform approach provides an alternate solution methodology which, to the author's knowledge, has not been applied to large finite arrays.

The need to account for array truncation in large arrays especially at grazing incident angles along with the short-comings of existing hybrid finite-infinite analysis techniques motivates this present research. Specifically, by more accurately modeling the currents induced on a semi-infinite array, the scattering from an arbitrarily large finite array can be synthesized in a manner analogous to that used by Felsen and Carin. The resulting formulation should provide more accurate radar cross section (RCS) predictions, especially in the areas where existing hybrid techniques fail.

### *1.1 Problem Statement*

Improved FSS analysis methods are required for the design of advanced antenna radomes used in modern aircraft. Existing techniques based on infinite array models cannot account for the perturbations caused by edge effects at radome-to-aircraft boundaries nor the radome curvature characteristic of conformal designs. Finite array analysis methods, while able to handle these phenomena, are restricted to relatively small array sizes by modern day computer memory limitations, especially if dielectric layers are involved. The infinite/finite hybrid techniques proposed to date may not sufficiently represent the true coupling between the edge elements and the central portion of a large array. The objectives of this research are first, to develop and test a new hybrid PMM/MM approach which addresses this coupling issue to more accurately predict the performance of large

finite planar arrays and second, to use this approach to analyze the isolated “diffraction” of a single FSS termination.

## 1.2 Solution Approach

This dissertation presents a new approach to combining infinite array and small finite array analysis based on the concept of a “physical basis function” (PBF). Although couched in different terms, the PBF concept was originally proposed by Morita [24] and later Tew and Tsai [38] in an effort to apply the MM to infinite planar structures. Burnside, Yu, and Marhefka [5] then applied it to the wedge diffraction problem, combining the geometrical theory of diffraction (GTD) with the MM. To the author’s knowledge, however, the present work represents the first application of the PBF concept to periodic structures.

The core of the PBF concept involves a fairly straight-forward application of *a priori* knowledge of the induced current behavior to the MM. Consider the currents impressed on a large planar array by a plane wave illumination (large implying many wavelengths). Starting from an edge and moving toward the center of the array, there will be some point where the current amplitudes become approximately constant over a large central section of the finite array. Over this portion one can use the PMM to determine the representative admittance or impedance of these elements. This PBF can then be used along with the edge element basis functions to create a coupling matrix which relates the unknown current expansion coefficients to known coefficients dependent on the incident field. The coupling matrix now explicitly incorporates the influence of the “infinite” portion of a large finite array into the small finite array analysis in a manner analogous to how the interconnection matrix of diakoptic theory [13] combines the impedances of individual structural elements into a composite structure matrix. This technique represents a departure from traditional hybrid methods which calculate the currents induced on the two portions of the array separately and then combine their effects in the far-field through a radiation integral analogous to the physical optics approximation. The remainder of this section lays out the general hybrid PMM/MM approach using a wire array in free-space as an example geometry.

Consider the semi-infinite array of thin wires shown in Figure 2a. Note that the wires in the array are infinitely long and form an array which continues forever to the right. Using the surface equivalence theorem, one defines a new geometry where impressed currents radiate into free-space. Specifically, one replaces the perfect electric conductor (PEC) with a Huygens' surface and defines impressed surface currents of the form

$$\begin{aligned}\overline{\mathbf{J}}_s &= \hat{\mathbf{n}} \times \overline{\mathbf{H}} \\ \overline{\mathbf{M}}_s &= \overline{\mathbf{E}} \times \hat{\mathbf{n}}\end{aligned}\tag{1}$$

where  $\overline{\mathbf{J}}_s$  and  $\overline{\mathbf{M}}_s$  are the impressed electric and magnetic surface currents,  $\hat{\mathbf{n}}$  is the outward normal of the Huygens' surface, and  $\overline{\mathbf{H}}$  and  $\overline{\mathbf{E}}$  are the magnetic and electric fields at the Huygens' surface in the original problem. With a thin wire approximation, the electric surface currents are modeled by  $\hat{\mathbf{z}}$  directed filamentary currents at the center of the wires. There are no impressed magnetic currents since the total tangential electric field is identically zero on the PEC surface in the original problem. The resulting equivalent problem is depicted in Figure 2b.

The equivalent problem contains an infinite number of unknown currents making a numerical solution via a traditional MM approach impossible. In order to make the problem tractable, one assumes the current amplitudes vary significantly only over the first  $B$  elements. The remaining elements have approximately equal amplitude currents which differ by a Floquet phasing factor dependent on the incident plane wave direction. This assumption reduces the problem to that of finding  $(B + 1)$  unknowns as shown in Figure 3.

One next forms an integral equation relating the unknown currents to the known incident field. As is common in these formulations, the total tangential electric field boundary condition is used to

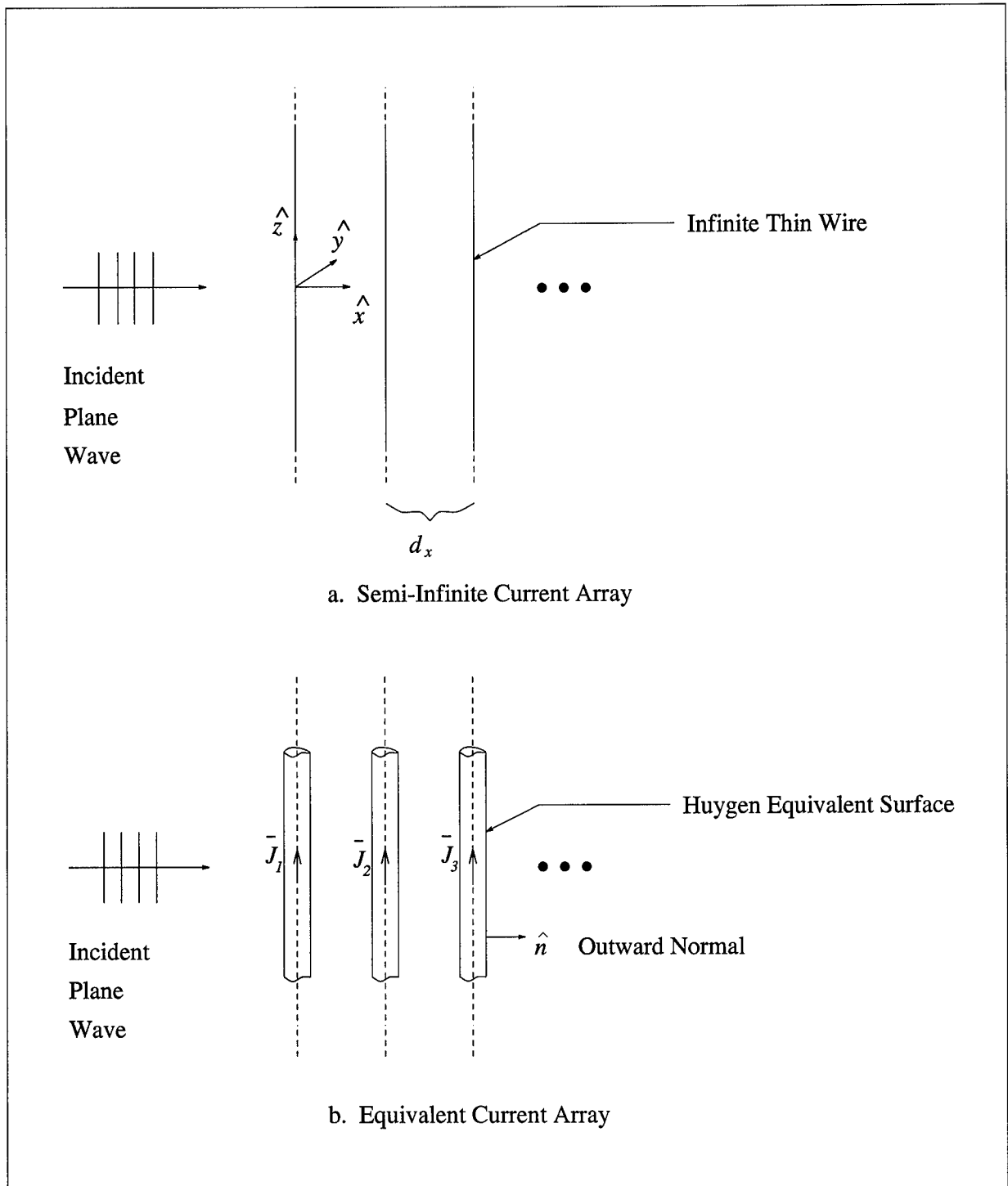


Figure 2. Semi-Infinite Wire Array



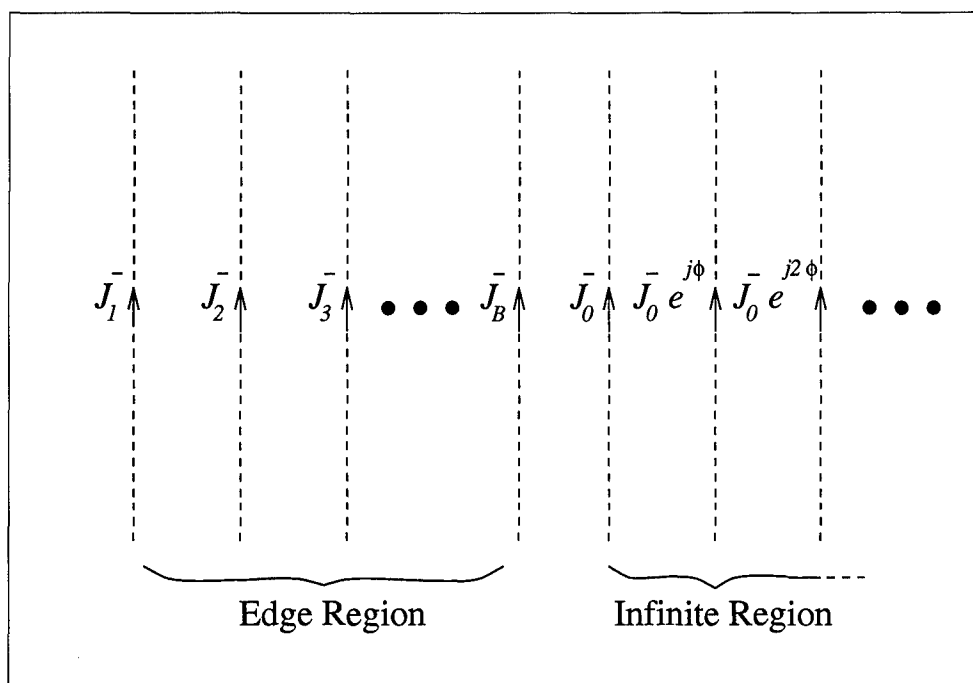


Figure 3. Equivalent Geometry

obtain an integral equation of the form

$$\begin{aligned}
 \hat{n} \times \bar{E} &= 0 \\
 \hat{n} \times \left( \bar{E}^i + \sum_{b=0}^B \bar{E}^s(\bar{J}_b) \right) &= 0 \\
 \hat{n} \times \bar{E}^i &= -\hat{n} \times \sum_{b=0}^B \bar{E}^s(\bar{J}_b) \Big|_{\bar{\rho} \in S}
 \end{aligned} \tag{2}$$

where  $\hat{n}$  is the outward normal of the Huygens' surface,  $\bar{E}^i$  is the incident electric field on the wire surfaces ( $S$ ), and  $\bar{E}^s(\bar{J}_b)$  is the scattered electric field due to the  $b^{\text{th}}$  current element. Note that in general, one can directly express the fields due to a current via the radiation integral and the appropriate dyadic Green's function [39]

$$\bar{E}^s(\bar{J}_b) = j\omega\mu \int_S \bar{J}_b(\bar{R}') \cdot \bar{\Gamma}(\bar{R}, \bar{R}') d\bar{R}' \tag{3}$$

where  $\bar{\Gamma}(\bar{\mathbf{R}}, \bar{\mathbf{R}}')$  is the dyadic Green's function,  $\bar{\mathbf{J}}_b(\bar{\mathbf{R}}')$  is the  $b^{\text{th}}$  element current density, and  $\bar{\mathbf{R}}'$  and  $\bar{\mathbf{R}}$  denote the source and observation locations respectively.

One now solves Equation (2) via the MM by first expanding the unknown currents with appropriate known basis functions,  $\bar{\phi}_b(\bar{\rho}')$ . In this case,  $B$  impulse basis functions and one PBF are required. These take the form

$$\bar{\mathbf{J}}_b(\bar{\rho}') \approx J_b \bar{\phi}_b(\bar{\rho}') \quad (4)$$

where

$$\bar{\phi}_b(\bar{\rho}') = \hat{z} \begin{cases} \sum_{q=0}^{\infty} \delta(\bar{\rho}' - \bar{\rho}_q) e^{-j\beta \hat{\mathbf{s}} \cdot \bar{\rho}_q} & b = 0 \\ \delta(\bar{\rho}' - \bar{\rho}_b) & b = 1, 2, \dots, B \end{cases} \quad (5)$$

and

$$\bar{\rho}_q = \hat{x} q d_x \quad (6)$$

Note that  $\bar{\rho}_{q=0}$  locates the "edge" of the PBF and  $\hat{\mathbf{s}}$  denotes the incident plane wave propagation direction. Inserting Equation (4) in Equation (2), one obtains the expression

$$\hat{\mathbf{n}} \times \bar{\mathbf{E}}^i = -\hat{\mathbf{n}} \times \sum_{b=0}^B \bar{\mathbf{E}}^s (J_b \bar{\phi}_b(\bar{\rho}')) + \bar{\epsilon}(\bar{\rho}, J_0, J_1, \dots, J_B) \Big|_{\bar{\rho} \in S} \quad (7)$$

where  $\bar{\epsilon}$  is the error function associated with the current approximation.

Following Harrington's MM formulation [18], the next step in the numerical solution involves defining an inner product and forcing a chosen set of  $(B+1)$  testing functions,  $\bar{\theta}_t(\bar{\rho})$ , to be orthogonal to the error function. For the wire geometry, the filamentary current nature suggests a Dirac delta testing function. In order to avoid the Green's function singularity, one places the test location a wire radius away from the basis function for the self-coupling terms. One also defines the testing function associated with the PBF to be nonzero only over a chosen reference wire element to keep the coupling matrix elements bounded. Dotted these testing functions into Equation (7) and taking

the inner product results in the expression

$$\begin{aligned} \int_S \left[ \hat{\mathbf{n}} \times \overline{\mathbf{E}}^i(\bar{\boldsymbol{\rho}}) \right] \cdot \bar{\boldsymbol{\theta}}_t(\bar{\boldsymbol{\rho}}) d\bar{\boldsymbol{\rho}} &= - \int_S \left[ \hat{\mathbf{n}} \times \sum_{b=0}^B \overline{\mathbf{E}}^s(J_b \bar{\boldsymbol{\phi}}_b(\bar{\boldsymbol{\rho}})) \right] \cdot \bar{\boldsymbol{\theta}}_t(\bar{\boldsymbol{\rho}}) d\bar{\boldsymbol{\rho}} \\ &= - \sum_{b=0}^B J_b \int_S \left[ \hat{\mathbf{n}} \times \overline{\mathbf{E}}^s(\bar{\boldsymbol{\phi}}_b(\bar{\boldsymbol{\rho}})) \right] \cdot \bar{\boldsymbol{\theta}}_t(\bar{\boldsymbol{\rho}}) d\bar{\boldsymbol{\rho}} \end{aligned} \quad (8)$$

where  $t = 0, 1, \dots, B$  and  $\overline{\mathbf{E}}^s(\bar{\boldsymbol{\phi}}_b(\bar{\boldsymbol{\rho}}))$  is the field at  $\bar{\boldsymbol{\rho}}$  radiated by the  $b^{\text{th}}$  basis function. Equation (8) now defines a  $(B + 1) \times (B + 1)$  matrix equation which can be expressed in matrix form as

$$\begin{bmatrix} V_0 \\ V_t \end{bmatrix} = \begin{bmatrix} Z_{00} & Z_{0b} \\ Z_{t0} & Z_{tb} \end{bmatrix} \begin{bmatrix} J_0 \\ J_b \end{bmatrix} \quad (9)$$

where the 0 subscript denotes the basis and testing modes associated with the PBF. Clearly the "influence" of the neighboring infinite array on the edge elements is contained in the cross-coupling terms,  $Z_{0b}$  and  $Z_{t0}$ . Note the terms with the  $t$  and  $b$  subscripts actually represent sub-arrays and sub-matrices associated with the edge elements. One can calculate the entries in the matrix Equation (9) for the wire array from Equation (3) by using the appropriate dyadic Green's function.

$$V_0 = e^{-j\beta \hat{\mathbf{s}} \cdot \bar{\boldsymbol{\rho}}_0} \quad (10)$$

$$V_t = e^{-j\beta \hat{\mathbf{s}} \cdot \bar{\boldsymbol{\rho}}_t} \quad (11)$$

$$Z_{00} = -\frac{\omega\mu}{4} \sum_{q=0}^{\infty} H_0^{(2)}(\beta|\bar{\boldsymbol{\rho}}_0 - \bar{\boldsymbol{\rho}}_q|) e^{-j\beta \hat{\mathbf{s}} \cdot \bar{\boldsymbol{\rho}}_q} \quad (12)$$

$$Z_{0b} = -\frac{\omega\mu}{4} H_0^{(2)}(\beta|\bar{\boldsymbol{\rho}}_0 - \bar{\boldsymbol{\rho}}_b|) \quad (13)$$

$$Z_{t0} = -\frac{\omega\mu}{4} \sum_{q=0}^{\infty} H_0^{(2)}(\beta|\bar{\boldsymbol{\rho}}_t - \bar{\boldsymbol{\rho}}_q|) e^{-j\beta \hat{\mathbf{s}} \cdot \bar{\boldsymbol{\rho}}_q} \quad (14)$$

$$Z_{tb} = -\frac{\omega\mu}{4} H_0^{(2)}(\beta|\bar{\boldsymbol{\rho}}_t - \bar{\boldsymbol{\rho}}_b|) \quad (15)$$

One can also invoke the reciprocity theorem [17] to exploit symmetries in the edge element sub-matrix thereby reducing the matrix fill time. Standard matrix equation techniques can then be employed to solve the system, obtaining the desired current coefficients.

The final step in the hybrid PMM/MM procedure involves using the calculated current expansion coefficients to determine the scattered fields via a radiation integral. Specifically, one finds the field from a large finite array by solving the semi-infinite array problem twice, once for each edge. One then synthesizes the currents on the finite array by shifting the edge element currents appropriately and assigning the “central” elements the PBF current amplitude with an appropriate linear phase. The radar echo width is then calculated from the scattered fields.

### *1.3 Dissertation Summary*

The remaining chapters take the general procedure just outlined and apply it to two geometries; a two-dimensional wire array and a three-dimensional slot array, both in a stratified dielectric media. Chapter II begins by deriving the coupling matrix entries for the wire array. It presents both spatial and spectral domain forms for the radiation from the PBF and edge element basis functions as well as addresses the complexities introduced by adding a dielectric slab to the geometry. Next, the chapter formulates the excitation vector entries, again taking into account the slab boundaries. Finally, the chapter concludes with a discussion of how the solution vector entries can be used to calculate a far-field radiation pattern for a large finite array. Chapter III gives the corresponding analysis for the slot array. Chapter IV examines the validity of the PBF formulation through reference code and measurement comparisons. In general, the array’s induced currents are compared, since radar echo width (REW) calculations tend to smooth out errors in the solution vector. For the measurement comparisons, however, the author was forced to use RCS calculations as only measured RCS data was available. Finally, Chapter V re-caps the dissertation, summarizing the salient results and suggesting areas for future research.

## II. Two-Dimensional Semi-Infinite Wire Array

A journey of a thousand miles begins with a single step.

- A Chinese Proverb

As a proof-of-concept, this chapter develops the hybrid PMM/MM solution given by Equation (9) for the simple two-dimensional wire geometry depicted in Figure 4. The resulting expressions form the basis for the wire computer code validated in Chapter IV. Equation (9) naturally breaks down into three parts. This chapter follows this organization by first examining the coupling matrix, followed by the excitation vector, and finally the solution vector. Where appropriate, each of these sections is divided into subsections covering the homogeneous and stratified media cases respectively.

### 2.1 Coupling Matrix

The free-space analysis used to illustrate the PBF concept in Chapter I forms the common starting point for both the dielectric coated wire and slot arrays. In the wire case, the array is in a

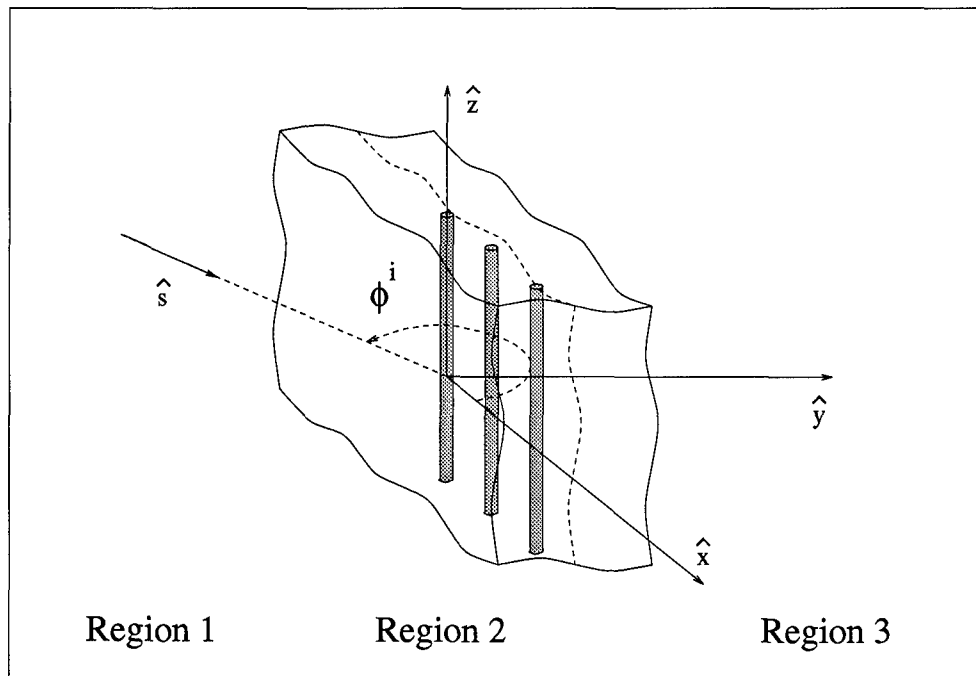


Figure 4. Semi-Infinite Wire Array Geometry

homogeneous media with region two's constitutive parameters (see Figure 4). Since the filamentary currents are  $\hat{z}$  directed, one can write Equation (8) as the scalar equation

$$E_z^i(\bar{\rho}_t) = -\frac{\omega\mu}{4} \left[ J_o \sum_{q=0}^{\infty} H_0^{(2)}(\beta|\bar{\rho}_t - \bar{\rho}_q|) e^{-j\beta\hat{s}\cdot\bar{\rho}_q} + \sum_{b=1}^B J_b H_0^{(2)}(\beta|\bar{\rho}_t - \bar{\rho}_b|) \right], \quad \bar{\rho}_t \in S \quad (16)$$

where  $\bar{\rho}_t$  (test function location) is confined to the Huygens surface of the  $t^{\text{th}}$  wire,  $\bar{\rho}_q$  (PBF element location) is confined to the center of the  $q^{\text{th}}$  wire,  $\bar{\rho}_b$  (basis function location) is confined to the center of the  $b^{\text{th}}$  wire, and all quantities related to the constitutive parameters are those of region two. Note how the shifting property of the Dirac delta function reduces the surface integrals to point evaluations. Equation (16) forces equality between the fields radiated by the equivalent currents and the incident field at these points on the Huygens surface.

Equation (16) is known as a “spatial domain” expression. In order to account for the dielectric slab, one could derive a non-free-space Green's function satisfying the appropriate field boundary conditions at the slab boundaries. The author chose an alternative approach based on a “spectral domain” representation of Equation (16). In the spectral domain, one deals with plane wave field expansions. Thus, planar boundaries can be introduced with relative ease via Fresnel coefficients [17]. In addition, the spectral domain summations are, in general, more convergent than their spatial domain counterparts, leading to more efficient computer codes. The means for transforming to the spectral domain vary for the different parts of Equation (16). Specifically, one can partition the right hand side into two parts representing the fields radiated by the PBF and the fields radiated by the individual edge elements. The following subsections develop the spectral domain representation of these fields which are related to the coupling matrix entries through the unknown current coefficients,  $J_b$ .

### 2.1.1 Physical Basis Function.

#### 2.1.1.1 Physical Basis Function Radiating to Test Function in a Homogeneous Media.

Figure 5 depicts the PBF in a homogeneous media with constitutive parameters  $\epsilon_2$  and  $\mu_2$ . One can

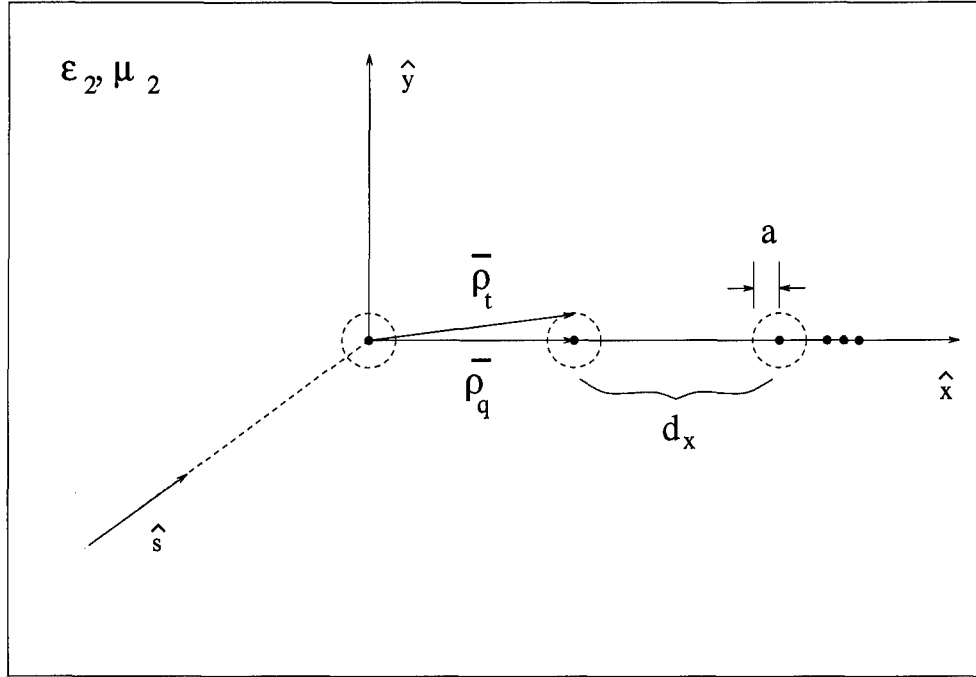


Figure 5. PBF Radiating to Test Function Location in Homogeneous Media

express the fields radiated by the PBF in the spatial domain as a collection of cylindrical waves.

$$\begin{aligned}
 E_z^{PBF}(\bar{\rho}_t) &= -\frac{\omega\mu J_0}{4} \sum_{q=0}^{\infty} H_0^{(2)}(\beta|\bar{\rho}_t - \bar{\rho}_q|) e^{-j\beta\hat{s}\cdot\bar{\rho}_q} \\
 &= -\frac{\omega\mu J_0}{4} \sum_{q=0}^{\infty} H_0^{(2)}\left(\beta\sqrt{(qd_x - x_t)^2 + y_t^2}\right) e^{-j\beta s_x qd_x}
 \end{aligned} \quad (17)$$

Taking a hint from Munk's work [26, 28], one would like to use the Poisson sum formula to convert Equation (17) to the spectral domain. Unfortunately, the one-sided summation prevents a direct application of the Poisson sum formula. Appendix A presents a one-sided version of the regular Poisson sum formula [29] applicable to summations such as in Equation (17). Equipped with this formula, one can convert Equation (17) to a collection of plane waves. Specifically, one uses the transform pair [3]

$$g(t) = \frac{e^{j(xt - y\sqrt{\beta^2 - t^2})}}{\pi\sqrt{\beta^2 - t^2}} \Leftrightarrow G(\omega) = H_0^{(2)}\left(\beta\sqrt{(\omega - x)^2 + y^2}\right) \quad (18)$$

with the following variable substitutions in Equation (185)

$$\omega_o = d_x \quad (19)$$

$$t = -\beta s_x \quad (20)$$

to arrive at the spectral domain expression

$$\begin{aligned} E_z^{PBF}(\bar{\rho}_t) &= -\frac{\omega\mu J_0}{4d_x} \sum_{k=-\infty}^{\infty} \left\{ \frac{e^{-j \left[ x_t(\beta s_x + \frac{k2\pi}{d_x}) + y_t \sqrt{\beta^2 - (\beta s_x + \frac{k2\pi}{d_x})^2} \right]}}{\sqrt{\beta^2 - (\beta s_x + \frac{k2\pi}{d_x})^2}} \right. \\ &\quad \left. - \frac{j}{\pi} \int_{-\infty}^{\infty} \frac{e^{-j[-x_t\tau + y_t \sqrt{\beta^2 - \tau^2}]} e^{j \frac{d_x}{2} (\beta s_x + \frac{k2\pi}{d_x} + \tau)}}{\sqrt{\beta^2 - \tau^2} (\beta s_x + \frac{k2\pi}{d_x} + \tau)} d\tau \right\} \\ &= -\frac{\eta J_0}{4d_x} \sum_{k=-\infty}^{\infty} \left\{ \frac{e^{-j\beta \hat{\rho} \cdot \bar{\rho}_t}}{\rho_y} + \frac{j}{\pi} \int_{-\infty}^{\infty} \frac{e^{-j\beta \hat{\tau} \cdot \bar{\rho}_t} e^{-j\beta \frac{d_x}{2} (\tau_x - \rho_x)}}{\tau_y (\tau_x - \rho_x)} d\tau_x \right\} \quad (21) \end{aligned}$$

where the plane wave propagation vectors are

$$\begin{aligned} \hat{\rho} &= \hat{x} \left( s_x + \frac{k\lambda}{d_x} \right) + \hat{y} \sqrt{1 - \left( s_x + \frac{k\lambda}{d_x} \right)^2} \\ &= \hat{x} \rho_x + \hat{y} \rho_y \quad (22) \end{aligned}$$

$$\hat{\tau} = \hat{x} \tau_x + \hat{y} \sqrt{1 - \tau_x^2} \quad (23)$$

Note that both  $\rho_y$  and  $\tau_y$  are defined to be either positive real or negative imaginary in order to satisfy the radiation boundary condition. (*i.e.* The fields must be bounded at infinity.) This also restricts  $y_t$  to the upper half-plane.

Equation (21) gives the spectral domain representation of the fields radiated by the PBF in a homogeneous media. As promised, this form is more convergent than the spatial domain form owing to the exponential damping in the higher order spectral terms. Specifically, when  $\left| s_x + \frac{k\lambda}{d_x} \right| > 1$  and  $|\tau_x| > 1$  the plane waves become evanescent, decaying rapidly for test locations out of the array plane. It is also interesting to note the one-sided Poisson sum generates both discrete and continuous



spectra. The discrete spectrum incorporates the periodic nature of the array whereas the continuous spectrum accounts for the diffraction effects caused by the array termination. In fact, the similarity of the continuous spectral integral to the diffraction integral encountered in the half-plane scattering problem provides clues to its efficient evaluation.

The first of these clues allows one to remove the weak singularity,  $\frac{1}{\tau_y}$ , from the integrand. Felsen and Marcuvitz [11] suggest the variable substitution

$$\tau_x = \sin(\nu) \quad (24)$$

$$\tau_y = \cos(\nu) \quad (25)$$

$$d\tau_x = \cos(\nu) d\nu \quad (26)$$

leading to the *angular* spectral integral

$$I_k = \oint_C \frac{e^{-j\beta[(x_t + \frac{d_x}{2}) \sin(\nu) + y_t \cos(\nu)]}}{(\sin(\nu) - \rho_x)} d\nu \quad (27)$$

The integration contour,  $C$ , lies in the regions of the complex  $\nu$  plane where  $Im\{\cos(\nu)\} < 0$  as indicated by the shaded areas in Figure 6. The deviation of  $C$  from the real axis represents a slight loss in the wave number  $\beta$ . Note the pole at  $\nu_o = \sin^{-1}(\rho_x)$  is not shown in the figure. One can further simplify Equation (27) by defining a new cylindrical coordinate system displaced from the origin by one half the inter-element spacing (Figure 7).

With the definitions

$$\tilde{\rho}_t = \sqrt{\left(x_t + \frac{d_x}{2}\right)^2 + y_t^2} \quad (28)$$

$$\tilde{\phi}_t = \tan^{-1} \left( \frac{\left(x_t + \frac{d_x}{2}\right)}{y_t} \right) \quad (29)$$

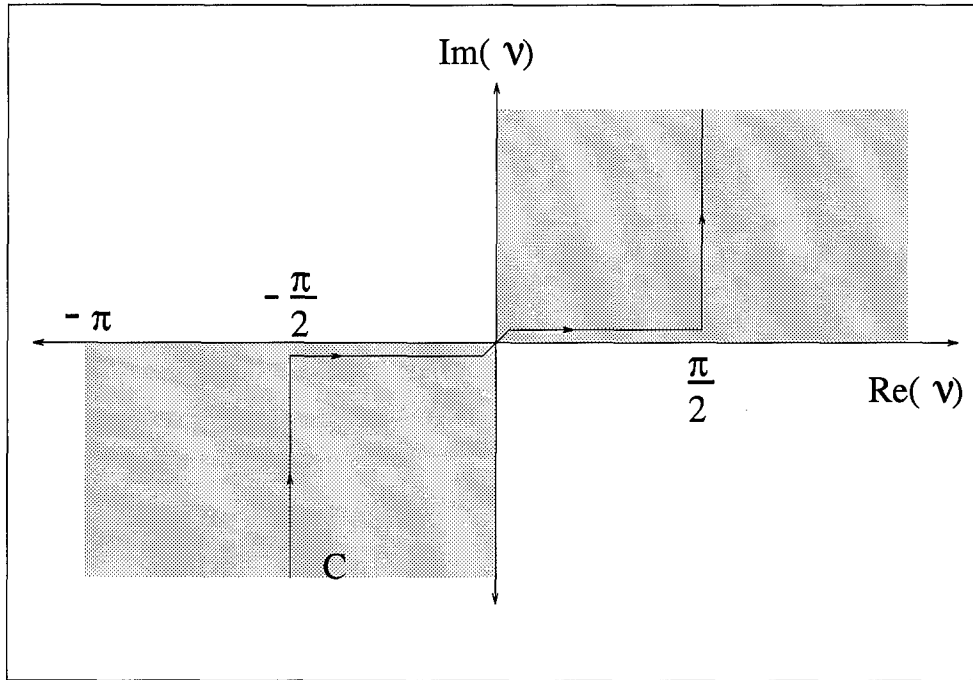


Figure 6. Angular Spectral Integral Contour

and the cosine addition formula, the angular spectral integral becomes

$$I_k = \oint_C \frac{e^{-j\beta\tilde{\rho}_t \cos(\nu - \tilde{\phi}_t)}}{(\sin(\nu) - \rho_x)} d\nu \quad (30)$$

One is now faced with the task of evaluating Equation (30). Even though it is a principle value integral, the non-integrable singularity at  $\nu_o$  makes straight-forward numerical integration difficult. Again taking a clue from its similarity to a diffraction integral, one might consider evaluating Equation (30) asymptotically. In fact, for many of the off-diagonal coupling matrix terms,  $\beta\tilde{\rho}_t$  can be considered a large parameter. Appendix C presents such an asymptotic evaluation, clearly demonstrating the tremendous computational advantage over numerical evaluation schemes.

Where asymptotic evaluation is not possible, one must evaluate Equation (30) numerically. The author found the following singularity extraction technique works quite well. One first breaks the integration contour into three regions, the vertical path  $[-(\frac{\pi}{2} + j\infty), -\frac{\pi}{2}]$ , the real axis  $(-\frac{\pi}{2}, \frac{\pi}{2})$ ,

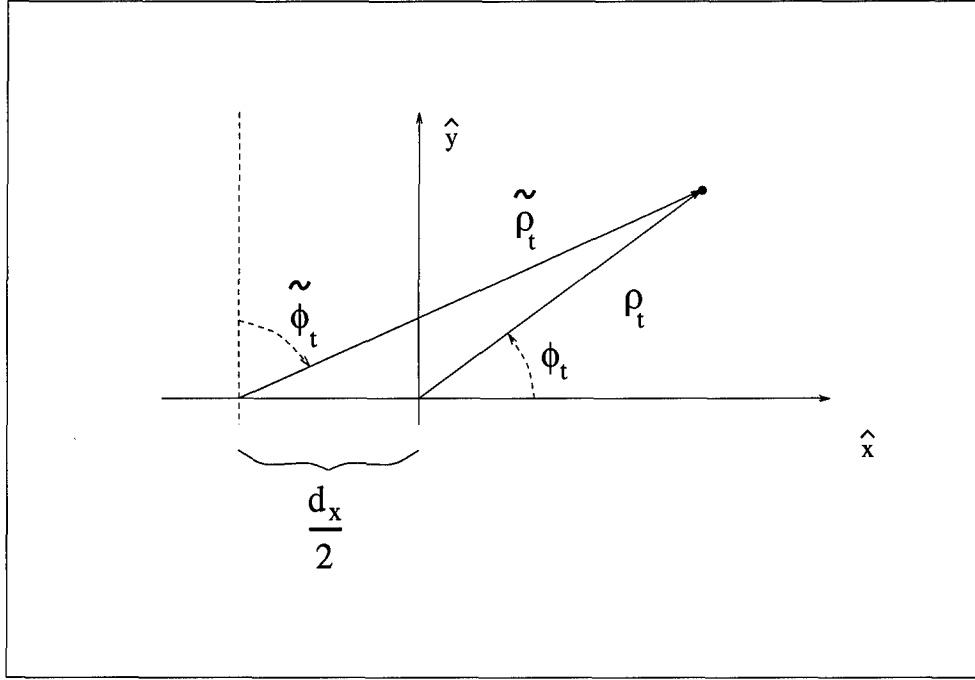


Figure 7. Alternate Cylindrical Coordinate System

and the vertical path  $(\frac{\pi}{2}, \frac{\pi}{2} + j\infty]$ . Along the vertical paths, one redefines  $\nu_{old} = \mp(\frac{\pi}{2} + j\nu_{new})$  where  $0 < \nu_{new} < \infty$ , transforming them to the real axis. Thus, the angular spectrum transformation for these paths becomes

$$\tau_x = \mp \sin\left(\frac{\pi}{2} + j\nu\right) = \mp \cosh(\nu) \quad (31)$$

Equation (30) now can be written

$$\begin{aligned} I_k &= \left[ -j \int_0^{\infty} \frac{e^{j\beta\tilde{\rho}_t \sin(j\nu + \tilde{\phi}_t)}}{(\cosh(\nu) + \rho_x)} d\nu + \int_{-\frac{\pi}{2}}^{\frac{\pi}{2}} \frac{e^{-j\beta\tilde{\rho}_t \cos(\nu - \tilde{\phi}_t)}}{(\sin(\nu) - \rho_x)} d\nu + j \int_0^{\infty} \frac{e^{j\beta\tilde{\rho}_t \sin(j\nu - \tilde{\phi}_t)}}{(\cosh(\nu) - \rho_x)} d\nu \right] \\ &= I_1 + I_2 + I_3 \end{aligned} \quad (32)$$

where the principle value occurs in only one integral for a particular value of  $\rho_x$ .

One next forces the numerator of the appropriate singular integral to go to zero exactly at the singular point, effectively removing the singularity. The extracted singular integral is then in a form

suitable for an analytic solution. Thus, Equation (32) becomes

$$\begin{aligned}
 I_k = & \left[ \int_0^{\infty} \frac{(-je^{j\beta\tilde{\rho}_t} \sin(j\nu + \tilde{\phi}_t) - N1_o)}{(\cosh(\nu) + \rho_x)} d\nu + N1_o \int_0^{\infty} \frac{d\nu}{(\cosh(\nu) + \rho_x)} \right. \\
 & + \int_{-\frac{\pi}{2}}^{\frac{\pi}{2}} \frac{(e^{-j\beta\tilde{\rho}_t} \cos(\nu - \tilde{\phi}_t) - N2_o)}{(\sin(\nu) - \rho_x)} d\nu + N2_o \int_{-\frac{\pi}{2}}^{\frac{\pi}{2}} \frac{d\nu}{(\sin(\nu) - \rho_x)} \\
 & \left. + \int_0^{\infty} \frac{(je^{j\beta\tilde{\rho}_t} \sin(j\nu - \tilde{\phi}_t) - N3_o)}{(\cosh(\nu) - \rho_x)} d\nu + N3_o \int_0^{\infty} \frac{d\nu}{(\cosh(\nu) - \rho_x)} \right] \quad (33)
 \end{aligned}$$

where

$$N1_o = -je^{j\beta\tilde{\rho}_t} \sin(j\nu_o + \tilde{\phi}_t) \quad (34)$$

$$N2_o = e^{-j\beta\tilde{\rho}_t} \cos(\nu_o - \tilde{\phi}_t) \quad (35)$$

$$N3_o = je^{j\beta\tilde{\rho}_t} \sin(j\nu_o - \tilde{\phi}_t) \quad (36)$$

Abramowitz and Stegun [1] provide analytic solutions for the extracted integrals

$$\int_0^{\infty} \frac{d\nu}{(\cosh(\nu) + \rho_x)} = \begin{cases} \frac{2}{\sqrt{1-\rho_x^2}} \tan^{-1} \left( \frac{\sqrt{1-\rho_x^2}}{1+\rho_x} \right) \\ \frac{1}{\sqrt{\rho_x^2-1}} \ln \left| \frac{1+\rho_x + \sqrt{\rho_x^2-1}}{1+\rho_x - \sqrt{\rho_x^2-1}} \right| \end{cases} \quad (37)$$

$$\int_{-\frac{\pi}{2}}^{\frac{\pi}{2}} \frac{d\nu}{(\sin(\nu) - \rho_x)} = \begin{cases} 0 \\ \frac{2}{\sqrt{\rho_x^2-1}} \left[ \tan^{-1} \left( \frac{1-\rho_x}{\sqrt{\rho_x^2-1}} \right) - \tan^{-1} \left( \frac{1+\rho_x}{\sqrt{\rho_x^2-1}} \right) \right] \end{cases} \quad (38)$$

$$\int_0^{\infty} \frac{d\nu}{(\cosh(\nu) - \rho_x)} = \begin{cases} \frac{2}{\sqrt{1-\rho_x^2}} \tan^{-1} \left( \frac{\sqrt{1-\rho_x^2}}{1-\rho_x} \right) \\ \frac{1}{\sqrt{\rho_x^2-1}} \ln \left| \frac{1-\rho_x + \sqrt{\rho_x^2-1}}{1-\rho_x - \sqrt{\rho_x^2-1}} \right| \end{cases} \quad (39)$$

where one chooses either the upper or lower line for  $\rho_x^2 < 1$  or  $\rho_x^2 > 1$ , respectively. Thus, the spectral domain expression for the fields radiated in a homogeneous media can be written

$$E_z^{PBF}(\bar{\rho}_t) = -\frac{\eta J_0}{4d_x} \sum_{k=-\infty}^{\infty} \left\{ \frac{e^{-j\beta \hat{\rho} \cdot \bar{\rho}_t}}{\rho_y} + \frac{j e^{j\beta \rho_x \frac{d_x}{2}}}{\pi} I_k \right\} \quad (40)$$

where  $I_k$  is evaluated either asymptotically or numerically.

Equations (17) and (40) provide alternative representations for the field radiated by the PBF. These expressions, with the  $J_0$  constant removed, define the mutual coupling between the basis and testing functions. Since filling the coupling matrix constitutes a significant portion of the overall computation time, one would like to use the most efficient form. The next few paragraphs examine both the spatial and spectral domain expressions for the free-space semi-infinite wire array Green's function calculated from Equations (17) and (40) by multiplying with the constant  $\frac{j}{\omega \mu J_0}$ . Figure 5's geometry, with parameters  $d_x = 0.1\lambda_o$ ,  $\hat{s} = -[\hat{x} \cos(30^\circ) + \hat{y} \sin(30^\circ)]$ , and  $(\epsilon_2, \mu_2) = (\epsilon_o, \mu_o)$ , serves as a typical test case. The test location,  $\bar{\rho}_t$ , is scanned along a path parallel to the  $\hat{x}$  axis at an "elevation" of  $y_t = 0.1\lambda_o$ .

Figure 8 contains the Green's function's real and imaginary components and magnitude as the test point sweeps past the array edge. As one would expect, the magnitude of the Green's function decays monotonically to the left, away from the array edge. Conversely, as the test point moves to the right over the array, the magnitude settles down to the same value one obtains from a fully infinite array. Note that the data in this figure can come from either the spatial or spectral domain expressions. The question is which one is more efficient.

Figure 9 shows the number of terms required by each expression to converge to the criteria

$$\left| \frac{\text{Sum} - \text{Truth}}{\text{Truth}} \right| < 0.0001 \quad (41)$$

The "Truth" represents the value obtained from either expression pushed to the point where the next term does not alter the previous partial sum by more than machine accuracy. In addition, the author used the "circle-average" summation acceleration technique described in Appendix B to reduce the

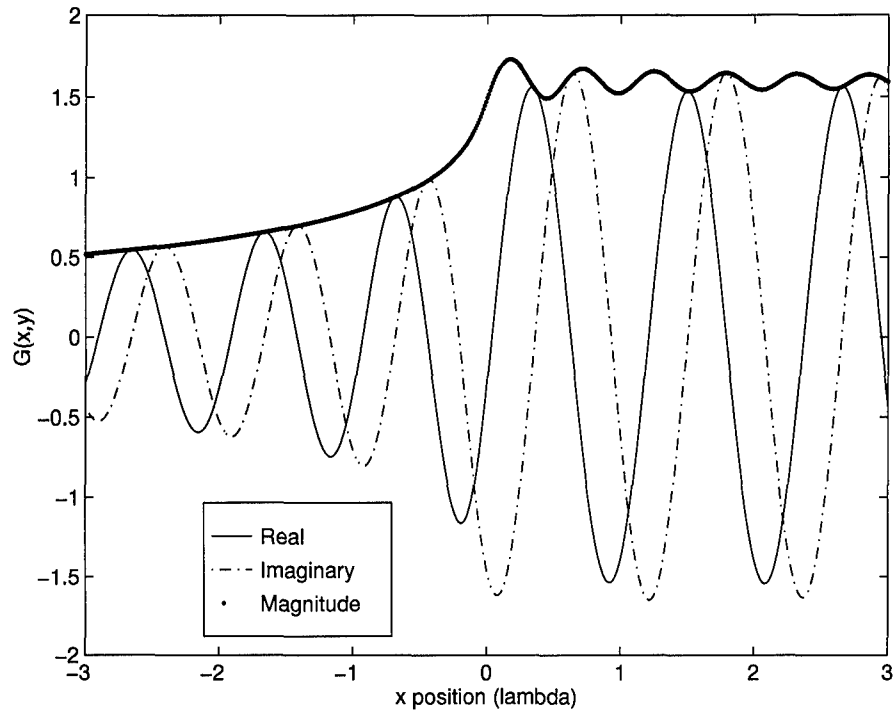


Figure 8. Semi-Infinite Wire Array Green's Function

number of terms required by the spatial domain expression. The spectral domain summation did not require acceleration. Clearly, the spectral domain is the domain of choice if one is interested in reducing the number of summation terms.

The final figure in this section numerically confirms the proper evaluation of the continuous spectral integral in Equation (40). From Equations (174) and (185) in Appendix A, it is clear that, as the test point moves to the right over the semi-infinite array, the continuous spectrum should settle down to a value equal to the discrete spectrum which, in turn, is exactly half the value obtained for a fully infinite array. Figure 10 plots the discrete and continuous spectra in the complex plane as the test point moves on the scan path from  $1.0\lambda_0$  to the left of the array edge to  $1.0\lambda_0$  to the right of the array edge. The points designated by the "+" show the discrete and continuous spectra have nearly the same magnitude and phase over the array. As the test point moves past the array edge ("x") to a location left of the array ("o"), notice how the magnitudes again become similar, but now are strongly

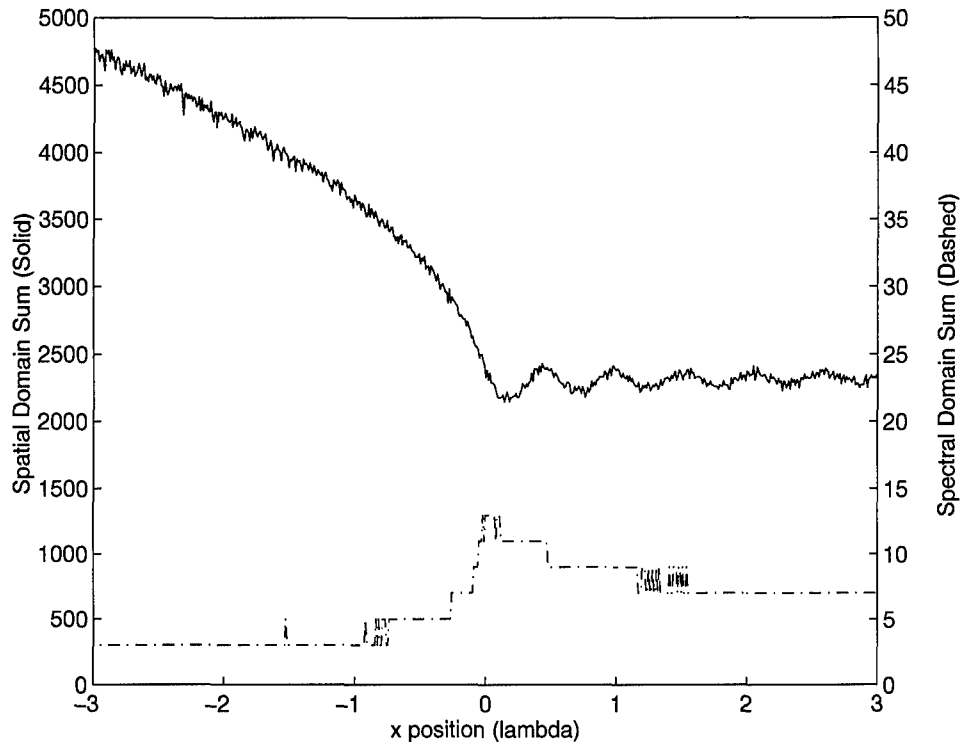


Figure 9. Number of Terms Required for Convergence

“out of phase.” The resulting cancelation reduces the field magnitude as the test point moves away from the array.

To re-cap, this section first developed and then examined the spatial and spectral domain expressions for the mutual coupling terms associated with the PBF in a homogeneous media. The results clearly demonstrate that, for most cases where the test location is out of the plane of the array, the spectral domain expression is preferred. The next section addresses the geometry containing a dielectric slab. There the other advantage of the spectral domain form will be apparent, namely, the ease with which one can introduce planar boundaries.

*2.1.1.2 Physical Basis Function Radiating to Test Function in a Stratified Media.* As mentioned earlier, the homogeneous media analysis forms the foundation for introducing a layered structure. Consider adding a dielectric slab to Figure 5. In addition to the direct coupling between the

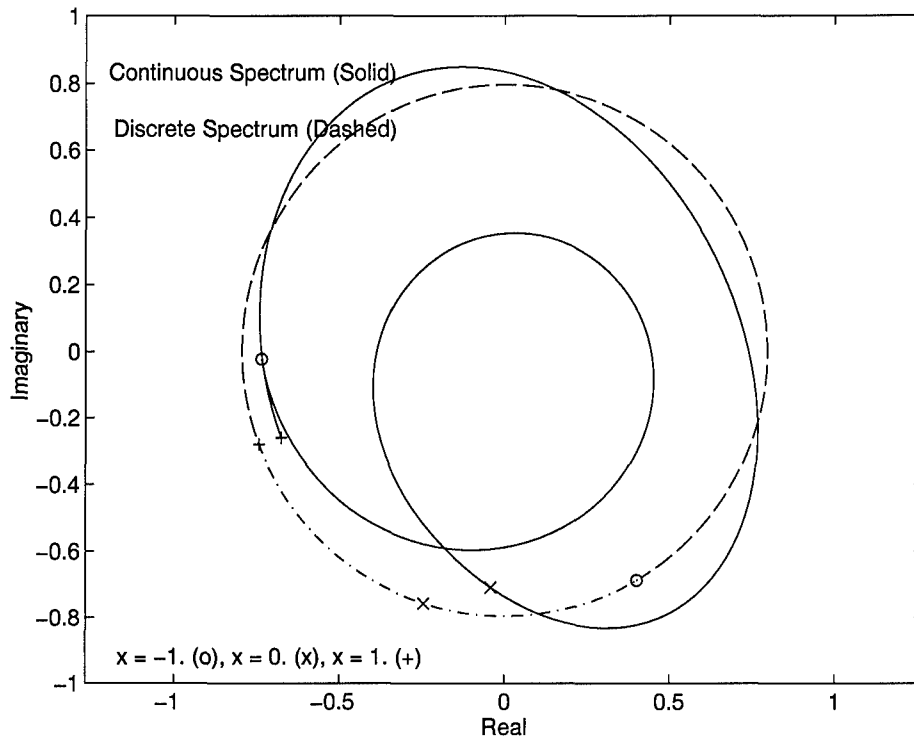


Figure 10. Complex Spectra

PBF and the test function at  $\bar{\rho}_t$ , one must now account for the plane waves reflected back and forth between the two boundaries (Figure 11). Fortunately, these boundaries are infinite parallel planes. One can use the concept of effective Fresnel coefficients [17] to calculate the plane waves' magnitude and phase as they reflect off the boundaries. In essence, the problem comes down to determining the composite effect of a plane wave radiated by the PBF rattling between the slab boundaries and then terminating at the test location.

In his work on periodic surfaces in stratified dielectric media, Munk [26, 28] developed a set of effective reflection and transmission coefficients useful for propagating a plane wave through an arbitrary number of parallel dielectric slabs. His coefficients use a polarization decomposition based on the plane of incidence shown in Figure 12. According to Munk's convention,  $\eta$  lies in the plane of incidence and is measured from the negative  $\hat{y}$  axis, whereas  $\alpha$  lies in the  $xz$  plane and is measured from the  $\hat{x}$  axis. The author adopts Munk's convention for this research. The interested reader is



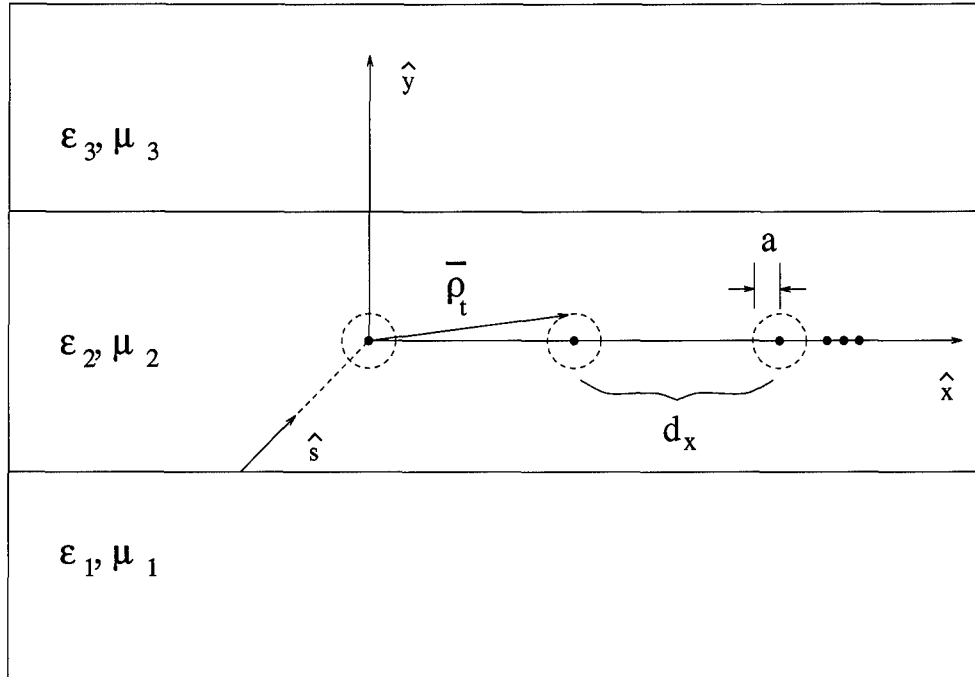


Figure 11. PBF Radiating to Test Function Location in Stratified Media

referred to the cited reports for details concerning the coefficients' development. Since the incident plane wave propagation vector is confined to the  $xy$  plane, the  $\hat{z}$  polarized fields are perpendicularly polarized and require the following reflection and transmission coefficients<sup>1</sup>

$$\tau_{l,l+1} = \frac{2\eta_{(l+1)}\varrho_{y(l)}}{\eta_{(l+1)}\varrho_{y(l)} + \eta_{(l)}\varrho_{y(l+1)}} \quad (42)$$

$$\Gamma_{l,l+1} = \frac{\eta_{(l+1)}\varrho_{y(l)} - \eta_{(l)}\varrho_{y(l+1)}}{\eta_{(l+1)}\varrho_{y(l)} + \eta_{(l)}\varrho_{y(l+1)}} \quad (43)$$

where  $\varrho_{y(l)}$  is the plane wave propagation vector's  $\hat{y}$  component in the  $l^{\text{th}}$  slab and  $\eta_{(l)}$  is the slab's impedance. Note these coefficients apply to half-space boundaries only. For the multi-layer geometries discussed in Chapter III, one must use the *effective* Fresnel coefficients defined by Munk.

<sup>1</sup>These are valid for waves propagating in a direction with a positive  $\hat{y}$  component. One can calculate the reflection coefficient for waves with a negative  $\hat{y}$  component from the relationship,  $\Gamma_{l+1,l} = -\Gamma_{l,l+1}$ .

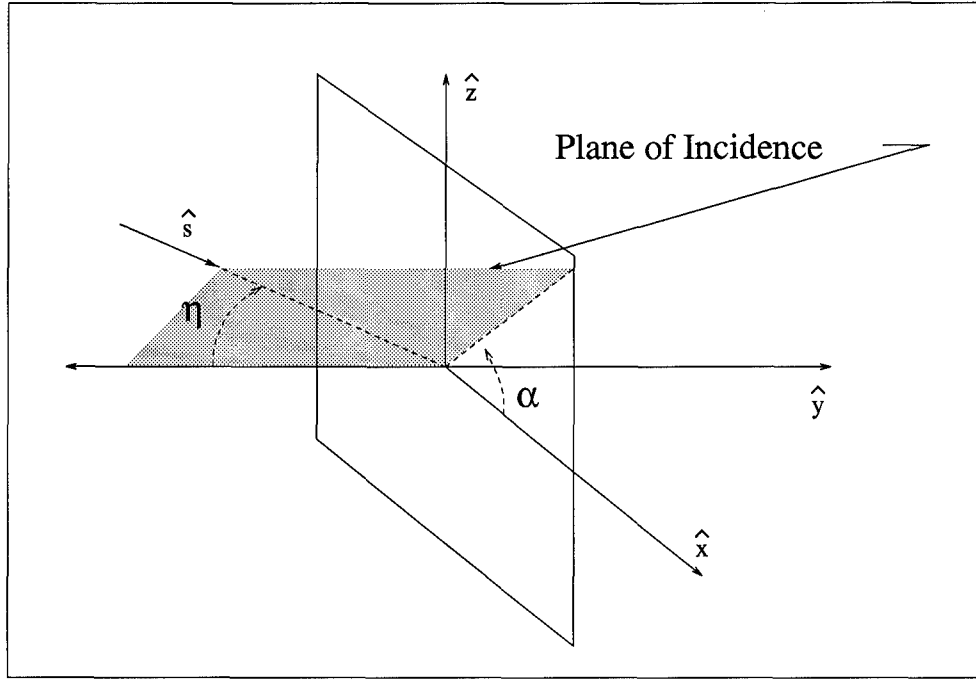


Figure 12. Plane Wave Polarization Decomposition

Now, to determine the composite plane wave at  $\bar{\rho}_t$ , one groups the bouncing plane waves into the four infinite summations shown in Figure 13. These summations are defined in terms of the plane wave's departure and arrival directions. For example, summation one consists of the plane waves leaving the PBF reference location,  $(x_0, y_0)$ , with a positive  $\hat{y}$  component and arriving at the test location,  $(x_t, y_t)$ , with a positive  $\hat{y}$  component. Summation two consists of the plane waves with a negative  $\hat{y}$  departure and positive  $\hat{y}$  arrival. Summation three consists of plane waves with a positive  $\hat{y}$  departure and a negative  $\hat{y}$  arrival. Finally, summation four consists of the plane waves with a negative  $\hat{y}$  departure and a negative  $\hat{y}$  arrival. Mathematically, these summations can be expressed

$$E_z^{direct} [1 + \Gamma_{23}\Gamma_{21}e^{-j\beta_2 2(y_2-y_1)\ell_{y2}} + \Gamma_{23}^2\Gamma_{21}^2e^{-j\beta_2 4(y_2-y_1)\ell_{y2}} + \dots] \quad (44)$$

$$E_z^{direct} [\Gamma_{21}e^{-j\beta_2 2(y_b-y_1)\ell_{y2}} + \Gamma_{21}^2\Gamma_{23}e^{-j\beta_2 2(y_b-2y_1+y_2)\ell_{y2}} + \dots] \quad (45)$$

$$E_z^{direct} [\Gamma_{23}e^{-j\beta_2 2(y_2-y_t)\ell_{y2}} + \Gamma_{23}^2\Gamma_{21}e^{-j\beta_2 2(2y_2-y_1-y_t)\ell_{y2}} + \dots] \quad (46)$$

$$E_z^{direct} [\Gamma_{21}\Gamma_{23}e^{-j\beta_2 2(y_b-y_t+y_2-y_1)\ell_{y2}} + \Gamma_{21}^2\Gamma_{23}^2e^{-j\beta_2 2(y_b-y_t+2(y_2-y_1))\ell_{y2}} + \dots] \quad (47)$$

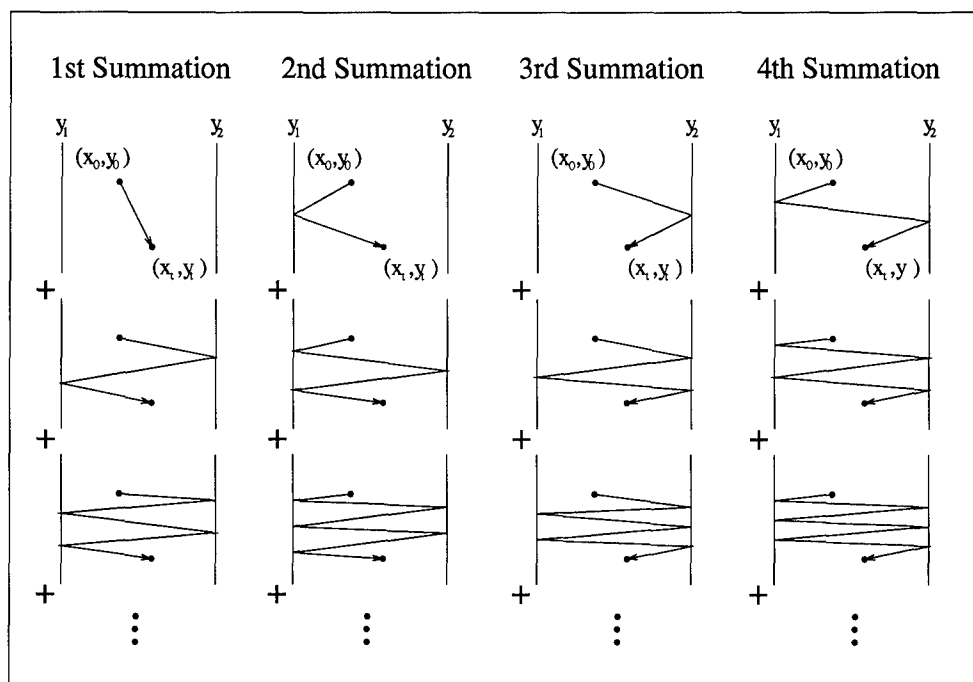


Figure 13. Decomposition of the Plane Waves Internally Reflected in the Dielectric Slab

where  $E_z^{direct}$  is the plane wave propagating directly to the test location without any bounces. In particular,  $E_z^{direct}$  is a spectral component from either the discrete or continuous spectra of the homogeneous media Equation (21). The author found it numerically expedient to subtract out the direct term from Equation (44) and express it in the spatial domain. The remaining summations are in the form of geometric series which can be expressed in closed form. Combining these summations, one arrives at a multiplier to the homogeneous media field expression which accounts for the presence of the stratified media. Munk calls this multiplier a “T-factor.”[26, 28]

One can now express the field radiated by the PBF in the dielectric slab as

$$\begin{aligned}
E_z^{PBF}(\bar{\rho}_t) = & -\frac{\beta_2 \eta_2 J_0}{4} \left[ \sum_{q=0}^{\infty} H_0^{(2)}(\beta_2 |\bar{\rho}_t - \bar{\rho}_q|) e^{-j\beta_2 \hat{\mathbf{s}}_2 \cdot \bar{\rho}_q} \right. \\
& + \frac{1}{\beta_2 d_x} \sum_{k=-\infty}^{\infty} \left\{ \frac{e^{-j\beta_2 \hat{\rho}_2 \cdot \bar{\rho}_t}}{\rho_{y2}} T(\rho_{y2}) \right. \\
& \left. \left. + \frac{j}{\pi} \int_{-\infty}^{\infty} \frac{e^{-j\beta_2 \hat{\mathbf{r}} \cdot \bar{\rho}_t} e^{-j\beta_2 \frac{d_x}{2} (\tau_x - \rho_{x2})}}{\tau_y (\tau_x - \rho_{x2})} T(\tau_y) d\tau_x \right\} \right] \quad (48)
\end{aligned}$$

where the T-factor<sup>2</sup> is

$$T(\rho_{y2}) = \frac{\Gamma_{23} e^{-j2\beta_2 (y_2 - y_1) \rho_{y2}} (1 - \Gamma_{12} e^{j2\beta_2 y_1 \rho_{y2}}) - \Gamma_{12} e^{j2\beta_2 y_1 \rho_{y2}} (1 + \Gamma_{23} e^{-j2\beta_2 y_2 \rho_{y2}})}{1 + \Gamma_{12} \Gamma_{23} e^{-j2\beta_2 (y_2 - y_1) \rho_{y2}}} \quad (49)$$

Since Equation (48) is based on the homogeneous expression, the spectral integral has the same singularities as before. One can use the same regularization procedures to remove the weak  $\frac{1}{\tau_y}$  singularity and the singularities associated with the  $k$  dependent grating lobes. Unlike the homogeneous media case however, one must deal with the singularities introduced by the T-factor. These singularities occur when the dielectric slab has a greater permittivity<sup>3</sup> than the surrounding material, causing the spectral terms to excite surface waves in the dielectric slab. Quantitatively, this occurs when the denominator in Equation (49) goes to zero. Lets examine this situation in more detail.

Using Equation (23) in Equation (49), one can write the condition for a surface wave singularity as

$$1 + \Gamma_{12} \Gamma_{23} e^{-j2\beta_2 (y_2 - y_1) \sqrt{1 - \tau_{x2}^2}} = 0 \quad (50)$$

<sup>2</sup>The expression, as written, used the fact the PBF is located at  $y_0 = 0$ .

<sup>3</sup>Assuming non-magnetic materials.

where from Equation (43)

$$\Gamma_{12} = \frac{\sqrt{\frac{\epsilon_1}{\epsilon_2} - \tau_{x2}^2} - \sqrt{1 - \tau_{x2}^2}}{\sqrt{\frac{\epsilon_1}{\epsilon_2} - \tau_{x2}^2} + \sqrt{1 - \tau_{x2}^2}} \quad (51)$$

$$\Gamma_{23} = \frac{\sqrt{1 - \tau_{x2}^2} - \sqrt{\frac{\epsilon_3}{\epsilon_2} - \tau_{x2}^2}}{\sqrt{1 - \tau_{x2}^2} + \sqrt{\frac{\epsilon_3}{\epsilon_2} - \tau_{x2}^2}} \quad (52)$$

and  $\tau_{x2}$  sweeps through the range  $-\infty < \tau_{x2} < \infty$ . Recalling that Equation (48) is based on a closed form representation of the infinite series, one might be concerned with its validity over the entire  $\tau_{x2}$  range. Fortunately, as Skinner [33] indicated in his dissertation, one can add a slight loss to the  $\hat{y}$  propagation direction and thus extend the equation's valid range to the entire integration range. This approach also jives with the physical reality that no material is perfectly lossless. For  $|\tau_{x2}| < \min\left(\sqrt{\frac{\epsilon_1}{\epsilon_2}}, \sqrt{\frac{\epsilon_3}{\epsilon_2}}\right)$ , the corresponding plane wave forms such an acute angle with the slab normal that some of the wave escapes the surface (*i.e.*  $|\Gamma| < 1$ ) and no singularity exists. On the other hand, when  $|\tau_{x2}| > 1$ , the  $\hat{y}$  propagation becomes purely evanescent and the reflection coefficients can be written

$$\Gamma_{12} = \frac{\sqrt{\tau_{x2}^2 - \frac{\epsilon_1}{\epsilon_2}} - \sqrt{\tau_{x2}^2 - 1}}{\sqrt{\tau_{x2}^2 - \frac{\epsilon_1}{\epsilon_2}} + \sqrt{\tau_{x2}^2 - 1}} \quad (53)$$

$$\Gamma_{23} = \frac{\sqrt{\tau_{x2}^2 - 1} - \sqrt{\tau_{x2}^2 - \frac{\epsilon_3}{\epsilon_2}}}{\sqrt{\tau_{x2}^2 - 1} + \sqrt{\tau_{x2}^2 - \frac{\epsilon_3}{\epsilon_2}}} \quad (54)$$

where  $\epsilon_2 > \epsilon_1, \epsilon_3$ . Thus,

$$\left| \Gamma_{12} \Gamma_{23} e^{-j2\beta_2(y_2 - y_1)} \sqrt{1 - \tau_{x2}^2} \right| < 1 \quad (55)$$

and again no singularity exists. Therefore, the surface wave singularities are confined to the range,  $\min\left(\sqrt{\frac{\epsilon_1}{\epsilon_2}}, \sqrt{\frac{\epsilon_3}{\epsilon_2}}\right) < |\tau_{x2}| < 1$  and can be found by solving Equation (50) for  $\tau_{x2}$ .

Since Equation (50) is a transcendental equation, one must use an iterative technique such as Newton-Raphson to locate the singularities. Figures 14, 15, and 16 contain plots of the T-factor in

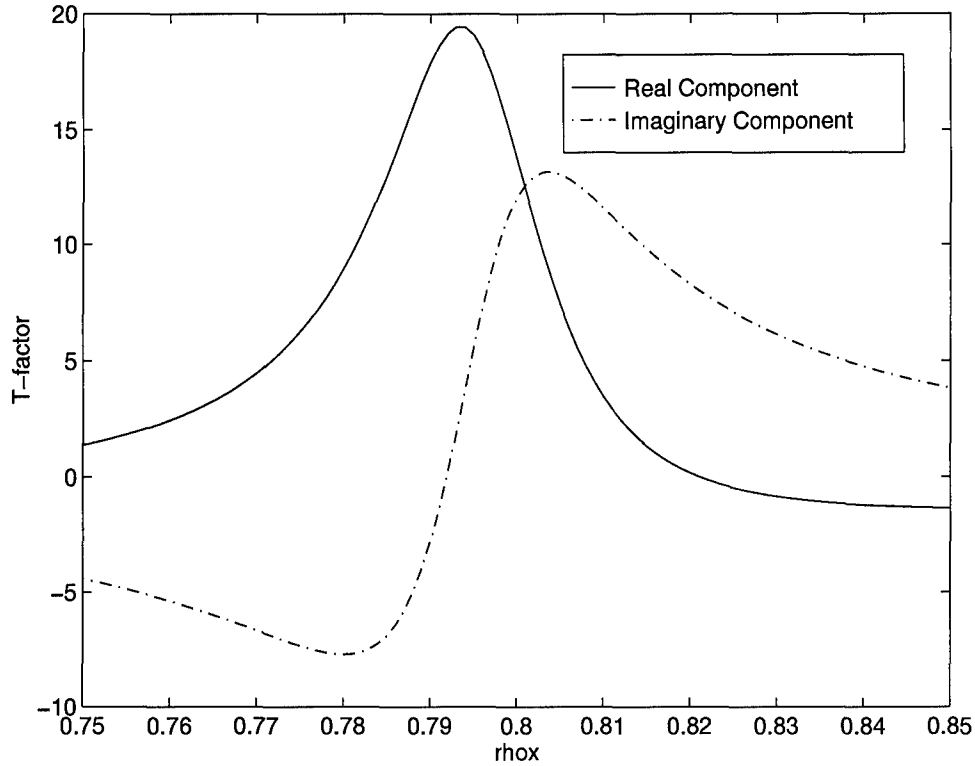


Figure 14. T-factor Singularity in a  $\epsilon_2 = 2\epsilon_0$ ,  $0.2\lambda_0$  Thick Slab with a 0.1 Loss

the neighborhood of one of these singularities. The geometry in these plots consists of a  $0.2\lambda_0$  thick slab in free-space with a relative permittivity  $\epsilon_2 = 2\epsilon_0$  and a  $\hat{y}$  directed loss of 0.1, 0.01, and 0.001 respectively. As Skinner [33] found in his work, the area under the real and imaginary curves approaches a limiting value as the loss goes to zero. Based on this observation, the author chose to handle the T-factor singularities by adding a slight  $\hat{y}$  directed loss to the denominator and integrating the continuous spectrum finely in the neighborhood of the former singularity.

Equation (56) gives the final form for the field radiated by the PBF. The author implemented this expression in the two-dimensional wire code validated in Chapter IV.

$$\begin{aligned}
 E_z^{PBF}(\bar{\rho}_t) = & -\frac{\beta_2 \eta_2 J_0}{4} \left[ \sum_{q=0}^{\infty} H_0^{(2)}(\beta_2 |\bar{\rho}_t - \bar{\rho}_q|) e^{-j\beta_2 \hat{s}_2 \cdot \bar{\rho}_q} \right. \\
 & \left. + \frac{1}{\beta_2 d_x} \sum_{k=-\infty}^{\infty} \left\{ \frac{e^{-j\beta_2 \hat{\rho}_2 \cdot \bar{\rho}_t}}{\rho_{y2}} T(\rho_{y2}) + \frac{j e^{j\beta_2 \rho_{x2} \frac{d_x}{2}}}{\pi} I_k \right\} \right] \quad (56)
 \end{aligned}$$

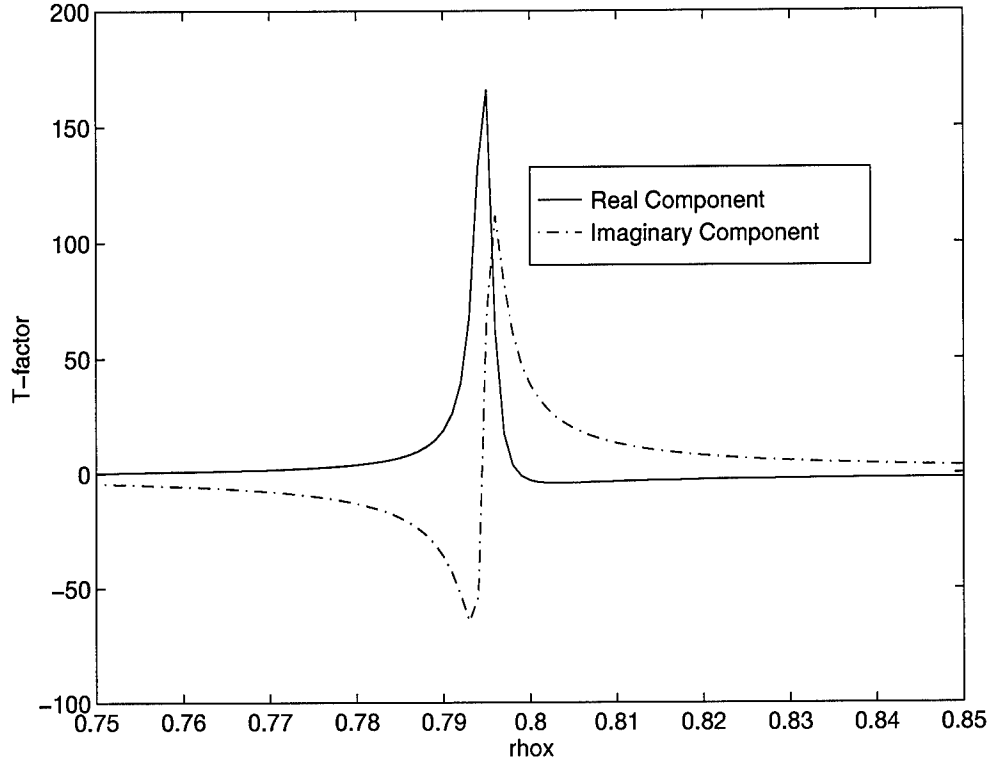


Figure 15. T-factor Singularity in a  $\epsilon_2 = 2\epsilon_o$ ,  $0.2\lambda_o$  Thick Slab with a 0.01 Loss

where

$$\begin{aligned}
 I_k = & \left[ \int_0^{\infty} \frac{\left( -j e^{j\beta_2 \tilde{\rho}_t} \sin(j\nu + \tilde{\phi}_t) T(-\cosh(\nu)) - N1_o \right)}{(\cosh(\nu) + \rho_{x2})} d\nu + N1_o \int_0^{\infty} \frac{d\nu}{(\cosh(\nu) + \rho_{x2})} \right. \\
 & + \int_{-\frac{\pi}{2}}^{\frac{\pi}{2}} \frac{\left( e^{-j\beta_2 \tilde{\rho}_t} \cos(\nu - \tilde{\phi}_t) T(\sin(\nu)) - N2_o \right)}{(\sin(\nu) - \rho_{x2})} d\nu + N2_o \int_{-\frac{\pi}{2}}^{\frac{\pi}{2}} \frac{d\nu}{(\sin(\nu) - \rho_{x2})} \\
 & \left. + \int_0^{\infty} \frac{\left( j e^{j\beta_2 \tilde{\rho}_t} \sin(j\nu - \tilde{\phi}_t) T(\cosh(\nu)) - N3_o \right)}{(\cosh(\nu) - \rho_{x2})} d\nu + N3_o \int_0^{\infty} \frac{d\nu}{(\cosh(\nu) - \rho_{x2})} \right] \quad (57)
 \end{aligned}$$

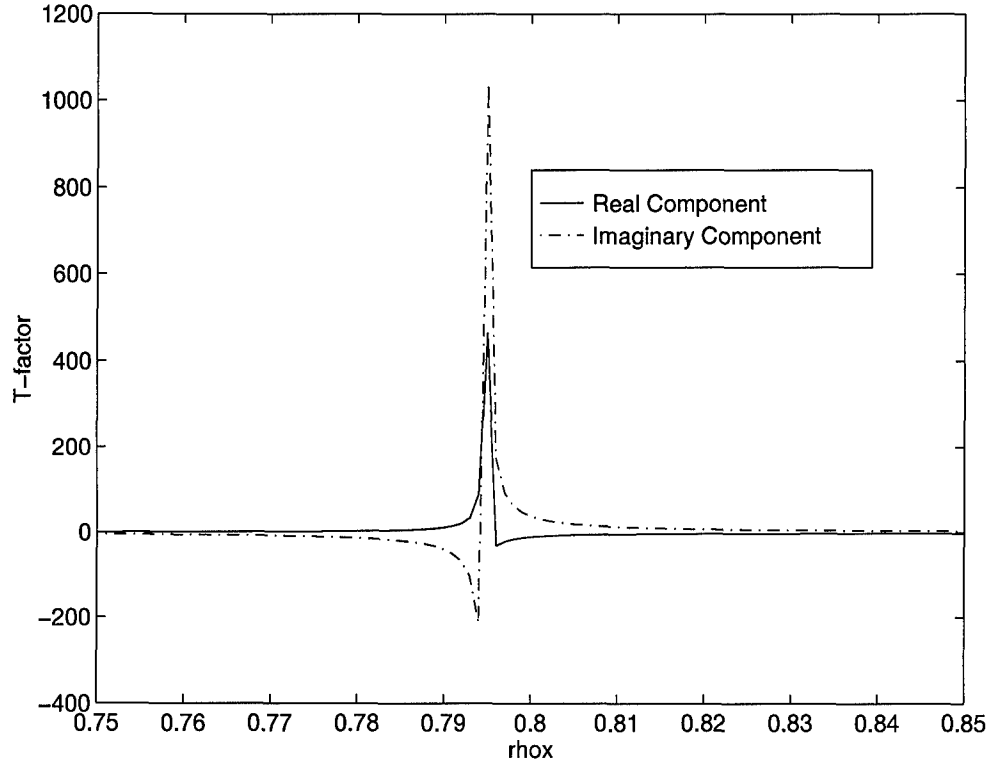


Figure 16. T-factor Singularity in a  $\epsilon_2 = 2\epsilon_o$ ,  $0.2\lambda_o$  Thick Slab with a 0.001 Loss

and

$$N1_o = -je^{j\beta_2 \tilde{\rho}_t \sin(j\nu_o + \tilde{\phi}_t)} T(-\cosh(\nu_o)) \quad (58)$$

$$N2_o = e^{-j\beta_2 \tilde{\rho}_t \cos(\nu_o - \tilde{\phi}_t)} T(\sin(\nu_o)) \quad (59)$$

$$N3_o = je^{j\beta_2 \tilde{\rho}_t \sin(j\nu_o - \tilde{\phi}_t)} T(\cosh(\nu_o)) \quad (60)$$

As before, the extracted integrals are computed using Equations (37), (38), and (39)<sup>4</sup>. Figure 17 plots the PBF magnitude using Equation (56) for four different slab permittivities over an  $\hat{x}$  directed scan similar to that of Figure 8. In this case,  $d_x = 0.3\lambda_o$ ,  $\hat{s}_3 = -[\hat{x} \cos(30^\circ) + \hat{y} \sin(30^\circ)]$ , and

<sup>4</sup>A note of caution concerning the singularity extraction procedure for the grating lobe singularities; The numerator must be a fairly well-behaved function in the vicinity of the singularity. Thus, in order to use the extraction procedure, one must ensure the T-factor singularity is sufficiently far away from the grating lobe singularity. The author found that, in practice, this condition is not unduly restrictive.



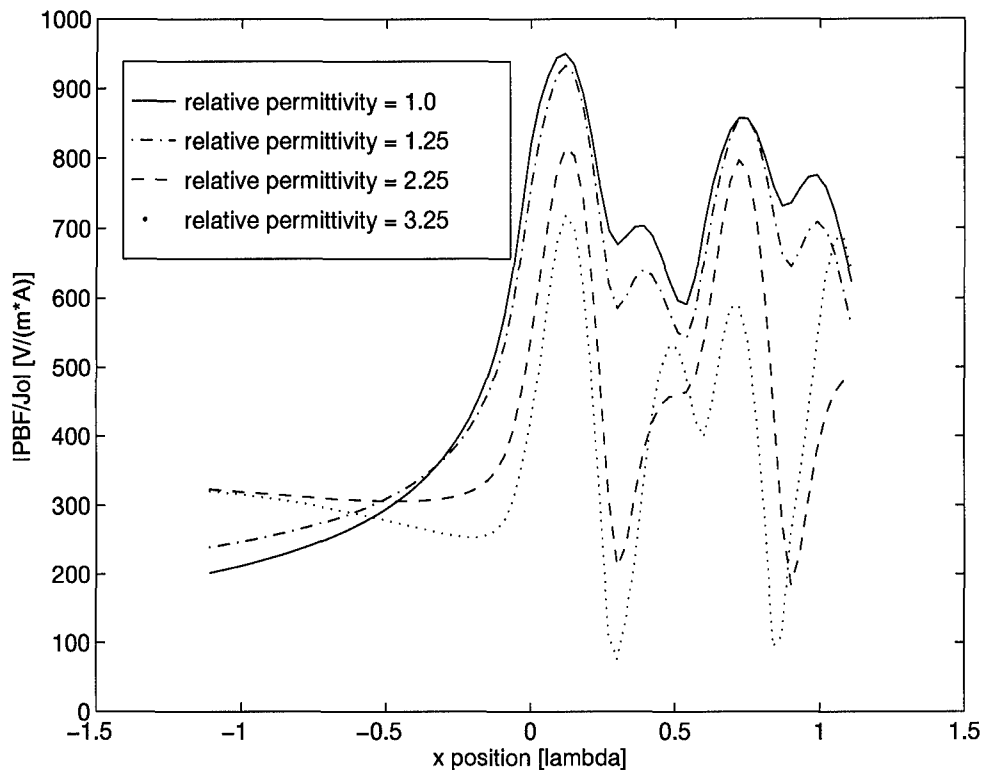


Figure 17. PBF Radiation in the Presence of a Dielectric Slab of Various Relative Permittivities

$y_t = 0.05\lambda_o$ . The dielectric slab boundaries are at  $y_1 = -0.1\lambda_o$ , and  $y_2 = 0.1\lambda_o$  with the external regions one and three defined to be free-space. Finally, a 0.01 T-factor loss tangent ensures the field values are converged. As one might expect, the  $\epsilon_r = 1$  case decays monotonically to the left of the array edge. Surface waves become apparent as one increases the relative permittivity. Also, the field curves change smoothly as the relative permittivity increases, giving confidence in the numerical implementation.

The final figure in this section shows the effect of changing the “elevation” of the scan path above the array. Figure 18 plots the PBF fields for  $y_t = 0.01\lambda_o$ ,  $0.025\lambda_o$ , and  $0.05\lambda_o$  above the array in a free-space dielectric slab. One may note the effect of the individual wires on the field as the observation point approaches the array plane. As expected, the field magnitude increases dramatically in the neighborhood of each wire. Even so, the field values remain comfortably bounded with  $y_t$

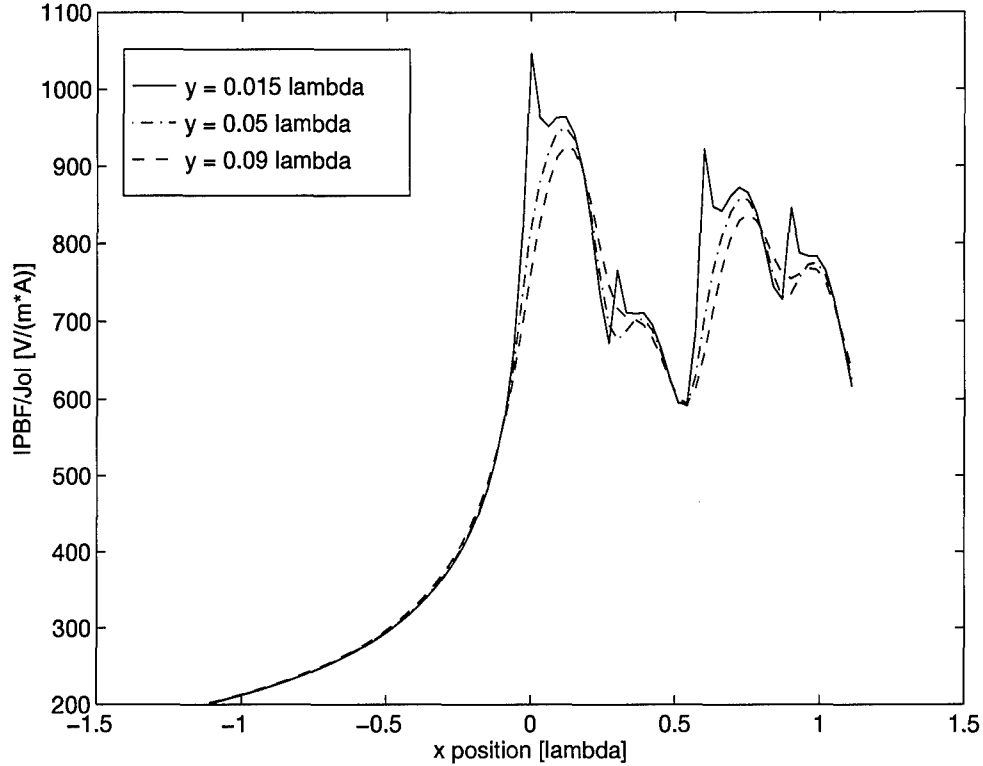


Figure 18. PBF Radiation for Various Scan Path Elevations above the Array Plane

as close as  $0.015\lambda_0$  away, allowing one to use a fairly small wire radius for the coupling matrix, self-impedance calculations.

This completes the PBF subsection. Equation (56), with  $J_o$  divided out, gives the impedance between the PBF and the test functions. The only restriction involves keeping the test location out of the array plane for the self-impedance terms. The subsection addressed issues concerning the spectral integral's evaluation along with the difficulties encountered when one introduces a stratified media. The next subsection completes the coupling matrix section with the development of an expression for the radiation from an individual edge element in a stratified media.

### 2.1.2 Edge Element Basis Function.

**2.1.2.1 Edge Element Basis Function Radiating to Test Function in a Homogeneous Media.** Returning to Equation (16), one can express the field radiated by a single edge element in

a homogeneous media as

$$E_z^{edge}(\bar{\rho}_t) = -\frac{\omega\mu J_b}{4} H_0^{(2)}(\beta|\bar{\rho}_t - \bar{\rho}_b|) \quad (61)$$

One would like to convert Equation (61) to the spectral domain in anticipation of introducing a stratified media. In order to accomplish this, the author took what may first appear to be a circuitous route. Using the array scanning method (ASM) reported by Munk and Burrell[27], the author envisioned a “pseudo-array” around the edge element. The array allows one to introduce the Poisson sum formula to transform to the spectral domain. The field due to the original edge element can then be extracted using Fourier methods by identifying the element as the central term in a Fourier series. Appendix D details this procedure.

#### 2.1.2.2 Edge Element Basis Function Radiating to Test Function in a Stratified Media.

Based on the homogeneous media development, one can introduce a dielectric slab to the geometry in exactly the same manner as for the PBF. In fact, the T-factor expression developed in Section 2.1.1.2 can be used without modification. As before, one finds it expedient to decompose the edge element field into direct and bounce path components

$$E_z^{edge}(\bar{\rho}_t) = E_z^{direct}(\bar{\rho}_t) + E_z^{bounce}(\bar{\rho}_t) \quad (62)$$

with  $E_z^{direct}(\bar{\rho}_t)$  kept in the spatial domain and  $E_z^{bounce}(\bar{\rho}_t)$  expressed as a spectral summation. Equation (61) provides the direct component where again all constitutive parameters are those of region two. One can use the ASM to derive an expression for the bounce component.

One first defines a “pseudo-array” around the edge wire located at  $\bar{\rho}_b$

$$E_z^{array}(\bar{\rho}_t) = -\frac{\omega_2\mu_2 J_b}{4} \sum_{q=-\infty}^{\infty} H_0^{(2)}(\beta_2|\bar{\rho}_t - \bar{\rho}_{qb}|) e^{-j\beta_2 \hat{\mathbf{s}}^{ASM} \cdot \bar{\rho}_{qb}} \quad (63)$$

where

$$\bar{\rho}_{qb} = \hat{x} (q\tilde{d}_x - (b-1)d_x) \quad (64)$$

$$\hat{s}^{ASM} = \hat{x} s_x^{ASM} + \hat{y} \sqrt{1 - s_x^{ASM2}} \quad (65)$$

In order to isolate the surface wave pole excitation to the central term of the spectral sum, one sets the inter-element spacing to  $\tilde{d}_x = \frac{\lambda_2}{2}$ . Now, from Equation (174) in Appendix A and the frequency shift property of the Fourier transform, one can transform Equation (63) to the spectral domain form

$$E_z^{array}(\bar{\rho}_t) = -\frac{\eta_2 J_b}{2\tilde{d}_x} \sum_{k=-\infty}^{\infty} \frac{e^{-j\beta_2 [\hat{\rho}^{ASM} \cdot \bar{\rho}_t - \rho_x^{ASM}(b-1)d_x]}}{\rho_y^{ASM}} \quad (66)$$

where

$$\hat{\rho}^{ASM} = \hat{x} \left( s_x^{ASM} + \frac{k\lambda_2}{\tilde{d}_x} \right) + \hat{y} \sqrt{1 - \left( s_x^{ASM} + \frac{k\lambda_2}{\tilde{d}_x} \right)^2} \quad (67)$$

Using the spectral form in the ASM integrand, one can introduce the T-factor to account for the dielectric slab. Upon interchanging the order of summation and integration, the final expression for the bounce term in Equation (62) can be written

$$E_z^{bounce}(\bar{\rho}_t) = -\frac{\eta_2 J_b}{2\lambda_2} \sum_{k=-\infty}^{\infty} \int_{-1}^1 \frac{e^{-j\beta_2 [\hat{\rho}^{ASM} \cdot \bar{\rho}_t - \rho_x^{ASM}(b-1)d_x]}}{\rho_y^{ASM}} T(\rho_x^{ASM}) ds_x^{ASM} \quad (68)$$

where  $T(\rho_x^{ASM})$  is given by Equation (49).

The ASM integral in Equation (68) has singularities due to the  $\frac{1}{\rho_y^{ASM}}$  term and the T-factor. One can remove the weak  $\frac{1}{\rho_y^{ASM}}$  singularity with the variable transformation

$$(s_x^{ASM} + 2k) = \sin(\nu) \quad (69)$$

$$\sqrt{1 - (s_x^{ASM} + 2k)^2} = \cos(\nu) \quad (70)$$

$$ds_x^{ASM} = \cos(\nu) d\nu \quad (71)$$

where  $(s_x^{ASM} + 2k) = \rho_x^{ASM}$  with  $\tilde{d}_x = \frac{\lambda_2}{2}$ . Moving to a shifted cylindrical coordinate system, one defines

$$\tilde{\rho}_t = \sqrt{(x_t - (b-1)d_x)^2 + y_t^2} \quad (72)$$

$$\tilde{\phi}_t = \tan^{-1} \left( \frac{(x_t - (b-1)d_x)}{y_t} \right) \quad (73)$$

The ASM integral then transforms to

$$I_k = \int_{\sin^{-1}(2k-1)}^{\sin^{-1}(2k+1)} e^{-j\beta_2 \tilde{\rho}_t \cos(\nu - \tilde{\phi}_t)} T(\sin(\nu)) d\nu \quad (74)$$

where the integration range traces out a segment of the integration contour shown in Figure 6. In particular, for a given  $k$  value, the integration path lies on either of the two vertical paths or the real axis between  $-\frac{\pi}{2}$  and  $\frac{\pi}{2}$ . One can handle the T-factor singularities as before by adding a slight loss to the denominator associated with propagation in the  $\hat{y}$  direction.

Equation (62), along with Equations (61), (68), and (74), gives the final form for the field radiated by an edge element. As an example of an edge element calculation, consider the field magnitude plot in Figure 19. As in the PBF case, the edge element field is sampled over an  $\hat{x}$  directed scan at  $y_t = 0.05\lambda_o$  above the element. The element is centered in a  $0.2\lambda_o$  thick slab whose relative permittivity varies from 1 to 3.25. The figure clearly shows the onslaught of surface waves as the permittivity rises, just as Figure 17 did for the PBF.

*2.1.3 Test Function Location Convention.* Sections 2.1.1 and 2.1.2 developed expressions for the fields radiated by the two basis function types. The values of these fields at the locations defined by the impulsive testing functions are directly proportional to the coupling between the particular basis and testing functions through the unknown current coefficient. Consequently, the author used Equations (56) and (62) to calculate the coupling matrix entries by dividing out the unknown current coefficients. Equation (9) gives the basis and testing function ordering in the coupling matrix. To avoid confusion, Figure 20 shows the exact basis and testing function locations for a semi-infinite

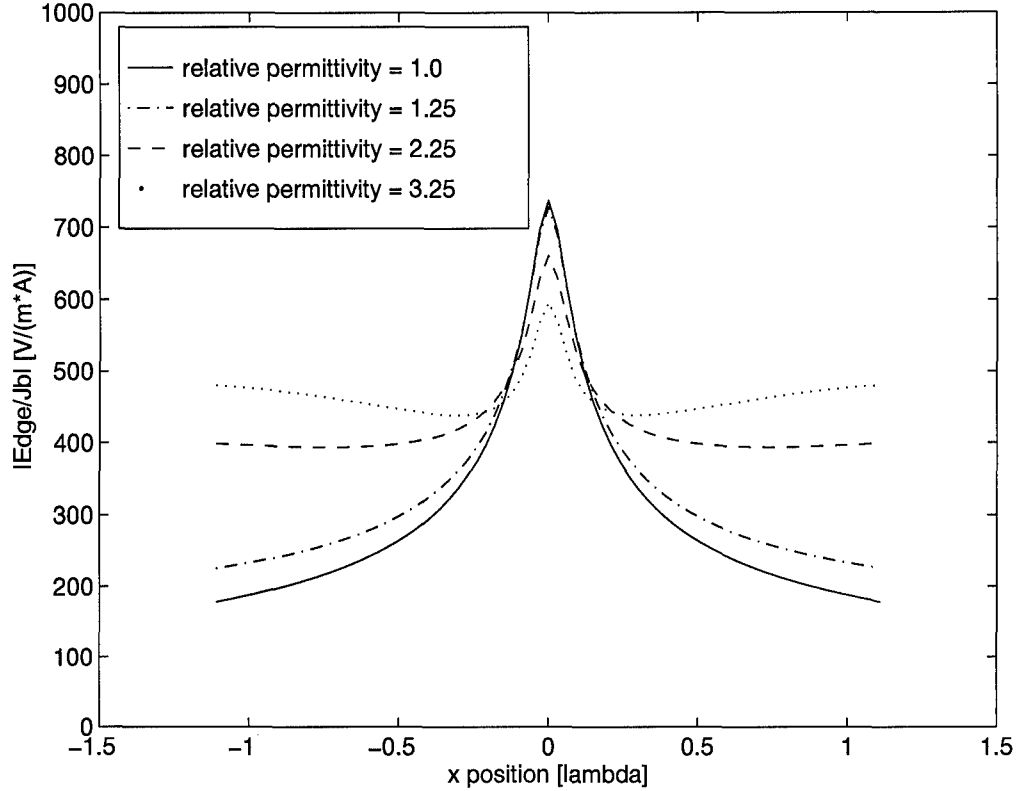


Figure 19. Edge Element Radiation in the Presence of a Dielectric Slab of Various Relative Permittivities

wire array with three edge elements. In particular, notice how the PBF overlaps the edge element basis functions. In essence, the edge element current coefficients modify the PBF current coefficient for the first three elements. The author found the optimal PBF test location lies one inter-element distance from the inner-most edge element toward the infinite part of the array. Intuitively, this makes sense, since the inner-most edge element should have the strongest coupling with the infinite portion of the array.

## 2.2 Excitation Vector

Turning now to the left hand side of Equation (9), consider the free-space geometry shown in Figure 5. The source of the incident field lies out at infinity and has an amplitude sufficient to produce a  $1.0 \left(\frac{V}{m}\right)$  plane wave at the dielectric slab's left-most boundary. Furthermore, the Dirac delta testing functions convert the inner-product integrals to simple function evaluations. The excitation vector

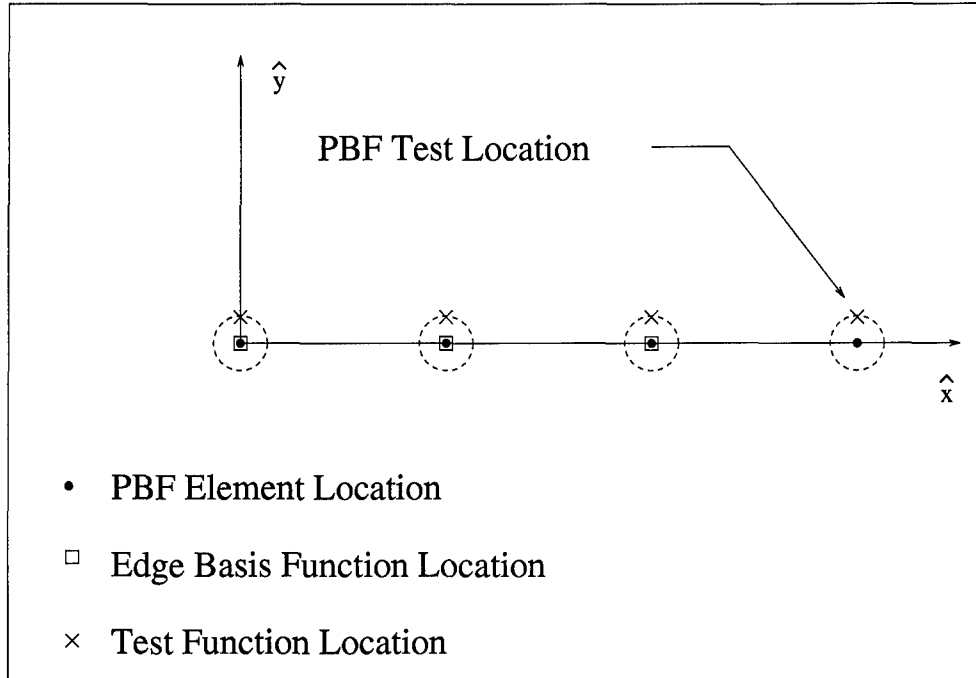


Figure 20. Basis and Testing Function Locations for Semi-Infinite Wire Array

entries are then

$$E_z^i(\bar{\rho}_t) = e^{-j\beta\hat{s}\cdot\bar{\rho}_t} \quad (75)$$

where  $\bar{\rho}_t$  is the test function location indicated in Figure 20.

One can introduce a stratified media to the geometry using the T-factor concept once again. Unlike the coupling matrix case, the plane wave reference location lies just outside the left-most dielectric boundary. One must first use an effective transmission coefficient to take the plane wave inside the slab.

$$\tau_{12}^e = \frac{\tau_{12}}{1 + \Gamma_{12}\Gamma_{23}e^{-j2\beta_2(y_2-y_1)s_{y2}}} \quad (76)$$

where the superscript,  $e$ , identifies an effective Fresnel coefficient and from Equation (42)

$$\tau_{12} = \frac{2\sqrt{\frac{\epsilon_1}{\epsilon_2} - s_{x2}^2}}{\sqrt{\frac{\epsilon_1}{\epsilon_2} - s_{x2}^2} + \sqrt{1 - s_{x2}^2}} \quad (77)$$

Equation (76) takes into account the reflected plane waves bouncing between the dielectric boundaries to form a composite field at the left boundary. One obtains the T-factor by simply adding the appropriate phase to shift the composite plane wave to  $\bar{\rho}_t$ .

$$T_{ex}(s_{y2}) = \tau_{12}^e e^{-j\beta_2 2(y-y_1)s_{y2}} \quad (78)$$

The final expression for the excitation vector entries in a dielectric slab is then

$$E_z^i(\bar{\rho}_t) = T_{ex}(s_{y2}) e^{-j\beta_2 (s_{x2}x_t + s_{y2}y_t)} \quad (79)$$

Note, one can obtain the incident plane wave propagation vector  $\hat{x}$  component by phase matching at the  $y = y_1$  boundary.

$$s_{x2} = \sqrt{\frac{\epsilon_1}{\epsilon_2}} s_{x1} \quad (80)$$

### 2.3 Solution Vector and Far-Field Radiation

One now has the coupling matrix and excitation vectors filled. The unknown current coefficients can be calculated from Equation (9) through a variety of linear system techniques. Plugging these coefficients into Equation (4) gives the approximation of the induced scattering currents. For the particular basis function scheme shown in Figure 20, one can write

$$\begin{aligned} J_z(\bar{\rho}) \approx & \sum_{b=0}^2 (J_0 e^{-j\beta_2 b d_x s_x} + J_{(b+1)}) \delta \left( \sqrt{(x - b d_x)^2 + y^2} \right) \\ & + J_0 \sum_{b=3}^{\infty} e^{-j\beta_2 b d_x s_x} \delta \left( \sqrt{(x - b d_x)^2 + y^2} \right) \end{aligned} \quad (81)$$

This current approximation, plugged into the radiation integral, gives an expression for the fields scattered by a semi-infinite wire array. One can then calculate the echo-width from the definition

$$\sigma_{2D} = \lim_{\rho \rightarrow \infty} 2\pi\rho \left| \frac{E_z^s(\rho)}{E_z^i(\rho)} \right|^2 \quad (82)$$



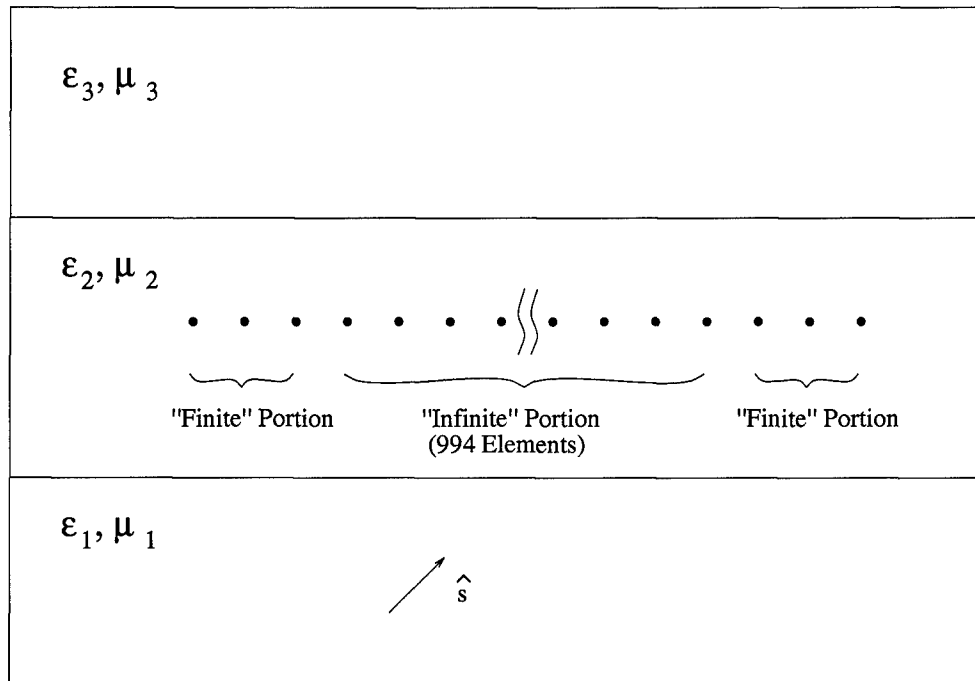


Figure 21. Large Finite Wire Array

where  $|E_z^i(\rho)| = 1.0 \left(\frac{V}{m}\right)$  and  $E_z^s(\rho)$  is calculated using the large argument approximation of the Hankel function.

Since, in practice, all arrays are finite, one would like to use the previous analysis to determine the fields from a large finite array. Consider the wire array depicted in Figure 21. Using a finite technique such as Skinner's[33] to calculate the echo-width, one is faced with solving a 1000 by 1000 matrix problem. Alternatively, one could model the large array in two parts where the currents on the left and right halves are those computed for the two corresponding semi-infinite arrays. With the left-most wire in Figure 21 at the origin, Equation (81) gives the currents for the left half elements. One can calculate the right half currents by solving the complement semi-infinite wire array problem shown in Figure 22, where  $\hat{s}$  is reflected across the  $-\hat{y}$  axis. The resulting currents must be given the appropriate phase shift to place them in the proper phase relationship with the left half currents. Assuming three individual edge elements were necessary for each semi-infinite array, the combined array problem results in two, four by four matrix problems.

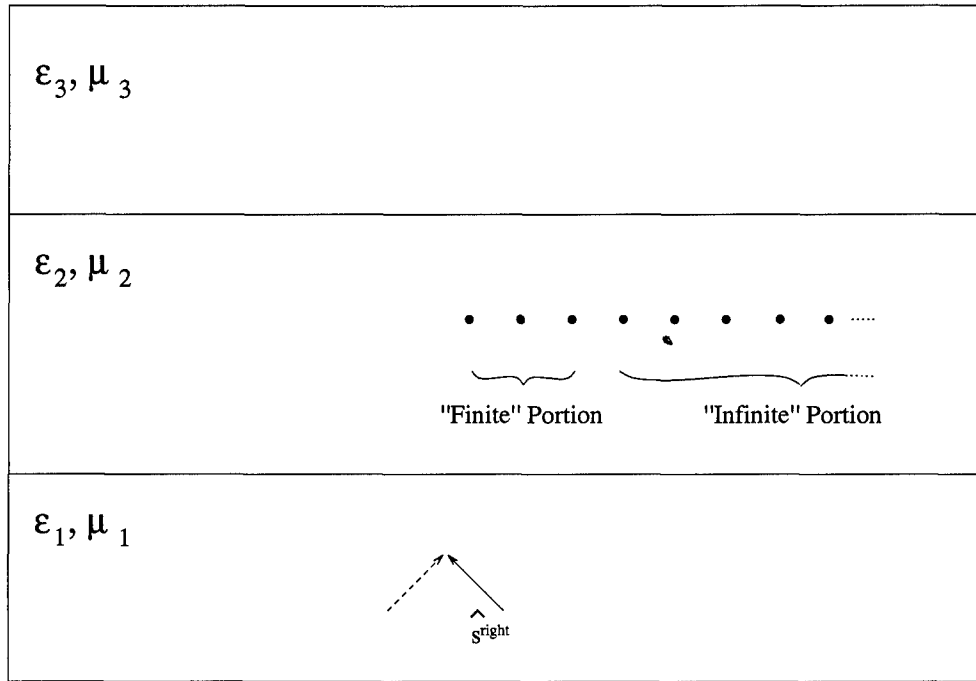


Figure 22. Complementary Semi-Infinite Array Problem for the Large Finite Array Right Edge

Several observations are now in order. First, for most large array problems, the system solution eats up a major portion of the total computation time. As a conservative estimate, the number of machine operations required to solve the system increases as  $N^3$  with the number of unknowns. Thus, one can achieve tremendous computational savings using the hybrid PMM/MM method. In addition, one can increase the finite array size in Figure 21 almost without limit with virtually no computational penalty. This is a consequence of the fact the edge element perturbations beyond the PBF test location are insignificant. Second, the hybrid PMM/MM method has a “built-in” check for the number of required edge elements. Specifically, if the PBF current coefficient calculated in the left edge problem is significantly different from the PBF current coefficient from the right edge problem, more edge elements need to be modeled. Since this requires a costly system recalculation, one should start with a good a-priori estimate for the number of edge elements. Hansen and Gammon[16] provide just such an estimate based on their Gibbsian model for finite scanned arrays. Their estimate,

$$N = \frac{6}{\cos^2(\phi^i)} \quad (83)$$

assumes a symmetric edge element perturbation valid for incident angles away from grazing. Finally, note that for the truly semi-infinite array, the PBF does not contribute to the far-field pattern, except perhaps at a finite number of angles associated with grating lobe directions. This observation is completely analogous to how the Physical Optics (PO) currents do not contribute to the far-field pattern in a Physical Theory of Diffraction (PTD) solution for the scattering from a half-plane.

This chapter developed the hybrid PMM/MM method outlined in Chapter I. Using a simple two-dimensional wire geometry as a proof-of-concept, the chapter clearly demonstrated the method's benefits. The actual validation of a computer code based in this development is presented in Chapter IV. The next chapter turns from the proof-of-concept geometry to a more practical, slotted array problem.

### III. Three-Dimensional Semi-Infinite Slot Array

The sciences do not try to explain, they hardly even try to interpret, they mainly make models. By a model is meant a mathematical construct which, with the addition of certain verbal interpretations, describes observed phenomena. The justification of such a mathematical construct is solely and precisely that it is expected to work.

- John von Neumann

This chapter applies the hybrid PMM/MM approach to the slotted ground plane shown in Figure 23. The array consists of slot columns which can be shifted or “skewed” in the  $\hat{z}$  direction. A multi-layer dielectric media encapsulates the slotted array, providing a good approximation to a practical radome design.

As in the wire array problem, one first examines the geometry with the goal of reducing the domain of the unknown currents. Using the equivalence principle, one arrives at the equivalent geometry shown in Figure 24. Note how the now complete ground plane breaks the problem into

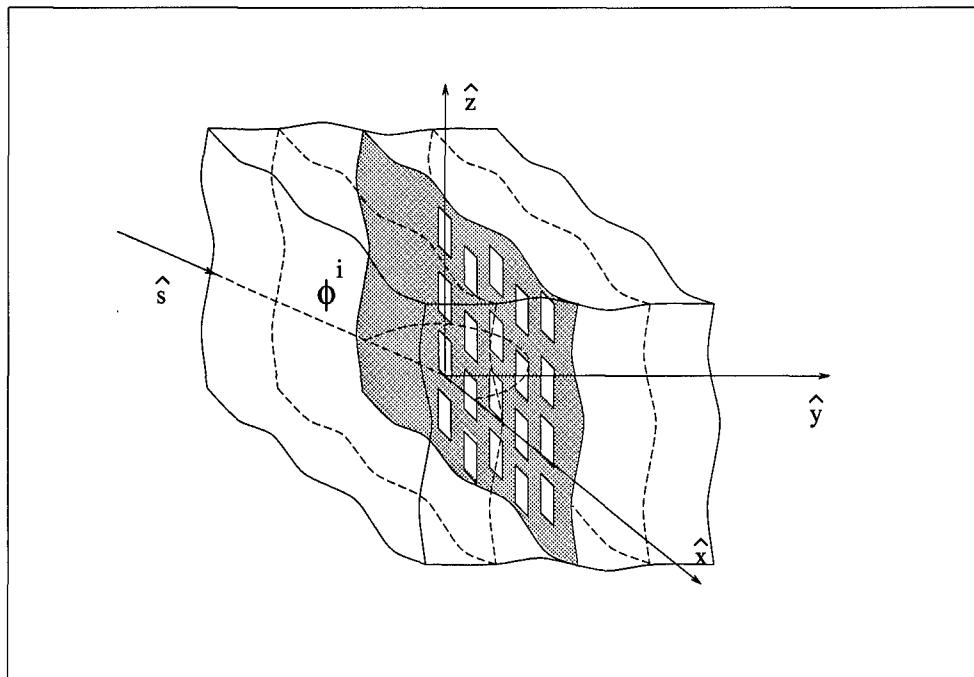


Figure 23. Semi-Infinite Slot Array Geometry

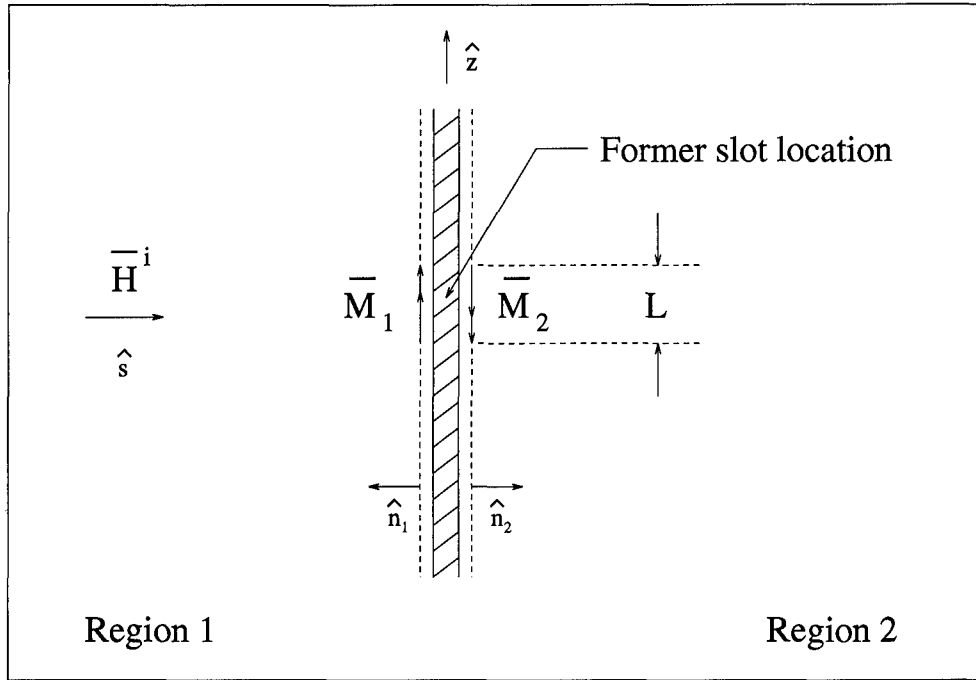


Figure 24. Equivalent Slot Array Geometry

two regions. The advantage of this particular equivalent geometry lies in the fact the only non-zero currents are magnetic currents restricted to the former slot locations. Equation (84) defines these currents in terms of the outward surface normals and the total electric field in the original geometry.

$$\overline{\mathbf{M}}_{1,2} = \overline{\mathbf{E}} \times \hat{\mathbf{n}}_{1,2} \quad (84)$$

Even though Figure 24 shows a thick ground plane, for this analysis the author assumes an infinitely thin ground plane. As a result, the continuity of the tangential electric field provides a coupling between the two half-space problems, effectively cutting the number of unknowns in half. Based on the tangential magnetic field boundary condition, one can write a magnetic field integral equation relating the unknown scattering currents,  $\overline{\mathbf{M}}_1$ , to the known incident fields. Specifically,

$$\hat{\mathbf{n}}_1 \times \overline{\mathbf{H}}^{gi} = -\hat{\mathbf{n}}_1 \times [\overline{\mathbf{H}}_1^s(\overline{\mathbf{M}}_1) + \overline{\mathbf{H}}_2^s(\overline{\mathbf{M}}_1)] \Big|_{\overline{\mathbf{R}} \in S} \quad (85)$$

where the generalized incident field,  $\overline{H}^{gi}$ , accounts for the presence of the ground plane and field equality holds only at the former slot locations,  $S$ . In a manner analogous to the thin wire approximation of Chapter II, one can simplify Equation (85) using a thin slot approximation. The vector equation becomes a scalar, resulting in the relationship between the  $\hat{z}$  directed fields,

$$H_z^{gi} = -\hat{z} \cdot [\overline{H}_1^s(\hat{z}M_z) + \overline{H}_2^s(\hat{z}M_z)] \Big|_{\overline{R} \in S} \quad (86)$$

Equation (86) can be solved using the PMM/MM procedure with the current approximation,

$$M_z(\overline{R}') \approx \sum_{b=0}^B M_b \phi_b(\overline{R}') \Big|_{\overline{R}' \in S} \quad (87)$$

and the inner product definition,

$$\langle \theta_t(\overline{R}), \phi_b(\overline{R}) \rangle = \int_S \theta_t(\overline{R}) \phi_b(\overline{R}) d\overline{R} \quad (88)$$

where  $\phi_b(\overline{R})$  and  $\theta_t(\overline{R})$  are periodic basis and testing functions associated with the slot columns. Plugging Equation (87) in Equation (86) and performing the inner product, one arrives at the matrix equation analogous to Equation (8) of Chapter I,

$$\int_S H_z^{gi}(\overline{R}) \theta_t(\overline{R}) d\overline{R} = -\sum_{b=0}^B M_b \int_S \hat{z} \cdot [\overline{H}_1^s(\hat{z}\phi_b(\overline{R}')) + \overline{H}_2^s(\hat{z}\phi_b(\overline{R}'))] \theta_t(\overline{R}) d\overline{R} \quad (89)$$

where  $t = 0, 1, \dots, B$ . The remainder of this chapter examines each component of Equation (89), beginning with the coupling matrix.

### 3.1 Coupling Matrix

The coupling matrix elements based on magnetic currents represent admittances defined by Equation (90).

$$Y_{tb} = -\int_S \hat{z} \cdot [\overline{H}_1^s(\hat{z}\phi_b(\overline{R}')) + \overline{H}_2^s(\hat{z}\phi_b(\overline{R}'))] \theta_t(\overline{R}) d\overline{R} \quad (90)$$

Just as for Chapter II's wire array, the basis functions,  $\phi_b(\bar{\mathbf{R}}')$ , take on two distinct forms depending on their location in the array. Those near the array's edges model single slot columns, while those obeying Floquet phasing model the entire center portion of the array. The next subsection examines the latter, beginning with the homogeneous media problem and then introducing a stratified dielectric media.

### 3.1.1 Physical Basis Function.

#### 3.1.1.1 Physical Basis Function Radiating to Test Function in a Homogeneous Media.

The slot array problem adds another level of complexity to the two-dimensional wire array problem by introducing a third dimension. Fortunately, the array is fully periodic in this dimension<sup>1</sup>, allowing one to reduce the problem to that of determining the induced currents on a single reference slot. The remaining currents in the associated slot column are then related to the reference slot via a Floquet phase shift. In fact, looking at the slot array as an array of slot columns, one finds a tremendous similarity between the wires of Chapter II and the slot columns here. This fact allows one to build on the development of Chapter II in deriving analogous expressions for the slot array.

One begins the analysis with the semi-infinite array of  $\hat{\mathbf{z}}$  directed Hertzian dipoles depicted in Figure 25. One can obtain the radiation from the slot array by integrating the magnetic dipole array along the slot's long dimension.<sup>2</sup> From Equation (90) it is apparent one needs the  $\hat{\mathbf{z}}$  component of the magnetic field radiated by the PBF in order to calculate the admittance. The author uses the electric vector potential to obtain the magnetic field produced by the magnetic currents [17]. Specifically, one can write the vector potential from the  $qm^{th}$  Hertzian dipole as,

$$\bar{\mathbf{F}}_{qm}(\bar{\mathbf{R}}) = \hat{\mathbf{z}} \frac{\epsilon M_{PBF} e^{-j|\bar{\mathbf{R}} - \bar{\mathbf{R}}_{qm}|}}{4\pi|\bar{\mathbf{R}} - \bar{\mathbf{R}}_{qm}|} dz' \quad (91)$$

where  $q$  is the column index associated with the  $\hat{\mathbf{x}}$  direction,  $m$  is the row index associated with the  $\hat{\mathbf{z}}$  direction, and  $M_{PBF}$  is the magnetic current value at  $\bar{\mathbf{R}}_{qm}$ . Recalling the PBF obeys Floquet

<sup>1</sup>For this research, the author defines this to be the  $\hat{\mathbf{z}}$  direction.

<sup>2</sup>This assumes a thin slot analogous to Chapter II's thin wire.

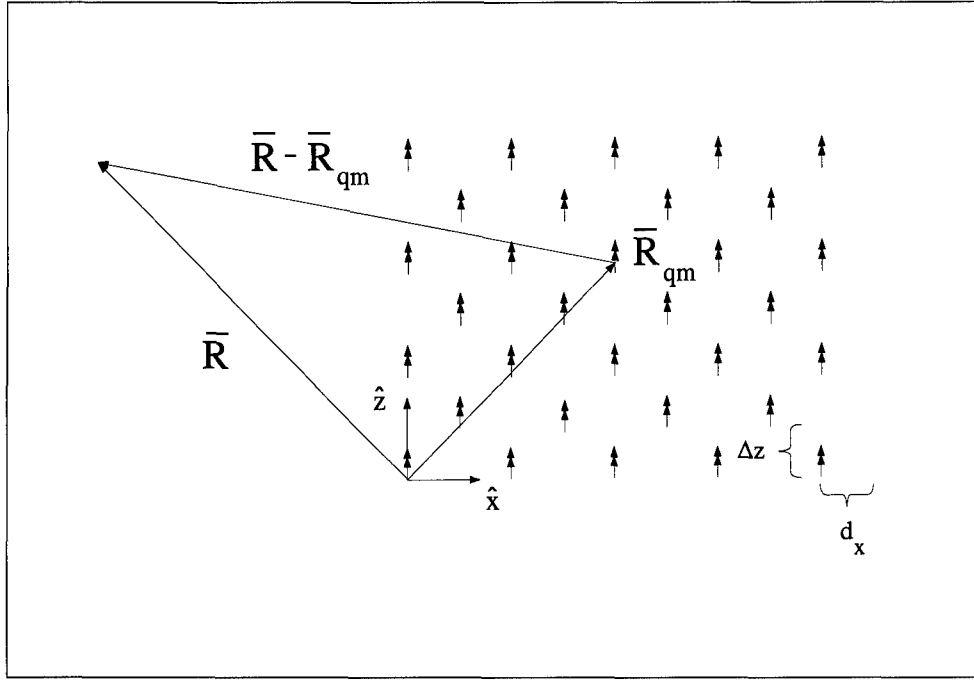


Figure 25. Hertzian Dipole PBF Radiating to Test Location in Homogeneous Media

phasing in the semi-infinite direction, one can express the vector potential from the entire semi-infinite Hertzian dipole array as,

$$\begin{aligned} \overline{\mathbf{F}}(\overline{\mathbf{R}}) &= \hat{\mathbf{z}} \frac{\epsilon M_{PBF} dz'}{4\pi} \\ &\sum_{q=0}^{\infty} \sum_{m=-\infty}^{\infty} \frac{e^{-j\beta[q(d_x s_x + \Delta z s_z) + m d_z s_z]} e^{-j\beta\sqrt{(q d_x - x)^2 + y^2 + (m d_z + q \Delta z - z)^2}}}{\sqrt{(q d_x - x)^2 + y^2 + (m d_z + q \Delta z - z)^2}} \end{aligned} \quad (92)$$

Equation (92) represents a completely spatial domain expression. For reasons given in Chapter II, one desires a spectral domain form based on a plane wave expansion. In the  $\hat{\mathbf{z}}$  direction, one can use the Poisson sum formula to transform the row summation to the spectral domain. Plugging the transform pair [3],

$$\frac{e^{jzt}}{j2} H_0^{(2)}(\rho\sqrt{\beta^2 - t^2}) \Leftrightarrow \frac{e^{-j\beta\sqrt{\rho^2 + (\omega - z)^2}}}{\sqrt{\rho^2 + (\omega - z)^2}} \quad (93)$$



in Equation (174) of Appendix A, one obtains,

$$\begin{aligned} \overline{F}(\overline{\mathbf{R}}) &= \hat{z} \frac{\epsilon M_{PBF} dz'}{j4d_z} \\ &\sum_{n=-\infty}^{\infty} e^{-j\beta z r_z} \sum_{q=0}^{\infty} H_0^{(2)}\left(\beta r_\rho \sqrt{(q d_x - x)^2 + y^2}\right) e^{-j\beta q d_x (s_x - \frac{n\lambda}{d_x})} \end{aligned} \quad (94)$$

where,

$$\begin{aligned} r_\rho &= \sqrt{1 - \left(s_z + \frac{n\lambda}{d_z}\right)^2} \\ &= \sqrt{1 - r_z^2} \end{aligned} \quad (95)$$

Equation (94) is a mixed spectral/spatial domain form, hereafter referred to as the “spatial” domain expression. Notice the similarities between the inner summation in Equation (94) and the spatial domain expression for the wire in Equation (17). Clearly, the slot column radiates cylindrical waves which propagate or become evanescent depending on the direction component,  $r_z$ .

To obtain the complete spectral domain expression, one uses the one-sided Poisson sum formula given in Equation (185) to transform the column summation in Equation (94) to the spectral domain. With the Fourier transform pair given by Equation (18) and a few algebraic manipulations, one obtains,

$$\begin{aligned} \overline{F}(\overline{\mathbf{R}}) &= \hat{z} \frac{\epsilon M_{PBF} dz'}{j4\beta d_x d_z} \\ &\sum_{n=-\infty}^{\infty} \sum_{k=-\infty}^{\infty} \left\{ \frac{e^{-j\beta(xr_x + yr_y + zr_z)}}{r_y} + \frac{j}{\pi} \int_{-\infty}^{\infty} \frac{e^{-j\beta(x\tau_x + y\tau_y + z\tau_z)} e^{-j\beta \frac{d_x}{2}(\tau_x - r_x)}}{\tau_y(\tau_x - r_x)} d\tau_x \right\} \end{aligned} \quad (96)$$

where,

$$r_x = s_x - \frac{n\Delta z\lambda}{d_x d_z} + \frac{k\lambda}{d_x} \quad (97)$$

$$r_y = \sqrt{r_\rho^2 - r_x^2} \quad (98)$$

$$\tau_y = \sqrt{r_\rho^2 - \tau_x^2} \quad (99)$$

As for the wire array, Equation (96) is a plane wave expansion containing both discrete and continuous spectra.

Equations (92), (94), and (96) give three alternate forms of the electric vector potential radiated by the Hertzian dipole array. Using these expressions along with the superposition principle and image theory, one can obtain the vector potential from a finite length magnetic dipole array in the presence of a ground plane. The thin slot assumption, applied to  $\hat{z}$  directed slots, converts the superposition integral into a line integral in  $z$ . If one assumes the basis function has a piecewise sinusoidal (PWS) shape,

$$\phi_b(z') = \frac{\sin\left(\beta\left(\frac{L}{2} - |z'|\right)\right)}{\sin\left(\frac{\beta L}{2}\right)} \quad (100)$$

one can express the spectral domain form of the vector potential from either region 1 or region 2 as,

$$\begin{aligned} \overline{\mathbf{F}}(\overline{\mathbf{R}}) &= \hat{z} \frac{\epsilon M_{PBF} dz'}{j4\beta d_x d_z} \sum_{n=-\infty}^{\infty} \sum_{k=-\infty}^{\infty} \left\{ \frac{e^{-j\beta(xr_x + yr_y + zr_z)}}{r_y} \right. \\ &\quad \left. + \frac{j}{\pi} \int_{-\infty}^{\infty} \frac{e^{-j\beta(x\tau_x + y\tau_y + zr_z)} e^{-j\beta\frac{d_x}{2}(\tau_x - r_x)}}{\tau_y(\tau_x - r_x)} d\tau_x \right\} \int_{-\frac{L}{2}}^{\frac{L}{2}} \phi_b(z') e^{j\beta(z' + z_b)r_z} dz' \\ &= \hat{z} \frac{\epsilon M_{PBF} dz'}{j4\beta d_x d_z} \sum_{n=-\infty}^{\infty} \sum_{k=-\infty}^{\infty} \left\{ \frac{e^{-j\beta(xr_x + yr_y + zr_z)}}{r_y} \right. \\ &\quad \left. + \frac{j}{\pi} \int_{-\infty}^{\infty} \frac{e^{-j\beta(x\tau_x + y\tau_y + zr_z)} e^{-j\beta\frac{d_x}{2}(\tau_x - r_x)}}{\tau_y(\tau_x - r_x)} d\tau_x \right\} P^b \end{aligned} \quad (101)$$

where  $z_b$  is the center of the PWS and  $P^b$  is the integral evaluation,

$$P^b = \frac{2 \left[ \cos \left( \frac{\beta r_z L}{2} \right) - \cos \left( \frac{\beta L}{2} \right) \right]}{\beta \sin \left( \frac{\beta L}{2} \right) (1 - r_z^2)} e^{j\beta z_b r_z} \quad (102)$$

referred to as a "pattern factor." Equipped with the vector potential, one can now determine the magnetic field from the relationships [17],

$$\overline{\mathbf{E}}^s(\overline{\mathbf{R}}) = \frac{-1}{\epsilon} \nabla \times \overline{\mathbf{F}}(\overline{\mathbf{R}}) \quad (103)$$

$$\overline{\mathbf{H}}^s(\overline{\mathbf{R}}) = \frac{-1}{j\omega\mu} \nabla \times \overline{\mathbf{E}}^s(\overline{\mathbf{R}}) \quad (104)$$

Plugging Equation (101) into Equation (103) gives the spectral domain form of the scattered electric field,

$$\begin{aligned} \overline{\mathbf{E}}^s(\overline{\mathbf{R}}) = & \frac{1}{2d_x d_z} \left[ \hat{\mathbf{x}} \sum_{n=-\infty}^{\infty} \sum_{k=-\infty}^{\infty} \left\{ e^{-j\beta(xr_x + yr_y + zr_z)} \right. \right. \\ & \left. \left. + \frac{j}{\pi} \int_{-\infty}^{\infty} \frac{e^{-j\beta(xr_x + yr_y + zr_z)} e^{-j\beta \frac{d_x}{2}(\tau_x - r_x)}}{(\tau_x - r_x)} d\tau_x \right\} P^b \right. \\ & - \hat{\mathbf{y}} \sum_{n=-\infty}^{\infty} \sum_{k=-\infty}^{\infty} \left\{ \begin{array}{l} r_x \\ r_y \end{array} e^{-j\beta(xr_x + yr_y + zr_z)} \right. \\ & \left. + \frac{j}{\pi} \int_{-\infty}^{\infty} \frac{\tau_x e^{-j\beta(xr_x + yr_y + zr_z)} e^{-j\beta \frac{d_x}{2}(\tau_x - r_x)}}{\tau_y (\tau_x - r_x)} d\tau_x \right\} P^b \left. \right] \quad (105) \end{aligned}$$

and Equation (105) into Equation (104) gives the  $\hat{\mathbf{z}}$  component of the scattered magnetic field,

$$\begin{aligned} H_z^s(\overline{\mathbf{R}}) = & \frac{-Y}{2d_x d_z} \sum_{n=-\infty}^{\infty} \sum_{k=-\infty}^{\infty} \left\{ \frac{r_\rho^2 e^{-j\beta(xr_x + yr_y + zr_z)}}{r_y} \right. \\ & \left. + \frac{j r_\rho^2 e^{-j\beta(zr_z - \frac{d_x}{2} r_x)}}{\pi} \int_{-\infty}^{\infty} \frac{e^{-j\beta \left[ \left( x + \frac{d_x}{2} \right) \tau_x + y\tau_y \right]}}{\tau_y (\tau_x - r_x)} d\tau_x \right\} P^b \quad (106) \end{aligned}$$

where  $Y$  is the intrinsic admittance of the homogeneous media. The spatial domain forms are found by plugging Equation (94) into Equation (103),

$$\begin{aligned} \overline{\mathbf{E}}^s(\overline{\mathbf{R}}) = & \frac{\beta}{j2d_z} \sum_{n=-\infty}^{\infty} \sum_{q=0}^{\infty} r_\rho e^{-j\beta \left[ qd_x \left( s_x - \frac{n\Delta z\lambda}{d_x d_z} \right) + r_z \right]} \\ & \frac{H_1^{(2)} \left( \beta r_\rho \sqrt{(qd_x - x)^2 + y^2} \right)}{\sqrt{(qd_x - x)^2 + y^2}} [\hat{\mathbf{x}}y + \hat{\mathbf{y}}(qd_x - x)] P^b \end{aligned} \quad (107)$$

and Equation (107) into Equation (104),

$$H_z^s(\overline{\mathbf{R}}) = \frac{-\omega\epsilon}{2d_z} \sum_{n=-\infty}^{\infty} \sum_{q=0}^{\infty} r_\rho^2 e^{-j\beta [qd_x (s_x - \frac{n\Delta z\lambda}{d_x d_z}) + r_z]} H_0^{(2)} \left( \beta r_\rho \sqrt{(qd_x - x)^2 + y^2} \right) P^b \quad (108)$$

Equations (106) and (108) give the  $\hat{\mathbf{z}}$  component of the magnetic field radiated by the PBF in a homogeneous media. One obtains the coupling matrix terms associated with the PBF by taking the inner product of either Equation (106) or Equation (108) with a PWS testing function,  $\theta_t(\overline{\mathbf{R}})$ , as indicated by Equation (90). Before proceeding, however, it is numerically expedient to transform Equation (106) to the angular spectral domain.

Defining the continuous spectral integral as,

$$I_{nk} = \int_{-\infty}^{\infty} \frac{e^{-j\beta \left[ \left( x + \frac{d_x}{2} \right) \tau_x + y \sqrt{r_\rho^2 - \tau_x^2} \right]}}{\sqrt{r_\rho^2 - \tau_x^2} (\tau_x - r_x)} d\tau_x \quad (109)$$

one must consider two cases depending on the value of  $r_\rho$ . The first case occurs when  $r_z^2 < 1$ , making  $r_\rho$  a strictly positive, real number. One can then divide  $\tau_x$  by  $r_\rho$ , resulting in,

$$I_{nk} = \frac{1}{r_\rho} \int_{-\infty}^{\infty} \frac{e^{-j\beta \left[ \left( x + \frac{d_x}{2} \right) \tau'_x + y \sqrt{1 - \tau_x'^2} \right]}}{\sqrt{1 - \tau_x'^2} \left( \tau'_x - \frac{r_x}{r_\rho} \right)} d\tau'_x \quad (110)$$

where  $\tau'_x = \frac{\tau_x}{r_\rho}$ . Equation (110) now has exactly the same form as the spectral integral in Equation (21). As before, one removes the weak singularity,  $\frac{1}{\sqrt{1 - \tau_x'^2}}$ , from the integrand via the variable

substitution,  $\tau'_x = \sin(\nu)$ . With the displaced coordinate system,  $\tilde{\rho} = \sqrt{(x + \frac{d_x}{2})^2 + y^2}$  and  $\tilde{\phi} = \tan^{-1}\left(\frac{(x + \frac{d_x}{2})}{y}\right)$ , one obtains the angular spectral integral,

$$I_{nk} = \frac{1}{r_\rho} \oint_C \frac{e^{-j\beta r_\rho \tilde{\rho} \cos(\nu - \tilde{\phi})}}{\left(\sin(\nu) - \frac{r_x}{r_\rho}\right)} d\tau'_x \quad (111)$$

where the integration contour,  $C$ , is shown in Figure 6. Finally, one extracts the singularity,  $\nu_o = \sin^{-1}\left(\frac{r_x}{r_\rho}\right)$ , resulting in the expression,

$$\begin{aligned} I_{nk} = & \frac{1}{r_\rho} \left[ \int_0^\infty \frac{-je^{j\beta r_\rho \tilde{\rho} \sin(j\nu + \tilde{\phi})} - N1_o}{\left(\cosh(\nu) + \frac{r_x}{r_\rho}\right)} d\nu + N1_o \int_0^\infty \frac{d\nu}{\left(\cosh(\nu) + \frac{r_x}{r_\rho}\right)} \right. \\ & + \int_{-\frac{\pi}{2}}^{\frac{\pi}{2}} \frac{e^{-j\beta r_\rho \tilde{\rho} \cos(\nu - \tilde{\phi})} - N2_o}{\left(\sin(\nu) - \frac{r_x}{r_\rho}\right)} d\nu + N2_o \int_{-\frac{\pi}{2}}^{\frac{\pi}{2}} \frac{d\nu}{\left(\sin(\nu) - \frac{r_x}{r_\rho}\right)} \\ & \left. + \int_0^\infty \frac{je^{j\beta r_\rho \tilde{\rho} \sin(j\nu - \tilde{\phi})} - N3_o}{\left(\cosh(\nu) - \frac{r_x}{r_\rho}\right)} d\nu + N3_o \int_0^\infty \frac{d\nu}{\left(\cosh(\nu) - \frac{r_x}{r_\rho}\right)} \right] \quad (112) \end{aligned}$$

where,

$$N1_o = -je^{j\beta r_\rho \tilde{\rho} \sin(j\nu_o + \tilde{\phi})} \quad (113)$$

$$N2_o = e^{-j\beta r_\rho \tilde{\rho} \cos(\nu_o - \tilde{\phi})} \quad (114)$$

$$N3_o = je^{j\beta r_\rho \tilde{\rho} \sin(j\nu_o - \tilde{\phi})} \quad (115)$$

and,

$$\int_0^{\infty} \frac{d\nu}{\left(\cosh(\nu) \pm \frac{r_x}{r_\rho}\right)} = \begin{cases} \frac{2}{\sqrt{1-\left(\frac{r_x}{r_\rho}\right)^2}} \tan^{-1} \left( \frac{\sqrt{1-\left(\frac{r_x}{r_\rho}\right)^2}}{1 \pm \frac{r_x}{r_\rho}} \right) \\ \frac{1}{\sqrt{\left(\frac{r_x}{r_\rho}\right)^2 - 1}} \ln \left| \frac{1 \pm \frac{r_x}{r_\rho} + \sqrt{\left(\frac{r_x}{r_\rho}\right)^2 - 1}}{1 \pm \frac{r_x}{r_\rho} - \sqrt{\left(\frac{r_x}{r_\rho}\right)^2 - 1}} \right| \end{cases} \quad (116)$$

$$\int_{-\frac{\pi}{2}}^{\frac{\pi}{2}} \frac{d\nu}{\left(\sin(\nu) - \frac{r_x}{r_\rho}\right)} = \begin{cases} 0 \\ \frac{2}{\sqrt{\left(\frac{r_x}{r_\rho}\right)^2 - 1}} \left[ \tan^{-1} \left( \frac{1 - \frac{r_x}{r_\rho}}{\sqrt{\left(\frac{r_x}{r_\rho}\right)^2 - 1}} \right) - \tan^{-1} \left( \frac{1 + \frac{r_x}{r_\rho}}{\sqrt{\left(\frac{r_x}{r_\rho}\right)^2 - 1}} \right) \right] \end{cases} \quad (117)$$

where one chooses either the upper or lower line for  $\left(\frac{r_x}{r_\rho}\right)^2 < 1$  or  $\left(\frac{r_x}{r_\rho}\right)^2 > 1$ , respectively.

The second case occurs when  $r_z^2 > 1$ . Using the variable substitution,  $\tilde{r}_\rho = \sqrt{r_z^2 - 1}$ , the weak singularity goes away, removing the need to transform to the angular spectrum. The continuous spectral integral can now be written,

$$I_{nk} = j \int_{-\infty}^{\infty} \frac{e^{-j\beta \left[ \left(x + \frac{d_x}{2}\right) \tau_x - jy \sqrt{\tilde{r}_\rho^2 + \tau_x^2} \right]}}{\sqrt{\tilde{r}_\rho^2 + \tau_x^2} (\tau_x - r_x)} d\tau_x \quad (118)$$

Extracting the  $\tau_x = r_x$  singularity, one has,

$$I_{nk} = j \left[ \int_{-\infty}^{\infty} \frac{e^{-j\beta \left[ \left(x + \frac{d_x}{2}\right) \tau_x - jy \sqrt{\tilde{r}_\rho^2 + \tau_x^2} \right]}}{\sqrt{\tilde{r}_\rho^2 + \tau_x^2} (\tau_x - r_x)} d\tau_x - N_o + N_o \int_{-\infty}^{\infty} \frac{d\tau_x}{(\tau_x - r_x)} \right] \quad (119)$$

where,

$$N_o = \frac{e^{-j\beta \left[ \left(x + \frac{d_x}{2}\right) r_x - jy \sqrt{\tilde{r}_\rho^2 + r_x^2} \right]}}{\sqrt{\tilde{r}_\rho^2 + r_x^2}} \quad (120)$$

Note the singular integrand is an odd function causing the integral to evaluate to zero. Equations (112) and (119) are the continuous spectral forms the author implemented in the computer codes validated in Chapter IV.

At this point, one may proceed with the inner product integral to obtain the desired admittance matrix element. From Equation (90), there are actually two integrations to perform. These “one-sided” admittances correspond to the two half-spaces created by the ground plane. For symmetric dielectric stacks, the admittances are identical, requiring one to compute only one side and double the results. The spatial domain form comes from Equation (108). Assuming a PWS test function defined to be non-zero over the reference slot centered at  $\bar{\mathbf{R}} = \bar{\mathbf{R}}_t$ , one can write,

$$\begin{aligned}
Y_{tb} &= - \int_{S_t} H_z^s(\bar{\mathbf{R}}) \theta_t(\bar{\mathbf{R}}) d\bar{\mathbf{R}} \\
&= \frac{\omega\epsilon}{2d_z} \sum_{n=-\infty}^{\infty} \sum_{q=0}^{\infty} r_\rho^2 e^{-j\beta q d_x} \left( s_x - \frac{n\Delta z \lambda}{d_x d_z} \right) \\
&\quad H_0^{(2)} \left( \beta r_\rho \sqrt{(q d_x - x_t)^2 + y_t^2} \right) P^b \int_{-\frac{L}{2}}^{\frac{L}{2}} \theta_t(z) e^{-j\beta(z+z_t)r_z} dz \\
&= \frac{\omega\epsilon}{2d_z} \sum_{n=-\infty}^{\infty} \sum_{q=0}^{\infty} r_\rho^2 e^{-j\beta q d_x} \left( s_x - \frac{n\Delta z \lambda}{d_x d_z} \right) H_0^{(2)} \left( \beta r_\rho \sqrt{(q d_x - x_t)^2 + y_t^2} \right) P^b P^t \quad (121)
\end{aligned}$$

where the basis and testing function pattern factors are,

$$P_t^b = \frac{2 \left[ \cos \left( \frac{\beta r_z L}{2} \right) - \cos \left( \frac{\beta L}{2} \right) \right]}{\beta \sin \left( \frac{\beta L}{2} \right) (1 - r_z^2)} e^{\pm j\beta z_t r_z} \quad (122)$$

In a similar manner, the spectral domain form comes from Equation (106),

$$\begin{aligned}
Y_{tb} &= \frac{Y}{2d_x d_z} \sum_{n=-\infty}^{\infty} \sum_{k=-\infty}^{\infty} \left\{ \frac{r_\rho^2 e^{-j\beta(x_t r_x + y_t r_y)}}{r_y} \right. \\
&\quad \left. + \frac{j r_\rho^2 e^{j\beta \frac{d_x}{2} r_x}}{\pi} \int_{-\infty}^{\infty} \frac{e^{-j\beta \left[ (x_t + \frac{d_x}{2}) \tau_x + y_t \tau_y \right]}}{\tau_y (\tau_x - r_x)} d\tau_x \right\} P^b P^t \quad (123)
\end{aligned}$$

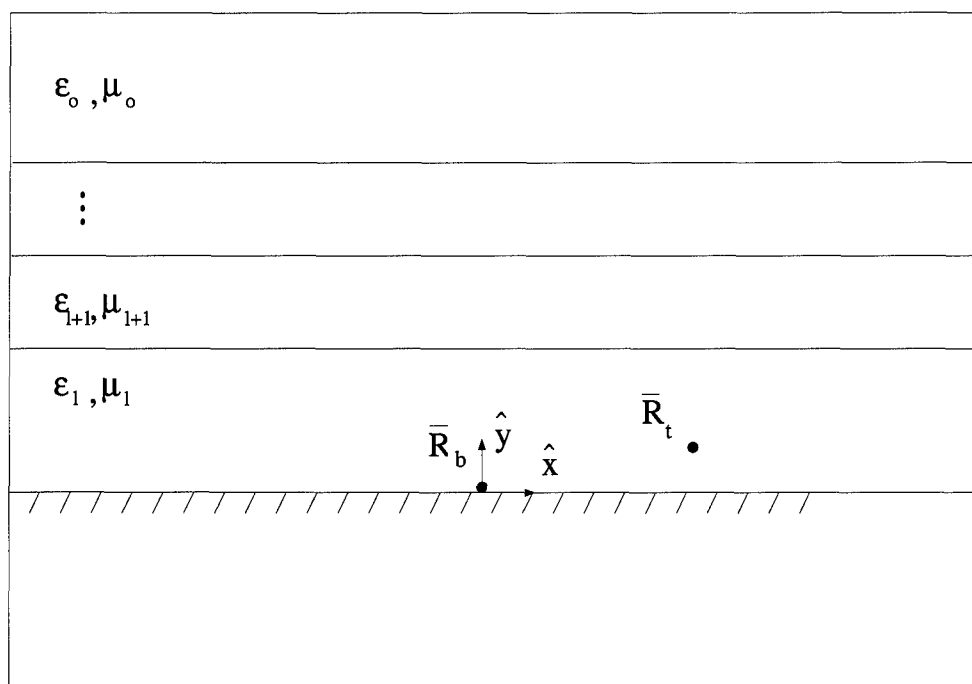


Figure 26. Geometry for PBF One-sided Admittance Problem

In order to avoid singularities in the self admittance calculations, the basis and testing functions must not coincide. As before, one places the testing function an “effective wire radius” out of the array plane. For thin slots, this is defined to be  $a = \frac{\text{slot width}}{4}$ .

This section developed both the spatial and spectral domain forms for the coupling between a finite length periodic basis function and a single finite length testing function. The homogeneous problem again forms the foundation for extending the development to a stratified dielectric media. The next section uses Equations (121) and (123) to develop the admittances for the slot array encased in a stratified dielectric media.

### 3.1.1.2 Physical Basis Function Radiating to Test Function in a Stratified Media.

Figure 26 depicts the one-sided admittance problem involving the PBF radiating to a test location in the presence of a stratified dielectric media. Similar to the wire array, one can use the T-factor concept to account for the presence of the dielectric layers. The plane wave nature of the spectral domain expressions allows one to break the propagation into a direct term and a term accounting for the



multiple bounces between the dielectric layers. Unlike the wire array, Figure 26 shows a multi-layer geometry. Consequently, the T-factor expression used here is slightly more complicated.

Recall the author uses Munk's convention to define the effective reflection and transmission coefficients. Also note the expressions developed heretofore assume the test locations have a positive  $\hat{y}$  component<sup>3</sup>. Consequently, the  $\hat{z}$  polarized magnetic fields require the following magnetic field related coefficients,

$$\tau_{l,l+1} = \frac{2\eta_{(l)}r_{y(l+1)}}{\eta_{(l+1)}r_{y(l)} + \eta_{(l)}r_{y(l+1)}} \quad (124)$$

$$\Gamma_{l,l+1} = \frac{\eta_{(l)}r_{y(l+1)} - \eta_{(l+1)}r_{y(l)}}{\eta_{(l)}r_{y(l)} + \eta_{(l+1)}r_{y(l+1)}} \quad (125)$$

$$\tau_{l,l+1}^e = \frac{\tau_{l,l+1}}{1 + \Gamma_{l,l+1}\Gamma_{l+1,l+2}^e e^{-j2\beta_1 d_l r_{y(l)}}} \quad (126)$$

$$\Gamma_{l,l+1}^e = \frac{\Gamma_{l,l+1} + \Gamma_{l+1,l+2}^e e^{-j2\beta_1 d_l r_{y(l)}}}{1 + \Gamma_{l,l+1}\Gamma_{l+1,l+2}^e e^{-j2\beta_1 d_l r_{y(l)}}} \quad (127)$$

where the  $e$  superscript denotes an effective coefficient. Equations (124) and (125) are Fresnel coefficients which give the transmitted and reflected field ratios at the dielectric interface between two half-spaces. The effective coefficients give the *composite* field ratios, accounting for the multiple reflections and transmissions in the multi-layer structure. The coefficient for a particular layer depends on those from the next layer in the  $\hat{y}$  direction. Therefore, one must start with the outer half-space layer and iteratively compute the coefficients down to the layer closest to the ground plane. Equipped with this inner-most effective reflection coefficient, one can repeat the T-factor analysis performed in Chapter II.

---

<sup>3</sup>This restriction does not limit the analysis. To account for region 1, one simply flips the geometry and mirrors the excitation vector through the  $\hat{z}$  axis.

In particular, one can break the plane waves into four summations as shown in Figure 13. These can be written in closed form and combined to give an expression for the field at  $\bar{\mathbf{R}}_t$ ,

$$H_z^{direct}(\bar{\mathbf{R}}_t) \left[ 1 + \frac{(1 + \Gamma_{i,l+1}^e e^{-j2\beta_l d_l r_{y(l)}}) + 2\Gamma_{i,l+1}^e e^{-j2\beta_l (y_{r,l} - y_t) r_{y(l)}}}{1 - \Gamma_{i,l+1}^e e^{-j2\beta_l d_l r_{y(l)}}} \right] \quad (128)$$

where  $y_{r,l}$  is the outer boundary of the  $l^{th}$  layer,  $y_b = 0$ , and  $\Gamma_{i,l-1}^e = 1$ . Expression (128) has a direct and bounce component. Note however, the homogeneous expressions developed in the previous section actually double the direct term through image theory in order to account for the ground plane. To use Expression (128), one must pull out a factor of two resulting in,

$$2H_z^{direct}(\bar{\mathbf{R}}_t) \left[ 1 + \frac{\Gamma_{i,l+1}^e (e^{-j2\beta_l d_l r_{y(l)}} + e^{-j2\beta_l (y_{r,l} - y_t) r_{y(l)}})}{1 - \Gamma_{i,l+1}^e e^{-j2\beta_l d_l r_{y(l)}}} \right] \quad (129)$$

where the second term in the square brackets is defined to be the T-factor.

Equipped with the T-factor, one may now rewrite Equation (106),

$$\begin{aligned} \bar{\mathbf{H}}_z^{bounce}(\bar{\mathbf{R}}) = & \frac{-Y_l}{2d_x d_z} \sum_{n=-\infty}^{\infty} \sum_{k=-\infty}^{\infty} \left\{ \frac{r_{\rho l}^2 e^{-j\beta_l (x r_{x l} + y r_{y l} + z r_{z l})}}{r_{y l}} T(r_{x l}) \right. \\ & \left. + \frac{j r_{\rho l}^2 e^{-j\beta_l (z r_{z l} - \frac{d_x}{2} r_{x l})}}{\pi} I_{nk} \right\} P_l^b \end{aligned} \quad (130)$$

The pattern factor here is modified in accordance with Kornbau's [21] work to account for the possibility of different permittivities on either side of the array ground plane. Kornbau used the arithmetic average of the permittivities in his calculations. Here, the author found the arithmetic average of the wave numbers worked equally as well. The redefined pattern factor is then,

$$P_l^b = \frac{2\beta_{avg} \left[ \cos\left(\frac{\beta_l r_{z l} L}{2}\right) - \cos\left(\frac{\beta_{avg} L}{2}\right) \right]}{\sin\left(\frac{\beta_{avg} L}{2}\right) (\beta_{avg}^2 - \beta_l^2 r_{z l}^2)} e^{j\beta_l z_b r_{z l}} \quad (131)$$

where  $\beta_{avg} = \frac{\beta_l + \beta_{l-1}}{2}$ . The continuous spectral integral can be expressed,

Case  $r_z^2 < 1$ :

$$\begin{aligned}
 I_{nk} = & \frac{1}{r_{\rho l}} \left[ \int_0^{\infty} \frac{-j e^{j\beta_1 r_{\rho l} \tilde{\rho}} \sin(j\nu + \tilde{\phi}) T(-r_{\rho l} \cosh(\nu)) - N1_o}{\left(\cosh(\nu) + \frac{r_{xl}}{r_{\rho l}}\right)} d\nu + N1_o \int_0^{\infty} \frac{d\nu}{\left(\cosh(\nu) + \frac{r_{xl}}{r_{\rho l}}\right)} \right. \\
 & + \int_{-\frac{\pi}{2}}^{\frac{\pi}{2}} \frac{e^{-j\beta_1 r_{\rho l} \tilde{\rho}} \cos(\nu - \tilde{\phi}) T(r_{\rho l} \sin(\nu)) - N2_o}{\left(\sin(\nu) - \frac{r_{xl}}{r_{\rho l}}\right)} d\nu + N2_o \int_{-\frac{\pi}{2}}^{\frac{\pi}{2}} \frac{d\nu}{\left(\sin(\nu) - \frac{r_{xl}}{r_{\rho l}}\right)} \\
 & \left. + \int_0^{\infty} \frac{j e^{j\beta_1 r_{\rho l} \tilde{\rho}} \sin(j\nu - \tilde{\phi}) T(r_{\rho l} \cosh(\nu)) - N3_o}{\left(\cosh(\nu) - \frac{r_{xl}}{r_{\rho l}}\right)} d\nu + N3_o \int_0^{\infty} \frac{d\nu}{\left(\cosh(\nu) - \frac{r_{xl}}{r_{\rho l}}\right)} \right] \quad (132)
 \end{aligned}$$

where,

$$N1_o = -j e^{j\beta_1 r_{\rho l} \tilde{\rho}} \sin(j\nu_o + \tilde{\phi}) T(-r_{\rho l} \cosh(\nu_o)) \quad (133)$$

$$N2_o = e^{-j\beta_1 r_{\rho l} \tilde{\rho}} \cos(\nu_o - \tilde{\phi}) T(r_{\rho l} \sin(\nu_o)) \quad (134)$$

$$N3_o = j e^{j\beta_1 r_{\rho l} \tilde{\rho}} \sin(j\nu_o - \tilde{\phi}) T(r_{\rho l} \cosh(\nu_o)) \quad (135)$$

and the analytic solutions for the extracted integrals are given in Equations (116) and (117), or

Case  $r_z^2 > 1$ :

$$I_{nk} = j \int_{-\infty}^{\infty} \frac{e^{-j\beta_1 \left[ \left(x + \frac{d_x}{2}\right) \tau_{xl} - jy \sqrt{\tilde{r}_{\rho l}^2 + \tau_{xl}^2} \right]} T(\tau_{xl}) - N_o}{\frac{\sqrt{\tilde{r}_{\rho l}^2 + \tau_{xl}^2}}{(\tau_{xl} - r_{xl})}} d\tau_{xl} \quad (136)$$

where,

$$N_o = \frac{e^{-j\beta_1 \left[ \left(x + \frac{d_x}{2}\right) r_{xl} - jy \sqrt{\tilde{r}_{\rho l}^2 + r_{xl}^2} \right]}}{\sqrt{\tilde{r}_{\rho l}^2 + r_{xl}^2}} T(r_{xl}) \quad (137)$$

The previous development gives the fields radiated to the test location minus the direct term. To arrive at the final expression for the admittance between the PBF and the test function, one simply

combines the spatial domain expression in Equation (121) for the direct term with Equation (130) for the bounce term to obtain,

$$Y_{tb} = \left[ \frac{\omega\epsilon_l}{2d_z} \sum_{n=-\infty}^{\infty} \sum_{q=0}^{\infty} r_{\rho l}^2 e^{-j\beta_l q d_z} \left( s_{xl} - \frac{n\Delta z \lambda_l}{d_x d_z} \right) H_0^{(2)} \left( \beta_l r_{\rho l} \sqrt{(q d_x - x_t)^2 + y_t^2} \right) P_l^b P_l^t \right. \\ \left. + \frac{Y_l}{2d_x d_z} \sum_{n=-\infty}^{\infty} \sum_{k=-\infty}^{\infty} \left\{ \frac{r_{\rho l}^2 e^{-j\beta_l (x_t r_{xl} + y_t r_{yl})}}{r_{yl}} T(r_{xl}) + \frac{j r_{\rho l}^2 e^{j\beta_l \frac{d_x}{2} r_{xl}}}{\pi} I_{nk} \right\} P_l^b P_l^t \right] \quad (138)$$

where  $P_l^t$  is the test function pattern factor obtained by changing the sign on the exponent in Equation (131). The author implemented Equation (138) in the slot code validated in Chapter IV. The T-factor singularities are handled as before by introducing a slight dielectric loss in the  $\hat{y}$  propagation direction and increasing the integrand sampling in the neighborhood of the former singularity.

This completes the development of the coupling matrix terms associated with the physical basis function. The next section derives expressions for the coupling terms associated with the individual edge element basis functions. With these, the coupling matrix is complete.

### 3.1.2 Edge Element Basis Function.

**3.1.2.1 Edge Element Basis Function Radiating to Test Function in a Homogeneous Media.** Consider a single periodic basis function entered at  $\bar{\mathbf{R}}_b$ . One can obtain the coupling between this column and a reference test mode located at  $\bar{\mathbf{R}}_t$  from Equation (121),

$$Y_{tb} = \frac{\omega\epsilon}{2d_z} \sum_{n=-\infty}^{\infty} r_{\rho}^2 H_0^{(2)} \left( \beta r_{\rho} \sqrt{(x_b - x_t)^2 + y_t^2} \right) P^b P^t \quad (139)$$

where  $P^b$  and  $P^t$  are defined by Equation (122). Recall this spatial domain expression results from the application of image theory to replace the array ground plane with a homogeneous media. Adding a stratified dielectric media complicates the problem considerably. Once again, the author chose to take advantage of the plane wave expansion in the ASM to handle the stratified media.

### 3.1.2.2 Edge Element Basis Function Radiating to Test Function in a Stratified Media.

The basic ASM approach involves creating a pseudo-array around the edge element in order to transform to the spectral domain. One can then use the T-factor developed in the PBF section to account for the stratified media. One obtains the fields from the original edge element via a Fourier transform. Defining the pseudo-array inner-column spacing,  $d_x^{ASM}$ , such that  $r_{xl}^{ASM} = s_{xl}^{ASM} + 2k$ , one obtains the following expression for the pseudo-array coupling,

$$Y_{tb}^{array} = \frac{Y_l}{d_x^{ASM} d_z} \sum_{n=-\infty}^{\infty} \sum_{k=-\infty}^{\infty} \frac{r_{\rho l}^2 e^{-j\beta_l [(x_t - x_b)r_{xl}^{ASM} + y_t r_{yl}^{ASM}]} }{r_{yl}^{ASM}} T(r_{xl}^{ASM}) P_l^b P_l^t \quad (140)$$

where  $r_{yl}^{ASM} = \sqrt{r_{\rho l}^2 - (r_{xl}^{ASM})^2}$ . One can write the coupling from the single edge element in terms of the ASM integral as,

$$Y_{tb}^{bounce} = \frac{Y_l}{d_z \lambda_l} \sum_{n=-\infty}^{\infty} \sum_{k=-\infty}^{\infty} r_{\rho l}^2 \left[ \int_{-1}^1 \frac{e^{-j\beta_l [(x_t - x_b)r_{xl}^{ASM} + y_t r_{yl}^{ASM}]} }{r_{yl}^{ASM}} T(r_{xl}^{ASM}) ds_{xl}^{ASM} \right] P_l^b P_l^t \quad (141)$$

where the bounce superscript indicates the direct coupling is not included. Next, one finds it numerically expedient to transform to the angular spectral domain,

$$Y_{tb}^{bounce} = \frac{Y_l}{d_z \lambda_l} \sum_{n=-\infty}^{\infty} \sum_{k=-\infty}^{\infty} r_{\rho l}^2 \left[ \begin{array}{c} \sin^{-1} \left( \frac{2k+1}{r_{\rho l}} \right) \\ \int e^{-j\beta_l r_{\rho l} \tilde{\rho} \cos(\nu - \tilde{\phi})} T(r_{\rho l} \sin(\nu)) d\nu \\ \sin^{-1} \left( \frac{2k-1}{r_{\rho l}} \right) \end{array} \right] P_l^b P_l^t \quad (142)$$

where,

$$\tilde{\rho} = \sqrt{(x_t - x_b)^2 + y_t^2} \quad (143)$$

$$\tilde{\phi} = \tan^{-1} \left( \frac{(x_t - x_b)}{y_t} \right) \quad (144)$$

All that remains is to combine the bounce term in Equation (142) with the direct term in Equation (139)<sup>4</sup> to arrive at the coupling expression implemented in the author's code.

$$Y_{tb} = Y_{tb}^{direct} + Y_{tb}^{bounce} \quad (145)$$

Equations (138) and (145) define all the entries in the coupling matrix. In order to expedite the edge treatment study, the author also incorporated the ability to apply a complex impedance to the individual slot columns. The next section details the required analysis.

*3.1.3 Edge Element Loading.* Consider the reference element of a periodic basis function. A typical slot load consists of a distributed resistance such an "r-card." One would like to convert the distributed r-card resistance to a lumped admittance which could then be added to the diagonal elements of the coupling matrix. Figure 27 depicts this concept for the PWS magnetic current mode. The author used a method suggested by English [9] to perform the conversion. One simply equates the dissipated power in both representations. From Equation (84), an electric field perpendicular to the slot's length produces a  $\hat{z}$  directed magnetic current. Thus, one can express the power in the distributed representation as,

$$\begin{aligned} P_o &= \int_{slot} dP \\ &= \frac{1}{L} \int_{-\frac{L}{2}}^{\frac{L}{2}} \frac{1}{2} E_x(z)^2 \frac{R_{\square}}{\left(\frac{L}{w}\right)} dz \\ &= \frac{R_{\square} M_o^2}{2L AR} \int_{-\frac{L}{2}}^{\frac{L}{2}} \left[ \frac{\sin\left(\beta\left(\frac{L}{2} - |z|\right)\right)}{\sin\left(\frac{\beta L}{2}\right)} \right]^2 dz \end{aligned} \quad (146)$$

---

<sup>4</sup>All quantities associated with the material parameters are taken to be those of the inner-most layer,  $l$ .

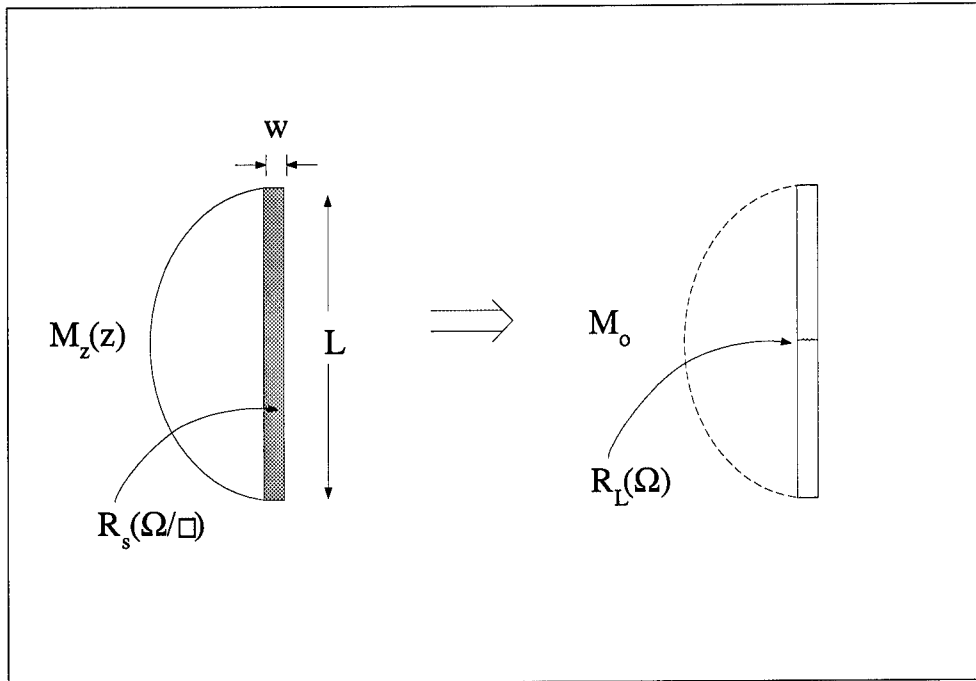


Figure 27. Distributed to Lumped Loading Conversion

where  $AR$  is the slot's aspect ratio. The power in the lumped representation is,

$$P_o = \frac{R_L M_o^2}{2} \quad (147)$$

Equating the two and solving for  $R_L$ , one obtains,

$$R_L = \frac{R_{\square}}{AR} \left[ \frac{\beta L - \sin(\beta L)}{2\beta L \sin\left(\frac{\beta L}{2}\right)} \right] \quad (148)$$

The reciprocal of Equation (148) gives the lumped admittance which the author adds to the appropriate self-admittance term in the coupling matrix.

The previous development assumes the mode represents the total edge element current rather than a perturbation of the PBF current, as in the scheme depicted in Figure 20. It is possible to derive the total edge element formulation from the perturbation formulation for an unloaded array. One

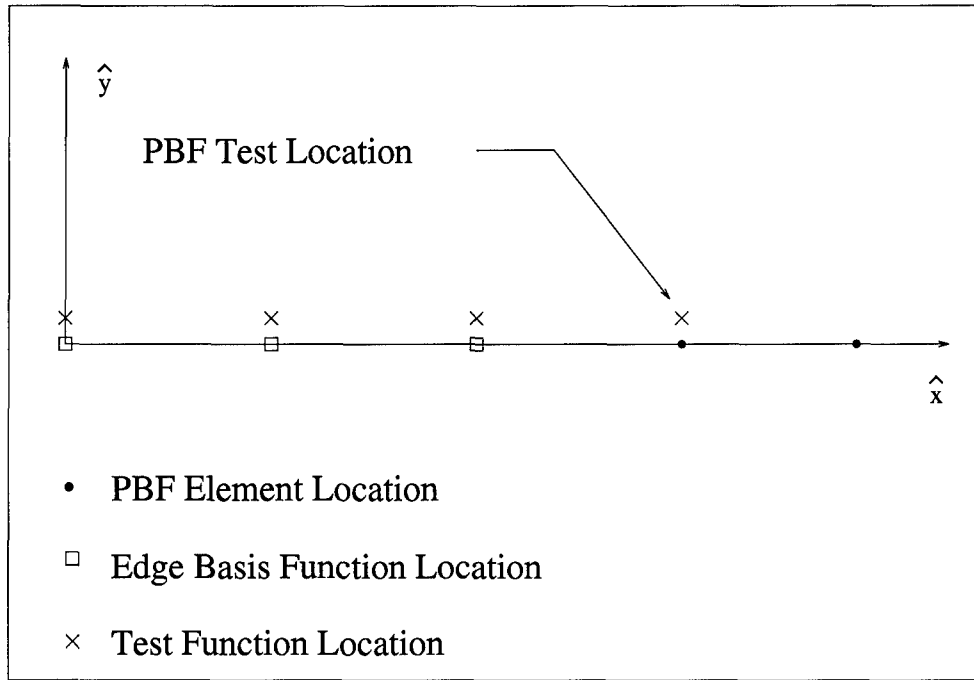


Figure 28. Alternate Basis and Testing Function Locations

can then apply the edge element loading to the new coupling matrix. Skinner suggests the following method to convert between the two unloaded formulations [32].

First, consider the perturbation formulation's matrix equation,

$$\begin{bmatrix} Y_{1,1} & Y_{1,2} & \cdots & Y_{1,N} & Y_{1,N+1} \\ Y_{2,1} & \ddots & & Y_{2,N} & Y_{2,N+1} \\ \vdots & & & \vdots & \vdots \\ Y_{N,1} & \cdots & & Y_{N,N} & Y_{N,N+1} \\ Y_{N+1,1} & \cdots & & Y_{N+1,N} & Y_{N+1,N+1} \end{bmatrix} \begin{bmatrix} V_1 \\ V_2 \\ \vdots \\ V_N \\ V_{N+1} \end{bmatrix} = \begin{bmatrix} I_1 \\ I_2 \\ \vdots \\ I_N \\ I_{N+1} \end{bmatrix} \quad (149)$$

where the subscripts 1 to  $N$  denote edge elements and  $N + 1$  denotes the PBF. The PBF test location is indicated in Figure 20.

Now, consider sliding the PBF to the right so its left edge element coincides with the old PBF test location, as in Figure 28. The edge modes in the new formulation represent the entire edge



element currents. Keeping the old PBF test location, one can express the new matrix equation as

$$\begin{bmatrix} Y_{1,1} & Y_{1,2} & \cdots & Y_{1,N} & \tilde{Y}_{1,N+1} \\ Y_{2,1} & \ddots & & Y_{2,N} & \tilde{Y}_{2,N+1} \\ \vdots & & & \vdots & \vdots \\ Y_{N,1} & \cdots & & Y_{N,N} & \tilde{Y}_{N,N+1} \\ Y_{N+1,1} & \cdots & & Y_{N+1,N} & \tilde{Y}_{N+1,N+1} \end{bmatrix} \begin{bmatrix} \tilde{V}_1 \\ \tilde{V}_2 \\ \vdots \\ \tilde{V}_N \\ \tilde{V}_{N+1} \end{bmatrix} = \begin{bmatrix} I_1 \\ I_2 \\ \vdots \\ I_N \\ I_{N+1} \end{bmatrix} \quad (150)$$

where the tilde indicates a different value than the perturbation formulation.

The key to Skinner's method lies in recognizing the following equivalences between the two formulations, based on the assumption both yield the same magnetic currents.

$$\begin{bmatrix} \tilde{V}_1 \\ \tilde{V}_2 \\ \vdots \\ \tilde{V}_N \\ \tilde{V}_{N+1} \end{bmatrix} = \begin{bmatrix} V_1 + V_{N+1} \\ V_2 + V_{N+1} \\ \vdots \\ V_N + V_{N+1} \\ V_{N+1} \end{bmatrix} \quad (151)$$

Once one has solved the perturbed system, the unknown unperturbed coupling matrix entries can be found using the new currents from Equation (151) and the known coupling matrix entries from Equation (149). For example, solving the first row in Equation (150) for the unknown coupling matrix entry  $\tilde{Y}_{1,N+1}$  yields the equation,

$$\tilde{Y}_{1,N+1} = \frac{1}{\tilde{V}_{N+1}} \left[ I_1 - Y_{1,1}\tilde{V}_1 - \cdots - Y_{1,N}\tilde{V}_N \right] \quad (152)$$

where the right hand side values are known. Equipped with the new coupling matrix representing total currents, one can now apply the shunt admittances to the diagonal entries as described earlier.

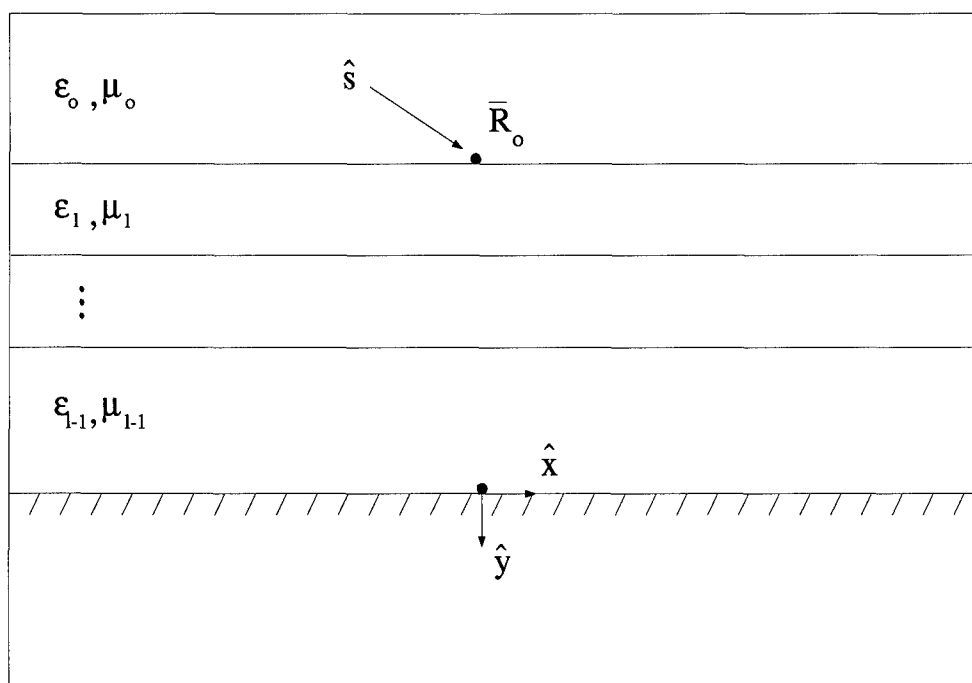


Figure 29. Plane Wave Illumination of Slot Column

### 3.2 Excitation Vector

The left hand side of Equation (89) defines the excitation vector entries,

$$\int_S H_z^{gi}(\bar{\mathbf{R}})\theta_t(\bar{\mathbf{R}}) d\bar{\mathbf{R}} \quad (153)$$

where the generalized incident field accounts for the presence of the ground plane. Since a plane wave illuminates the structure, the author once again uses a T-factor to account for the dielectric layers shown in Figure 29. One has complete freedom to define the incident plane wave. Since the validation data is entirely monostatic, the author chose to restrict the incident plane wave propagation to the xy plane. In particular, the author chose a  $1\left(\frac{A}{m}\right)$ ,  $\hat{z}$  polarized magnetic field with a phase reference at  $\bar{\mathbf{R}}_o$ . Assuming a homogeneous media, the magnetic field at the test location,  $(x_t, 0, z_t)$ , is then,

$$H_z^i(\bar{\mathbf{R}}_t) = e^{-j\beta_o(x_t s_{xo} + d_{total} s_{yo})} \quad (154)$$

Introducing the stratified media, one can find the  $\hat{y}$  propagating field just inside the first slab from Equation (126),

$$H_z^i(\bar{\mathbf{R}}_t) \left( \frac{\tau_{0,1}}{1 + \Gamma_{0,1} \Gamma_{1,2}^e e^{-j2\beta_1 d_1 r_{y1}}} \right) \quad (155)$$

One then propagates the fields through the remaining layers to the test location  $\bar{\mathbf{R}}_t$ .

$$H_z^i(\bar{\mathbf{R}}_t) \left[ \prod_{\xi=1}^{l-1} \tau_{\xi-1,\xi}^e e^{-j2\beta_\xi d_\xi r_{y\xi}} \right] \quad (156)$$

To get the total field at  $\bar{\mathbf{R}}_t$ , one sums the composite right-going field,

$$H_z^i(\bar{\mathbf{R}}_t) \left[ \prod_{\xi=1}^{l-1} \tau_{\xi-1,\xi}^e e^{-j2\beta_\xi d_\xi r_{y\xi}} \right] \quad (157)$$

and the composite left-going field,

$$H_z^i(\bar{\mathbf{R}}_t) \left[ \prod_{\xi=1}^{l-1} \tau_{\xi-1,\xi}^e e^{-j2\beta_\xi d_\xi r_{y\xi}} \right] \Gamma_{l-1,l}^e \quad (158)$$

to arrive at,

$$H_z^i(\bar{\mathbf{R}}_t) \left[ 2 \prod_{\xi=1}^{l-1} \tau_{\xi-1,\xi}^e e^{-j2\beta_\xi d_\xi r_{y\xi}} \right] = H_z^i(\bar{\mathbf{R}}_t) T_{ex}(s_{xo}) \quad (159)$$

where  $\Gamma_{l-1,l}^e = 1$ . To account for the inner product with the testing function, one uses the same pattern factor as before, arriving at,

$$\int_S H_z^{gi}(\bar{\mathbf{R}}) \theta_t(\bar{\mathbf{R}}) d\bar{\mathbf{R}} = e^{-j\beta_o s_{xo} x_t} T_{ex}(s_{xo}) P_{l-1}^t \quad (160)$$

### 3.3 Solution Vector and Far-Field Radiation

With the coupling matrix and excitation vectors filled, one can solve the system to obtain the unknown expansion coefficients. One simply plugs these coefficients back into the current approximation to obtain the desired scattering currents. For the code validated in Chapter IV, the author defined the edge element currents as perturbations of the PBF current. Thus, the scattering

current amplitudes,  $M_b$ , discussed below are actually a sum of the PBF and the particular edge element.

First, consider the homogeneous media case involving a periodic basis function centered at  $(x_b, 0, z_b)$ . The associated scattered magnetic field<sup>5</sup> can be written,

$$H_z^s(\bar{\mathbf{R}}) = \frac{-\omega\epsilon_l M_b}{2d_z} \sum_{n=-\infty}^{\infty} r_{\rho l}^2 e^{-j\beta_1 z r_z} H_0^{(2)}(\beta_l r_{\rho l} \rho_b) P_l^b \quad (161)$$

where  $\rho_b = \sqrt{(x_b - x)^2 + y^2}$ . Restricting the plane of incidence to the  $xy$  plane, one is interested in the scattered field a large distance away from the array. For monostatic scattering, only the  $n = 0$  term contributes to the far-field. One can use the large argument form of the Hankel function,

$$H_\nu^{(2)}(\beta_l r_{\rho l} \rho_b) \sim \sqrt{\frac{j2}{\pi\beta_l r_{\rho l} \rho_b}} j^\nu e^{-j\beta_l r_{\rho l} \rho_b} \quad (162)$$

to obtain a far-field approximation of the scattered magnetic field,

$$H_{z,ff}^s(\bar{\mathbf{R}}) \sim \frac{-\omega\epsilon_l M_b}{2d_z} \sqrt{\frac{j2}{\pi\beta_l r_{\rho l} \rho}} e^{-j\beta_l(\rho + x_b \sin(\eta_{obs}))} P_l^b \quad (163)$$

where  $\rho = \sqrt{x^2 + y^2}$  and  $\eta_{obs}$  is measured from the negative  $\hat{y}$  axis in the plane of incidence. Note, Equation (163) contains the approximations  $\rho_b \approx \rho$  and  $\rho_b \approx \rho + x_b \sin(\eta_{obs})$  for the amplitude and phase, respectively. One then sums the field contributions from each periodic basis function<sup>6</sup> to obtain the total scattered field,

$$H_{z,ff}^s(\bar{\mathbf{R}}) \sim \frac{-\omega\epsilon_l}{2d_z} \sqrt{\frac{j2}{\pi\beta_l r_{\rho l} \rho}} \sum_{b=1}^B M_b e^{-j\beta_l(\rho + x_b \sin(\eta_{obs}))} P_l^b \quad (164)$$

<sup>5</sup>One only needs the  $\hat{z}$  component since all the reference data is co-polarized.

<sup>6</sup>For the central portion of a large array, one simply adds the appropriate phase shift to the PBF coefficient and applies the result to the corresponding slot column.

In order to account for the stratified media, the author employed the ASM, using the T-factor defined by Equation (159). One can then write the scattered field from a single periodic basis function,

$$H_z^s(\bar{\mathbf{R}}) = \frac{-M_b}{\eta_l d_z \lambda_l} \sum_{n=-\infty}^{\infty} \sum_{k=-\infty}^{\infty} r_{\rho l}^2 \left[ \int_{-1}^1 \frac{e^{-j\beta_l [(x-x_b)r_{xl}^{ASM} + yr_{yl}^{ASM}]} T_{ex}(r_{xl}^{ASM}) ds_{xl}^{ASM}}{r_{yl}^{ASM}} \right] P_l^b \quad (165)$$

Once again keeping only the central term and restricting the plane of incidence to the  $xy$  plane, one obtains,

$$H_{z,ff}^s(\bar{\mathbf{R}}) \approx \frac{-M_b P_l^b}{\eta_l d_z \lambda_l} \int_{-1}^1 \frac{e^{-j\beta_l [(x-x_b)s_{xl}^{ASM} + ys_{yl}^{ASM}]} T_{ex}(s_{xl}^{ASM}) ds_{xl}^{ASM}}{s_{yl}^{ASM}} \quad (166)$$

In order to remove the weak singularity, one finds it desirable to transform to the angular spectral domain.

$$H_{z,ff}^s(\bar{\mathbf{R}}) \approx \frac{-M_b P_l^b}{\eta_l d_z \lambda_l} \int_{-\frac{\pi}{2}}^{\frac{\pi}{2}} e^{-j\beta_l \tilde{\rho}_b \cos(\nu - \tilde{\phi}_b)} T_{ex}(\sin(\nu)) d\nu \quad (167)$$

where,

$$\tilde{\rho}_b = \sqrt{(x-x_b)^2 + y^2} \quad (168)$$

$$\tilde{\phi}_b = \tan^{-1}\left(\frac{x-x_b}{y}\right) \quad (169)$$

The integrand in Equation (167) is highly oscillatory for large  $\tilde{\rho}_b$  values, making numerical integration virtually impossible. Fortunately, the integral lends itself to a stationary phase evaluation. In particular, one can identify  $\beta_l \tilde{\rho}_b$  as the large parameter and  $\nu_o = \tilde{\phi}_b$  as the stationary phase point. With the resulting asymptotic integral evaluation, one can express the scattered field as,

$$H_{z,ff}^s(\bar{\mathbf{R}}) \sim \frac{-M_b P_l^b}{\eta_l d_z \lambda_l} \sqrt{\frac{j2\pi}{\tilde{\rho}_b |\beta_l|}} T_{ex}(\sin(\nu_o)) e^{-j\beta_l \tilde{\rho}_b} \Bigg|_{\rho \rightarrow \infty} \quad (170)$$

Summing over the modes and applying the same approximations to  $\tilde{\rho}_b$  as in the homogeneous case, one arrives at,

$$H_{z,ff}^s(\overline{\mathbf{R}}) \sim \frac{-e^{j\beta_l \rho}}{\eta_l d_z} \sqrt{\frac{j}{\rho \lambda_l}} \sum_{b=1}^B M_b e^{-j\beta_l x_b} \sin(\eta_{obs}) T_{ex} \left( \frac{\beta_o}{\beta_l} \sin(\eta_{obs}) \right) P_l^b \Bigg|_{\rho \rightarrow \infty} \quad (171)$$

where  $\sin(\eta_o)$  is approximated by  $\frac{\beta_o}{\beta_l} \sin(\eta_{obs})$ .

In order to compare with the measured data, the author uses the echo width definition,

$$\sigma_{2D} = \lim_{\rho \rightarrow \infty} 2\pi\rho \frac{|H_z^s(\overline{\mathbf{R}})|^2}{|H_z^i(\overline{\mathbf{R}})|^2} \quad (172)$$

and Equation (171) to arrive at the expression,

$$\sigma_{2D} = \frac{\beta_l}{\eta_l^2 d_z^2} \left| \sum_{b=1}^B M_b e^{-j\beta_l x_b} \sin(\eta_{obs}) T_{ex} \left( \frac{\beta_o}{\beta_l} \sin(\eta_{obs}) \right) P_l^b \right|^2 \quad (173)$$

The author implemented Equation (173) in the computer code validated in Chapter IV. In particular, the author used the left and right semi-infinite array approach described in Chapter II to model the large finite slot arrays in the next chapter.

This chapter applied the hybrid PMM/MM method to a slotted ground plane embedded in a general stratified dielectric media. By modeling the individual slot columns with periodic basis functions, the author was able to build on the wire array analysis. The next chapter examines the computer codes based on this development in order to validate the method.

## IV. Validation

The triumphant vindication of bold theories - are these not the pride and justification of our life's work?

- *Sherlock Holmes (Sir Arthur Conan Doyle)*

The previous two chapters applied the hybrid PMM/MM technique to a two-dimensional wire array and a three-dimensional slot array. This chapter validates the hybrid technique using a two pronged approach based on both reference code and measurement comparisons. The reference codes allow one to directly examine the currents induced on the array elements. As mentioned earlier, this approach provides a more rigorous test of the technique's accuracy by avoiding the radiation integral's smoothing effect. Measurement comparisons are included despite the complications associated with simulating an infinite ground plane because, in many respects, "the proof is in the pudding." The author felt the best way to demonstrate the hybrid PMM/MM technique's usefulness is to test its ability to model "real world" radomes. As a consequence of the validation approach, the chapter breaks into two parts corresponding to the reference code and measurement comparisons. Within each part, the subject wire and slot array geometries are examined with an eye to not only build confidence in the technique, but also to highlight the situations where it is most useful. This chapter concludes with a motivating illustration of the hybrid technique's potential for handling large arrays.

### 4.1 Reference Code Comparison

One has a distinct advantage when using a reference code to validate a new technique. Unlike measurements, one has tremendous flexibility in choosing representative array geometries to truly "wring out" the technique. For the hybrid PMM/MM technique, the author attempted to find array geometries large enough to ensure the central element currents obey Floquet theory, yet small enough to allow the MM based reference codes to solve the problems in a reasonable time.

In addition to choosing appropriate problem geometries, one must be careful in choosing and using the reference codes. The reference code provides the "truth" baseline against which one measures the new technique. Obviously, one must have a certain amount of faith in the reference

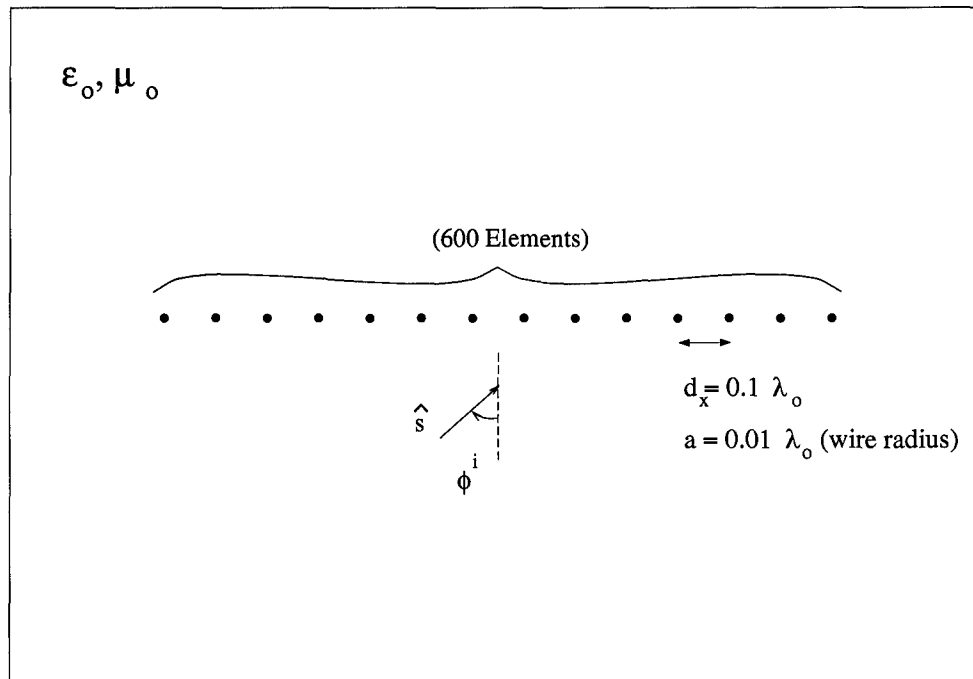


Figure 30. 600 Element Wire Array in Homogeneous Media Illuminated by Plane Wave at an Arbitrary Incident Angle

code's accuracy. The author made every attempt to use independently validated reference codes. In the following material, cases where the reference code results may be questionable are clearly noted.

*4.1.1 Wire Array in a Homogeneous Media.* The two-dimensional wire array serves as the prototype geometry throughout this research. Figure 30 depicts the specific scattering scenario the author chose to validate the hybrid PMM/MM technique. This particular array geometry represents a typical example of many tests the author performed in developing the hybrid technique.

The next series of figures compares the induced scattering current magnitude and phase for each element in the 600 element array. The reference values are generated by a standard 600 unknown MM analysis based on the two-dimensional free-space Green's function. For clarity, the figures leave out the central portion of the array. Enough elements are included however, to show where the currents are behaving according to Floquet theory.



Figures 31 and 32 show the induced currents on the left edge. Although not shown, the right array edge is a mirror copy of the left edge. The reference values are denoted by Xs and the hybrid PMM/MM values are denoted by Os. The array is illuminated by a plane wave incident normal to the array plane. The hybrid technique used 20 edge elements for both left and right hand problems. These figures clearly demonstrate the validity of the hybrid technique.

Figures 33 through 36 show equally as valid results for the array illuminated  $5^\circ$  off normal. In this scattering problem, the author used 30 edge elements for the leading edge (left edge) and 20 elements for the trailing edge (right edge). Note the linear phasing from element-to-element indicating the onset of the Floquet region.

Figures 37 through 40 show the array illuminated  $45^\circ$  off normal. Clearly, the leading edge perturbations are more pronounced. The author again used 30 edge elements for the left edge hybrid PMM/MM problem and 20 edge elements for the right. Note the larger element-to-element phase rotation caused by the off normal illumination. Once again, the hybrid technique captures the correct induced current behavior. In particular, note the smooth transition from the inner-most edge element to the PBF elements. The PBF coupling mitigates the edge effects normally present in a finite array made up of the edge elements, providing a distinct improvement over the hybrid approach proposed by Cwik and Mittra [8].

Figures 41 through 44 show the currents induced by a near grazing illumination of  $85^\circ$  off normal. The author used 100 edge elements for the leading edge and 3 edge elements for the trailing edge in this problem. Increasing the number of trailing edge elements does little to improve the solution accuracy. The author traced the problem to the direct coupling term in the PBF. Specifically, convergence inaccuracies in the spatial domain summation acceleration appear to be the culprit. For this extreme case, the author's implementation of the hybrid PMM/MM technique begins to have difficulty for the trailing edge element behavior. This trend also appears in other plots for angles very near grazing. As discussed in the conclusion, a different acceleration algorithm should eliminate this difficulty.

Incident Angle	MM Code (Unknowns)	MM Code (cpu secs)	PMM/MM Code (Unknowns, Left/Right Problem)	PMM/MM Code (cpu secs)
0°	600	35.6	20/20	0.5
5°	600	35.2	30/20	0.6
45°	600	35.2	30/20	1.2
85°	600	35.5	100/3	2.4

Table 1. Wire Array in Homogeneous Media Reference MM Code versus Hybrid PMM/MM Code Time Comparison

To conclude this subsection on the wire array in a homogeneous media, Table 1 highlights one of the hybrid PMM/MM technique's benefits. The author measured the execution times required for the MM and hybrid PMM/MM computer codes to calculate each of the scattering problems on a Sun Microsystems Sparc20 Workstation. Although not strictly an "apples-to-apples" comparison due to the brute force integration algorithms the author used in the hybrid code, the CPU times give a rough estimate of the computational savings possible. This information, coupled with the fact the MM computational burden scales with system size as  $N^3$  where the hybrid PMM/MM approach scales as  $N^0$  clearly demonstrates the PBF approach's value in large problems<sup>1</sup>. Note that unlike the MM, the hybrid technique does require recalculation of one row in the coupling matrix for each *monostatic* angle. Thus, in generating *monostatic* patterns, the hybrid method scales as  $N^1$  and may not provide as dramatic results, depending on the problem size. Of course, the larger the problem, the better the hybrid technique's performance relative to the MM. Also, no coupling matrix recalculation is required for *bistatic* patterns.

---

<sup>1</sup>This is true as long as the perturbations of the array's edge elements are adequately modeled by the number of edge elements used in the hybrid PMM/MM analysis.

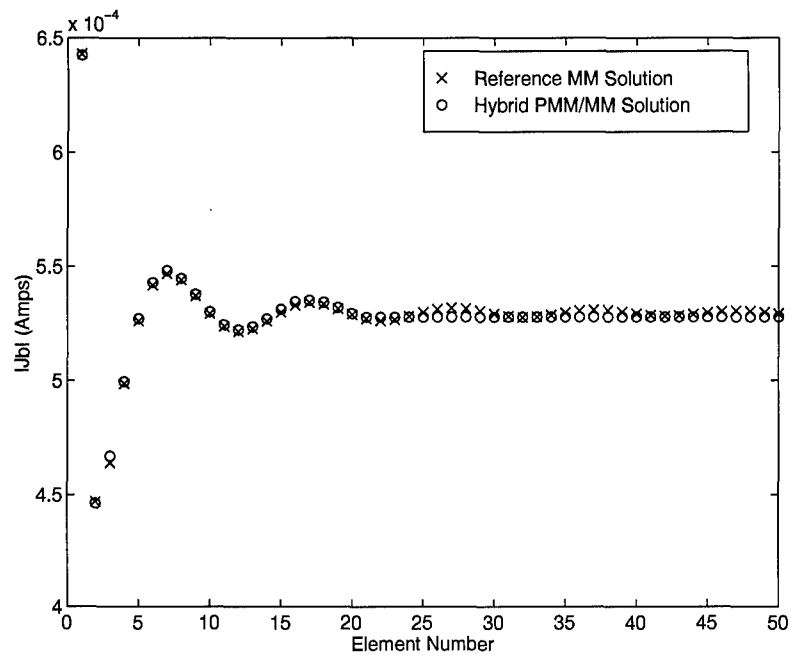


Figure 31. Induced Current Magnitude on Left 50 Elements of Wire Array with Normal Illumination

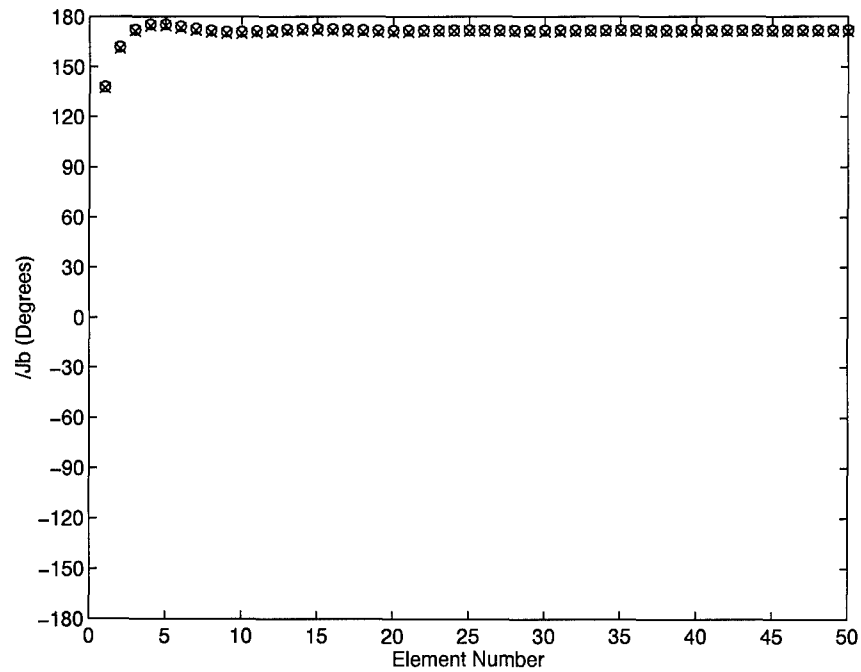


Figure 32. Induced Current Phase on Left 50 Elements of Wire Array with Normal Illumination

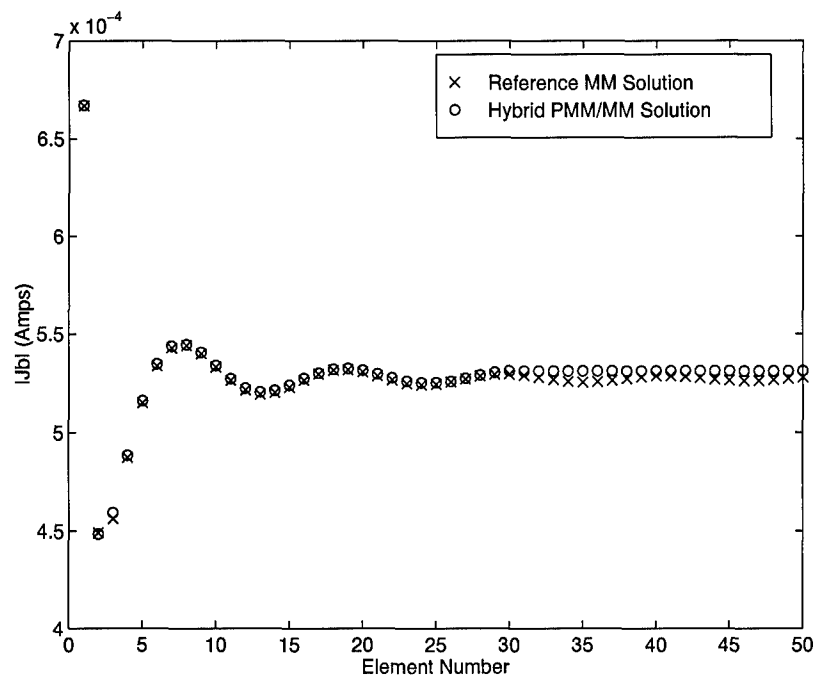


Figure 33. Induced Current Magnitude on Left 50 Elements of Wire Array with  $5^\circ$  off Normal Illumination

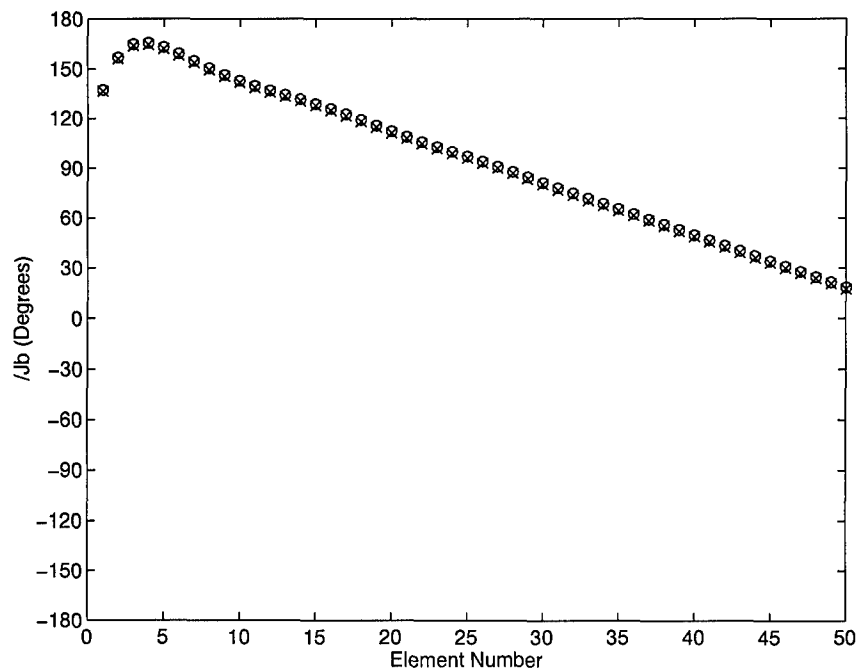


Figure 34. Induced Current Phase on Left 50 Elements of Wire Array with  $5^\circ$  off Normal Illumination

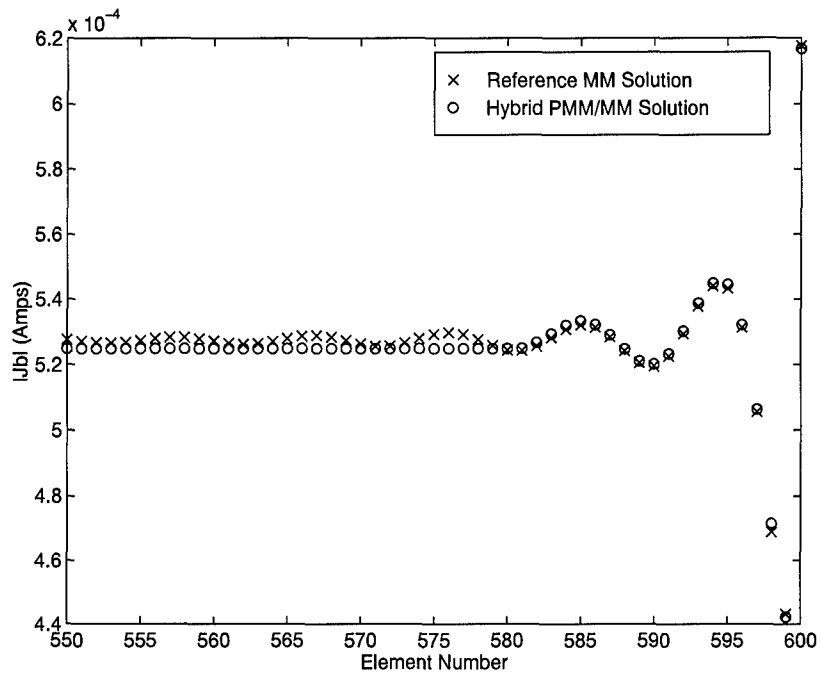


Figure 35. Induced Current Magnitude on Right 50 Elements of Wire Array with 5° off Normal Illumination

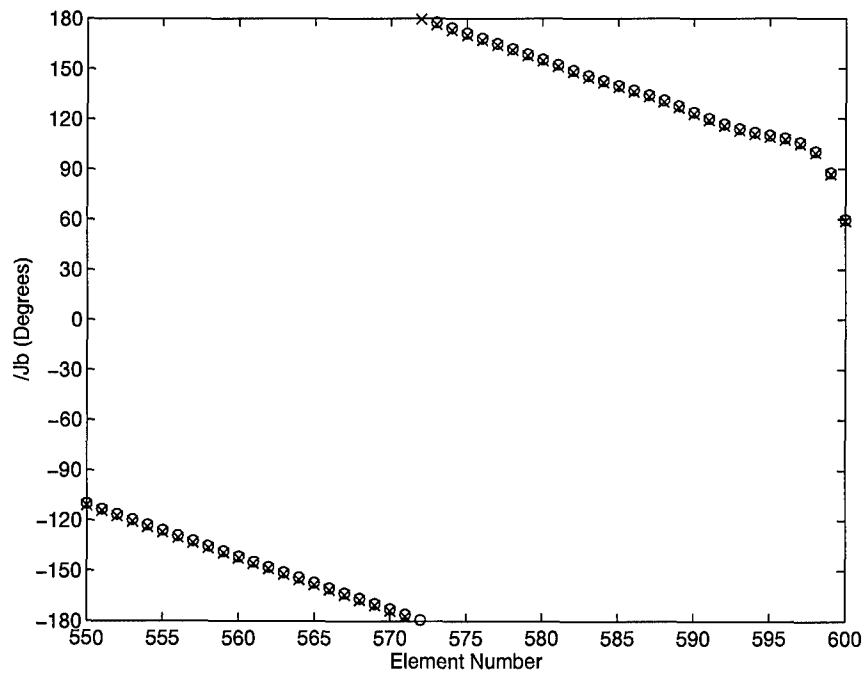


Figure 36. Induced Current Phase on Right 50 Elements of Wire Array with 5° off Normal Illumination

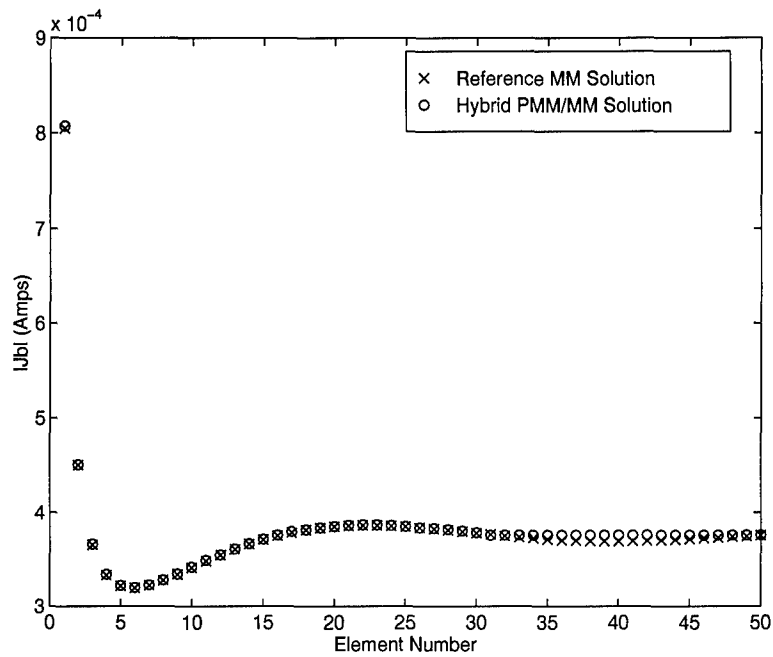


Figure 37. Induced Current Magnitude on Left 50 Elements of Wire Array with 45° off Normal Illumination

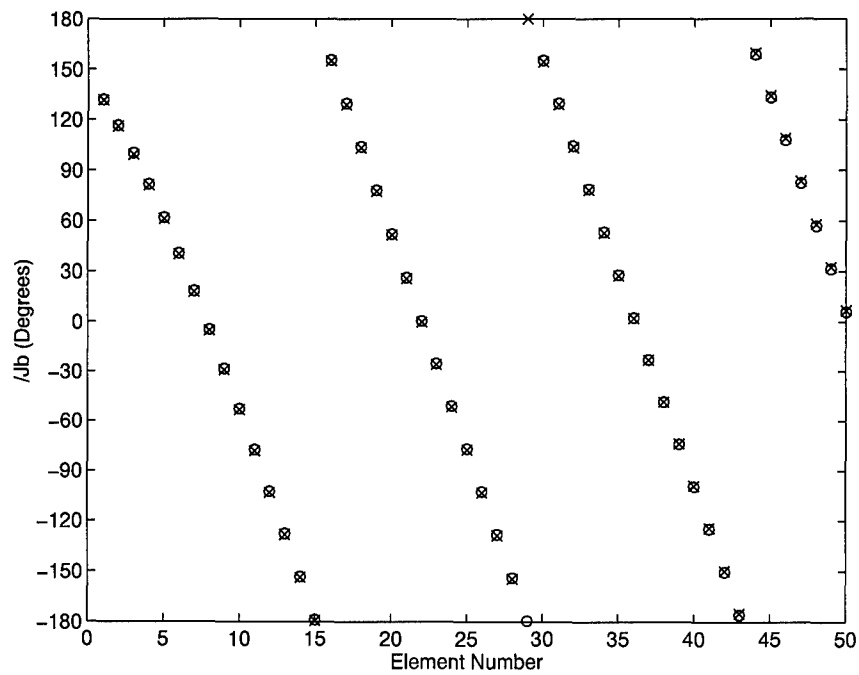


Figure 38. Induced Current Phase on Left 50 Elements of Wire Array with 45° off Normal Illumination

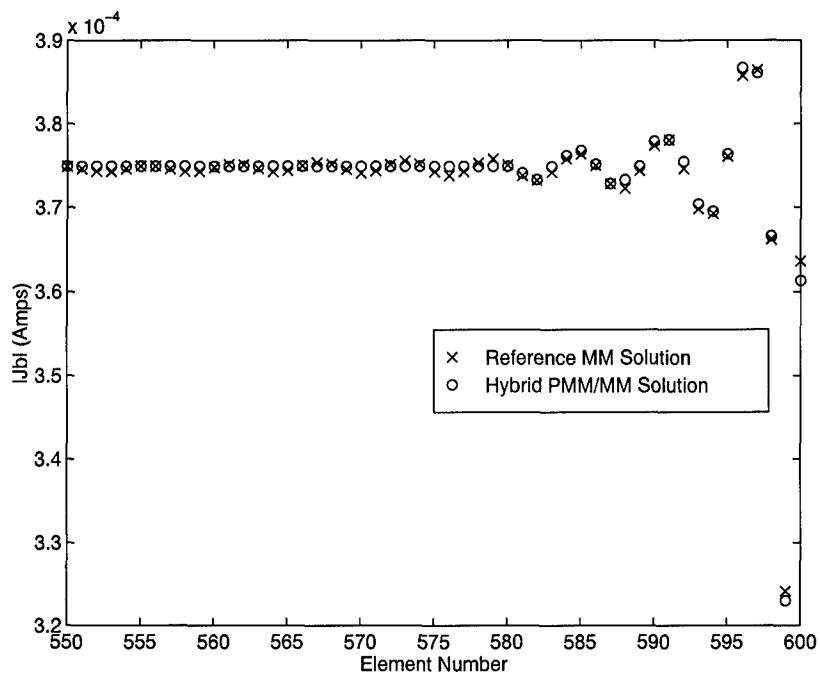


Figure 39. Induced Current Magnitude on Right 50 Elements of Wire Array with  $45^\circ$  off Normal Illumination

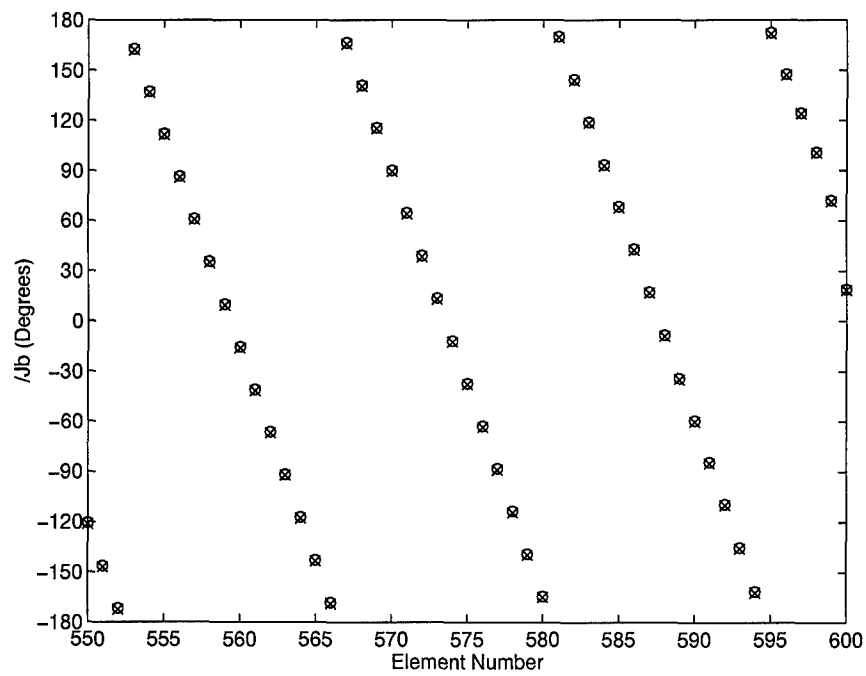


Figure 40. Induced Current Phase on Right 50 Elements of Wire Array with  $45^\circ$  off Normal Illumination

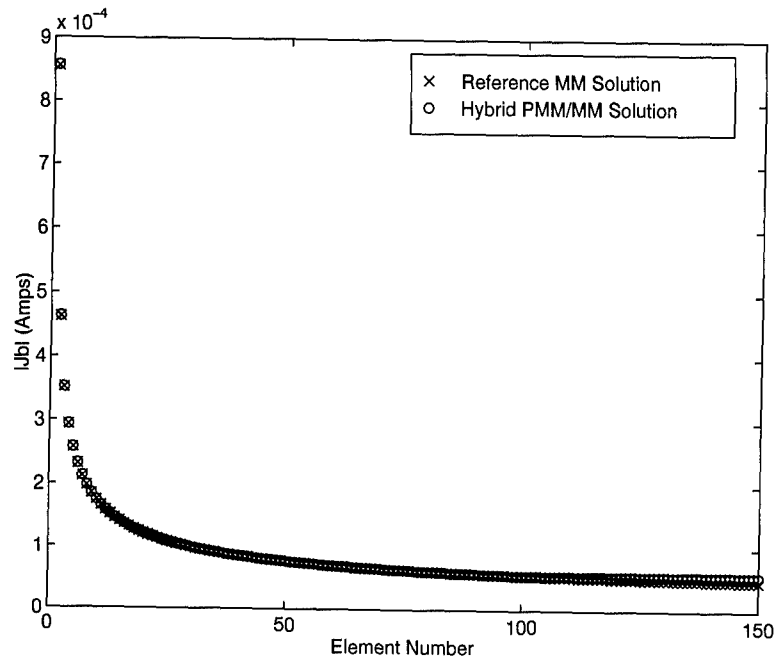


Figure 41. Induced Current Magnitude on Left 150 Elements of Wire Array with 85° off Normal Illumination

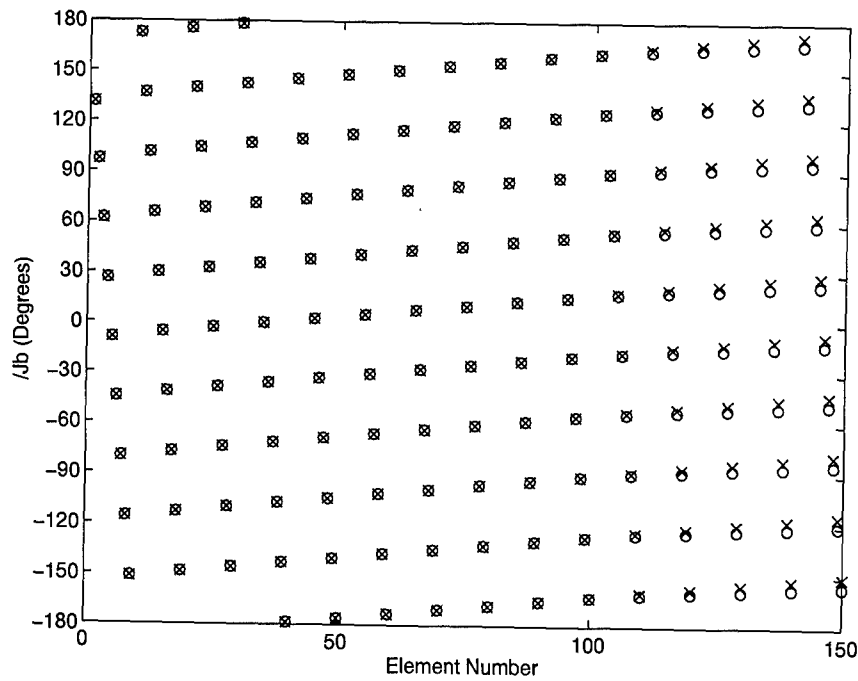


Figure 42. Induced Current Phase on Left 150 Elements of Wire Array with 85° off Normal Illumination



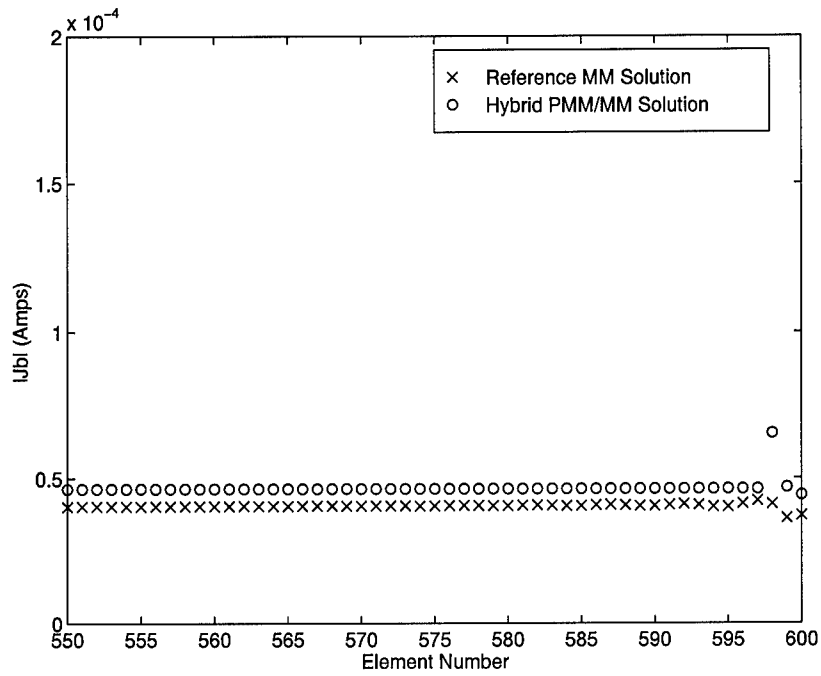


Figure 43. Induced Current Magnitude on Right 50 Elements of Wire Array with 85° off Normal Illumination

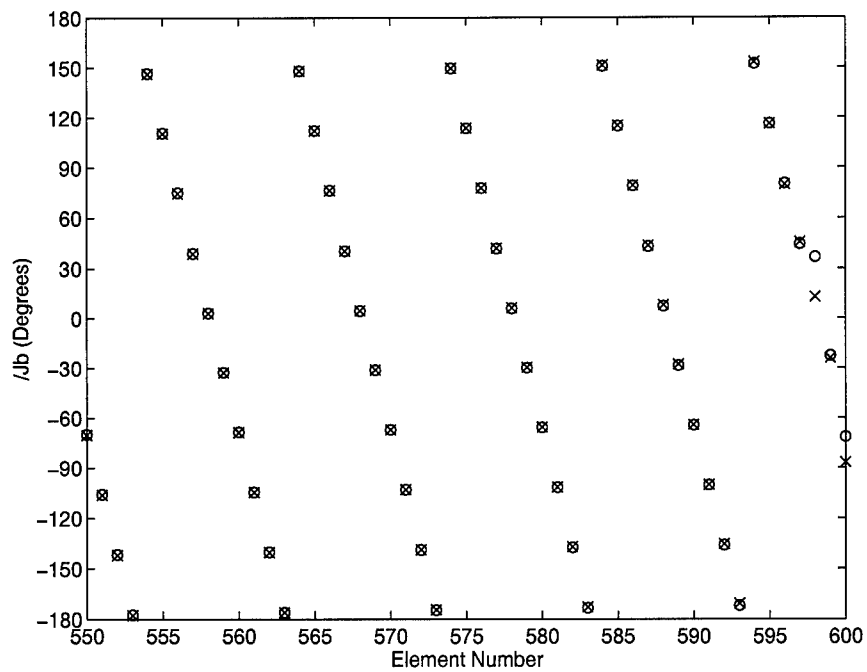


Figure 44. Induced Current Phase on Right 50 Elements of Wire Array with 85° off Normal Illumination

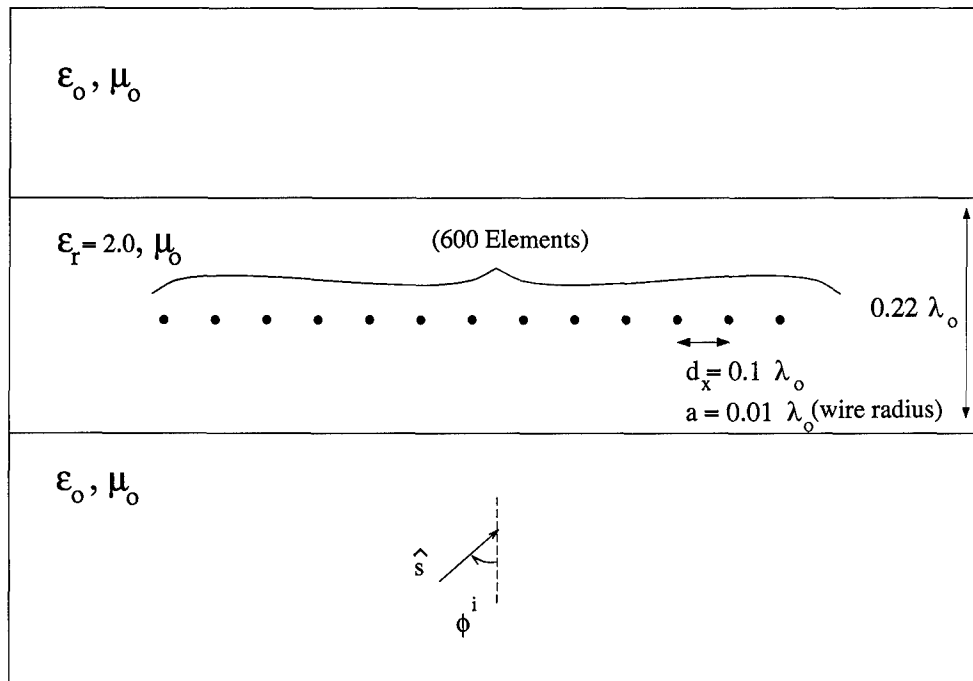


Figure 45. 600 Element Wire Array in a Dielectric Slab Illuminated by Plane Wave at an Arbitrary Incident Angle

4.1.2 *Wire Array in a Stratified Media.* This subsection turns to the problem of a wire array embedded in the dielectric slab shown in Figure 45. The author chose a MM code based on the ASM to provide the reference solutions. Again, the wire array contains 600 elements of which only the left and right edges are displayed.

Figures 46 and 47 show the wire array's left edge subject to normal incident illumination. As in the homogeneous case, the induced currents are symmetric about the middle of the array. The author used only 20 edge elements as before. Here the slab has strengthened the coupling between the elements, necessitating the inclusion of more edge elements to completely capture the edge perturbations. Note however, the elements that were modeled are very accurate.

Figures 48 through 51 show the results for the array illuminated  $5^\circ$  off normal. Here the author used 50 and 30 edge elements respectively in the hybrid PMM/MM analysis. Once again, the hybrid technique accurately models the induced currents.

Incident Angle	MM Code (Unknowns)	MM Code (cpu secs)	PMM/MM Code (Unknowns, Left/Right Problem)	PMM/MM Code (cpu secs)
0°	600	353.8	20/20	95.7
5°	600	357.3	50/30	170.0
45°	600	353.6	100/20	334.3
85°	600	356.8	200/20	1980.7

Table 2. Wire Array in Slab Reference MM Code versus Hybrid PMM/MM Code Time Comparison

Figures 52 through 55 show the induced currents for a plane wave incident 45° off normal. Examining the figures reveal 100 and 20 edge elements were sufficient to accurately model the leading and trailing edges in this scattering problem.

Finally, Figures 56 through 59 show the currents induced by a grazing illumination of 85° off normal. In this case, the author used 200 and 20 edge elements for the two semi-infinite subproblems. Notice the code calculates the trailing edge elements accurately. The dielectric slab decreases the angle of incidence *in the slab*, thus avoiding the numerical problems encountered in the homogeneous media geometry.

As for the homogeneous case, Table 2 contains the CPU times for the reference MM and hybrid PMM/MM based codes to compute each scattering scenario. Unlike the homogeneous case, these values represent a true “apples-to-apples” comparison since the reference code used the core of the hybrid code with the PBF “turned off.” While these computation times are not as dramatic as the homogeneous case, the fact remains as the problem size increases, the MM based system sizes quickly become prohibitively large, where as the hybrid PMM/MM based system size remains constant. Note, the large hybrid technique computation time for an 85° incident angle is a result of numerical difficulties in computing the continuous spectral integral and not truly indicative of the technique’s performance. Asymptotic evaluation would probably reduce this time.

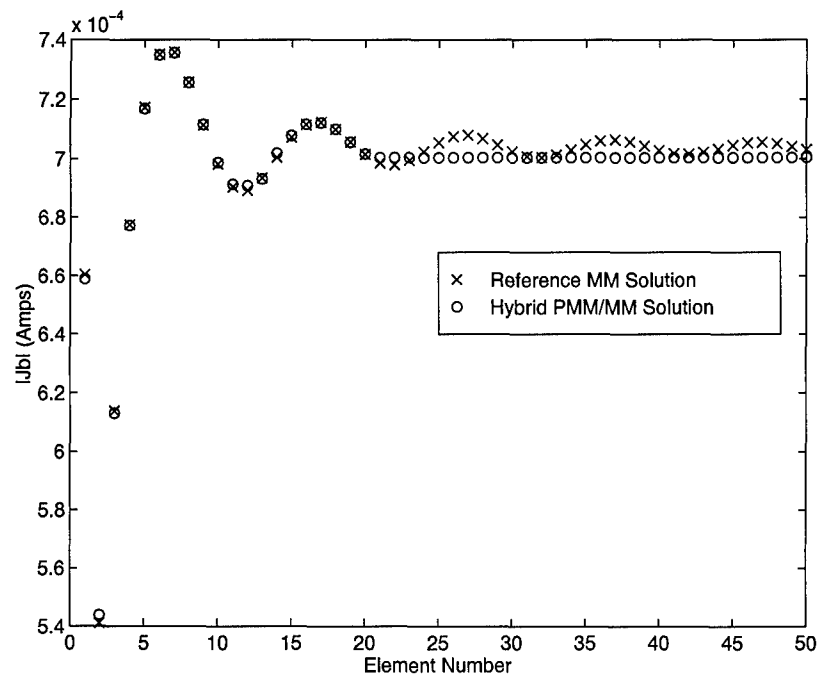


Figure 46. Induced Current Magnitude on Left 50 Elements of Wire Array in Slab with Normal Illumination

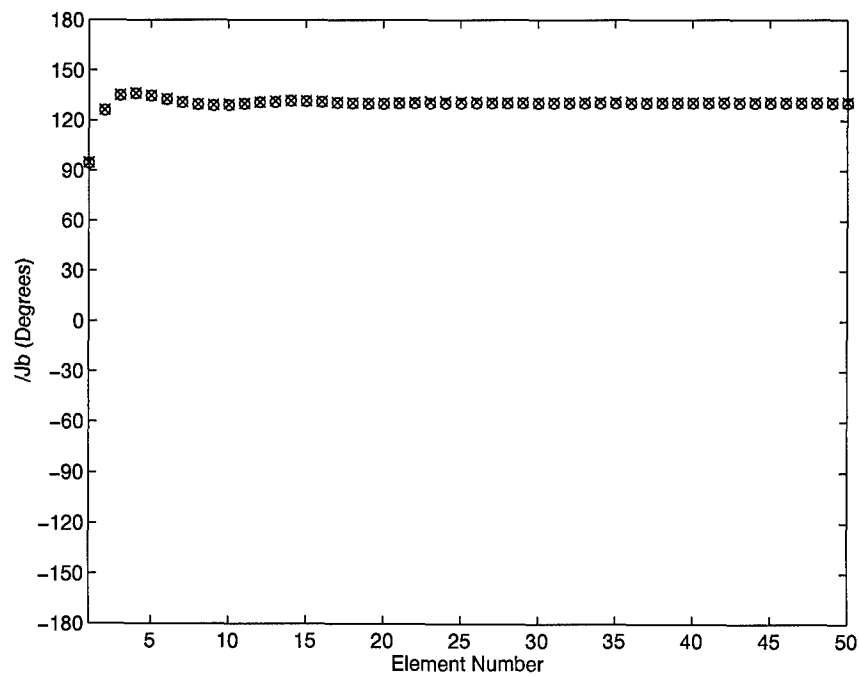


Figure 47. Induced Current Phase on Left 50 Elements of Wire Array in Slab with Normal Illumination

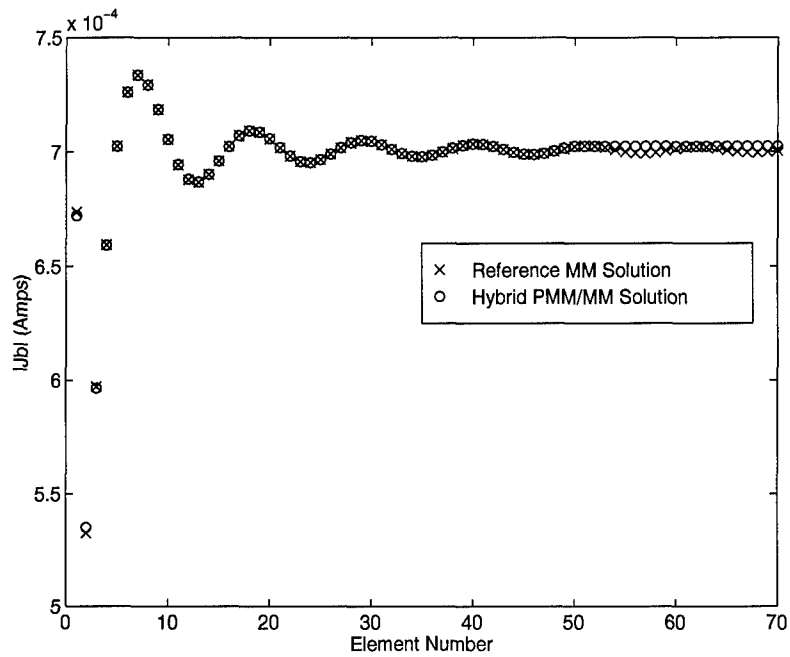


Figure 48. Induced Current Magnitude on Left 70 Elements of Wire Array in Slab with 5° off Normal Illumination

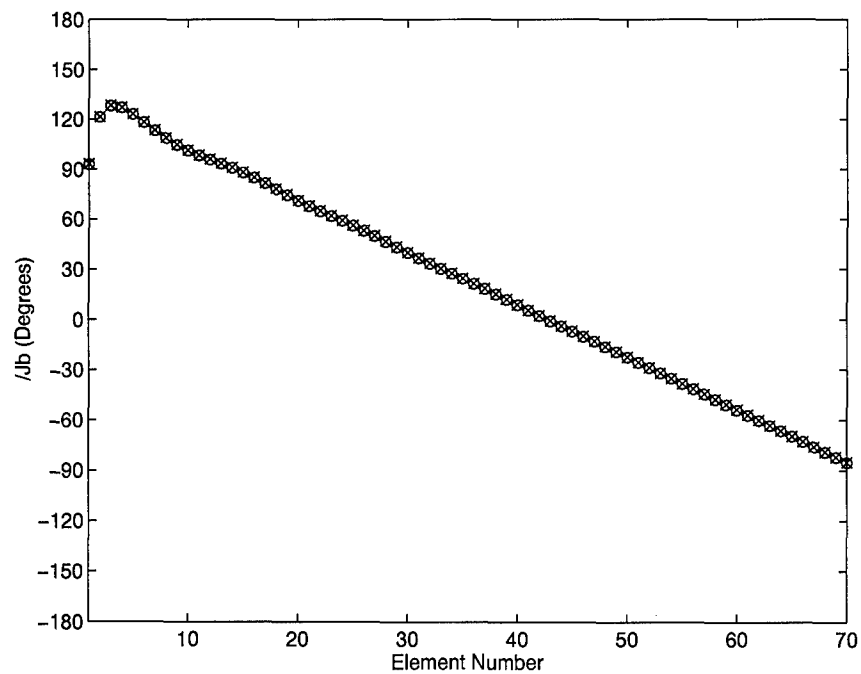


Figure 49. Induced Current Phase on Left 70 Elements of Wire Array in Slab with 5° off Normal Illumination

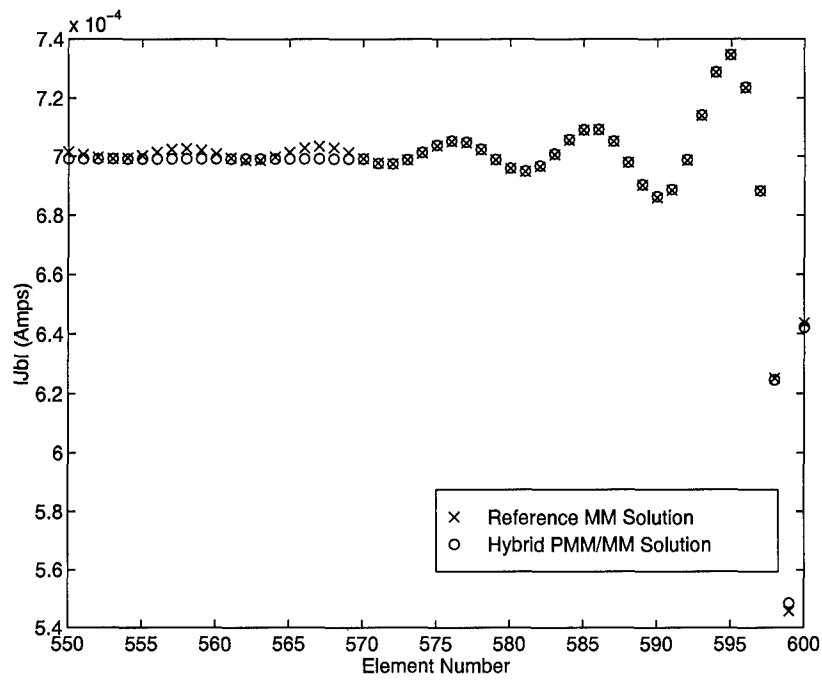


Figure 50. Induced Current Magnitude on Right 50 Elements of Wire Array in Slab with 5° off Normal Illumination

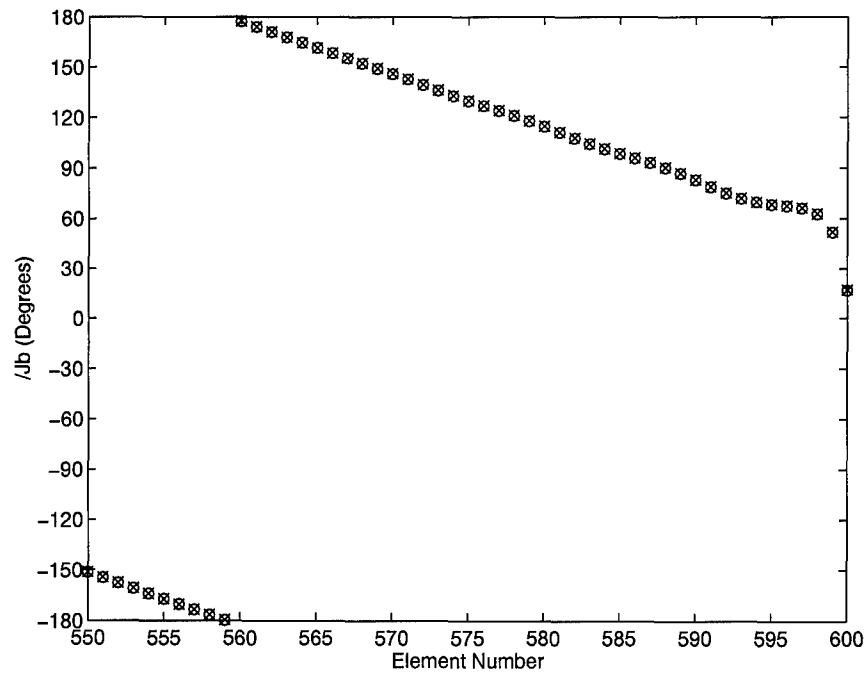


Figure 51. Induced Current Phase on Right 50 Elements of Wire Array in Slab with 5° off Normal Illumination

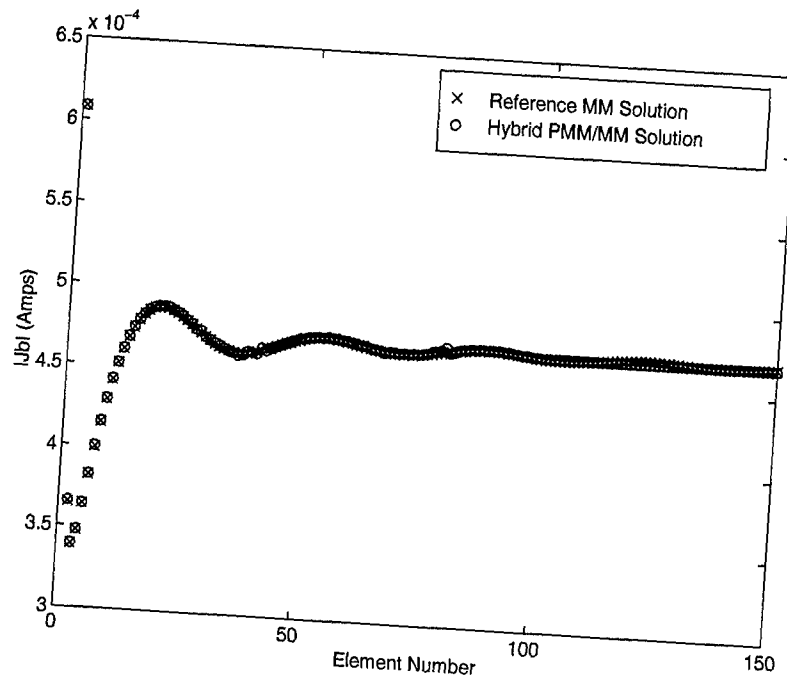


Figure 52. Induced Current Magnitude on Left 150 Elements of Wire Array in Slab with 45° off Normal Illumination

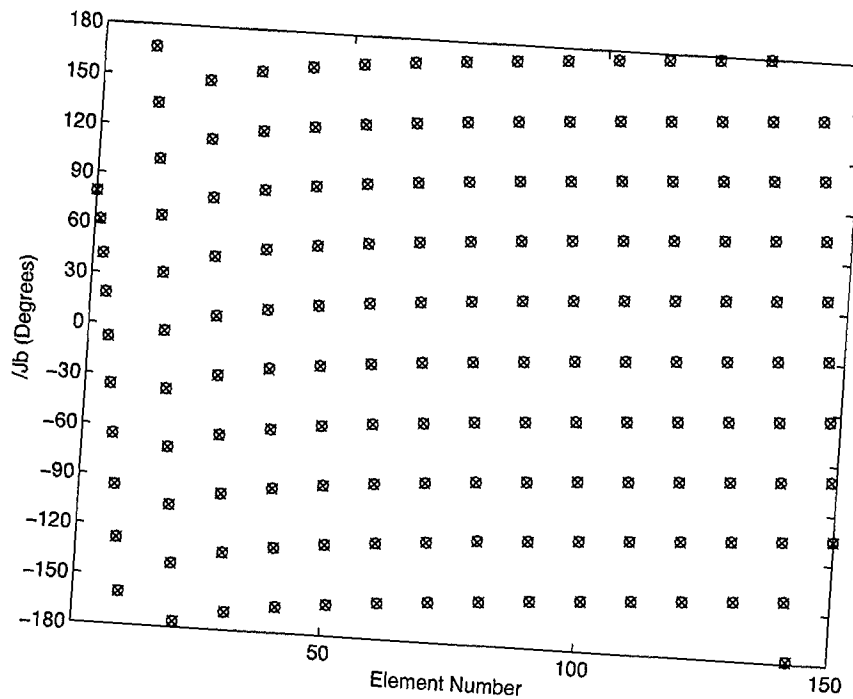


Figure 53. Induced Current Phase on Left 150 Elements of Wire Array in Slab with 45° off Normal Illumination

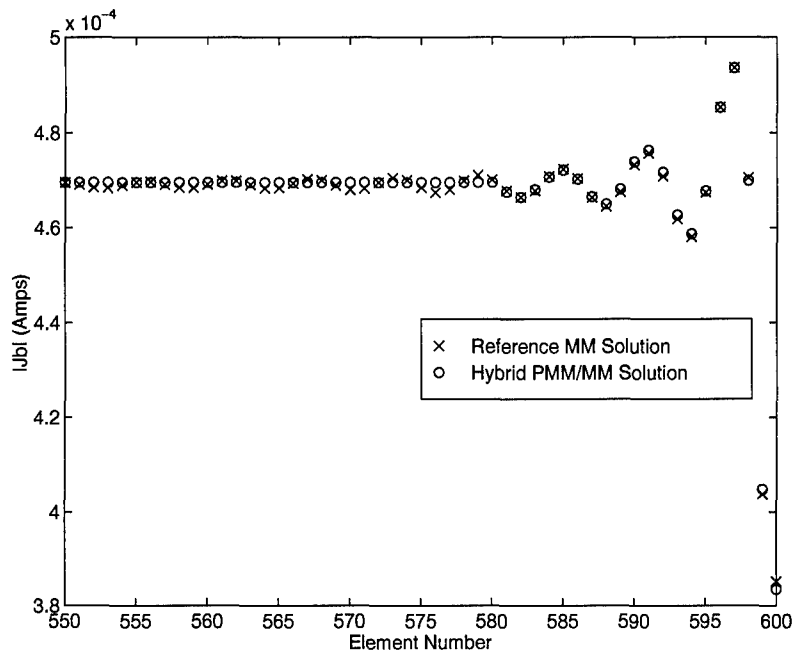


Figure 54. Induced Current Magnitude on Right 50 Elements of Wire Array in Slab with 45° off Normal Illumination

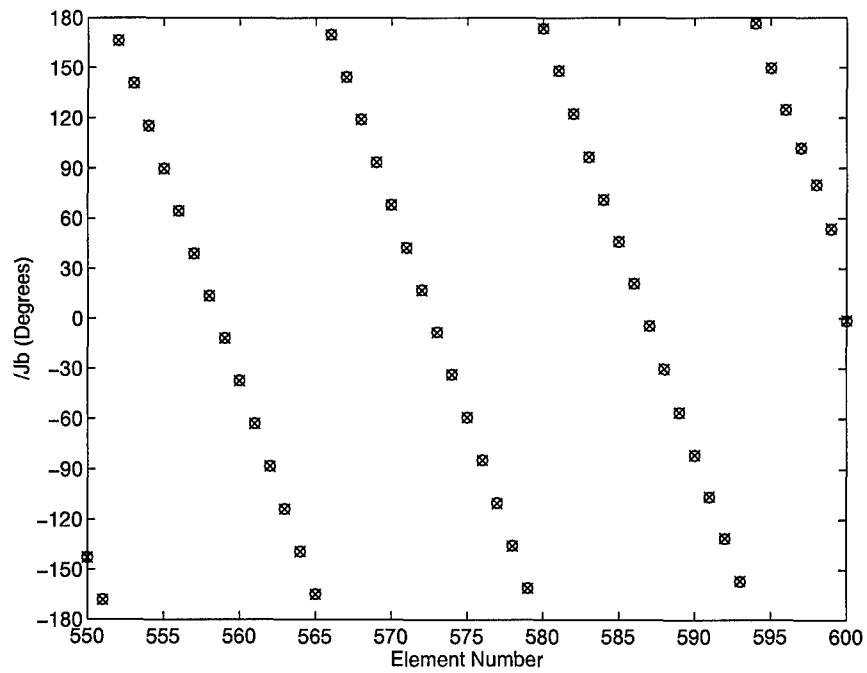


Figure 55. Induced Current Phase on Right 50 Elements of Wire Array in Slab with 45° off Normal Illumination



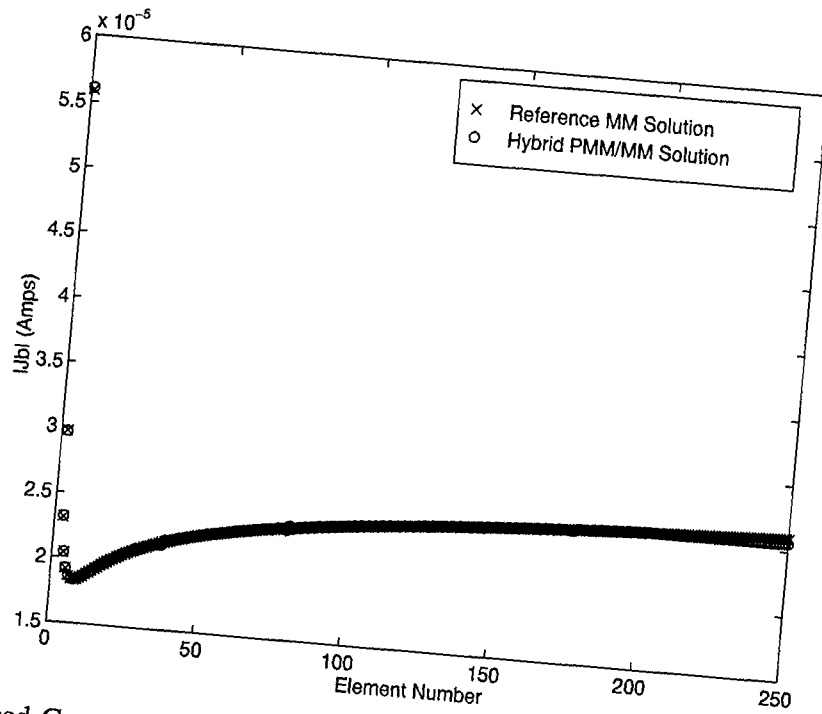


Figure 56. Induced Current Magnitude on Left 250 Elements of Wire Array in Slab with 85° off Normal Illumination

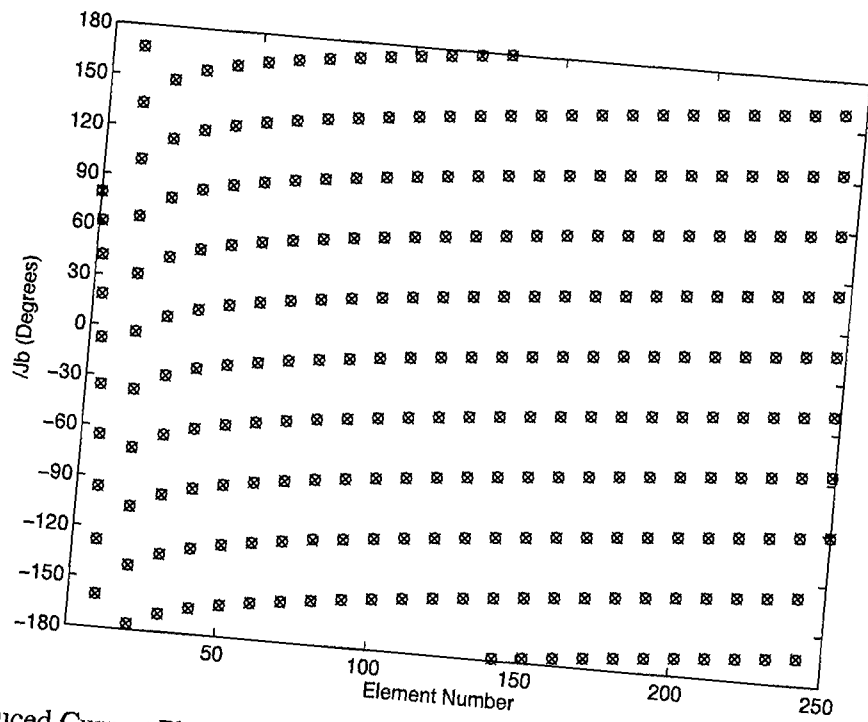


Figure 57. Induced Current Phase on Left 250 Elements of Wire Array in Slab with 85° off Normal Illumination

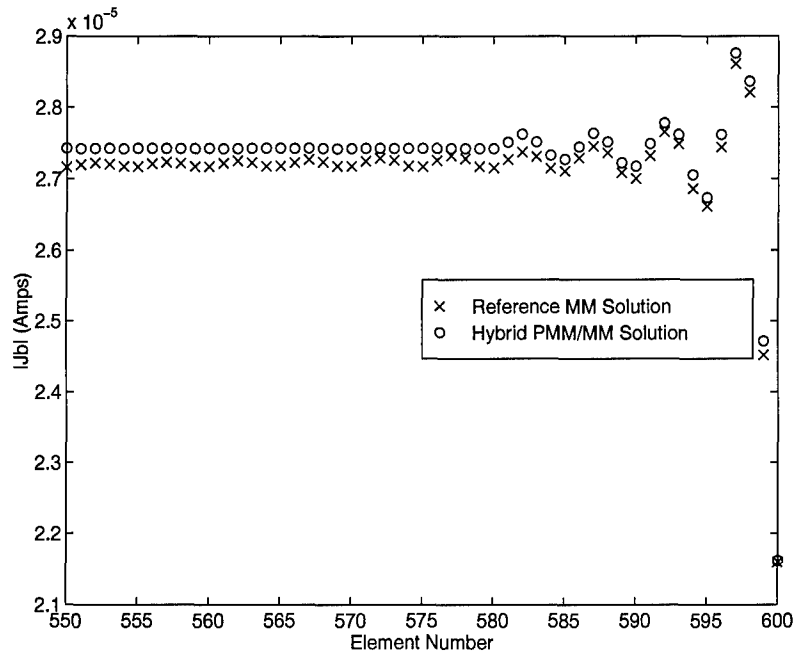


Figure 58. Induced Current Magnitude on Right 50 Elements of Wire Array in Slab with 85° off Normal Illumination

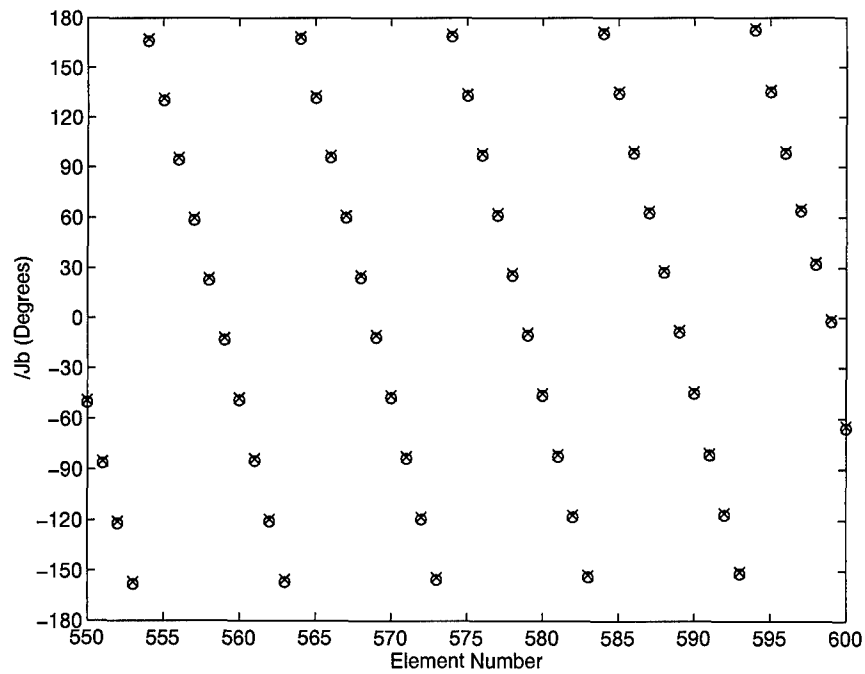


Figure 59. Induced Current Phase on Right 50 Elements of Wire Array in Slab with 85° off Normal Illumination

4.1.3 *Slot Array in a Homogeneous Media.* Having examined the two-dimensional wire array, the chapter now focuses on several slot array geometries. Slotted ground planes are a common form of radome. Thus, the following plots demonstrate the hybrid PMM/MM technique's applicability to practical radome design problems.

As for the wire arrays, the author validated the hybrid code against an ASM based MM code. In this case, two independent reference codes, one written by the author and one by Skinner [33], provide additional confidence in the solution accuracy. The reference code solutions represent the "truth" standard one uses to judge the hybrid code's validity. One desires both agreement between the reference codes and agreement with the hybrid code. In terms of testing the validity of this research, the latter comparison is by far the more important. Thus, one must examine the following figures with two separate questions in mind. One, do the two reference codes agree reasonably well? Two, does the hybrid code accurately represent the reference code solution?

Figure 23, at the beginning of Chapter III, depicts the general features of the slot arrays examined in the following sections. This particular section begins by examining a 100 column slot array in a homogeneous media. The elements are  $\hat{z}$  oriented slots 0.881 cm long and 0.038 cm wide. They form slot columns with inner-element spacing 1.27 cm in the  $\hat{z}$  direction and 1.1 cm in the  $\hat{x}$  direction. The columns create a non-skewed grid. A 15 GHz plane wave illuminates the array at 5°, 45°, and 85° off normal. Element number one always belongs to the leading edge of the array. In all cases, the author uses a single PWS mode per slot.

Figures 60 and 61 show the magnitude and phase of the currents induced on the column reference elements. The reference values are denoted by Xs and \*s, and the hybrid PMM/MM values are denoted by Os. The array is illuminated by a plane wave incident 5° off normal. The hybrid technique used 20 edge elements for both left and right hand problems. First, note the two reference codes agree reasonably well. The current perturbations near the edges are virtually identical in the two solutions. The main difference is a slight offset between the curves. This offset can be attributed to the different numerical approaches the two authors used. In fact, the good agreement is a testament to the validity of the underlying ASM approach. Second, compare the hybrid solution to the reference solutions. The agreement is excellent. Since the author's reference solution is generated by the hybrid

code with the PBF turned off, it provides a more accurate standard against which to judge the hybrid solution.

Figures 62 and 63 show the currents induced on the same array illuminated by a plane wave incident  $45^\circ$  off normal. Here, the hybrid technique used 25 edge elements for both left and right hand problems. In this case, the two reference codes provide virtually identical results. The hybrid solution accurately captures the edge element behavior for those elements modeled. However, a few more edge elements would give a slightly more accurate PBF value for the array's central portion.

Finally, Figures 64 and 65 show the currents induced on the same array illuminated by a plane wave incident  $85^\circ$  off normal. The hybrid technique used 30 edge elements for both left and right hand problems. The hybrid solution is a good approximation to the reference codes' solutions. However, as for the wire array, the author's code has difficulties capturing the trailing edge behavior at extreme grazing angles. Fortunately, in the homogeneous media where the problem occurs, these currents always have a much smaller magnitude than the leading edge currents, mitigating their influence in the far-field. Figure 66 demonstrates this fact with a monostatic radar echo area (REA) plot over the angle range from  $0^\circ$  to  $88^\circ$ . Although not implemented in the author's codes, it is apparent from the figure one could save computation time with little sacrifice in accuracy by only computing the leading edge semi-infinite problem at near grazing incident angles.

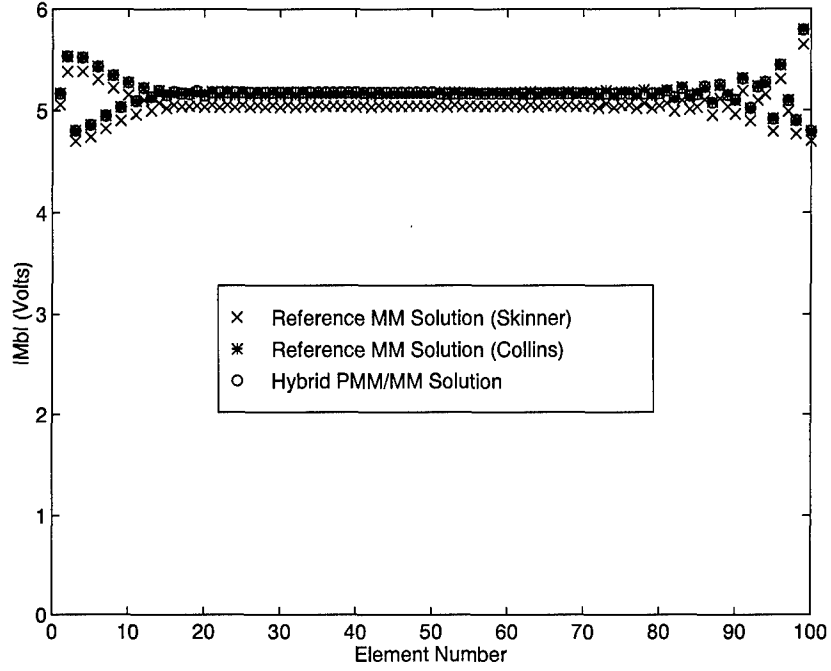


Figure 60. Induced Current Magnitude on 100 Element Slot Array with 5° off Normal Illumination

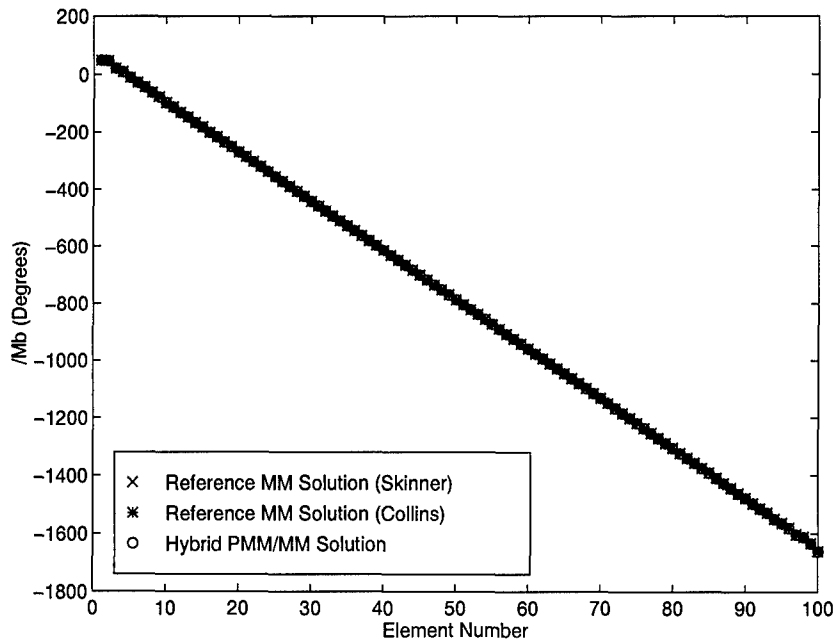


Figure 61. Induced Current Phase on 100 Element Slot Array with 5° off Normal Illumination

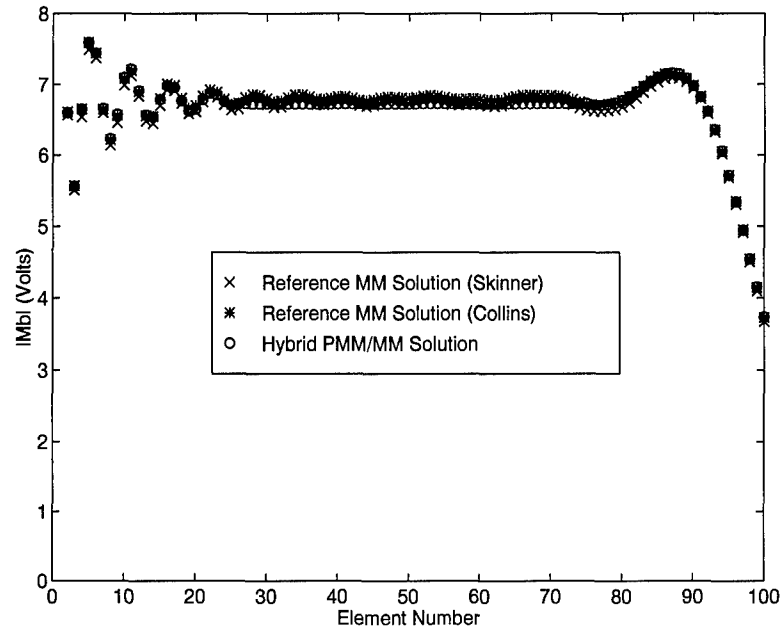


Figure 62. Induced Current Magnitude on 100 Element Slot Array with 45° off Normal Illumination

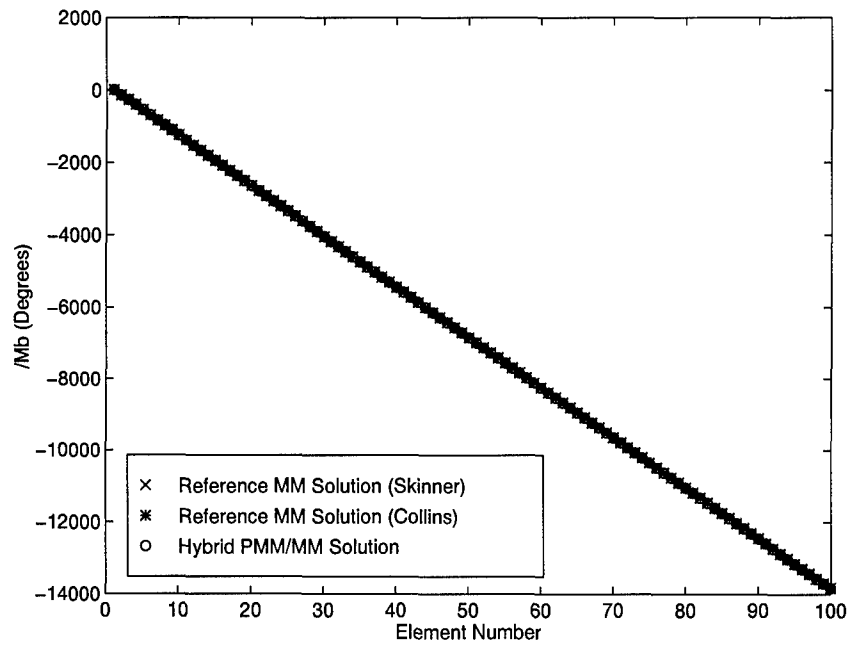


Figure 63. Induced Current Phase on 100 Element Slot Array with 45° off Normal Illumination

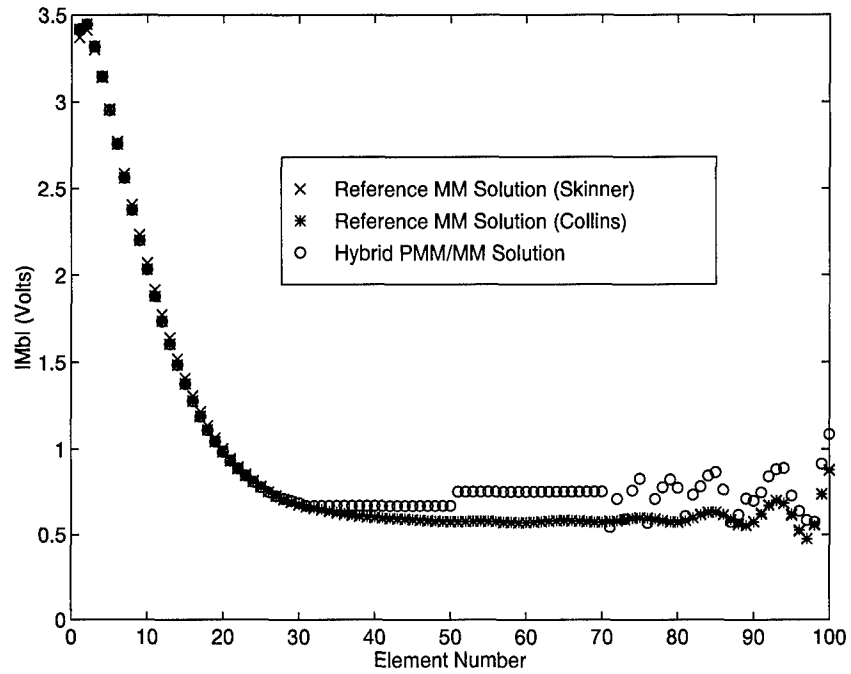


Figure 64. Induced Current Magnitude on 100 Element Slot Array with 85° off Normal Illumination

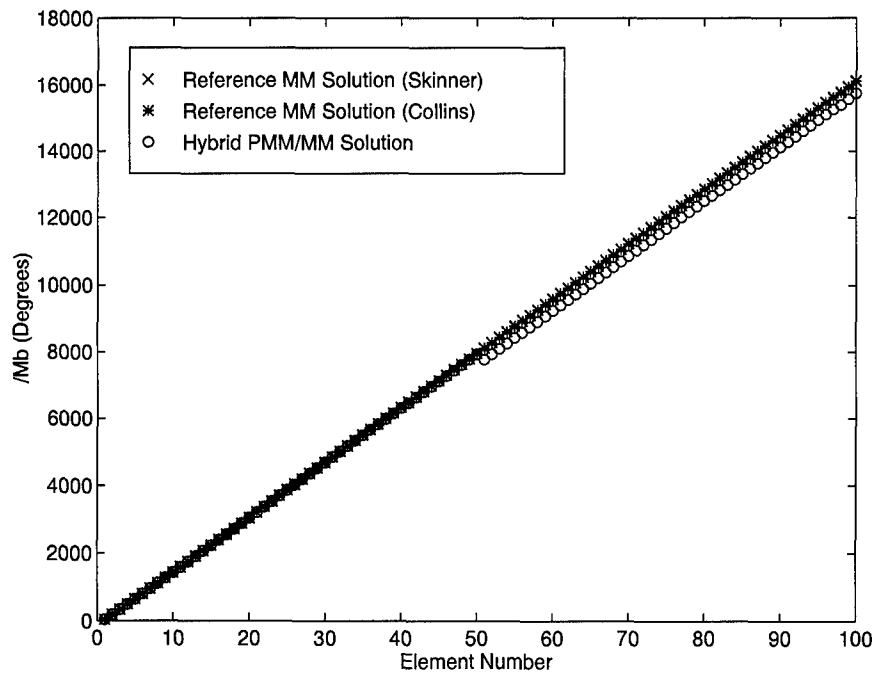


Figure 65. Induced Current Phase on 100 Element Slot Array with 85° off Normal Illumination

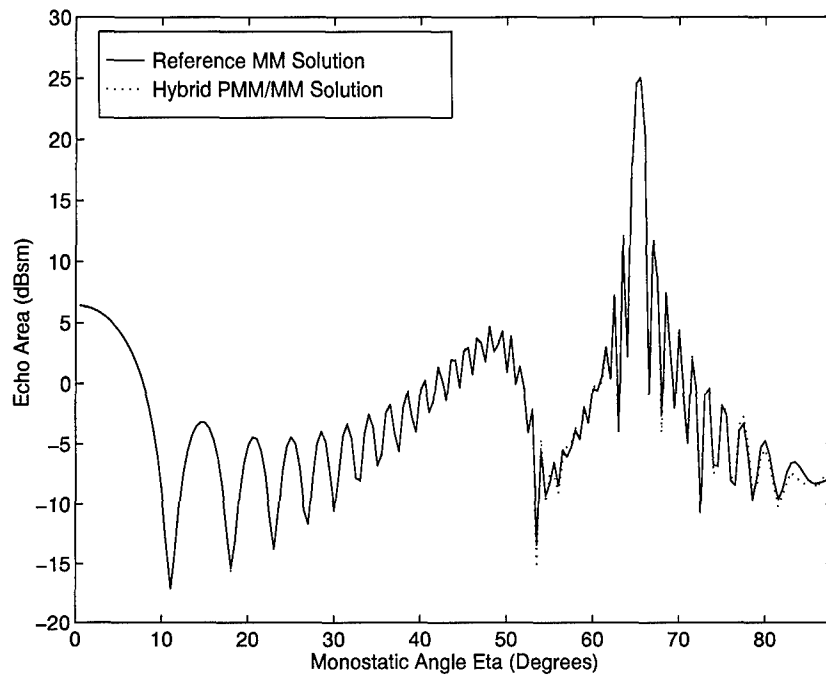


Figure 66. REA pattern at 15 GHz for 100 Column Slot Array in Homogeneous Media



*4.1.4 Slot Array in a Stratified Media.* This section adds a symmetric dielectric sandwich around the the array examined in the previous section. The top and bottom layers are 0.55875 cm thick and have relative permittivities of 2.0. Once again, the differences between the reference codes can be attributed to the authors' numerical implementations. Specifically, the authors use different approaches to handling the surface wave singularities introduced by the dielectric layers. For the single layer case, Skinner uses an analytic extraction technique to remove the T-factor singularities. This contrasts with the lossy dielectric approach described earlier. It is difficult to ascertain which solution is closer to the truth, but again, the main issue is how well the hybrid technique captures the MM solution. On this matter, the following figures speak for themselves.

Figures 67 and 68 show the current magnitude and phase induced on the column reference elements for a  $5^\circ$  off normal incident angle. The hybrid technique used 20 edge elements for both left and right hand problems. As for the homogeneous case, the hybrid PMM/MM accurately captures the induced currents, as differences in Figure 67 have been magnified by an expanded scale.

Figures 69 and 70 show the current magnitude and phase induced on the column reference elements for a  $45^\circ$  off normal incident angle. The hybrid technique used 20 edge elements for both left and right hand problems. Notice how the dielectric sandwich has modified the trailing edge current behavior. Once again, the hybrid technique compares well with the reference solution.

Figures 71 and 72 show the current magnitude and phase induced on the column reference elements for a  $85^\circ$  off normal incident angle. The hybrid technique used 20 edge elements for both left and right hand problems. Clearly, the leading edge requires more edge elements. Note how the PBF magnitudes for the two half problems differ. This provides a good indication more edge elements are necessary to improve the solution accuracy. In addition, one may note the trailing edge difficulties associated with the homogeneous array are virtually eliminated by the dielectric cladding, as seen earlier with the wire array. This can be attributed to refraction as the plane wave is bent toward normal upon entering the dielectric slab.

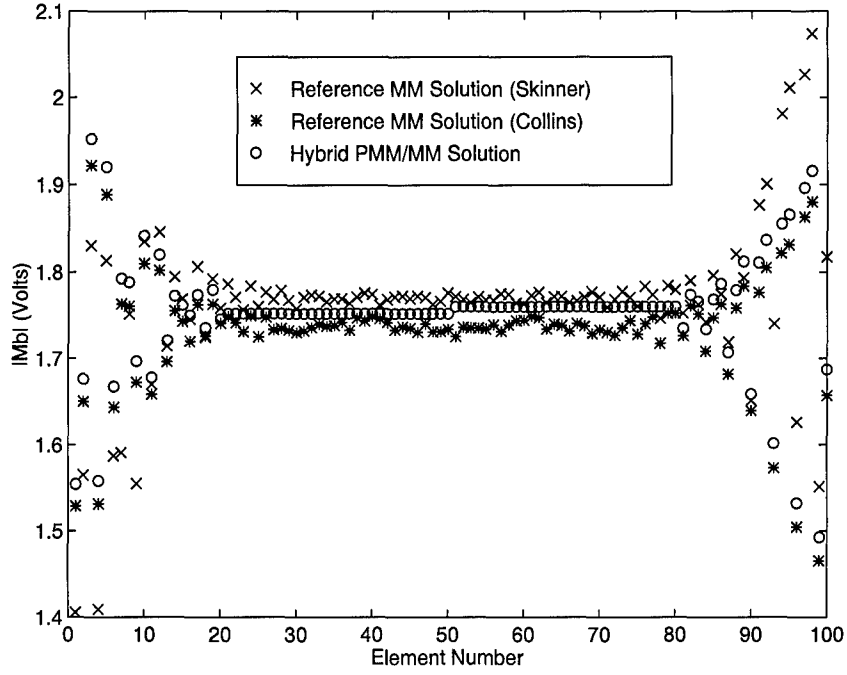


Figure 67. Induced Current Magnitude on 100 Element Slot Array in Stratified Media with 5° off Normal Illumination

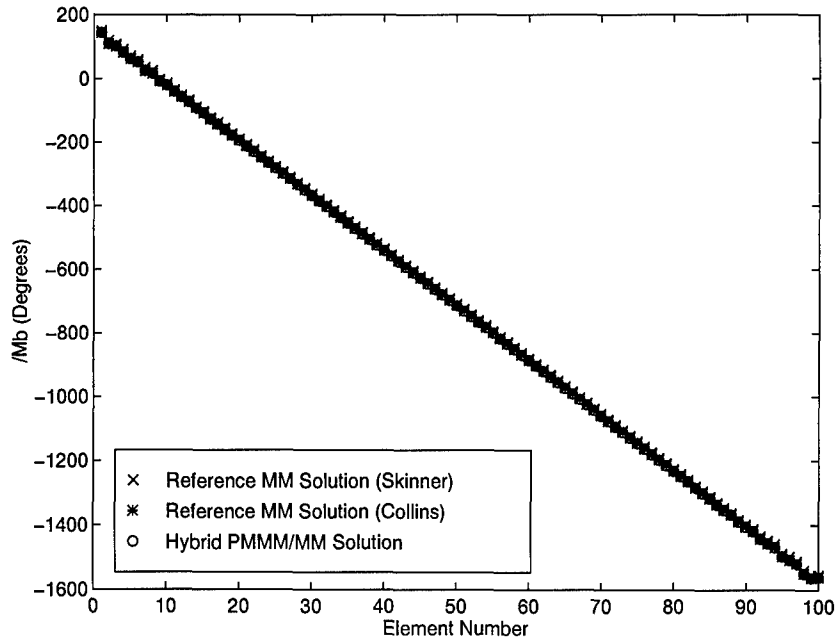


Figure 68. Induced Current Phase on 100 Element Slot Array in Stratified Media with 5° off Normal Illumination

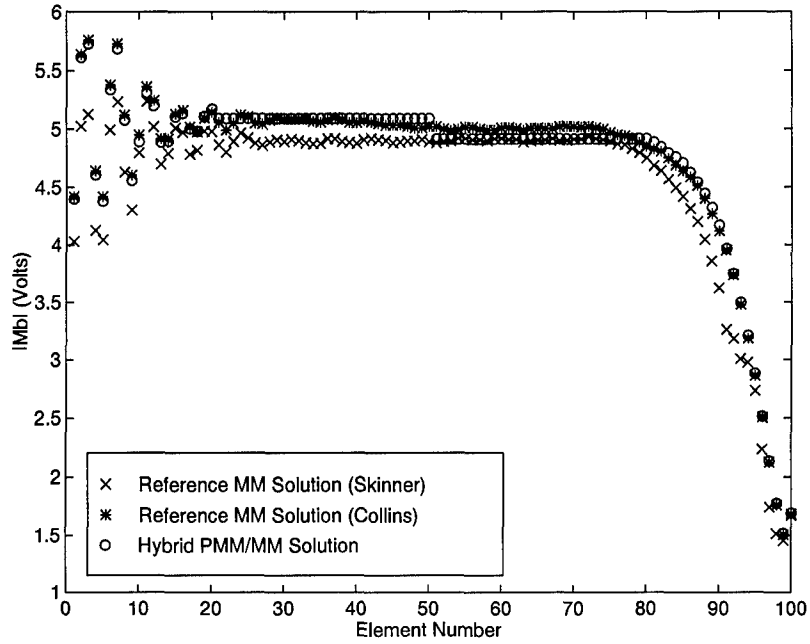


Figure 69. Induced Current Magnitude on 100 Element Slot Array in Stratified Media with 45° off Normal Illumination

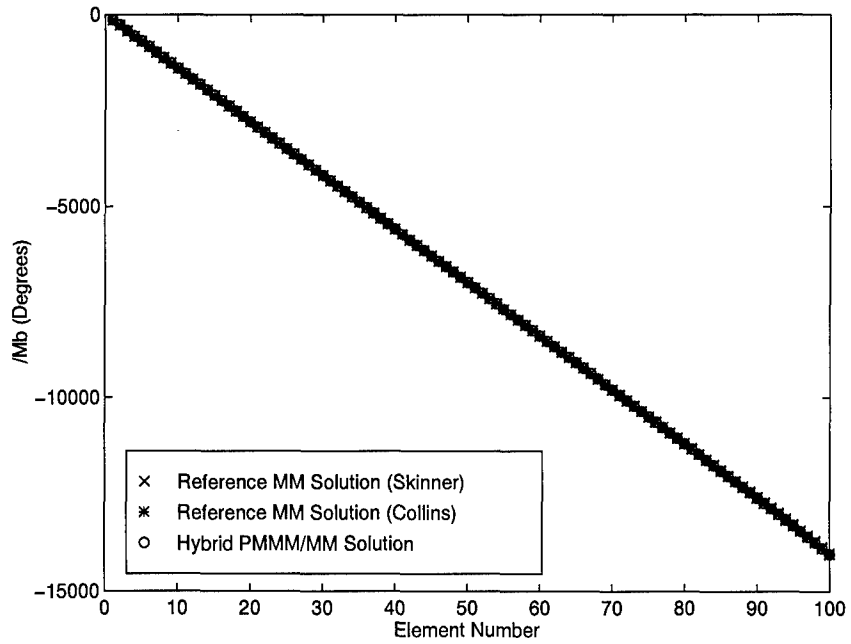


Figure 70. Induced Current Phase on 100 Element Slot Array in Stratified Media with 45° off Normal Illumination

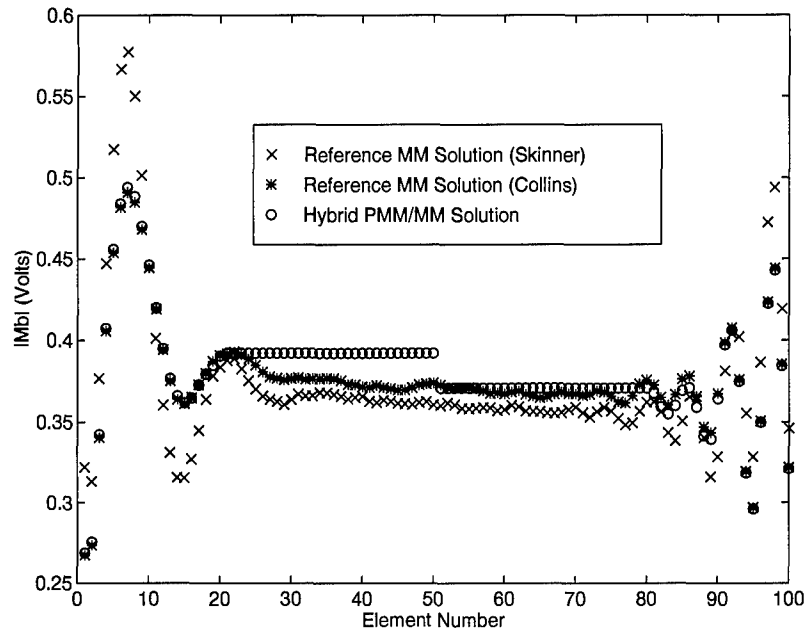


Figure 71. Induced Current Magnitude on 100 Element Slot Array in Stratified Media with 85° off Normal Illumination

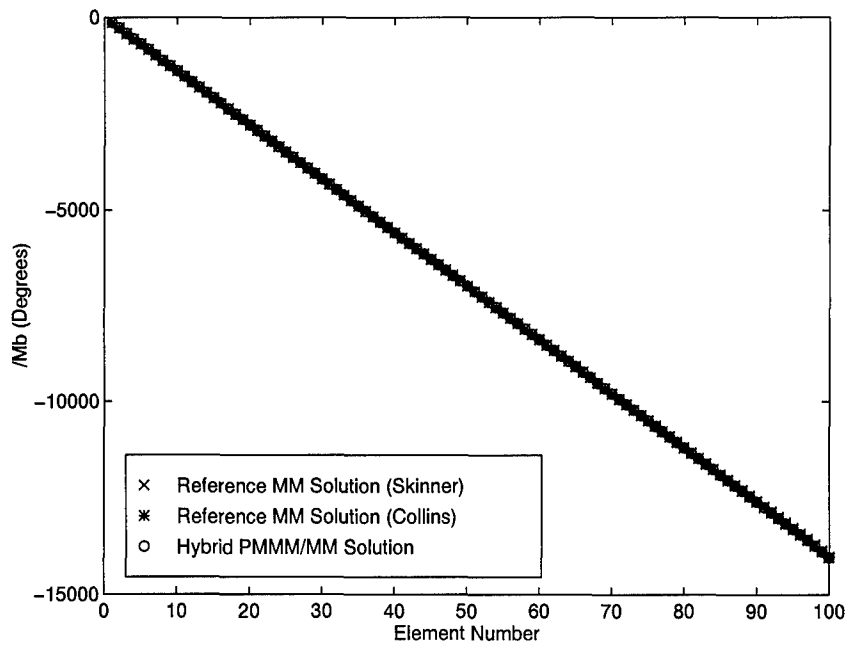


Figure 72. Induced Current Phase on 100 Element Slot Array in Stratified Media with 85° off Normal Illumination

*4.1.5 Slot Array with Loaded Edge Elements.* The ability to modify the edge element currents via loading is an important tool to the radome designer. This section presents the results of applying r-card to the first and last nine columns of the homogeneous media slot array described in section 4.1.3. Specifically, the outer three edge element modes are loaded with  $231 \frac{\Omega}{\square}$  r-card, the next three have  $6955 \frac{\Omega}{\square}$  r-card, and the final three have  $13910 \frac{\Omega}{\square}$  r-card.

Figures 73 through 78 show the effect of this treatment on the array, once again illuminated at  $5^\circ$ ,  $45^\circ$ , and  $85^\circ$  off normal. Note the two reference solutions and the hybrid solution all agree fairly well, except for the aforementioned difficulty with the trailing edge. The slight discrepancies in the loaded element currents are a result of Skinner approximating the slot current mode as a constant to calculate the lumped load. This contrasts with the author's method described in section 4.1.5. Since Skinner uses a different approach to determine the proper lumped load to apply to the admittance matrix, it is encouraging to see the same end result. This example demonstrates the code's usefulness in designing array edge treatments.

Section 4.1 validated the hybrid PMM/MM technique by comparing the author's numerical implementation to other reference codes based on the MM. Since the reference data is calculated data, the actual induced array currents can be compared, providing the most rigorous test of the hybrid technique's accuracy. The results clearly demonstrate the technique's validity and usefulness in predicting large finite array performance. To add another layer of confidence, the author also measured several radomes and compared the measured echo area with that calculated by the hybrid PMM/MM code. These results are presented in the next section.

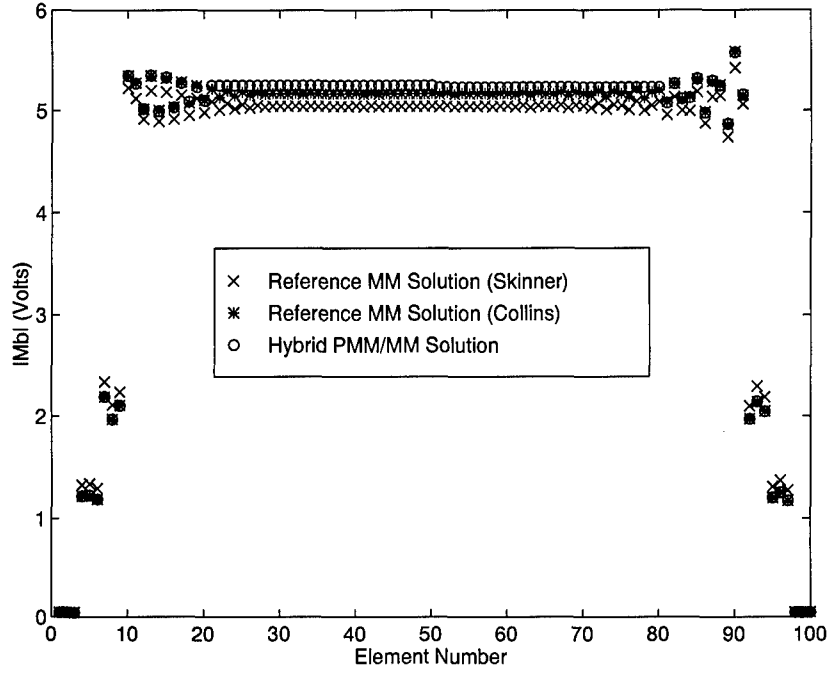


Figure 73. Induced Current Magnitude on 100 Element Loaded Slot Array with 5° off Normal Illumination

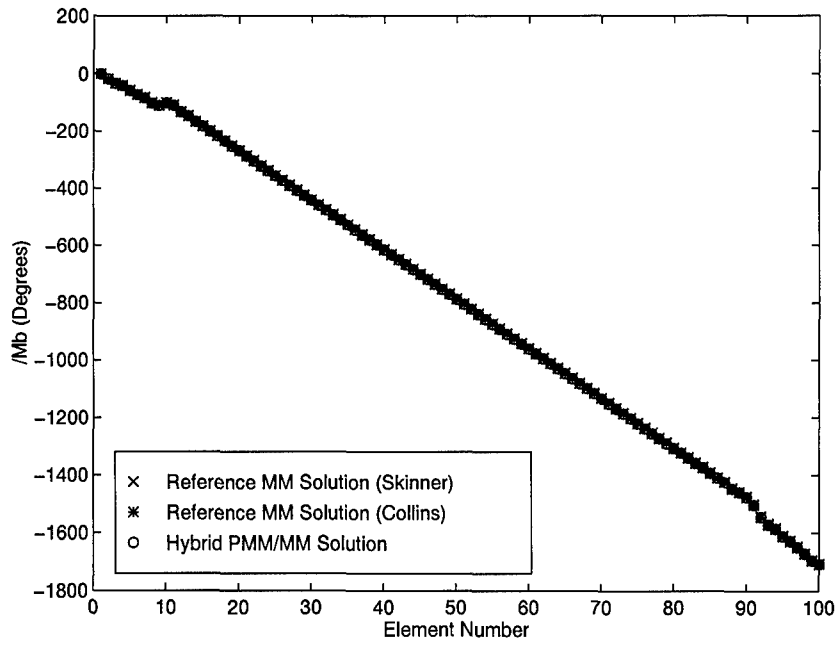


Figure 74. Induced Current Phase on 100 Element Loaded Slot Array with 5° off Normal Illumination

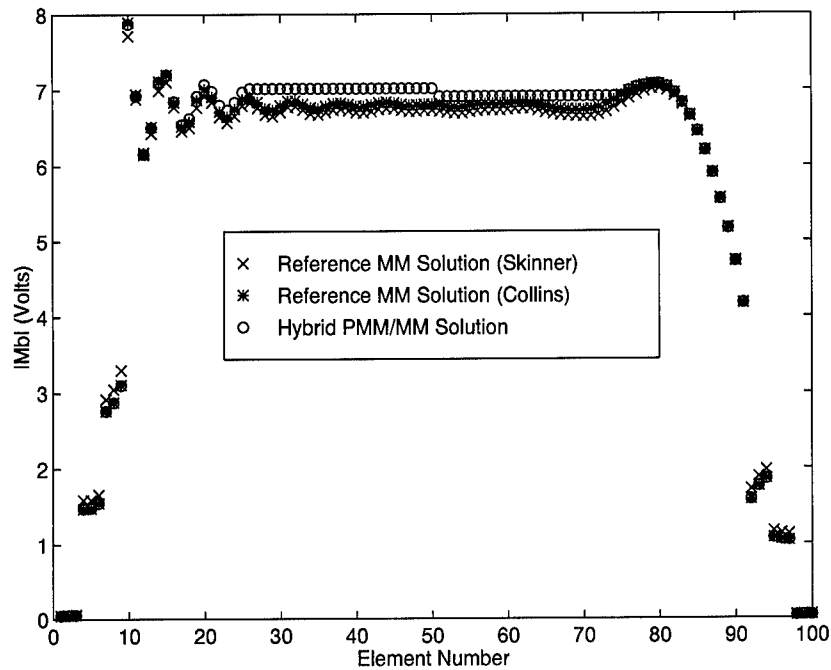


Figure 75. Induced Current Magnitude on 100 Element Loaded Slot Array with 45° off Normal Illumination

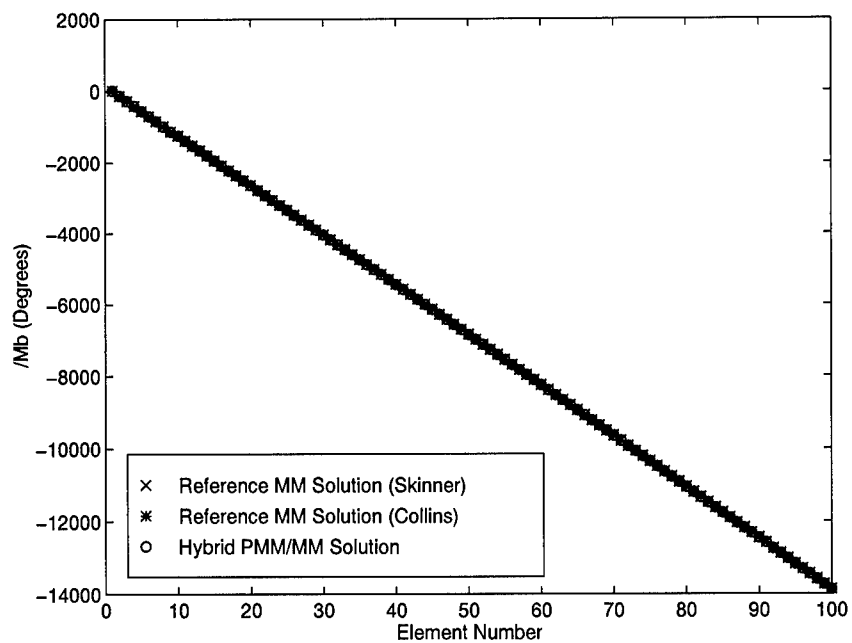


Figure 76. Induced Current Phase on 100 Element Loaded Slot Array with 45° off Normal Illumination

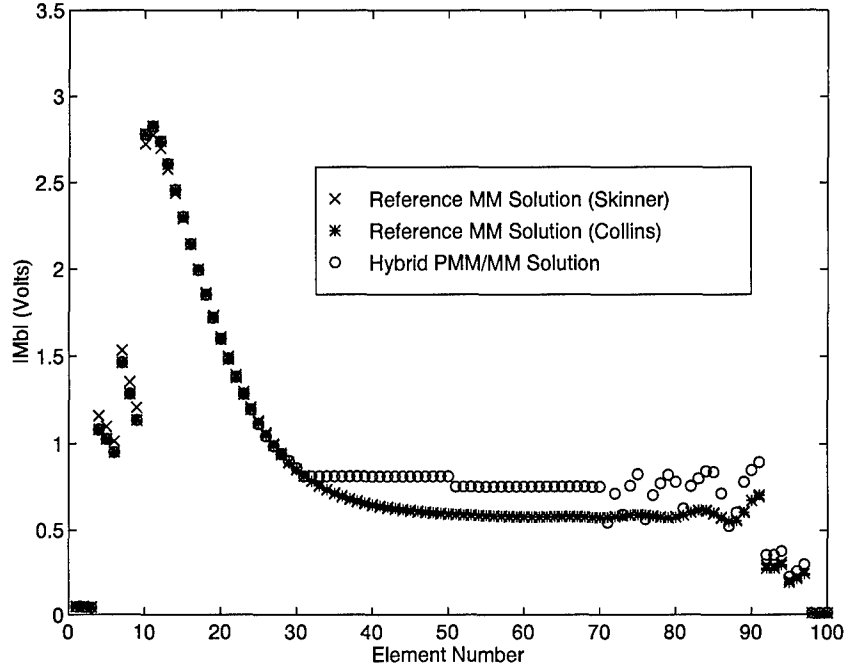


Figure 77. Induced Current Magnitude on 100 Element Loaded Slot Array with 85° off Normal Illumination

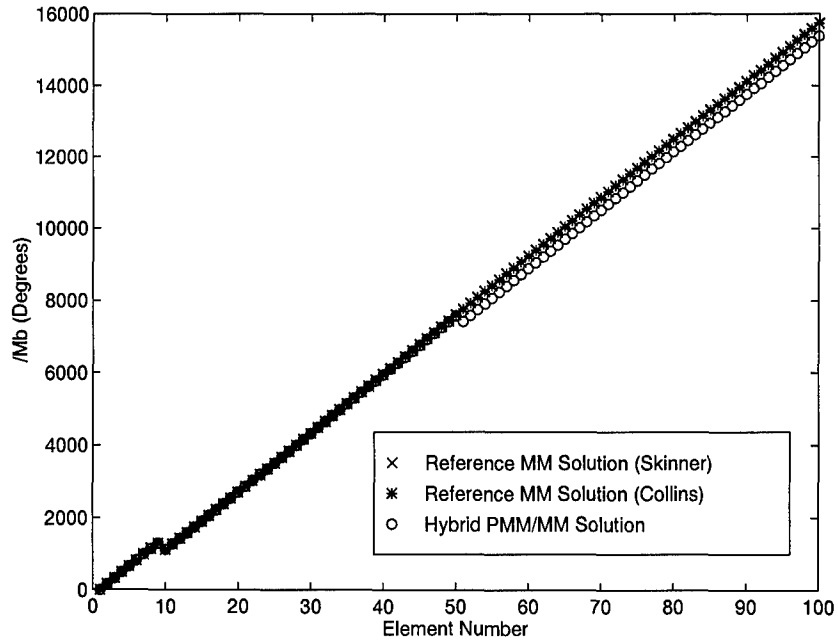


Figure 78. Induced Current Phase on 100 Element Loaded Slot Array with 85° off Normal Illumination



## 4.2 Measurement Comparison

Recall the geometries of concern consist of finite planar arrays made from slot columns infinite in one dimension. In addition, the slot arrays exist on infinite ground planes. These facts pose a somewhat difficult measurement problem, since infinite structures are hard to fit in a finite measurement facility. The challenge, then, is to approximate these structures with the finite resources available. The author attempted to design finite radomes that were large enough in the  $\hat{z}$  direction to approximate infinite columns. Fortunately, the thin slot pattern factors dramatically reduce the edge effects in the  $\hat{z}$  direction, allowing a relatively short column to adequately approximate an infinite column.

The Mission Research Corporation of Dayton, Ohio manufactured the two different radomes the author used during the measurement validation phase. The radomes were measured at the Wright Laboratory Multi-Spectral Measurement Facility, Wright-Patterson AFB, Ohio. Wright Laboratory also provided the test fixture used during the measurements.

The radomes consist of skewed grids of  $\hat{z}$  oriented slots 0.881 cm long and 0.038 cm wide. The slots form columns with inner-element spacing 1.27 cm in the  $\hat{z}$  direction and 1.1 cm in the  $\hat{x}$  direction. Each radome has 42 slot columns, creating a window approximately 45 cm wide ( $\hat{x}$ ) by 51 cm tall ( $\hat{z}$ ). The grids have a 45° skew angle. The first radome is simply a thin metal screen. The second radome is backed by a 0.15875 cm thick glass-epoxy layer with a relative permittivity of 4.5. The author measured each radome with and without a similar r-card edge treatment to that described in the previous section. In this case, resistivities of  $500 \frac{\Omega}{\square}$ ,  $750 \frac{\Omega}{\square}$ , and  $1500 \frac{\Omega}{\square}$  were used for a total of four radome configurations.

Figure 79 shows Wright Laboratory's test fixture. The test fixture attempts to simulate an infinite ground plane by mitigating any backscatter due to various mechanisms such as tip scatter and creeping waves. Its size also aids in gating out any interactions between the radome and test body.

Figures 82 and 83 show a radome mounted in the test body and the cavity beneath the radome, respectively. Since the radomes are transmissive within the band of interest (see Figures 80 and 81), the cavity creates a contamination source by re-radiating energy coupled into the cavity back



Figure 79. Radome Measurement Test Fixture

toward the radar. To mitigate this problem, the author filled the cavity with RAM to absorb most of the radiation transmitted into the cavity. As can be seen in the following plots, this technique was generally quite effective.

The final photograph shows a typical r-card treatment. The r-card consists of a thin polymer loaded with resistive material such as carbon. As shown in Figure 84, one attaches the film to the radome with spray adhesive. One then uses a putty knife to smooth out any bubbles trapped by the film. The author found the r-card material easy to work with and very consistent from measurement to measurement.

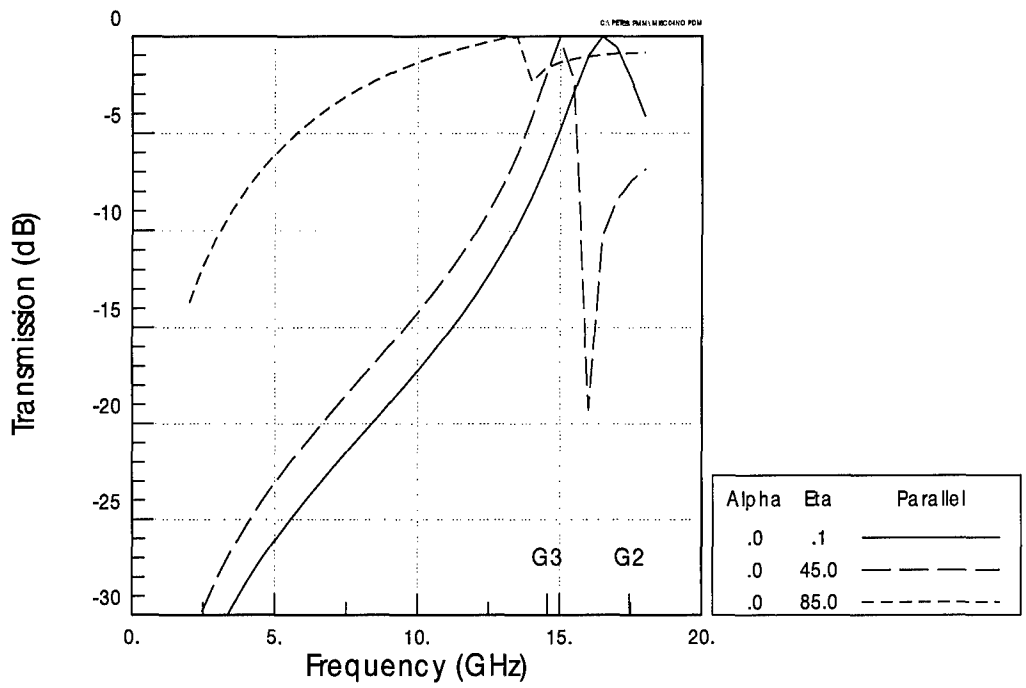


Figure 80. Metal Radome Transmission for Three Angles of Incidence

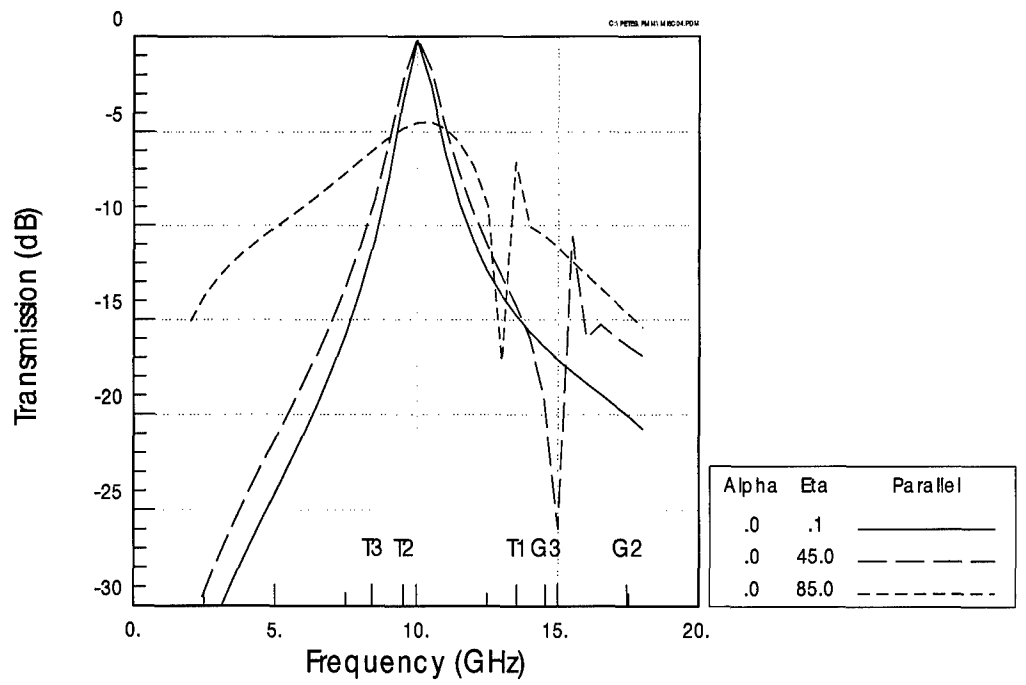


Figure 81. Dielectric Backed Radome Transmission for Three Angles of Incidence

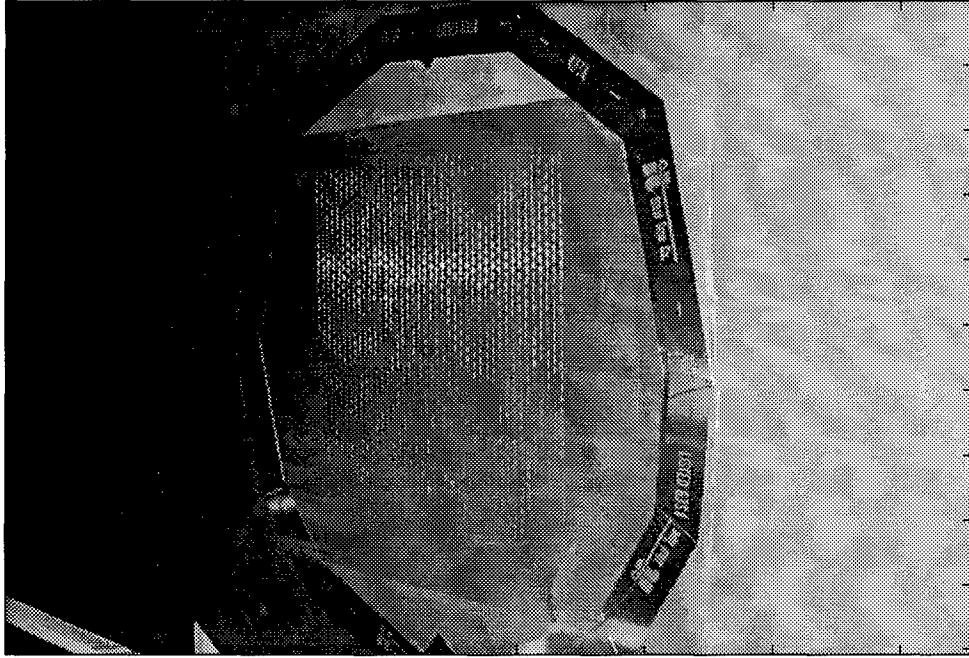


Figure 82. Radome Mounted in Test Fixture

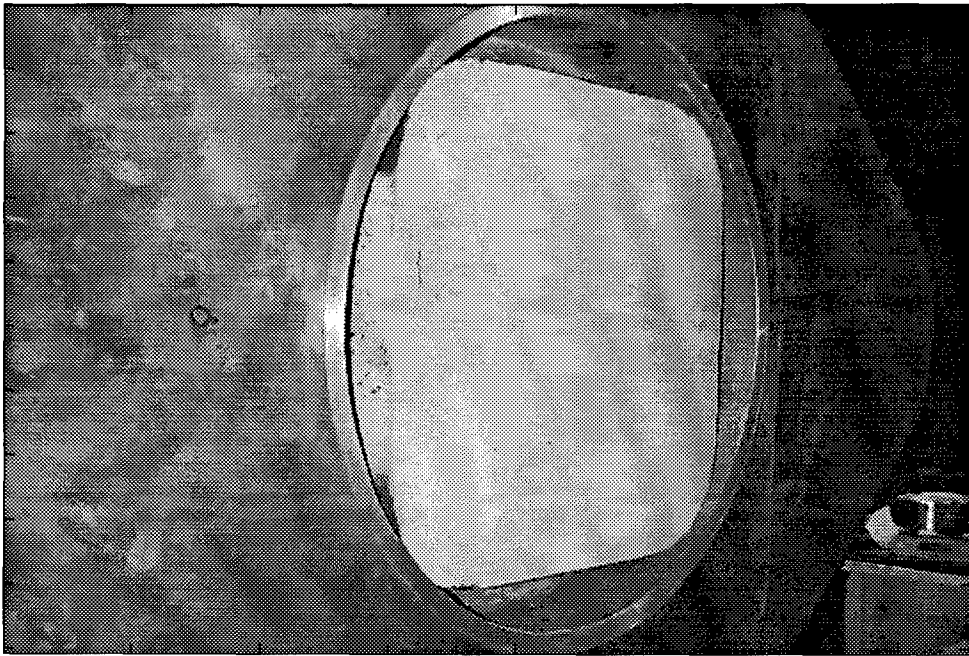


Figure 83. Test Fixture Cavity Treatment

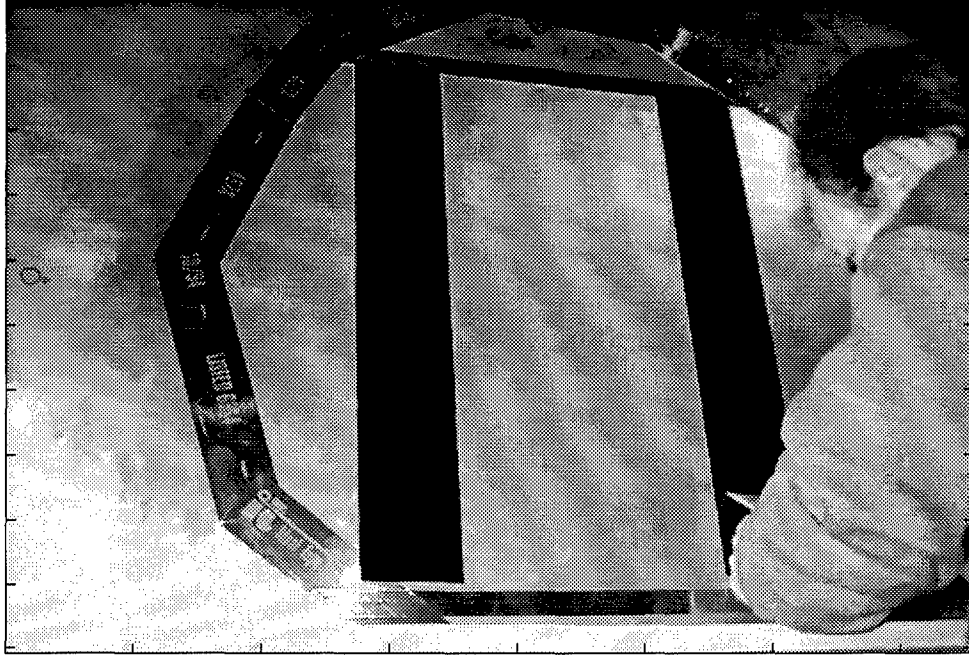


Figure 84. R-Card Application

Radome Configuration	Frequency Scans (GHz)	Patterns
Metal	2 to 18 (0.1)	-90° to -30° (0.2°)
Metal with r-card	2 to 18 (0.1)	-90° to -30° (0.2°)
Backed Metal	2 to 18 (0.1)	-90° to -30° (0.2°)
Backed Metal with r-card	2 to 18 (0.1)	-90° to -30° (0.2°)

Table 3. Radome Measurement Matrix

The Multi-Spectral Measurement Facility is able to take a tremendous amount of data in a very short time. Table 3 contains the test matrix for the four radome configurations. Frequency versus angle plots provide a convenient way to view a large amount of data. Figures 85 through 88 show the radar echo area (REA) for the four radome configurations. Note that 0° elevation corresponds to a grazing angle of incidence. The author chose to focus on the three frequencies, 13 GHz, 15 GHz, and 17 GHz, to validate the hybrid PMM/MM technique. The remainder of this section examines each of the four radomes at these frequencies.

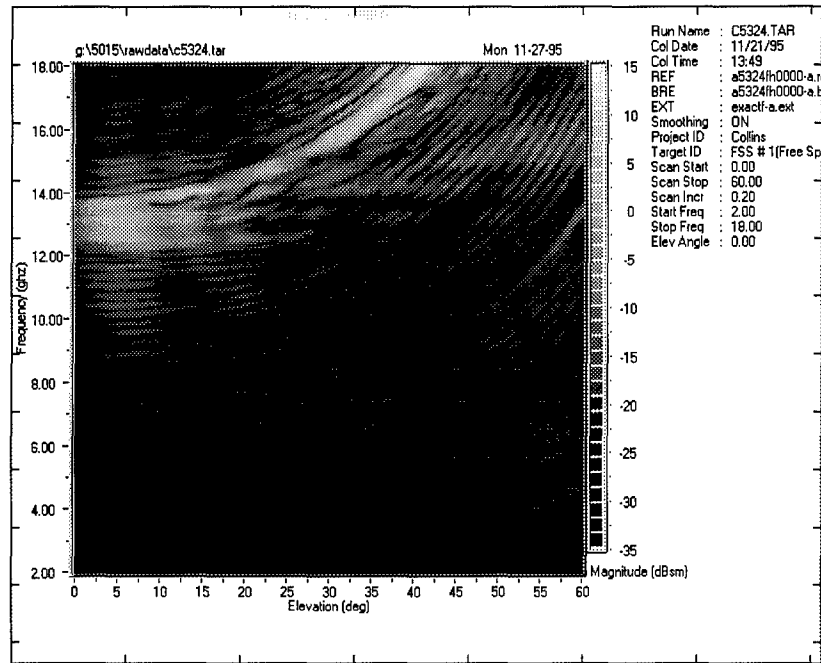


Figure 85. Frequency versus Angle Plot for Radome Configuration Number 1

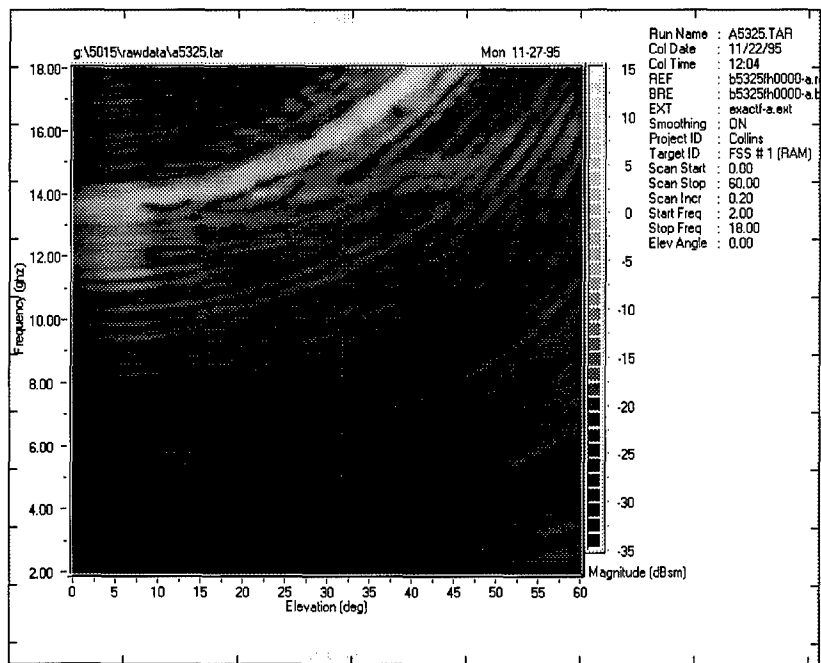


Figure 86. Frequency versus Angle Plot for Radome Configuration Number 2

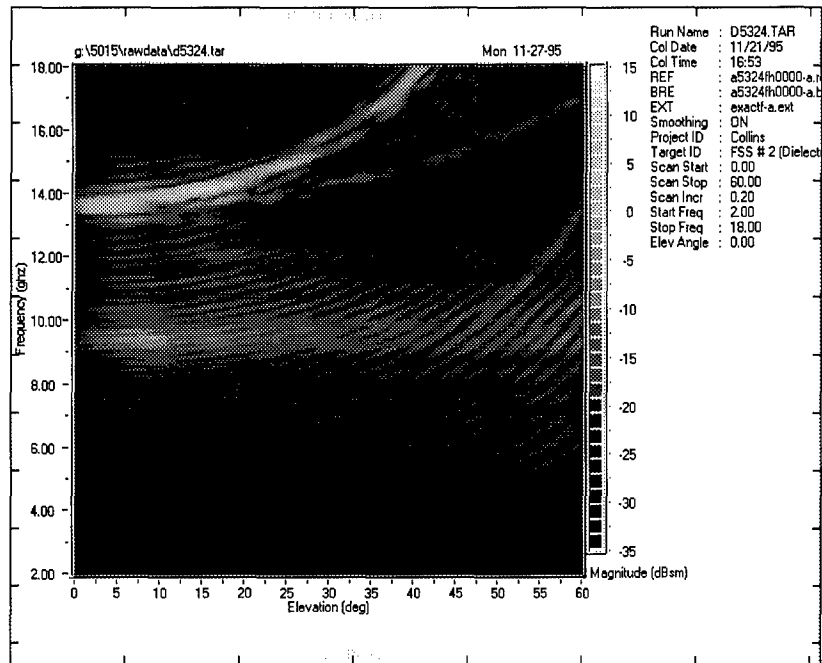


Figure 87. Frequency versus Angle Plot for Radome Configuration Number 3

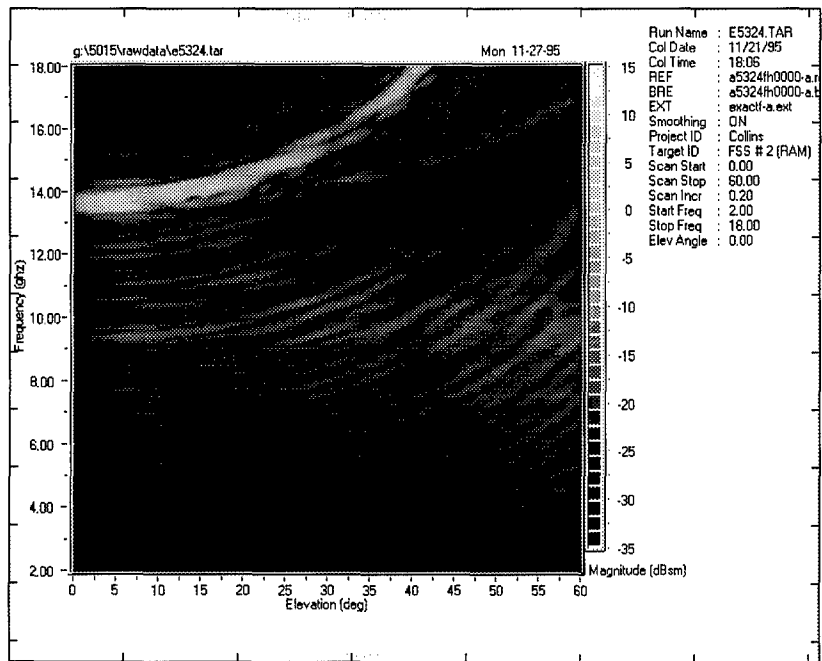


Figure 88. Frequency versus Angle Plot for Radome Configuration Number 4



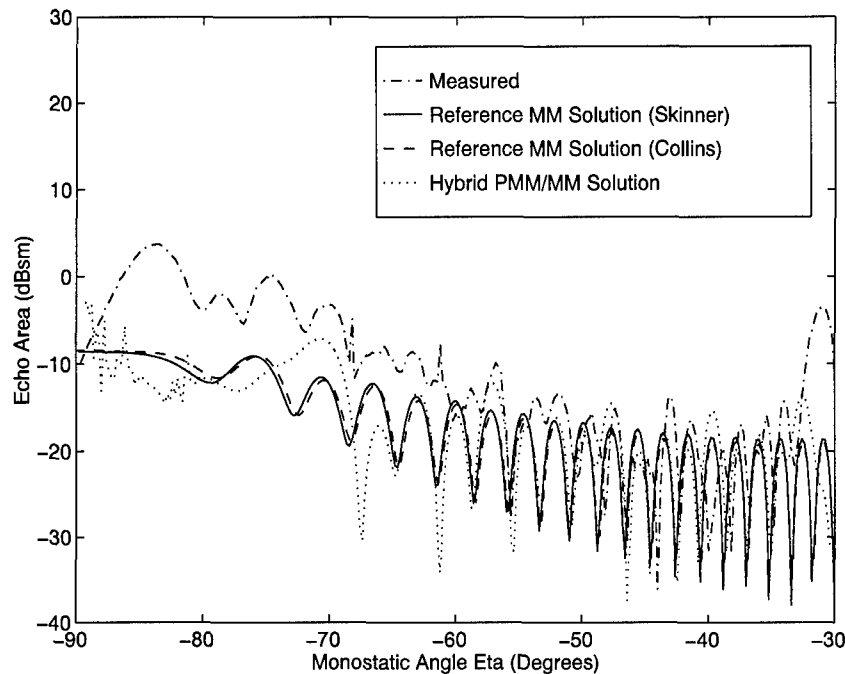


Figure 89. REA pattern at 13 GHz for Metal Radome in Stratified Media

4.2.1 *Dielectric Backed Metal Radome.* Figures 89 through 91 depict monostatic REA patterns at 13 GHz, 15 GHz, and 17 GHz respectively. Each plot contains measured data, reference code data calculated using the MM, and hybrid PMM/MM data based on 10 edge columns on either side of the array. Several features are worth noting in this figure series. First of all, the two reference codes agree quite well in all the figures. While not perfect, they also do a good job capturing the behavior of measured data, improving with increasing frequency. Second, the hybrid PMM/MM data agrees with the reference data fairly well over some regions but misses the mark in others. As an example, notice how the hybrid code misses the lobe at  $-50^\circ$  in Figure 90 completely. To understand what is happening here, one must examine the induced scattering currents. The following current plots highlight one of the code's useful features. Namely, the ability to access the scattering currents. This ability gives the radome designer insight into what is producing a particular REA pattern or perhaps the effectiveness of a particular edge treatment.

Figures 92 and 93 present the induced current magnitudes calculated by the author's MM and hybrid PMM/MM codes at 15 GHz. In the MM solution, notice how the dielectric layer creates a

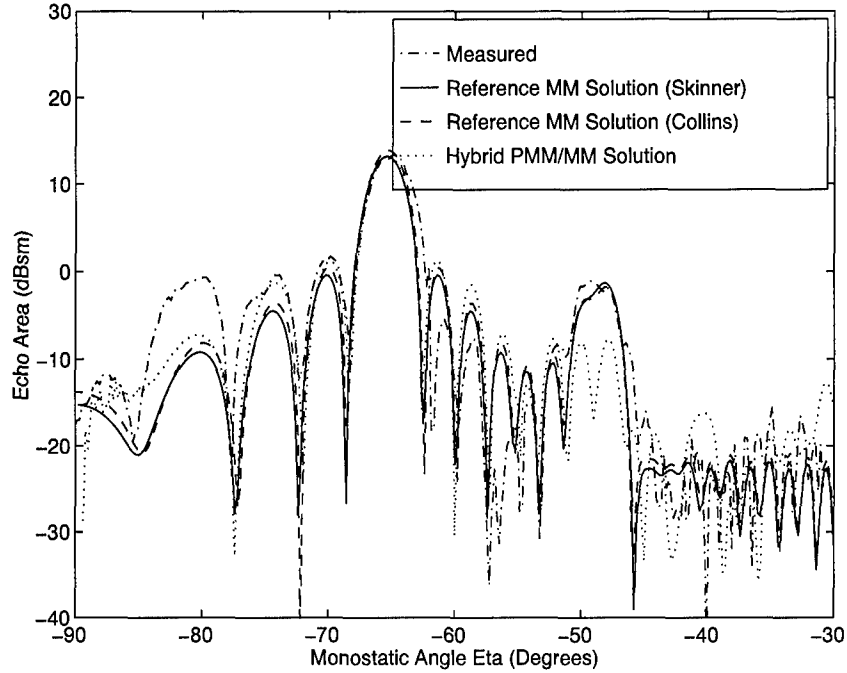


Figure 90. REA pattern at 15 GHz for Metal Radome in Stratified Media

strong coupling between the slot columns. This is evidenced by the absence of a central Floquet region, even at angles far away from grazing. The hybrid technique would be hard pressed to accurately model the central currents for a radome this narrow. Even more noticeable is the missing ridge at around  $-50^\circ$  in the hybrid solution. The author traced the problem to the continuous spectral integral evaluations for the PBF. In this case, the dielectric layer produces T-factor poles which lie either near grating lobe poles or near the branch points in the complex integration plane. The assumptions the author used to analytically extract the grating lobe pole may be violated, necessitating an alternative approach to dealing with the singularity.

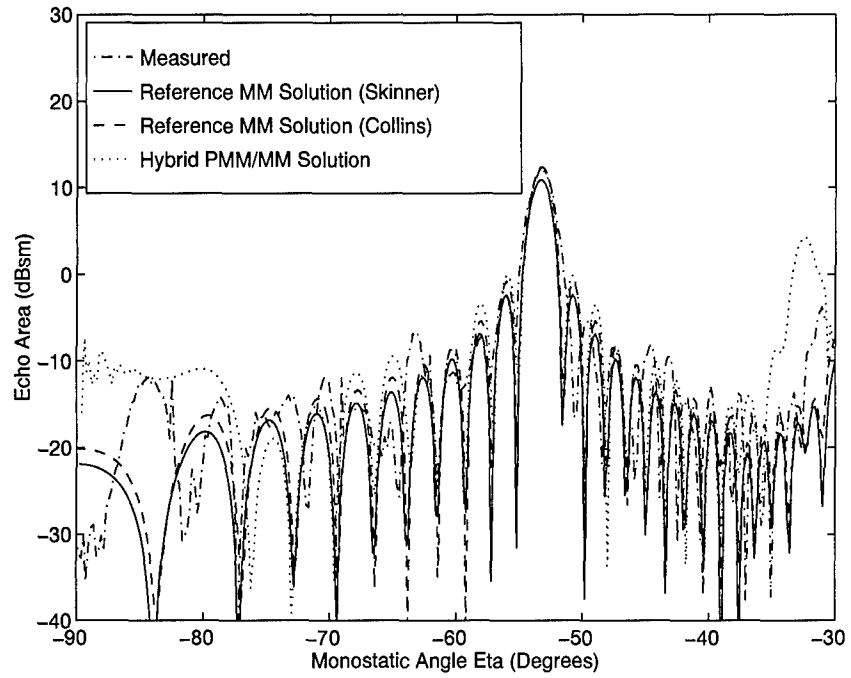


Figure 91. REA pattern at 17 GHz for Metal Radome in Stratified Media

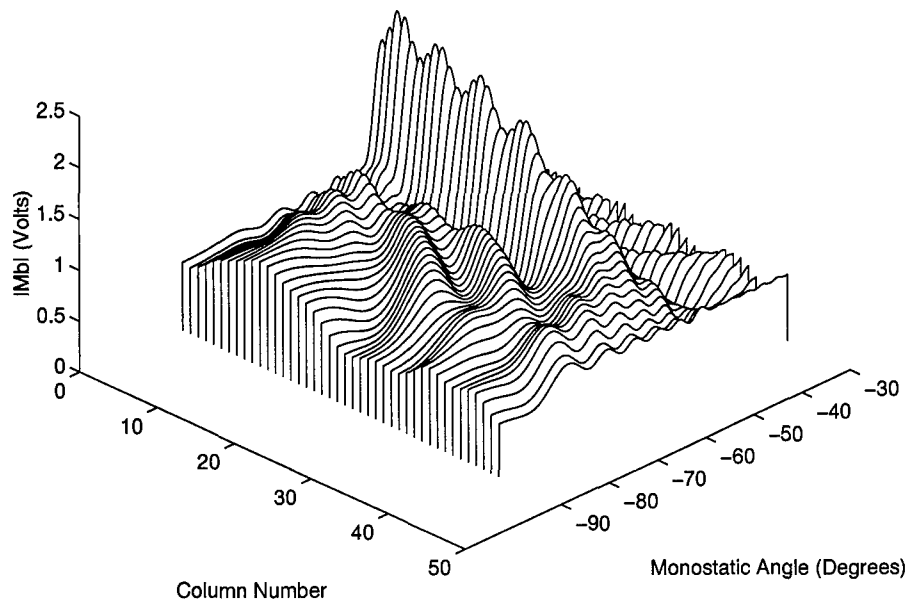


Figure 92. Induced Currents on Metal Radome in Stratified Media at 15 GHz

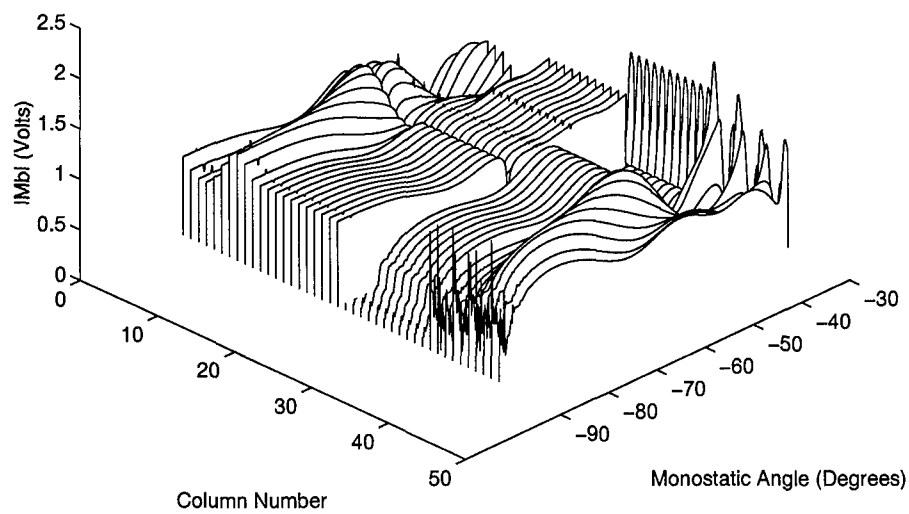


Figure 93. Hybrid PMM/MM Approximation to Induced Currents on Metal Radome in Stratified Media at 15 GHz

4.2.2 *Dielectric Backed Metal Radome with R-Card Edge Treatment.* Figures 94 through 96 depict the r-card treated dielectric backed metal radome's monostatic REA patterns at 13 GHz, 15 GHz, and 17 GHz respectively. As mentioned earlier, the hybrid PMM/MM code ran into numerical difficulties. Unfortunately, Skinner's reference MM code also had problems. Figure 94 contains the only usable data, which may be suspect. At the higher frequencies, Skinner's code returned NaNs (Not a Number), indicating numerical instability. Despite the lack of computed reference data, the author's MM code agrees quite well with the measured data. One may note how the edge treatments have widened the lobing structure, while reducing the side lobes. This behavior can be accounted for by examining the currents in Figures 97 and 98. The r-card has partially shorted out the outer edge currents, effectively reducing the width of the radome.

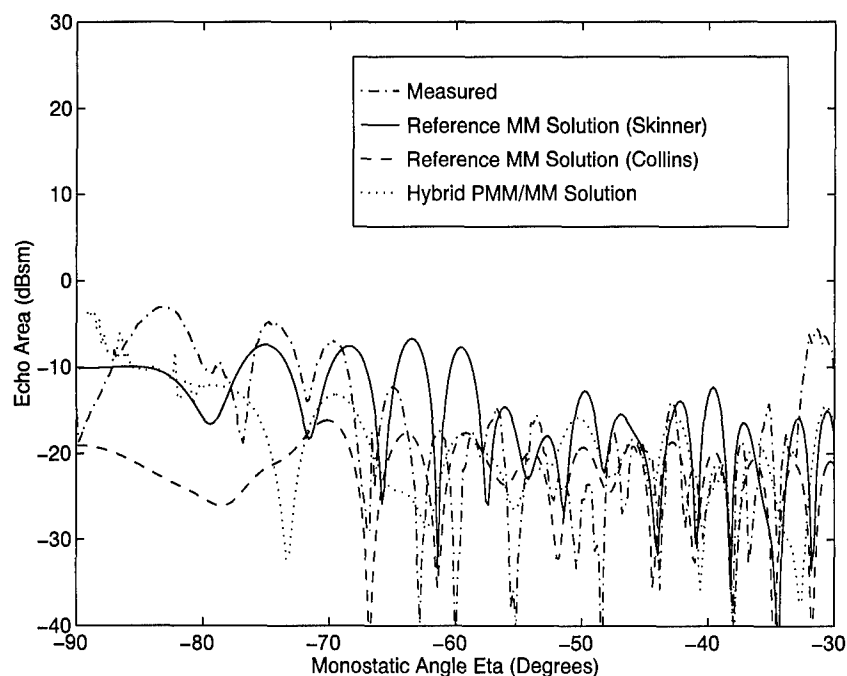


Figure 94. REA pattern at 13 GHz for R-Card Treated Metal Radome in Stratified Media

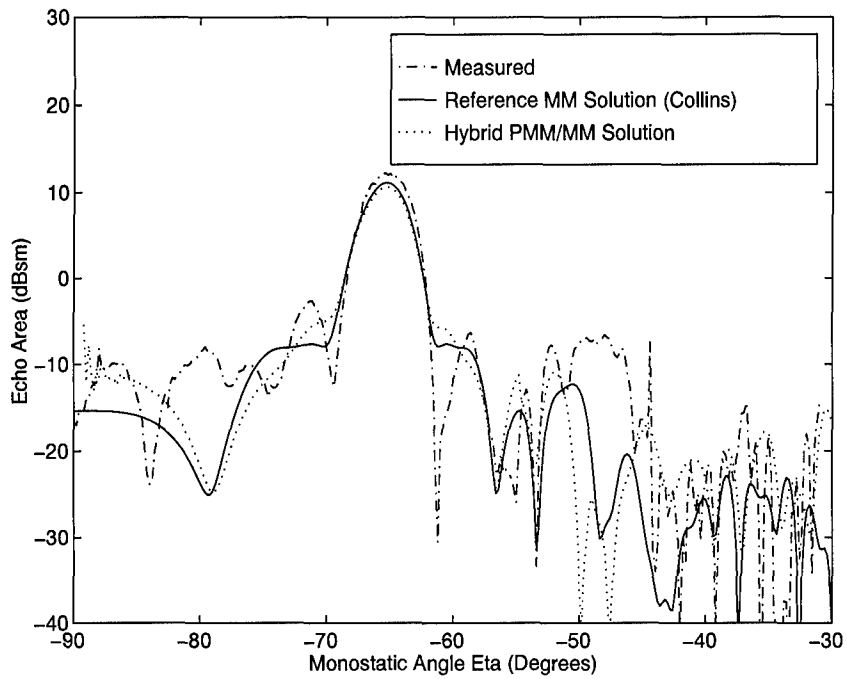


Figure 95. REA pattern at 15 GHz for R-Card Treated Metal Radome in Stratified Media

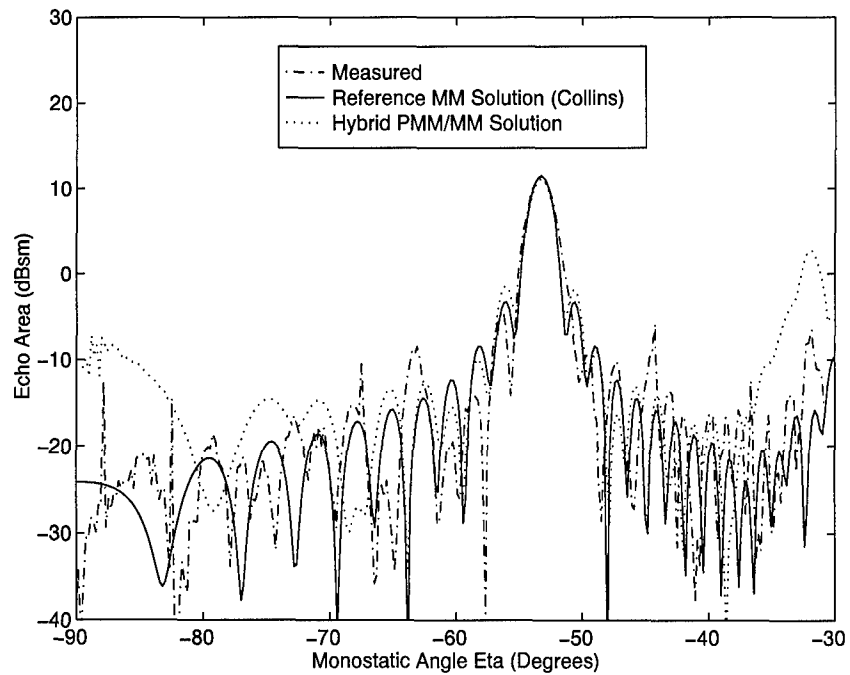


Figure 96. REA pattern at 17 GHz for R-Card Treated Metal Radome in Stratified Media

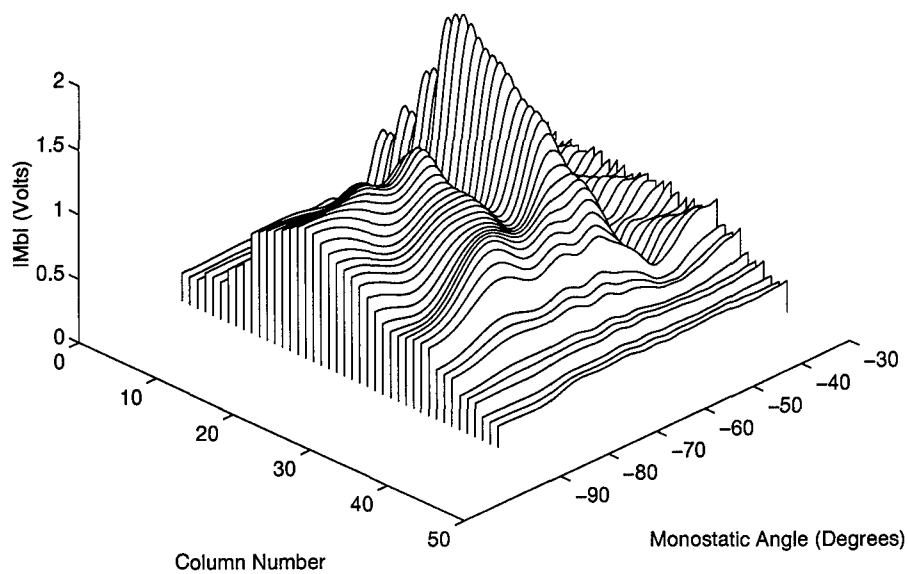


Figure 97. Induced Currents on R-Card Treated Metal Radome in Stratified Media at 15 GHz

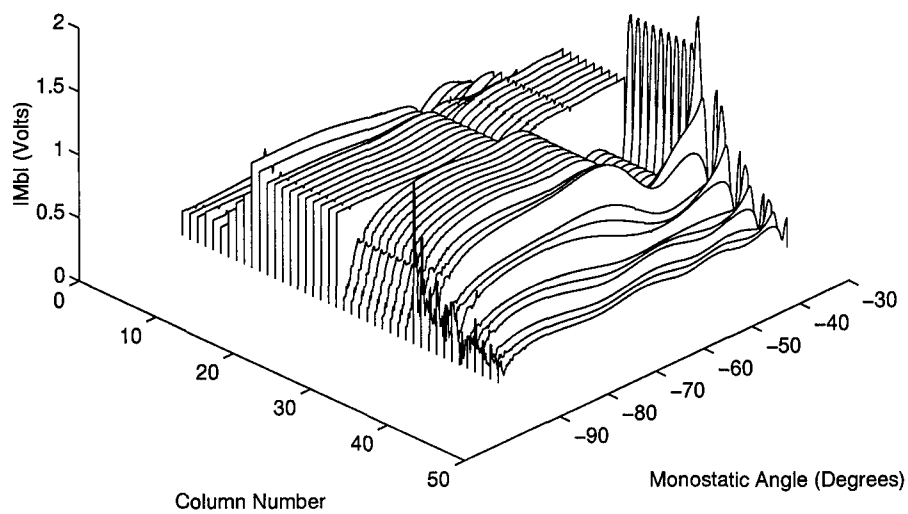


Figure 98. Hybrid PMM/MM Approximation to Induced Currents on R-Card Treated Metal Radome in Stratified Media at 15 GHz

4.2.3 *Metal Radome in Homogeneous Media.* Figures 99 through 101 contain monostatic REA patterns for the metal radome. The frequencies of interest are again 13 GHz, 15 GHz, and 17 GHz. Each plot contains measured data, reference code data, and hybrid PMM/MM data based on 16 edge columns on either side of the array. In examining the measured data, there appears to be a greater discrepancy with the predicted results than observed with the dielectric backed radome. Unfortunately, the measured data for the metal radome is somewhat suspect. There are several possible explanations. First, the metal foil's flimsiness may have contributed. In order to take background measurements for background subtraction, the author lightly adhered aluminum foil to the metal radome surface. Removing the foil without disturbing the metal radome proved nearly impossible. As a result, the background subtraction introduced phase errors which may have corrupted the measurements. Second, the test fixture may have been tilted slightly away from perpendicular to the radar's line-of-sight. The effect would be a reduction in peak height. Third and most probable, the cavity return may have corrupted the measurement. Since the metal radome is more transmissive in the frequency band of interest, the RAM inside the cavity wasn't able to completely absorb the coupled radiation causing, the gross lobing structure in Figure 99 and the grating lobe peak height discrepancies in Figures 100 and 101.

Turning now to the predicted results, note once again, the reference codes produce virtually identical solutions. One may also note the excellent agreement with the hybrid PMM/MM predictions. The only areas of deviation are near grazing. Based on Figures 102 through 107, it is clear the problem at grazing is caused once again by numerical problems at the trailing edge. Also, as the incident angle sweeps off normal, the Floquet portion at the center of the array shrinks to the point where the PBF is no longer useful. This effect is evidenced in the REA pattern by the hybrid solution departing from the MM solution as the incident angle approaches grazing. Before leaving these figures, it is interesting to note the current's behavior as the grating lobe enters the visible region near 13 GHz and moves toward normal with increasing frequency. The currents on one side of the grating lobe have a dramatically different behavior than those on the other side.



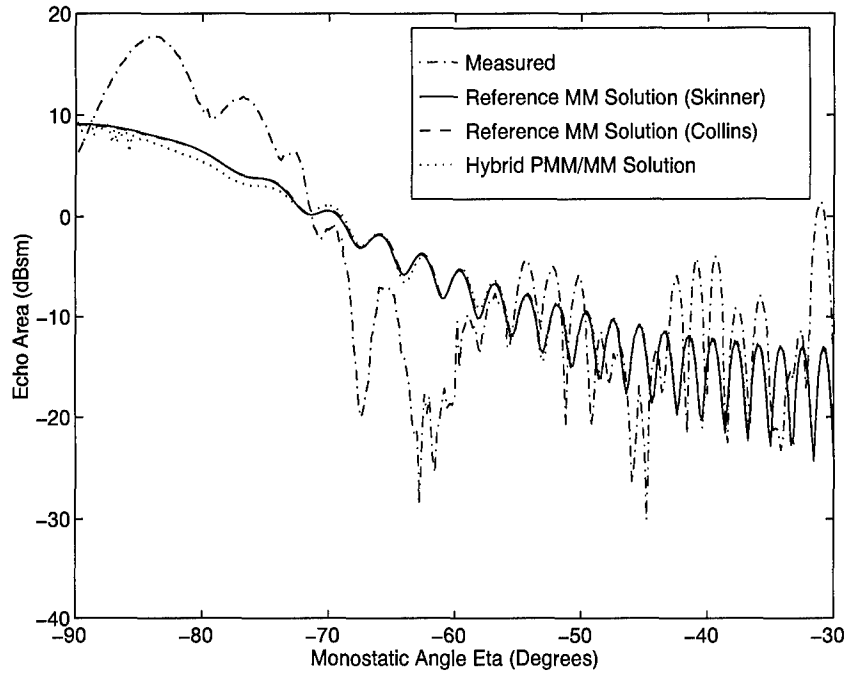


Figure 99. REA pattern at 13 GHz for Metal Radome in Homogeneous Media

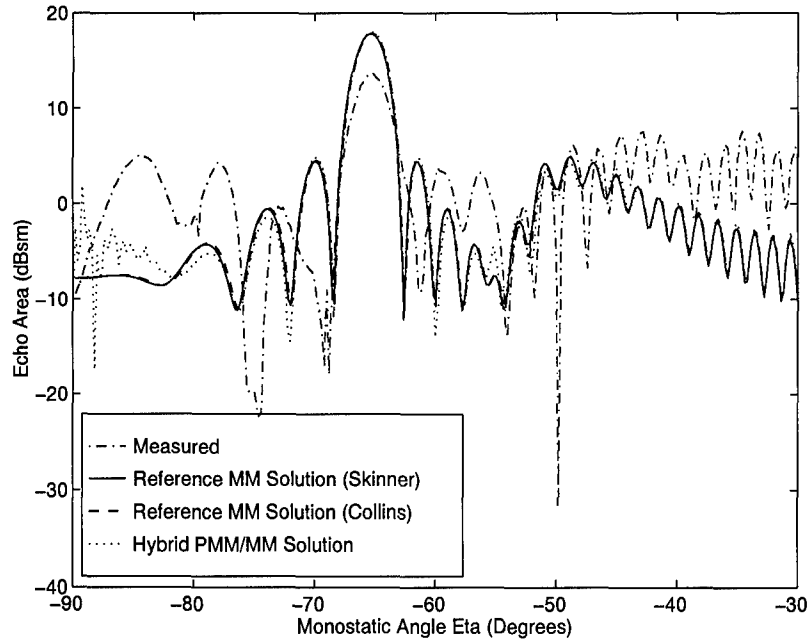


Figure 100. REA pattern at 15 GHz for Metal Radome in Homogeneous Media

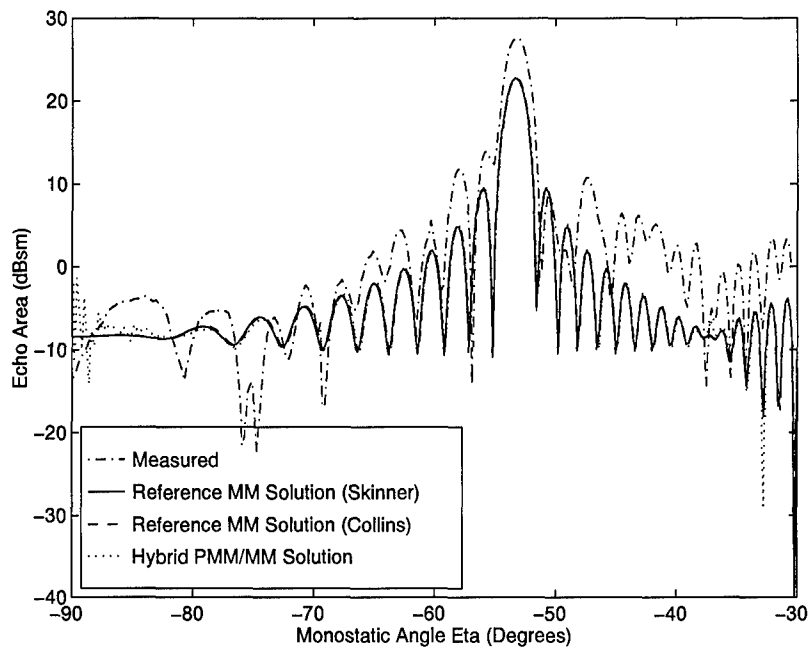


Figure 101. REA pattern at 17 GHz for Metal Radome in Homogeneous Media

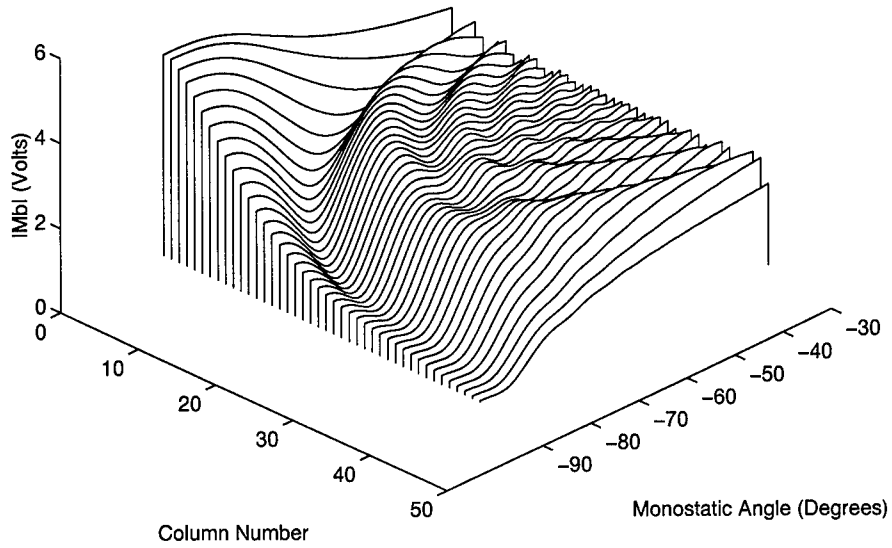


Figure 102. Induced Currents on Metal Radome in Homogeneous Media at 13 GHz

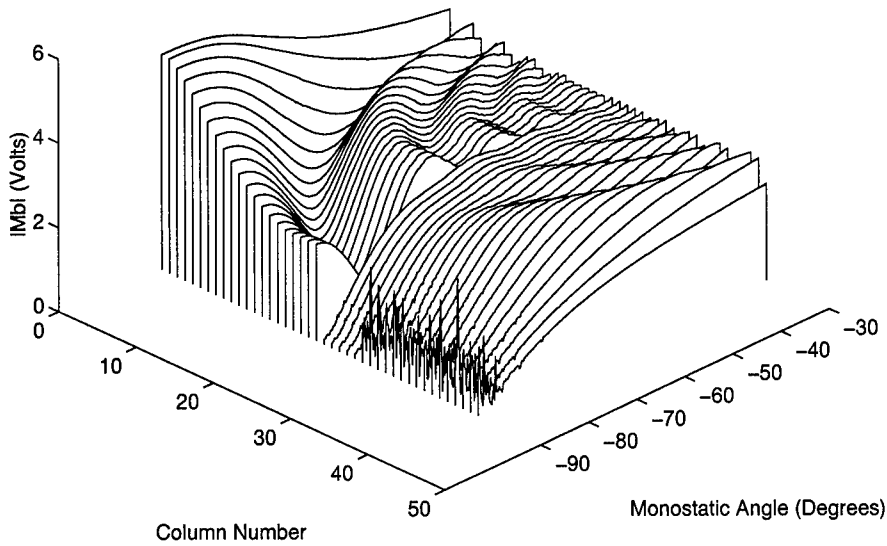


Figure 103. Hybrid PMM/MM Approximation to Induced Currents on Metal Radome in Homogeneous Media at 13 GHz

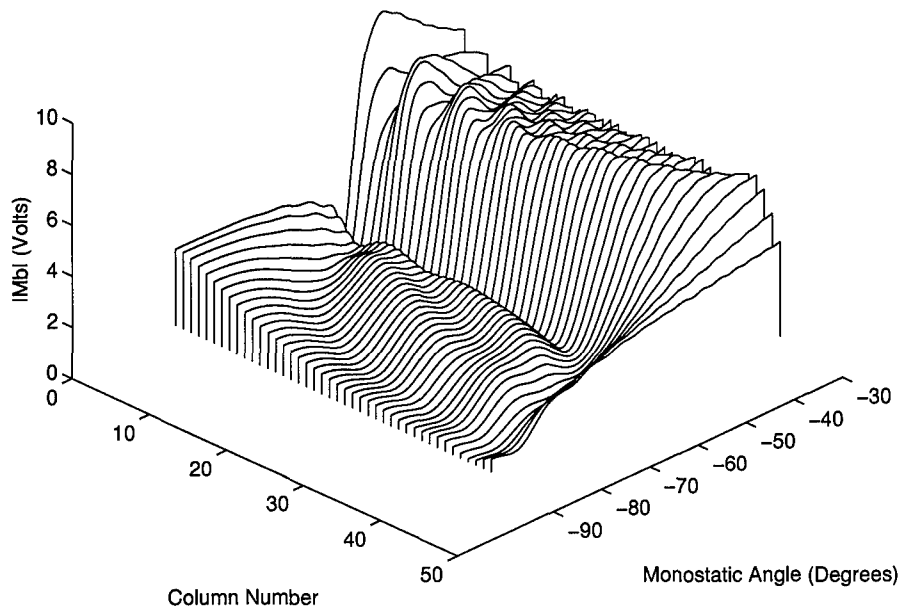


Figure 104. Induced Currents on Metal Radome in Homogeneous Media at 15 GHz

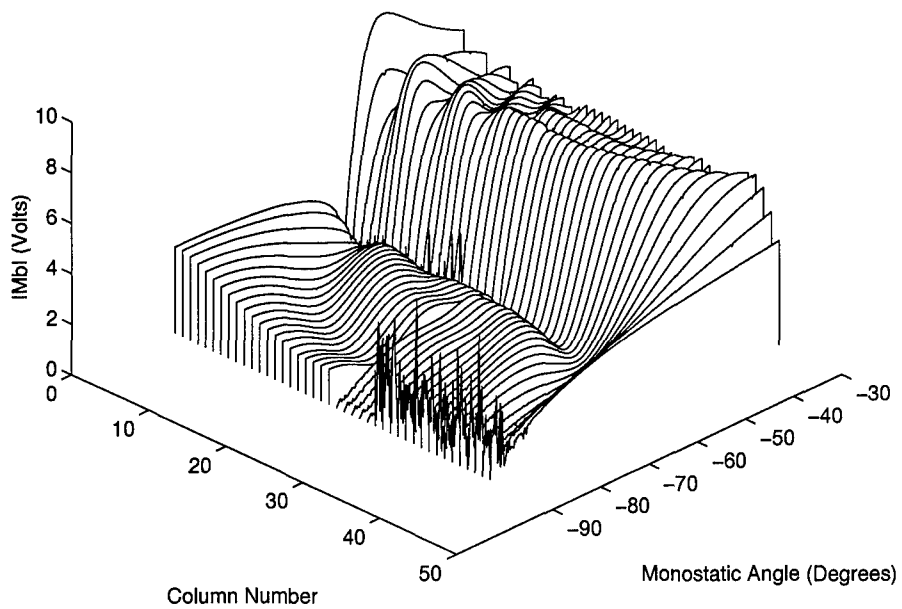


Figure 105. Hybrid PMM/MM Approximation to Induced Currents on Metal Radome in Homogeneous Media at 15 GHz

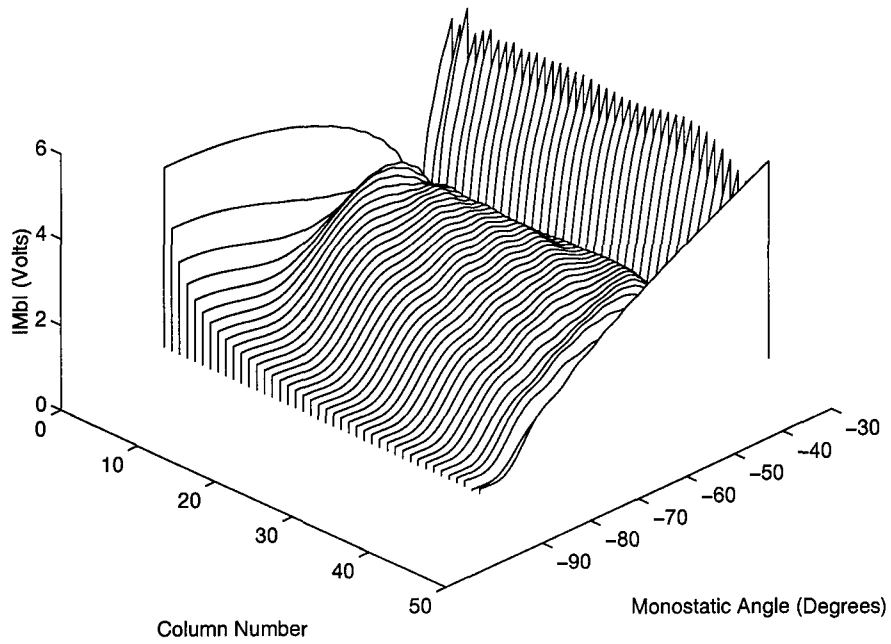


Figure 106. Induced Currents on Metal Radome in Homogeneous Media at 17 GHz

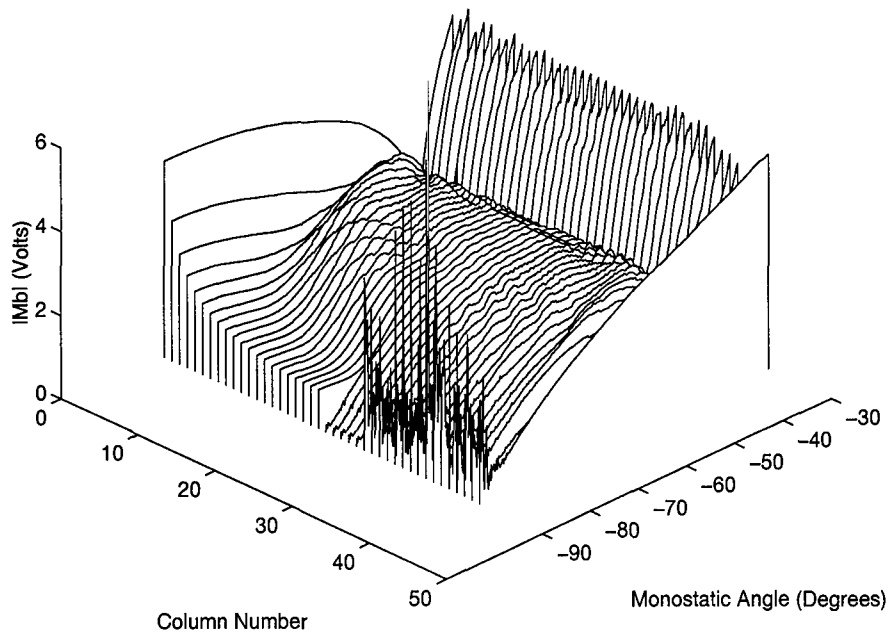


Figure 107. Hybrid PMM/MM Approximation to Induced Currents on Metal Radome in Homogeneous Media at 17 GHz

4.2.4 *Metal Radome in Homogeneous Media with R-Card Edge Treatment.* Figures 108 through 110 depict the r-card treated metal radome's monostatic REA patterns at 13 GHz, 15 GHz, and 17 GHz respectively. Each plot contains measured data, reference code data calculated using the MM, and hybrid PMM/MM data based on 16 edge columns on either side of the array. Once again, the calculated data does a good job predicting the radome's general performance. The measured data may have errors due to measurement difficulties as evidenced by the grating lobe peak discrepancies. Finally, these figures show where the hybrid PMM/MM solution best represents the actual array currents. Not surprisingly, this occurs when the currents have a good central Floquet region.

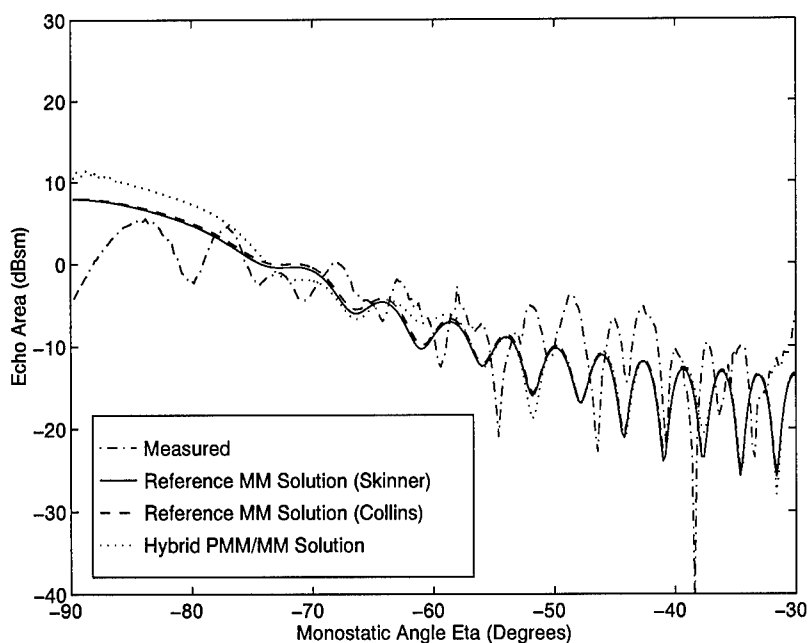


Figure 108. REA pattern at 13 GHz for R-Card Treated Metal Radome in Homogeneous Media

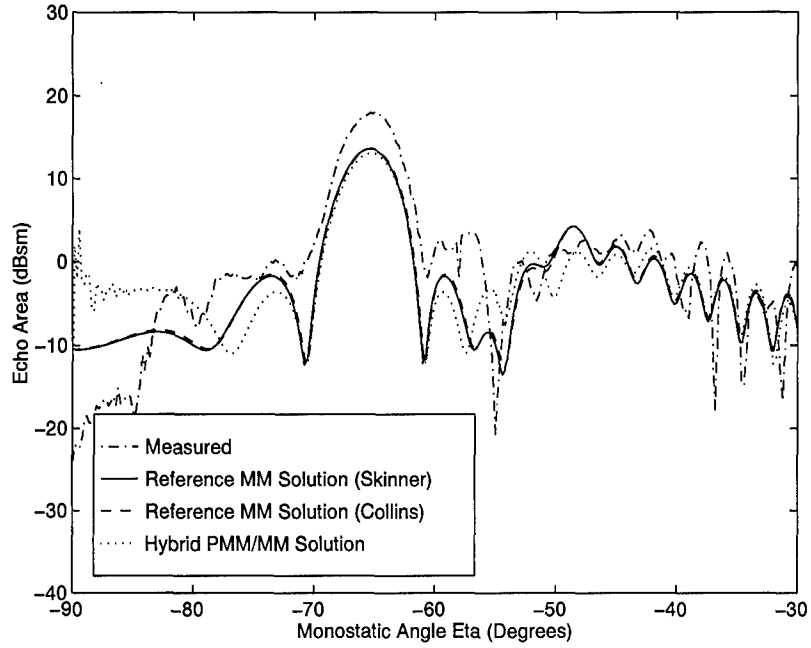


Figure 109. REA pattern at 15 GHz for R-Card Treated Metal Radome in Homogeneous Media

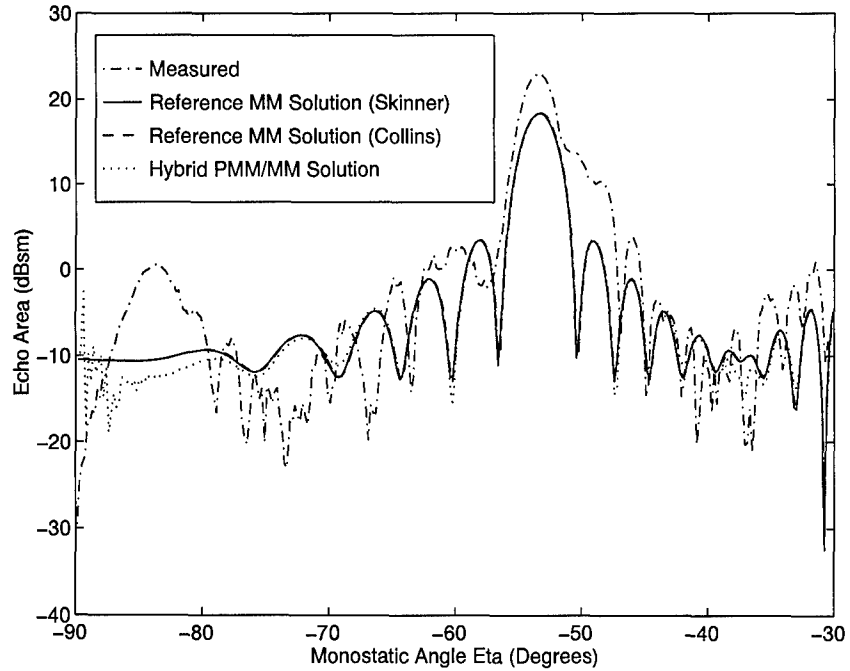


Figure 110. REA pattern at 17 GHz for R-Card Treated Metal Radome in Homogeneous Media

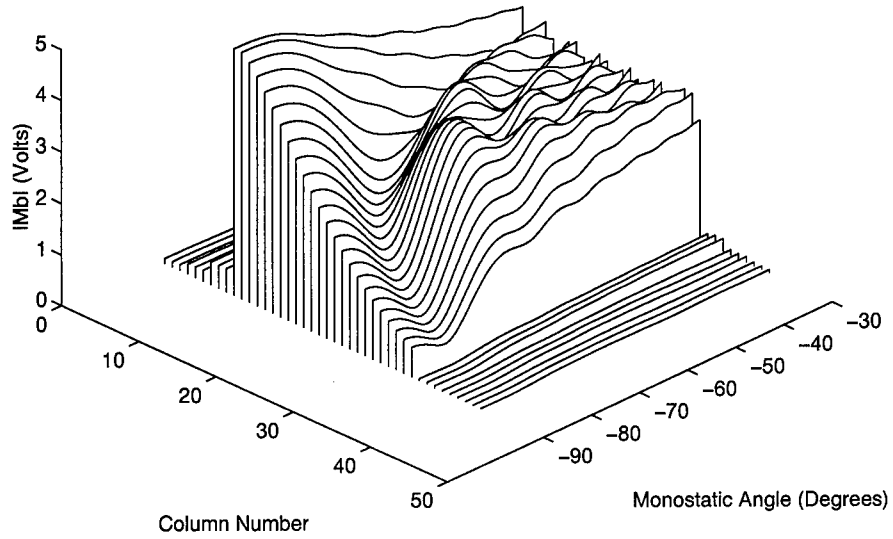


Figure 111. Induced Currents on R-Card Treated Metal Radome in Homogeneous Media at 13 GHz

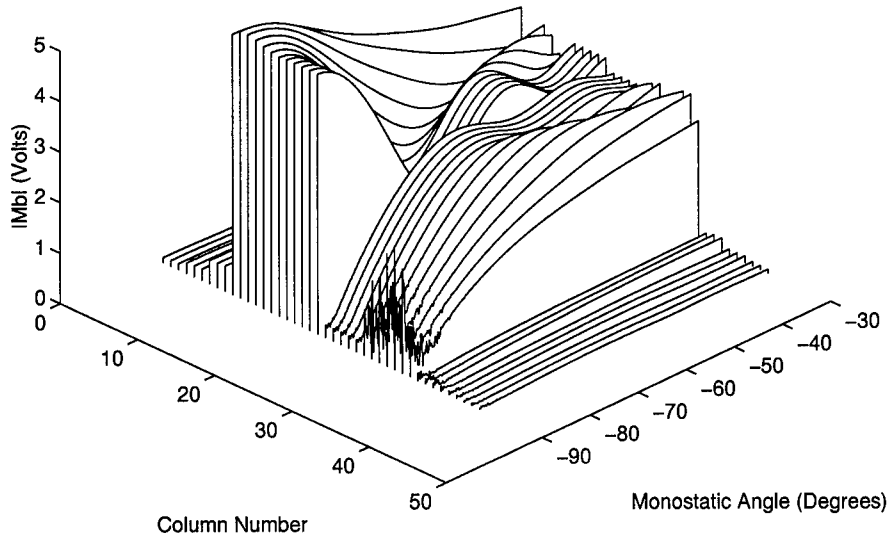


Figure 112. Hybrid PMM/MM Approximation to Induced Currents on R-Card Treated Metal Radome in Homogeneous Media at 13 GHz



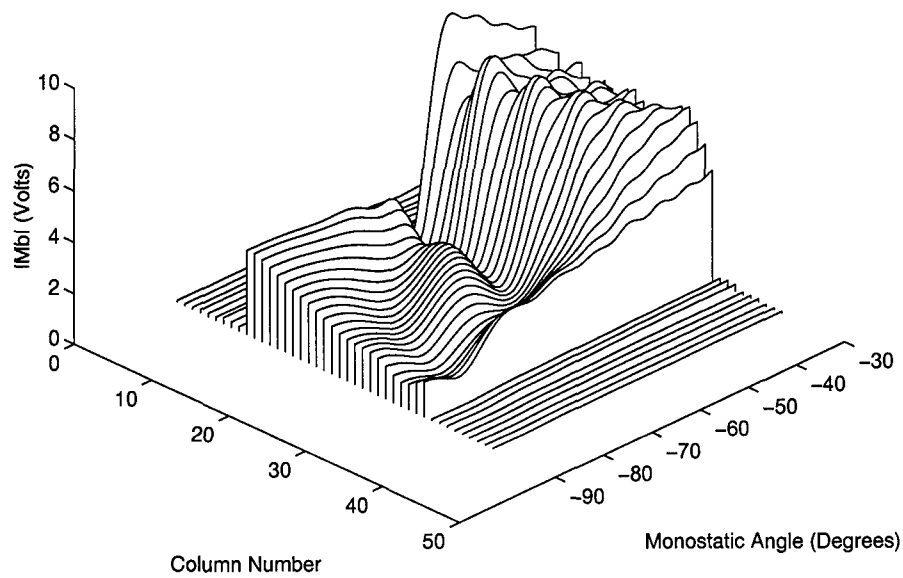


Figure 113. Induced Currents on R-Card Treated Metal Radome in Homogeneous Media at 15 GHz

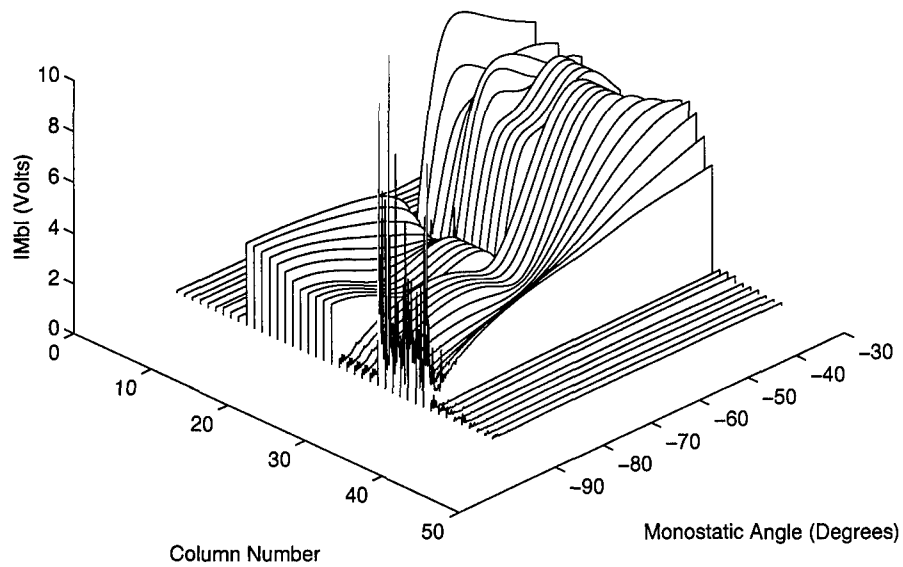


Figure 114. Hybrid PMM/MM Approximation to Induced Currents on R-Card Treated Metal Radome in Homogeneous Media at 15 GHz

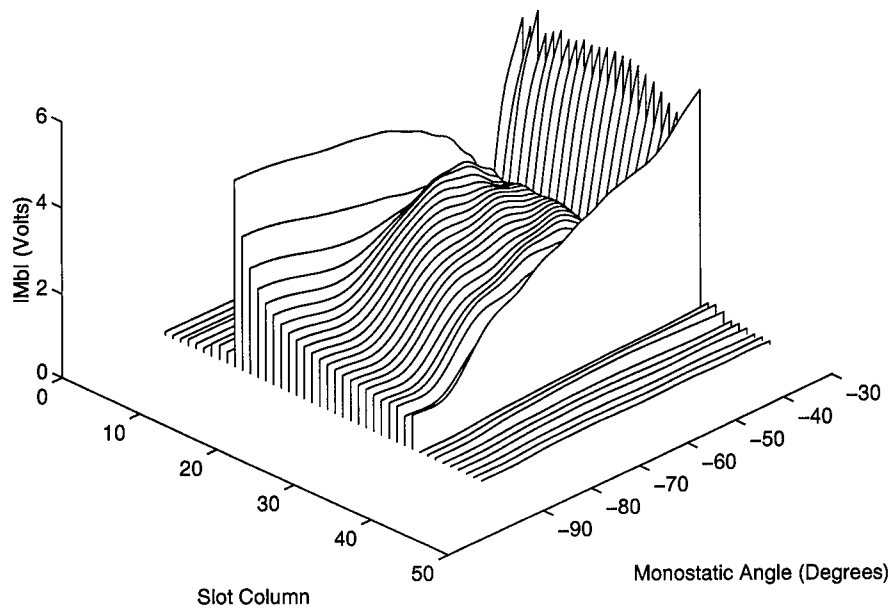


Figure 115. Induced Currents on R-Card Treated Metal Radome in Homogeneous Media at 17 GHz

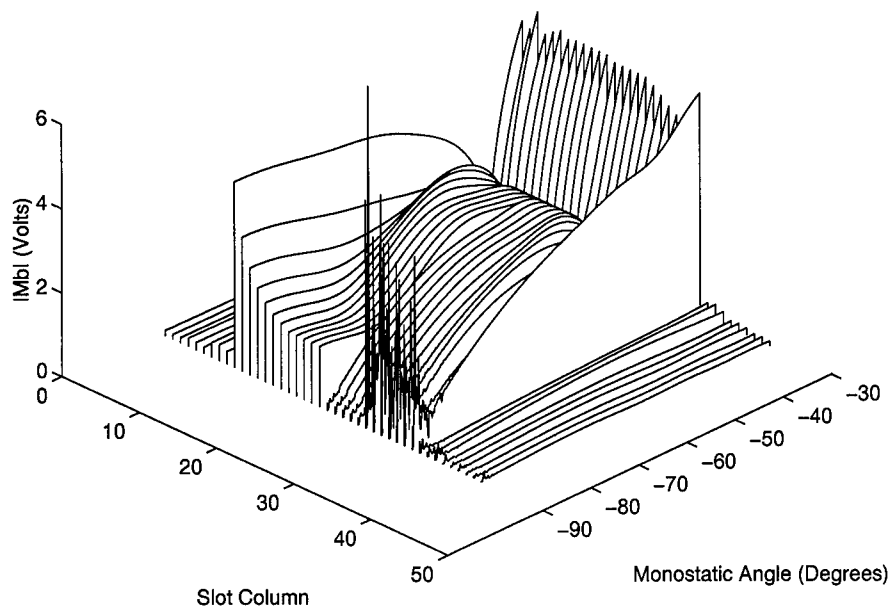


Figure 116. Hybrid PMM/MM Approximation to Induced Currents on R-Card Treated Metal Radome in Homogeneous Media at 17 GHz

### 4.3 Array Size Scaling

In this final section, the author presents an example array problem demonstrating the effect of array size on computation time for both MM and hybrid MM/PMM techniques. It addresses the question of why one would be interested using the hybrid technique if the MM analysis provides adequate solutions. To provide a fair comparison, the author used the same code with the PBF turned on and off. This approach eliminated any differences due to the MM's numerical implementation. The author used the same slotted array parameters as those in the homogeneous media examples presented earlier. The array is again illuminated by a 15 GHz plane wave, 5° off normal. The only variable is the number of slot columns comprising each array.

Table 4 presents the comparison between the two techniques for radomes with 100 to 900 slot columns. The codes were run on a Sun Microsystems Sparc20 Workstation. In obtaining the data for the table, the author assumed twenty edge elements were sufficient to capture all the current perturbations due to the array edges. Figure 60 clearly demonstrates this assumption is valid. Notice that while the MM is faster than the hybrid PMM/MM for a 100 column array, the hybrid technique quickly surpasses the MM for larger arrays. One may also observe that, while the MM matrix fill time claims the lion's share of the computation time early on, the system solve time quickly becomes the dominant bottleneck. Based on the table's data, the solve time increases as approximately  $N^{2.9}$ , where N indicates the system size. This is in contrast to the hybrid PMM/MM technique, whose computation time scales as approximately  $N^{0.0}$ . This study clearly demonstrates one of the technique's primary advantages over conventional approaches. Namely, the hybrid PMM/MM technique is able to sidestep the link between array size and system size by lumping the array's Floquet elements into a single unknown element. As stated earlier for the wire array, the computational improvement for calculations involving many *monostatic* angles may not be as dramatic since the hybrid method requires recalculation of one row in the coupling matrix for every incident angle.

This chapter represents the culmination of the previous chapters by putting the theory into practice. The previous data sets clearly demonstrate where the hybrid PMM/MM technique is useful as well as where its use is inappropriate. The overall agreement between the reference code and measured data give a high confidence level in the technique's validity. In general, where ever an

MM Code Unknowns	MM Code Fill (cpu secs)	MM Code Solve (cpu secs)	MM Code Total (cpu secs)
100	6.00	0.18	6.27
200	12.07	1.32	13.48
300	18.65	4.30	23.05
400	24.92	9.98	35.02
500	30.50	19.73	50.38
600	36.70	34.05	70.95
700	54.58	54.28	109.12
800	49.58	81.35	131.12
900	56.97	116.02	173.25
PMM/MM Code Unknowns: Left/Right	PMM/MM Code Fill (cpu secs)	PMM/MM Code Solve (cpu secs)	PMM/MM Code Total (cpu secs)
20/20	4.82/4.78	0.00/0.02	9.67
20/20	4.80/4.78	0.02/0.00	9.68
20/20	4.87/4.85	0.00/0.02	9.85
20/20	4.80/4.80	0.00/0.00	9.72
20/20	4.80/4.77	0.02/0.00	9.73
20/20	4.82/4.80	0.00/0.02	9.77
20/20	4.85/4.85	0.02/0.00	9.92
20/20	4.82/4.87	0.03/0.02	9.93
20/20	4.78/4.80	0.00/0.02	9.82

Table 4. Slot Array in Homogeneous Media Reference MM Code versus Hybrid PMM/MM Code Time Comparison

array is wide enough to have a well developed Floquet region, the hybrid PMM/MM technique is computationally superior to the MM formulation.

## V. Conclusion

Of making many books there is no end, and much study wearies the body. Now all has been heard; here is the conclusion of the matter: Fear God and keep His commandments, for this is the whole duty of man.

- *King Solomon*

This dissertation develops a hybrid periodic moment method/moment method (PMM/MM) based solution for the electromagnetic scattering from semi-infinite arrays of wires and slots, possibly embedded in a stratified dielectric media. These geometries are of interest in developing treatments to control the edge diffraction from large finite arrays. While a growing body of finite array research exists, none incorporates the physical basis function (PBF) concept presented here. The dissertation clearly demonstrates the benefits of the hybrid approach. With the exception of a few instances where the author's numerical implementation, not the formulation itself, produces inaccurate results, the hybrid code accurately generates the array's scattering currents in much less time than the reference moment method (MM) codes.

In the previous pages, the author develops each component of a complete moment method (MM) solution for both wire and slot arrays. Examining each piece separately, the author fills the coupling matrix consisting of individual edge element basis functions and a PBF capturing the Floquet behavior away from the array's edge. With an eye toward an efficient numerical implementation, both spatial and spectral domain forms are presented, along with various summation acceleration techniques. Dielectric boundaries are accounted for via Fresnel reflection and transmission coefficients. The author then turns to the excitation vector entries, again accounting for the dielectric boundaries in the spectral domain via Fresnel coefficients. Solving the system, the author discusses the scattering currents and their relationship to the scattered far-fields and echo widths. Various related ideas are also discussed including PBF testing and use in the excitation vector, a priori determination of the required number of edge elements, and edge element loading. Finally, the hybrid PMM/MM formulation is validated, using both independent reference solutions and actual array measurements. The author tests an r-card based edge treatment using the hybrid formulation. The resulting scattering currents and field patterns demonstrate the formulation's usefulness in array design.

This work represents the first attempt to incorporate a periodic basis function with individual edge basis functions in an effort to reduce the computational burden associated with large arrays. The computational savings demonstrated here suggest several areas for future research, taking advantage of this promising technique. First, the hybrid technique could be applied to more complex arrays. The author necessarily restricted the array complexity in order to focus on the PBF implementation issues. The technique's success motivates exploring more general element shapes and orientations in multi-array structures. The PBF could also be used in orthogonal directions, extending the finite-by-infinite arrays examined here to finite-by-finite geometries. Second, the numerical difficulties the author encountered point to explorations of alternative numerical PBF implementations. In particular, one may want to examine numerical integration algorithms tailored to the continuous spectral integrand's form. The asymptotic analysis for the homogeneous media case presented in Appendix C could be developed for stratified media to further increase computational efficiency. Additionally, there may be different approaches to handling the surface wave and grating lobe singularities. Finally, the grazing angle problem caused by the epsilon summation acceleration algorithm could be avoided by implementing an alternative algorithm such as those discussed in Appendix B. The last research area involves applying the new hybrid technique to the edge treatment design problem. One could easily take advantage of the technique's speed by incorporating it in an automated optimization scheme. Regardless of the optimization approach (gradient search, genetic algorithm, etc.), the parameter space can be searched much quicker due to the faster minimization function calculations. Of course, a priori knowledge of the required number of edge elements would also help speed the process. One could incorporate an approximation such as the Gibbsian model discussed at the end of Chapter II.

### Appendix A. One-Sided Poisson Sum Formula

The coupling matrix entries associated with periodic structures often involve slowly convergent infinite summations. The Poisson sum formula provides a convenient means to transform these summations into a more rapidly convergent form. In addition, the resulting plane wave representation allows the introduction of stratified dielectric layers with relative ease.

The semi-infinite array geometries of interest in this research lead to one-sided summations. Unfortunately, the original form of the Poisson sum is inappropriate in these cases. To alleviate this difficulty, a one-sided version of the Poisson sum formula is derived which can be used to transform these one-sided sums into equivalent, more rapidly convergent plane wave representations.

One begins the derivation by considering the normal two-sided Poisson sum formula given by Papoulis [29]

$$\sum_{q=-\infty}^{\infty} e^{jq\omega_0 t} F(q\omega_0) = T \sum_{k=-\infty}^{\infty} f(t \pm kT) \quad (174)$$

where  $f(t)$  and  $F(\omega)$  denote a function and its Fourier transform defined by

$$f(t) = \frac{1}{2\pi} \int_{-\infty}^{\infty} F(\omega) e^{j\omega t} d\omega \quad (175)$$

$$F(\omega) = \int_{-\infty}^{\infty} f(t) e^{-j\omega t} dt \quad (176)$$

and  $T = \frac{2\pi}{\omega_0}$ . Note the left hand side of Equation (174) contains a function with the linear phase progression characteristic of a spatial summation, making it an appropriate choice for conversion to a one-sided summation. This is accomplished by defining a continuous function  $G(\omega)$  such that

$$F(\omega) = G(\omega) \cdot U\left(\omega + \frac{\omega_0}{2}\right) \quad (177)$$

where  $U(\omega)$  is the Heaviside unit step function

$$U(\omega) = \begin{cases} 1, & \omega > 0 \\ 0, & \omega < 0 \end{cases} \quad (178)$$

The left hand side of Equation (174) can now be written as

$$\sum_{q=0}^{\infty} e^{jq\omega_o t} G(q\omega_o) \quad (179)$$

which can be identified with the spatial summations encountered in this dissertation.

Now lets examine the effect of this substitution on the right hand side of the double-sided Poisson sum formula. One needs to determine the inverse Fourier transform of the function  $G(\omega) \cdot U(\omega + \frac{\omega_o}{2})$ . Designating  $u(t)$  and  $g(t)$  as the inverse Fourier transforms of  $U(\omega)$  and  $G(\omega)$  respectively, one has from the convolution property of the Fourier transform [35]

$$G(\omega) \cdot U(\omega) \leftrightarrow \int_{-\infty}^{\infty} g(\tau)u(t - \tau)d\tau \quad (180)$$

In addition, the frequency shifting property of the Fourier transform gives [35]

$$U(\omega + \frac{\omega_o}{2}) \leftrightarrow u(t)e^{-j\frac{\omega_o}{2}t} \quad (181)$$

Substituting Equation (181) into Equation (180)

$$G(\omega) \cdot U(\omega + \frac{\omega_o}{2}) \leftrightarrow \int_{-\infty}^{\infty} g(\tau)u(t - \tau)e^{-j\frac{\omega_o}{2}(t-\tau)}d\tau = f(t) \quad (182)$$

At this point, one explicitly introduces the inverse Fourier transform of the step function (Recall the step function is in the frequency domain). The duality property of Fourier transform pairs applied



to the generalized Fourier transform of the step function results in [35]

$$u(t) = \frac{\delta(t)}{2} - \frac{1}{j2\pi t} \quad (183)$$

One can substitute Equation (183) in Equation (182) to obtain

$$f(t) = \frac{g(t)}{2} + \frac{j}{2\pi} \int_{-\infty}^{\infty} \frac{g(\tau) e^{-j\frac{\omega_o}{2}(t-\tau)}}{t-\tau} d\tau \quad (184)$$

based on the sifting property of the Dirac delta function. The remaining integral must be interpreted as a principal value integral to maintain the one-to-one correspondence between the Fourier transform pair.

With Equation (184), one can express the right hand side in terms of the new function  $g(t)$ . Substituting Equation (184) into the original Poisson sum formula leads to the new one-sided Poisson sum formula

$$\sum_{q=0}^{\infty} e^{jq\omega_o t} G(q\omega_o) = T \sum_{k=-\infty}^{\infty} \left\{ \frac{g(t \pm kT)}{2} + \frac{j}{2\pi} \int_{-\infty}^{\infty} \frac{g(\tau) e^{-j\frac{\omega_o}{2}(t \pm kT - \tau)}}{t \pm kT - \tau} d\tau \right\} \quad (185)$$

which is used throughout this research. Note the choice of plus or minus signs is completely arbitrary in implementing this formula as long as the choice is applied consistently.

The following example illustrates Equation (185)'s implementation. Consider the function,

$$g(t) = \frac{\sin(\frac{t}{2})}{\pi t} \quad (186)$$

and its Fourier transform [35]

$$G(\omega) = \text{rect}(\omega) = \begin{cases} 1, & |\omega| < 1/2 \\ 0, & |\omega| > 1/2 \end{cases} \quad (187)$$

Inserting these functions into Equation (185), one obtains

$$\sum_{q=0}^{\infty} e^{jq\omega_o t} \text{rect}(q\omega_o) = \frac{1}{\omega_o} \sum_{k=-\infty}^{\infty} \left\{ \frac{\sin(\frac{\gamma_k}{2})}{\gamma_k} + j \int_{-\infty}^{\infty} \frac{\sin(\frac{\tau}{2}) e^{-j\frac{\omega_o}{2}(\gamma_k - \tau)}}{\pi\tau(\gamma_k - \tau)} d\tau \right\} \quad (188)$$

where  $\gamma_k = t - \frac{2\pi k}{\omega_o}$ .

The principal value integral in Equation (188) can be evaluated using residue calculus. Specifically, the integrand is first broken into two parts using Euler's identity for the sine function. One then allows  $\tau$  to become complex where each integrand part has different regions of convergence. By carefully applying Cauchy's theory, one can relate the principal value integrals to the sum of the half residues at  $\tau = 0$  and  $\tau = \gamma_k$ . The resulting evaluation gives

$$\sum_{q=0}^{\infty} e^{jq\omega_o t} \text{rect}(q\omega_o) = \begin{cases} -\frac{j}{\omega_o} \sum_{k=-\infty}^{\infty} \frac{1}{\gamma_k} \left[ e^{j\frac{\gamma_k}{2}} - e^{-j\frac{\omega_o}{2}\gamma_k} \right], & 0 < \omega_o < 1 \\ \frac{2}{\omega_o} \sum_{k=-\infty}^{\infty} \frac{\sin(\frac{\gamma_k}{2})}{\gamma_k}, & 1 < \omega_o \end{cases} \quad (189)$$

which can be verified numerically. Note Equation (189) is valid for all values of  $t$  and positive values of  $\omega_o$  as long as  $\omega_o \neq \frac{1}{2q}$  for integer  $q$ . This restriction is a consequence of the "edge" of the rect function coinciding with one of the sample points in the left hand side of Equation (189).

The right hand side of Equation (189) provides an alternative representation which becomes attractive for small values of  $\omega_o$ . In that case, the left hand side will require many terms where the corresponding wide separation between successive values of  $\gamma_k$  will cause the right hand side summation to quickly converge. To demonstrate this fact, consider the particular case of  $\omega_o = 0.003$  and  $t = 4.4429$ . The left hand side summation in Equation (189) terminates after 166 terms resulting in a value of (60.299, 120.34). Table 5 lists the partial summations of the right hand side (RHS) for an increasing number of terms. The relative error between these summations and the left hand side (LHS) is also given. This example clearly illustrates the inverse bandwidth nature between the two representations as well as the importance of such a transformation.

K	$\sum_{k=-K}^K RHS$	$\left  \frac{LHS - RHS}{LHS} \right $
0	(60.198, 120.47)	0.00124
1	(60.365, 120.25)	0.00081
2	(60.282, 120.36)	0.00021

Table 5. Sequence of Partial Sums for the RHS

## Appendix B. Summation Acceleration Algorithms

When using the Method of Moments (MM) to solve electromagnetic scattering problems, infinite geometries invariably lead to infinite summations. The semi-infinite arrays of this research are no exception. In seeking a numerical solution, one is forced to truncate the summations in one way or another. The obvious choice is to terminate the summation after a given number of terms, but determining how many terms to include before truncation is not always a straight-forward problem. As is often the case, the obvious choice is not always the “best” choice. This appendix describes several algorithms which take advantage of the convergence characteristics of the infinite summation to accelerate its convergence. It turns out the two types of summations used in this research (spatial and spectral) have different convergence behaviors which affect the performance of each algorithm. These algorithms are the  $\epsilon$ -algorithm, the circle-fit algorithm, and the  $\rho$ -algorithm.

### B.1 $\epsilon$ -Algorithm

The  $\epsilon$ -algorithm was proposed by Wynn [41] as an efficient alternative to Shank's transformation [30] for estimating the limit of a sequence of partial sums. Unlike Shank's transformation, which requires a complete recalculation of the entire sequence for each estimate, Wynn's  $\epsilon$ -algorithm builds on the previously calculated estimates. The result is a pyramid of numbers whose peak contains the best estimate to the infinite sum's limit.

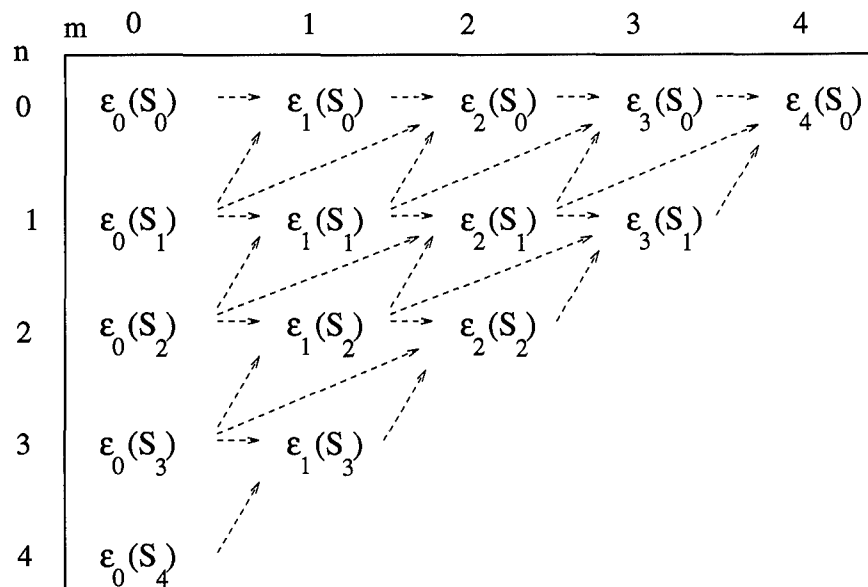
The entries in the pyramid are obtained from the so-called  $\epsilon_m(\cdot)$  function operating on a sequence of partial sums,  $S_n$ . The pyramid is formed by implementing the following equations

$$\epsilon_0(S_n) = S_n \quad (190)$$

$$\epsilon_1(S_n) = \frac{1}{[\epsilon_0(S_{n+1}) - \epsilon_0(S_n)]} \quad (191)$$

$$\epsilon_m(S_n) = \epsilon_{m-2}(S_{n+1}) + \frac{1}{[\epsilon_{m-1}(S_{n+1}) - \epsilon_{m-1}(S_n)]} \quad (192)$$

where  $\epsilon_{-1}(S_{n+1}) = 0$ . Graphically the process can be represented



Note that odd  $m$  values correspond to intermediate results which are necessary for the next estimate,  $\epsilon_{2m}(S_n) = e_m(S_n)$ , where  $e_m(\cdot)$  is the Shank's transformation. Clearly only two additional partial sum calculations are required to obtain the next estimate. The complete sequence of partial sums does not have to be recalculated resulting in tremendous computational savings.

As in all asymptotic series evaluations, care must be taken when applying them to a particular summation. Specifically, the  $\epsilon$ -algorithm works best for partial sums which tend to oscillate around their convergence value (*e.g.*, the spatial summations of this research). When applied to monotonically decreasing series such as those generated by the spectral summations, the  $\epsilon$ -algorithm's performance degrades somewhat. Even so, the author found it's acceleration significant enough to use it for both the spatial and spectral domain summations encountered in this research.

### B.2 Circle-Fit Algorithm

The second acceleration algorithm of interest also applies primarily to oscillatory summations. The circle-fit algorithm is a modification of the spiral average method proposed by Skinner [33]. Both are based the observation that, for a given test location, the consecutive spatial domain partial sums form a spiral about the convergence point in the complex plane. This phenomena is due to the fact

that the distances between each successive array element and the test point asymptotically approach the inner-element spacing. By estimating the center of the spiral, one obtains an approximation for the eventual convergence point.

The primary distinction between Skinner's spiral average algorithm and the circle-fit algorithm lies in the technique used to estimate the center of the spiral. Skinner determines the number of partial sums required to have a complete phase rotation in the complex plane. He then performs an arithmetic average of these partial sums to obtain his estimate. When the inner-element spacing does not lead to an integer number of phase rotations, Skinner must choose an error parameter and search for the correct number of partial sums required to obtain a phase rotation within an error percentage of an integer number of rotations.

In contrast, the circle-fit algorithm does not require an integer number of phase rotations. The only requirement is that there is some phase rotation over the collection of partial sums. As the name implies, the algorithm simply attempts to fit a circle to the sequence of partial sums. The center of the circle provides an estimate to the infinite sum.

As an illustration, consider the two-dimensional Green's function for a semi-infinite wire array

$$G(x, y) = \lim_{q \rightarrow \infty} \frac{-j}{4} \sum_{q=0}^{\infty} H_0^{(2)}(\beta \sqrt{(qd_x - x)^2 + y^2}) \quad (193)$$

For large  $q$  values one can use the asymptotic form of the Hankel function to express the summand as [1]

$$\begin{aligned} s_q &= H_0^{(2)}(\beta \sqrt{(qd_x - x)^2 + y^2}) \\ &\sim H_0^{(2)}(\beta |q| d_x), \quad q \rightarrow \infty \\ &\sim \sqrt{\frac{2j}{\pi \beta |q| d_x}} e^{-j\beta |q| d_x}, \quad q \rightarrow \infty \end{aligned} \quad (194)$$

Note that each summand contributes a component with a constant phase increment and a monotonically decreasing amplitude. Figure 117 depicts a typical sequence of partial sums.

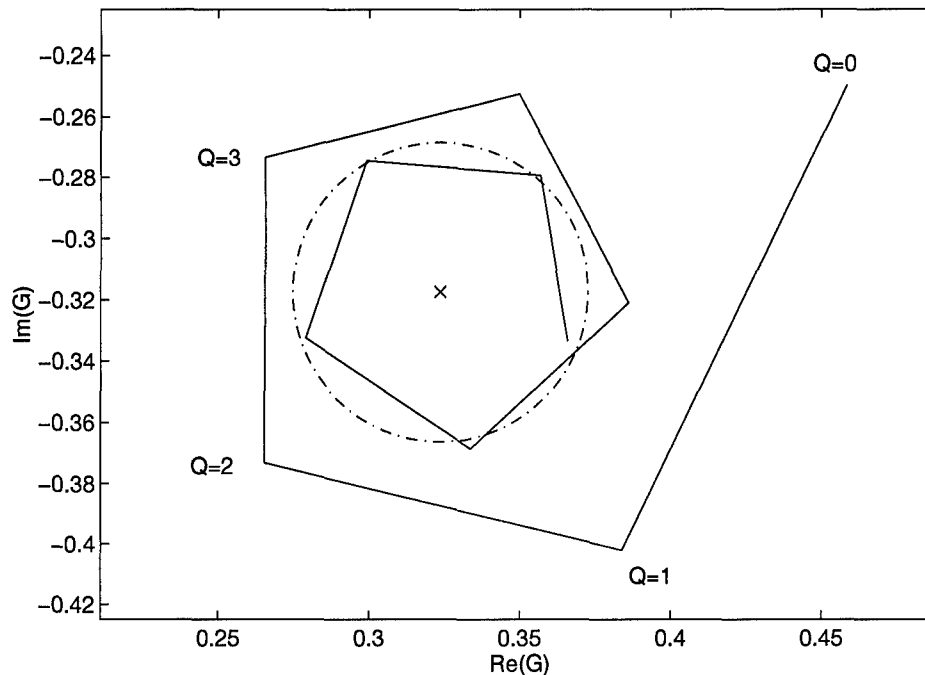


Figure 117. Circle-fit Algorithm for Two-dimensional Free-space Periodic Green's Function

The sequence was generated using Equation (193) with the parameters:  $d_x = 0.21\lambda$ ,  $x = 0.0$ ,  $y = 0.01\lambda$ . The figure also contains a plot of the "best fit" circle to the last five partial sums. The center of this circle represents the current estimate of the infinite sum. To obtain a final estimate, one compares the current estimate with the estimate generated from the next five partial sums. When the difference between subsequent estimates reaches a specified tolerance, one calls the process converged. Note in this case the estimates are generated after every fifth partial sum. In general, a new estimate could be generated using any number of previous partial sums (greater than three) every time a new partial sum is calculated.

The method for fitting the circles comes from a paper by Moura and Kitney [25]. In it they describe how to determine the circle which minimizes the *square error* between itself and the set of data points. Simply stated, the problem amounts to finding a center point,  $(x_o, y_o)$ , and a radius,  $r_o$ ,

such that the error defined by

$$E = \sum_{i=1}^N [(x_o - x_i)^2 + (y_o - y_i)^2 - r_o^2] \quad (195)$$

is minimized. This is accomplished by forcing the partial derivatives,  $\frac{\partial E}{\partial x_o}$ ,  $\frac{\partial E}{\partial y_o}$ , and  $\frac{\partial E}{\partial r_o}$  to be zero. The latter constraint gives a relationship between the data set,  $(x_i, y_i)$ , the circle's center point,  $(x_o, y_o)$ , and its radius,  $r_o$

$$r_o = \frac{1}{N} \sum_{i=1}^N [(x_o - x_i)^2 + (y_o - y_i)^2] \quad (196)$$

From the remaining constraints, Moura and Kitney derive a matrix equation whose solution gives the circle's center,  $(x_o, y_o)$ .

$$\begin{bmatrix} C_1 \\ C_2 \end{bmatrix} = \begin{bmatrix} G_{11} & G_{12} \\ G_{21} & G_{22} \end{bmatrix} \begin{bmatrix} x_o \\ y_o \end{bmatrix} \quad (197)$$

where

$$\begin{aligned} G_{11} &= 4 \sum_{i=1}^N x_i^2 - \frac{4}{N} \left[ \sum_{i=1}^N x_i \right]^2 \\ G_{12(21)} &= 4 \sum_{i=1}^N x_i y_i - \frac{4}{N} \sum_{j=1}^N x_j \sum_{k=1}^N y_k \\ G_{22} &= 4 \sum_{i=1}^N y_i^2 - \frac{4}{N} \left[ \sum_{i=1}^N y_i \right]^2 \\ C_1 &= -\frac{1}{N} \sum_{i=1}^N x_i^2 \sum_{j=1}^N x_j - \frac{1}{N} \sum_{i=1}^N y_i^2 \sum_{k=1}^N x_k + \sum_{i=1}^N y_i^2 x_i + \sum_{i=1}^N x_i^3 \\ C_2 &= -\frac{1}{N} \sum_{i=1}^N y_i^2 \sum_{j=1}^N y_j - \frac{1}{N} \sum_{i=1}^N x_i^2 \sum_{k=1}^N y_k + \sum_{i=1}^N x_i^2 y_i + \sum_{i=1}^N y_i^3 \end{aligned}$$

Significantly, this method is a *direct* method<sup>1</sup>, a fact crucial in maintaining the circle-fit algorithm's computational efficiency.

<sup>1</sup>A direct method implies the circle's defining parameters are calculated from the data points in one step. There is no iterative process to refine an initial guess.



Relative Error	Raw Sum (# terms/cpu secs)	Circle-fit Algorithm	$\epsilon$ -Algorithm
1.0E-1	10 / 0.001	5 / 0.001	2 / 0.001
1.0E-2	977 / 0.4	15 / 0.004	4 / 0.002
1.0E-3	24834 / 50.7	45 / 0.011	6 / 0.003
1.0E-4	NC	190 / 0.042	6 / 0.003
1.0E-5	NC	880 / 0.167	8 / 0.004
1.0E-6	NC	3865 / 0.766	10 / 0.005
1.0E-7	NC	11380 / 2.375	12 / 0.005

Table 6. Circle-fit and  $\epsilon$  Algorithms Applied to Equation (193)

Table 6 clearly demonstrates this efficiency by comparing the convergence characteristics of the two acceleration algorithms to the unaccelerated sum of Equation (193). The parameters here are the same as those used to generate Figure 117's plot. In the table the letters "NC" indicate the sum did not converge. Convergence is determined by calculating the relative error between each algorithm's estimate and a "truth" value obtained by setting the convergence tolerance to machine accuracy for either algorithm. The relative error is then defined by

$$\text{relative error} = \left| \frac{\text{estimate} - \text{truth}}{\text{truth}} \right| \quad (198)$$

Also, the CPU times are those obtained on a Sun Sparc10 workstation. Based on these results, the author chose the  $\epsilon$ -algorithm over the circle-fit algorithm.

### B.3 $\rho$ -Algorithm

The final algorithm considered reportedly performs best on monotonically decreasing summations. The  $\rho$ -algorithm was proposed by Singh and Singh as a more efficient alternative to the  $\epsilon$ -algorithm [31]. Originally derived by Wynn [42], the algorithm can be computed by the following

Relative Error	Raw Sum (# terms/cpu secs)	$\epsilon$ -Algorithm	$\rho$ -Algorithm
1.0E-1	5 / 0.003	4 / 0.003	2 / 0.003
1.0E-2	60 / 0.015	14 / 0.005	2 / 0.003
1.0E-3	607 / 0.129	132 / 0.056	4 / 0.003
1.0E-4	6078 / 1.4	136 / 0.056	4 / 0.003
1.0E-5	NC	730 / 0.123	6 / 0.003
1.0E-6	NC	NC	6 / 0.003
1.0E-7	NC	NC	8 / 0.003

Table 7.  $\epsilon$  and  $\rho$  Algorithms Applied to Equation (202)

equations

$$\rho_0(S_n) = S_n \quad (199)$$

$$\rho_1(S_n) = \frac{1}{[\rho_0(S_{n+1}) - \rho_0(S_n)]} \quad (200)$$

$$\rho_m(S_n) = \rho_{m-2}(S_{n+1}) + \frac{m}{[\rho_{m-1}(S_{n+1}) - \rho_{m-1}(S_n)]} \quad (201)$$

where  $\rho_{-1}(S_{n+1}) = 0$ . Notice the similarity to the  $\epsilon$ -algorithm. The difference lies in the numerator of the last equation. It is claimed this small change gives the  $\rho$ -algorithm a tremendous advantage over the  $\epsilon$ -algorithm when operating on a monotonically decreasing summand.

As a demonstration, consider the infinite summation

$$S = \sum_{k=1}^{\infty} \frac{1}{k^2} \quad (202)$$

Table 7 contains a comparison of the  $\epsilon$ -algorithm and  $\rho$ -algorithm along with the unaccelerated sum. Based on this data, the  $\rho$ -algorithm would be the algorithm of choice. In fact in their paper, Singh and Singh present relative error plots of this algorithm applied to both spectral and spatial Green's functions similar to those used in this research which clearly indicate a performance advantage over the  $\epsilon$ -algorithm.

Unfortunately, the author was not able to obtain the same performance. Table 8 shows the algorithm applied to the discrete spectral sum of Equation (203) with parameters:  $d_x = 0.21\lambda$ ,

Relative Error	Raw Sum (# terms/cpu secs)	$\epsilon$ -Algorithm	$\rho$ -Algorithm
1.0E-1	21 / 0.009	8 / 0.004	4 / 0.004
1.0E-2	70 / 0.024	14 / 0.006	16 / 0.005
1.0E-3	130 / 0.042	20 / 0.008	136 / 0.075
1.0E-4	196 / 0.064	32 / 0.012	170 / 0.109
1.0E-5	264 / 0.087	52 / 0.018	392 / 0.473
1.0E-6	333 / 0.106	74 / 0.028	NC
1.0E-7	404 / 0.127	84 / 0.036	NC

Table 8.  $\epsilon$  and  $\rho$  Algorithms Applied to Equation (203)

$x = 0.0, y = 0.001\lambda.$

$$G(x, y) = \frac{-j}{4\pi} \sum_{k=-\infty}^{\infty} \frac{e^{-j \left[ x \frac{2\pi k}{d_x} + y \sqrt{\beta^2 - \left( \frac{2\pi k}{d_x} \right)^2} \right]}}{\sqrt{\beta^2 - \left( \frac{2\pi k}{d_x} \right)^2}} \quad (203)$$

The  $\rho$ -algorithm actually requires more terms than the raw sum. Based on these results and other numerical experiments, the author decided the  $\epsilon$ -algorithm provided the most reliable acceleration in both the spatial and spectral domains. This fact coupled with the algorithm's relative simplicity made the  $\epsilon$ -algorithm the method of choice.

### *Appendix C. Continuous Spectrum Integral: Uniform Asymptotic Expansion*

The application of the Method of Moments (MM) to infinite periodic structures results in infinite summations. The summation acceleration algorithms of Appendix B provide one approach for evaluating these summations. Another approach involves transforming the summand to another, more convergent, form. The one-sided Poisson sum used in this research is an example of this technique. Unfortunately, the one-sided Poisson sum generates a continuous spectrum integral which is often difficult to evaluate numerically. In an attempt to mitigate this problem, the author investigated the following asymptotic integral evaluation. Although not universally applicable, the asymptotic integral evaluation significantly shortens the computation time required for many of the integrals encountered in this research.

The continuous spectrum<sup>1</sup> integral has the general form

$$I_k = \oint_C f(\nu) e^{\Omega q(\nu)} d\nu \quad (204)$$

where  $C$  is an infinite contour in the complex  $\nu$  plane,  $q(\nu)$  is an analytic function, and  $f(\nu)$  has a simple pole<sup>2</sup> located on  $C$ . The parameter  $\Omega$  is positive and, most important, often large. When this occurs, one can use an asymptotic approximation for  $I_k$  and still maintain reasonable accuracy.

At its core, the asymptotic integral evaluation is based on the exponential behavior of the integrand. Suppose  $Re\{q(\nu)\}$  in Equation (204) has a local maximum  $\nu_s$ , known as a saddle point, somewhere along  $C$ . In the neighborhood of  $\nu_s$ ,  $Re\{q(\nu_s)\} > Re\{q(\nu)\}$ . Since  $\Omega$  is a large positive value, the magnitude of the exponential function,  $|e^{\Omega q(\nu)}|$ , will be greatest at  $\nu_s$  and decay very rapidly away from  $\nu_s$ . As long as  $f(\nu)$  is analytic in the neighborhood of  $\nu_s$ , one can approximate  $I_k$  with only the integral contribution from the local maximum.

---

<sup>1</sup>This form is actually the angular spectrum resulting from the transformation  $\rho_x = \sin(\nu)$ .

<sup>2</sup>For the non-free-space geometries,  $f(\nu)$  may also contain singularities associated with surface waves trapped in the stratified media.

At this point, one usually applies a little finesse in an effort to make the local evaluation as easy as possible. For example, if  $f(\nu)$  is slowly varying in the neighborhood of  $\nu_s$ , it can be approximated by  $f(\nu_s)$  and pulled out of the integral

$$I_k \sim f(\nu_s) \int_{|\nu - \nu_s| < \epsilon} e^{\Omega q(\nu)} d\nu, \quad \Omega \rightarrow \infty \quad (205)$$

One can then perform a Taylor expansion of  $q(\nu)$  about  $\nu_s$ . Retaining the first two non-zero<sup>3</sup> terms, one arrives at the “canonical” form

$$I_k \sim f(\nu_s) e^{\Omega q(\nu_s)} \int_{|\nu - \nu_s| < \epsilon} e^{-\Omega |q''(\nu_s)| \frac{(\nu - \nu_s)^2}{2}} d\nu, \quad \Omega \rightarrow \infty \quad (206)$$

Since the integrand is exponentially dominant, one can extend the range of integration. Then, with the appropriate variable substitution, one can express the integral in terms of the gamma function. Closed form evaluation gives the final asymptotic form

$$I_k \sim \sqrt{\frac{-2\pi}{\Omega q''(\nu_s)}} f(\nu_s) e^{\Omega q(\nu_s)}, \quad \Omega \rightarrow \infty \quad (207)$$

Unfortunately, the integrals encountered in the dissertation rarely display the desired behavior without some manipulation. For example, one must deform  $C$  into what is commonly called the steepest descent path,  $C_{SDP}$ . Along  $C_{SDP}$ , the integrand displays the desired sub-dominant behavior away from the saddle point. Another difficulty occurs when  $f(\nu)$ 's singular point lies in the vicinity of the saddle point. One must then decompose  $f(\nu)$  into a regular and singular part. The regular part leads to the gamma function as before. The singular part leads to error function or Fresnel integrals which are well tabulated. Felsen and Marcuvitz provide an excellent overview of this process in their chapter on the asymptotic evaluation of integrals [11].

---

<sup>3</sup>Since  $\nu_s$  is a maximum,  $q'(\nu_s) = 0$  where the prime indicates differentiation with respect to the argument. Thus the next non-zero term is  $q''(\nu_s)$ .

To illustrate the benefits of asymptotic evaluation, consider the integral arising from the two-dimensional wire array in free-space

$$I_k = \oint_C \frac{e^{-j\beta\tilde{\rho}_t \cos(\nu - \tilde{\phi}_t)}}{\sin(\nu) - \rho_x} d\nu \quad (208)$$

where

$$\rho_x = s_x + \frac{k\lambda}{d_x} \quad (209)$$

and  $C$  is shown in Figure 6. The parameter  $\beta\tilde{\rho}_t$  represents the electrical distance from a point one half the inner-element spacing to the left of the array edge and  $\tilde{\phi}_t$  the angle measured from the array normal. Thus for many of the terms in the coupling matrix,  $\beta\tilde{\rho}_t$  is a “large”<sup>4</sup> parameter.

To perform an asymptotic evaluation, one must distort the principle value contour to the steepest descent path, accounting for any pole encirclement along the way. In addition, the principle value contour must be completed in order to invoke Cauchy residue theory to distort the contour. One can incorporate both factors in the analysis through the combined residue contribution

$$I_k \sim I_{C_{SDP}} + I_{residue} \quad (210)$$

Figure 118 depicts these contours for a typical saddle point/grating lobe pole configuration. The grating lobe pole occurs at  $\nu_o = \sin^{-1}(\rho_x)$  and the saddle point at  $\nu_s = \tilde{\phi}_t$ . The steepest decent path is defined by  $Im\{q(\nu)\} = Im\{q(\nu_s)\}$  which intersects the real axis at  $\nu_s$  and one of the vertical legs at  $\nu_i = \pm \cosh^{-1}\left(\frac{1}{|\sin(\tilde{\phi}_t)|}\right)$ , depending on the sign of  $\nu_s$ .

Felsen and Marcuvitz provide a uniform asymptotic evaluation valid even when the grating lobe pole and the saddle point come arbitrarily close to each other. Expressed in terms of the

---

<sup>4</sup>Of course, the definition of “large” depends on the accuracy one desires.

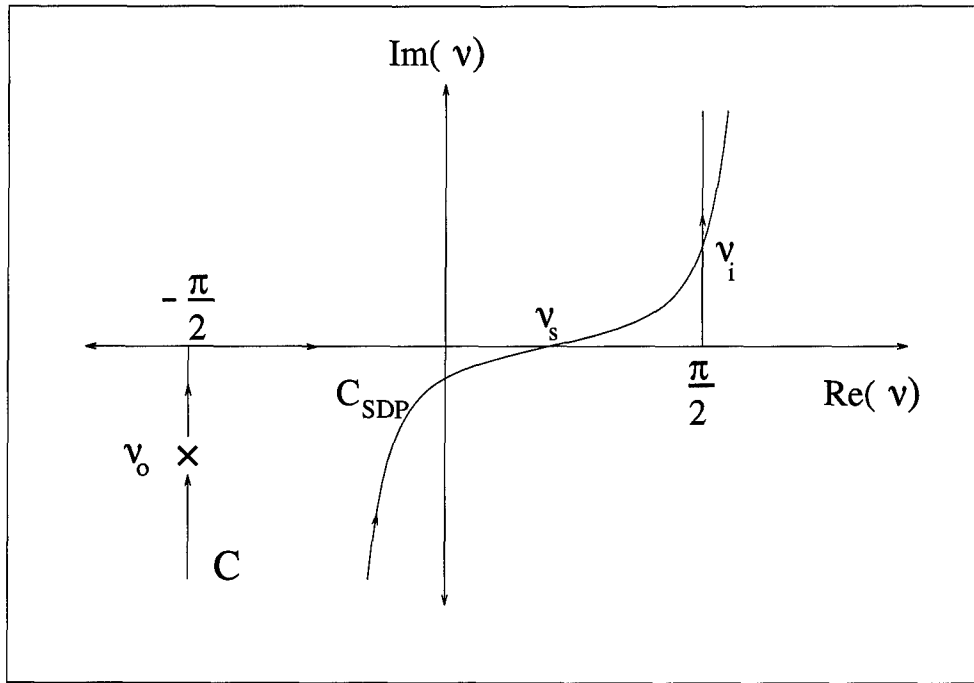


Figure 118. Angular Spectral Integral Steepest Descent Path

complementary error function, the evaluation is

$$\begin{aligned}
 I_{C_{SDP}} \sim & e^{-j\beta\tilde{\rho}_t} \left\{ e^{j\frac{\pi}{4}} \sqrt{\frac{2\pi}{\beta\tilde{\rho}_t}} \left[ \frac{1}{\sin(\tilde{\phi}_t) - \rho_x} - \frac{j}{\rho_y \sqrt{2[\cos(\nu_o - \tilde{\phi}_t) - 1]}} \right] \right. \\
 & \left. \pm j2\sqrt{\frac{\pi}{\rho_y}} e^{-j\beta\tilde{\rho}_t[\cos(\nu_o - \tilde{\phi}_t) - 1]} Q \left( \mp e^{j\frac{3\pi}{4}} \sqrt{\beta\tilde{\rho}_t[\cos(\nu_o - \tilde{\phi}_t) - 1]} \right) \right\} \quad (211)
 \end{aligned}$$

where

$$Q(x) = \int_x^\infty e^{-t^2} dt \quad (212)$$

$$\rho_y = \sqrt{1 - \rho_x^2} \quad (213)$$

Note that  $\rho_y$  is defined to be either positive real or negative imaginary. Abramowitz and Stegun [1] give efficient methods for evaluating  $Q(x)$  with a complex argument without resorting to numerical

integration. One can then calculate the remaining half-pole contribution from

$$I_{residue} = \pm \frac{j\pi e^{-j\beta\tilde{\rho}_t \cos(\nu_o - \tilde{\phi}_t)}}{\rho_y} \quad (214)$$

To obtain the correct residue contributions one must choose the proper signs in Equations (211) and (214). Specifically, the upper signs are chosen if one of the following conditions are satisfied.

1.  $\nu_s > 0$  and  $Re\{\nu_o\} < \nu_s$
2.  $\nu_s > 0$  and  $Im\{\nu_o\} > \nu_i$ , or
3.  $\nu_s < 0$ ,  $Re\{\nu_o\} < \nu_s$ , and  $Im\{\nu_o\} > -\nu_i$

If none are true, then one chooses the lower signs.

As in any approximation, the question of accuracy invariably arises. Figure 119 attempts to provide an answer to this question by comparing the asymptotic and numerical evaluations of Equation (208) using the parameters  $\beta = \frac{2\pi}{\lambda}$ ,  $s_x = -0.866$ ,  $d_x = 0.1\lambda$  and  $k = 0$ . The figure plots the relative error magnitude defined by

$$\text{relative error} = \left| \frac{\text{asymptotic} - \text{numerical}}{\text{numerical}} \right| \quad (215)$$

as a function of  $\tilde{\phi}_t$  for various values of  $\tilde{\rho}_t$ . Since the test locations in this dissertation are always a wire radius out of the array plane, it is clear  $\tilde{\phi}_t$  stays close to  $+90^\circ$  for most integral evaluations. Surprisingly,  $\tilde{\rho}_t$  can be as small as  $0.1\lambda$  over a wide  $\tilde{\phi}_t$  range while still maintaining a relative error less than 10%. This, coupled with the computational savings<sup>5</sup> shown in Table 9, make the asymptotic evaluation a very attractive alternative to a numerical solution.

---

<sup>5</sup>The CPU times are averages over 91 integral evaluations. The evaluations were performed on a Sun Sparc10 workstation using the MATLAB software package.



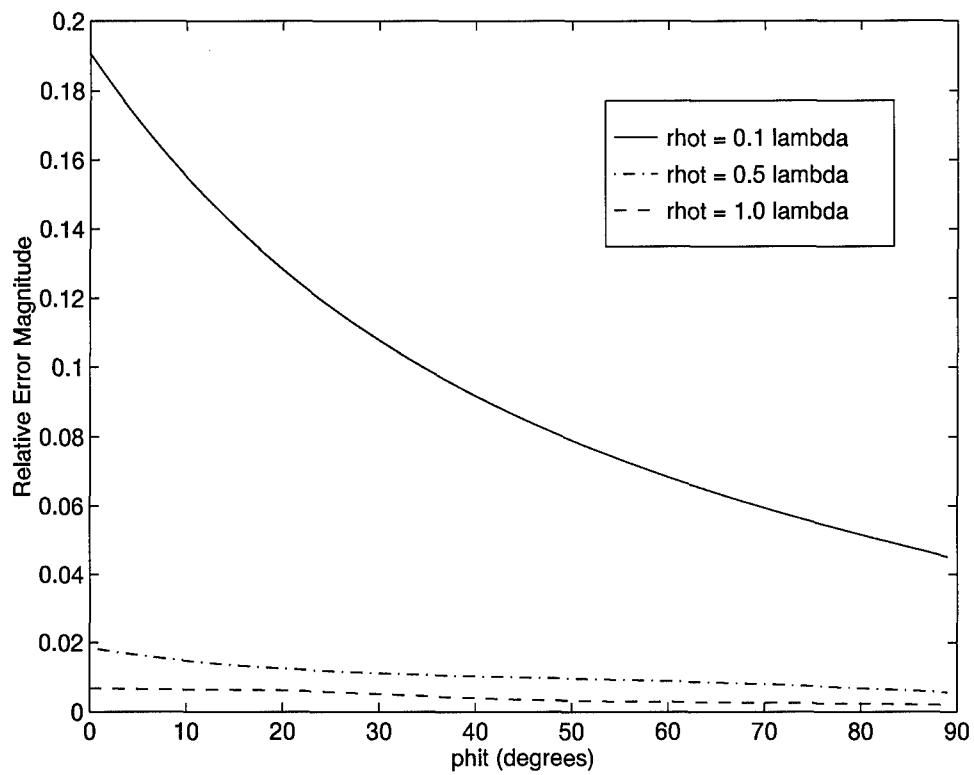


Figure 119. Numerical versus Asymptotic Integral Evaluation Error

$\bar{\rho}(\lambda)$	Asymptotic (cpu secs)	Numerical (cpu secs)
0.1	0.06	9.08
0.5	0.06	9.38
1.0	0.05	9.48

Table 9. Asymptotic and Numerical Integral Evaluation Time Comparison

### Appendix D. Array Scanning Method

Consider the problem of a single radiating element in the presence of a stratified dielectric medium. One must be able to determine the fields from such an element in order to calculate the coupling matrices found in this research<sup>1</sup>. Typically one might use a non-free-space Green's function to account for the slab boundaries. Unfortunately, this type of Green's function often produces difficult to evaluate, highly oscillatory integrands. This appendix briefly develops an alternative method called the Array Scanning Method (ASM). The author uses a two-dimensional wire problem to illustrate the ASM, thereby avoiding a tremendous amount of mathematical baggage which can mask the method's simplicity.

Figure 120 depicts a single infinite wire buried in a dielectric slab. One begins by expressing

<sup>1</sup>The coupling matrix entry is proportional to the field radiated by the basis function at the test location.

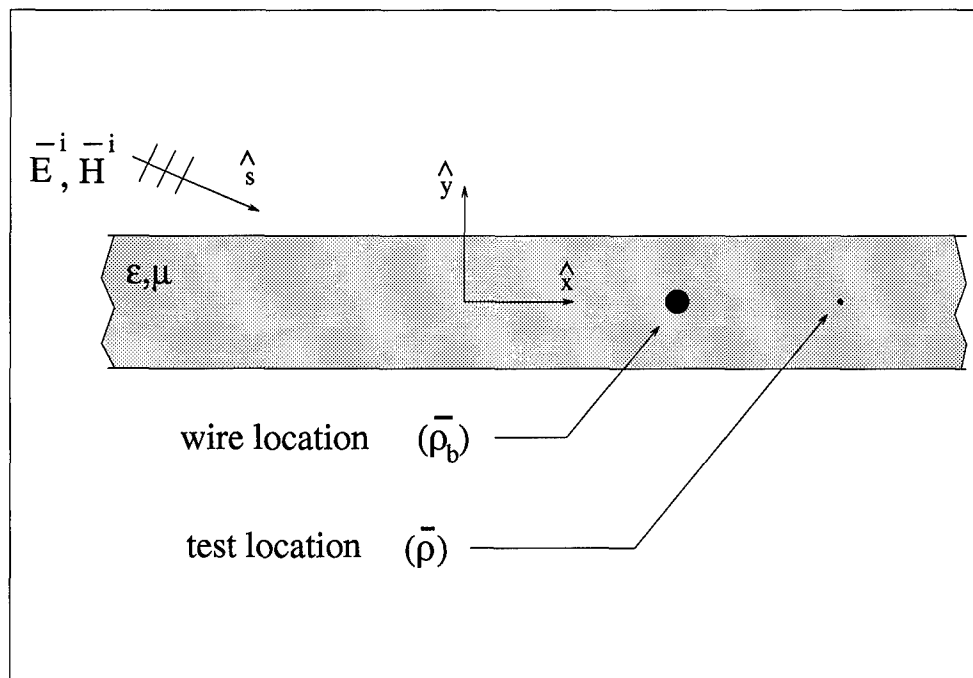


Figure 120. Single Wire in a Dielectric Slab

the field due to the wire in a *homogeneous* media as

$$\overline{\mathbf{E}}_{wire}(\overline{\rho}) = -\hat{z} \frac{\omega \mu J_b}{4} H_o^2(\beta |\overline{\rho} - \overline{\rho}_b|) \quad (216)$$

Now imagine creating an array of wires around this wire with inner-element spacing  $D_x$ .

$$\begin{aligned} \overline{\mathbf{E}}_{array}(\overline{\rho}) &= \hat{z} \sum_{q=-\infty}^{\infty} -\frac{\omega \mu J_b}{4} H_o^2(\beta |\overline{\rho} - \overline{\rho}_{qb}|) e^{-j\beta \hat{\mathbf{s}} \cdot \overline{\rho}_{qb}} \\ &= \hat{z} \sum_{q=-\infty}^{\infty} E_q e^{-j\beta s_x q D_x} \end{aligned} \quad (217)$$

One identifies Equation (217) as a Fourier series where  $\hat{z} E_0 = \overline{\mathbf{E}}_{wire}(\overline{\rho})$ . Using the Fourier method, one can extract the central coefficient ( $q = 0$ ) with an appropriately define inner product,

$$\begin{aligned} \overline{\mathbf{E}}_{wire}(\overline{\rho}) &= \frac{1}{T} \int_{-\frac{T}{2}}^{\frac{T}{2}} \overline{\mathbf{E}}_{array}(\overline{\rho}) e^{jq \frac{2\pi}{T} s_x} ds_x \Bigg|_{q=0} \\ &= \frac{D_x}{\lambda} \int_{-\frac{D_x}{\lambda}}^{\frac{D_x}{\lambda}} \overline{\mathbf{E}}_{array}(\overline{\rho}) ds_x \end{aligned} \quad (218)$$

where  $T = \frac{2\pi}{\beta D_x} = \frac{\lambda}{D_x}$ . Since one has total freedom in defining the array, one can choose the inner-element spacing to confine the integration range to the interval  $[-1, 1]$ . This corresponds to scanning the array phasing through an angle range restricted to real space, hence the name “array scanning” method.

At this point, one can express the field from the array in the spectral domain via the Poisson sum formula. It remains only to introduce the T-factor concept[26, 28] to incorporate the dielectric slab into the problem. The T-factor will not alter the phase relationship between the array elements and therefore does not alter the scan integration. Thus, one is left with an expression for the field from a single wire in terms of the field from an infinite array of wires.

One may wonder what has been gained through this series of manipulations. It appears one has exchanged a straight-forward integral evaluation for an infinite sum of integral evaluations. The ASM derives its efficiency from the exponential damping characteristics of the evanescent spectral terms. Thus only a few, much simpler, integral evaluations are required for convergence. The only penalty occurs when the T-factor contains surface wave singularities. In this case, the most expedient remedy involves introducing a slight loss in the dielectric and then integrating finely near the former singular point.

### Appendix E. Physical Basis Function (PBF) in the Excitation Vector

Throughout this dissertation, the author treats the PBF coefficient as an unknown quantity. Recall the PBF was introduced as an *a priori* encapsulation of the "infinite" nature of the central portion of a large array. One might ask why not go one step further and set the PBF coefficient value to that determined by a full infinite array analysis. It could then be included in the excitation vector, reducing the matrix dimension and eliminating the question of how to test the PBF. This appendix documents the author's investigation of this idea.

Consider the simple problem of a large wire array in a homogeneous media shown in Figure 121. Breaking the problem into two semi-infinite arrays, one could formulate the subproblem Moment Method (MM) matrix equation in the following two ways. Treating  $J_0$  as an unknown, one has from

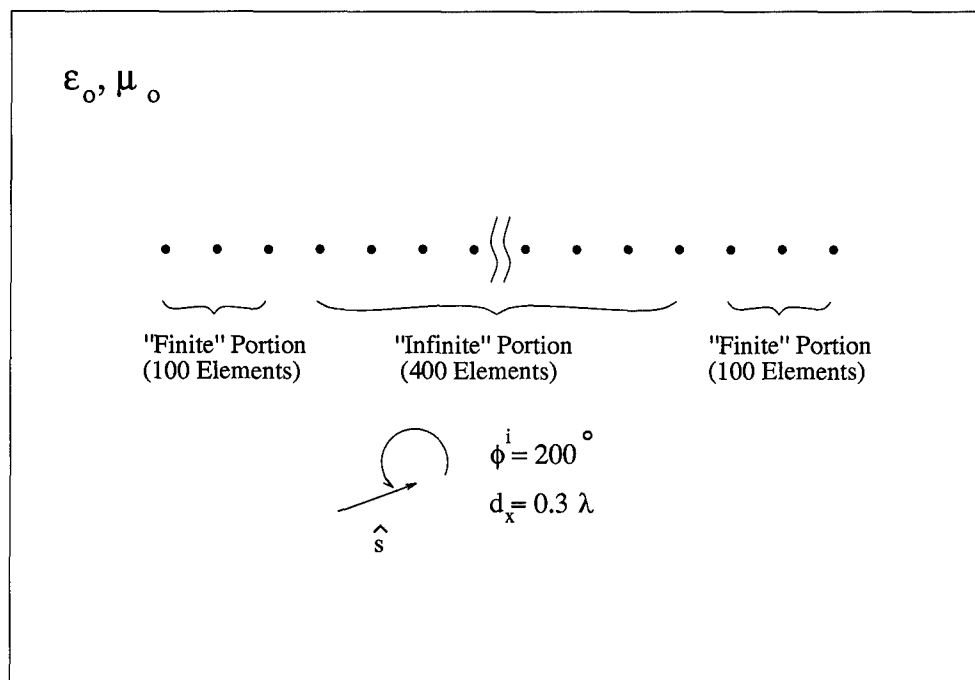


Figure 121. 600 Element Wire Array in Homogeneous Media

Equation (16)

$$E_z^i(\bar{\rho}_t) = -\frac{\omega\mu}{4} \left[ J_0 \sum_{q=0}^{\infty} H_0^{(2)}(\beta|\bar{\rho}_t - \bar{\rho}_q|) e^{-j\beta\hat{\mathbf{s}} \cdot \bar{\rho}_q} + \sum_{b=1}^B J_b H_0^{(2)}(\beta|\bar{\rho}_t - \bar{\rho}_b|) \right] \quad (219)$$

where the right hand side contains the unknown current coefficients. Recall  $\bar{\rho}_t$  is the test function location,  $\bar{\rho}_b$  is the basis function location, and  $\bar{\rho}_q$  is the PBF element location. The second formulation treats the PBF coefficient,  $J_0$ , as a known resulting in

$$E_z^i(\bar{\rho}_t) + \frac{\omega\mu J_0}{4} \sum_{q=0}^{\infty} H_0^{(2)}(\beta|\bar{\rho}_t - \bar{\rho}_q|) e^{-j\beta\hat{\mathbf{s}} \cdot \bar{\rho}_q} = -\frac{\omega\mu}{4} \sum_{b=1}^B J_b H_0^{(2)}(\beta|\bar{\rho}_t - \bar{\rho}_b|) \quad (220)$$

One can determine  $J_0$  from a full infinite array formed about the PBF test location,  $\bar{\rho}_0$ .

$$J_0 = -\frac{4E_z^i(\bar{\rho}_0)}{\omega\mu \sum_{q=-\infty}^{\infty} H_0^{(2)}(\beta|\bar{\rho}_0 - \bar{\rho}_q|) e^{-j\beta\hat{\mathbf{s}} \cdot \bar{\rho}_q}} \quad (221)$$

The following four figures compare the currents calculated with these two formulations (denoted by x's) to those calculated from a 600 unknown MM analysis (denoted by o's). Specifically, the current amplitudes for the first 110 edge elements are shown. Figures 122 and 123 plot the currents determined by Equation (219) with 100 unknown edge elements. For clarity, the first ten PBF elements are also shown. Note how the edge elements near the PBF are clamped to the PBF value. Now consider Figures 124 and 125 where Equations (220) and (221) are used. In this formulation, the edge perturbations near the PBF are no longer mitigated.

To understand why this is so, consider the matrix equation representing Equation (219).

$$\begin{bmatrix} V_0 \\ V_t \end{bmatrix} = \begin{bmatrix} Z_{00} & Z_{0b} \\ Z_{t0} & Z_{tb} \end{bmatrix} \begin{bmatrix} J_0 \\ J_b \end{bmatrix} \quad (222)$$

where the 0 subscript indicates the PBF. Compare Equation (222) with that of the second formulation.

$$\left[ V_t - J'_0 Z_{t0} \right] = \left[ Z_{tb} \right] \left[ J'_b \right] \quad (223)$$

where one calculates  $J'_0$  from a fully infinite array. Even if  $J'_0 = J_0$ , Equation (223) does not contain the constraint

$$V_0 = J_0 Z_{00} + [Z_{0b}] [J'_b] \quad (224)$$

Thus the second formulation is missing some of the coupling information between the PBF and the edge elements.

Based on the previous figures, it is apparent this coupling information plays a critical role in correcting the edge element currents nearest the PBF. As a result of this investigation, the author determined it is better to treat the PBF coefficient as an unknown despite what may appear to be an unnecessary increase in the resulting matrix size. One can always compare the PBF coefficient to that obtained from an infinite analysis "after-the-fact" to check if a sufficient number of edge elements were included in the calculation.

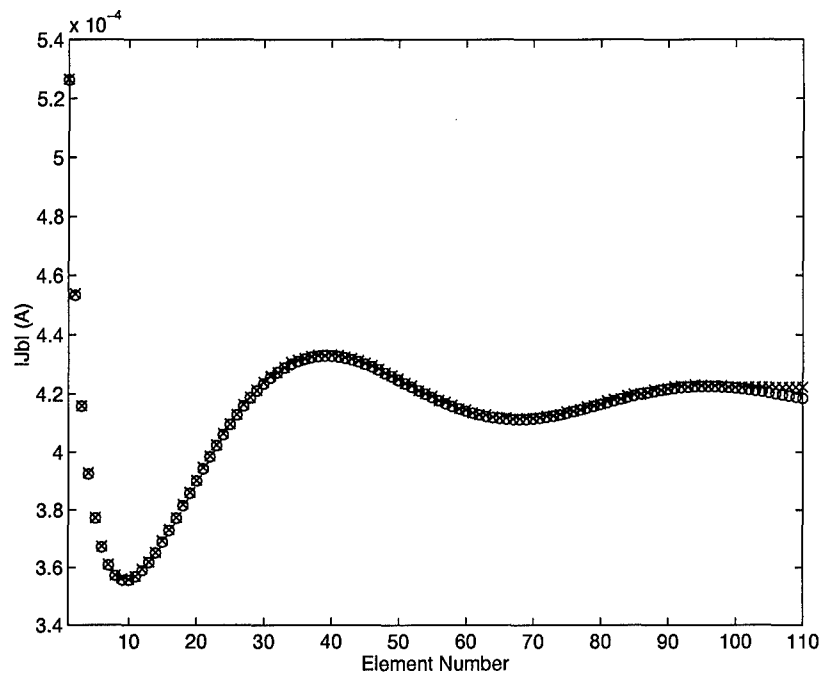


Figure 122. Left 110 Elements Based on First Formulation (Leading Edge of Array is Element 1)

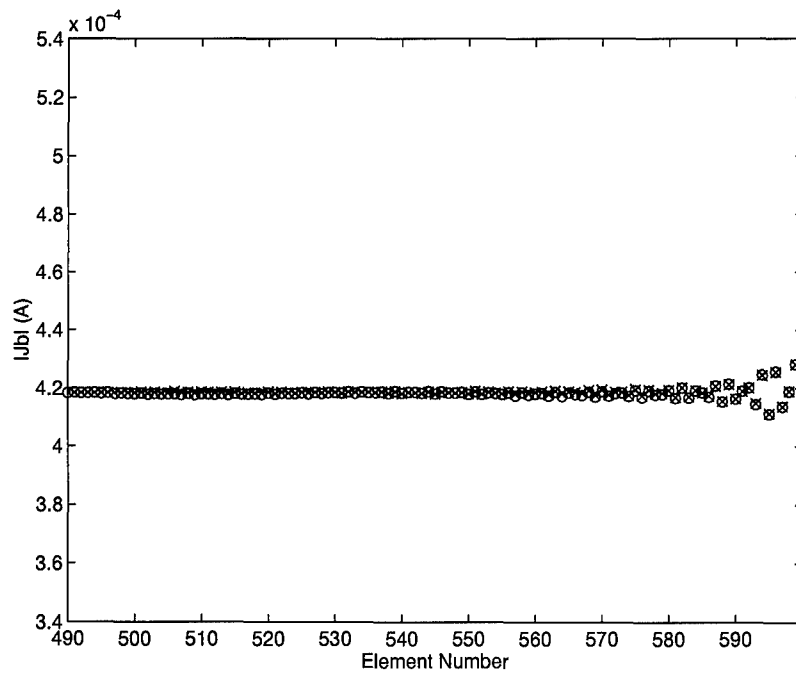


Figure 123. Right 110 Elements Based on First Formulation (Trailing Edge of Array is Element 600)



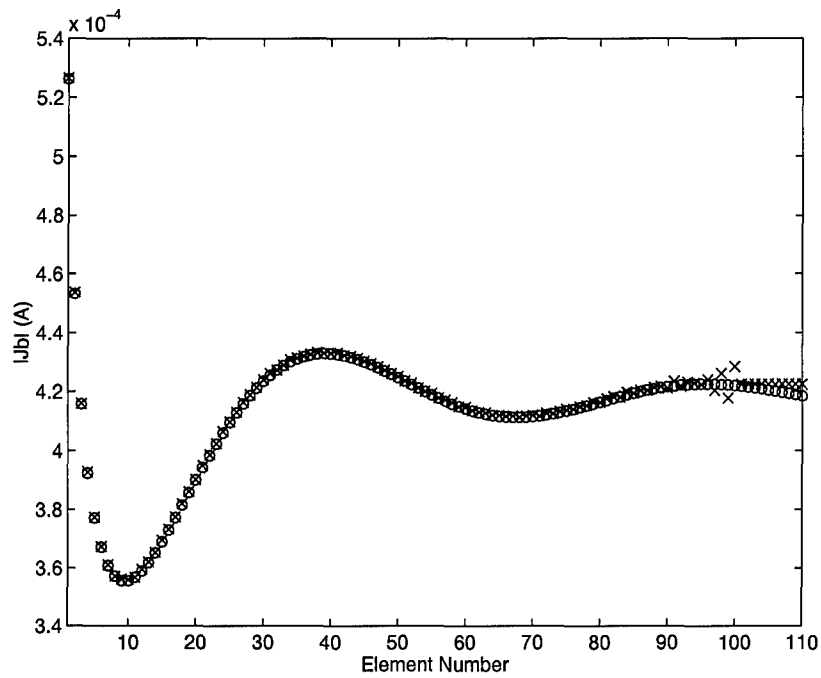


Figure 124. Left 110 Elements Based on Second Formulation (Leading Edge of Array is Element 1)

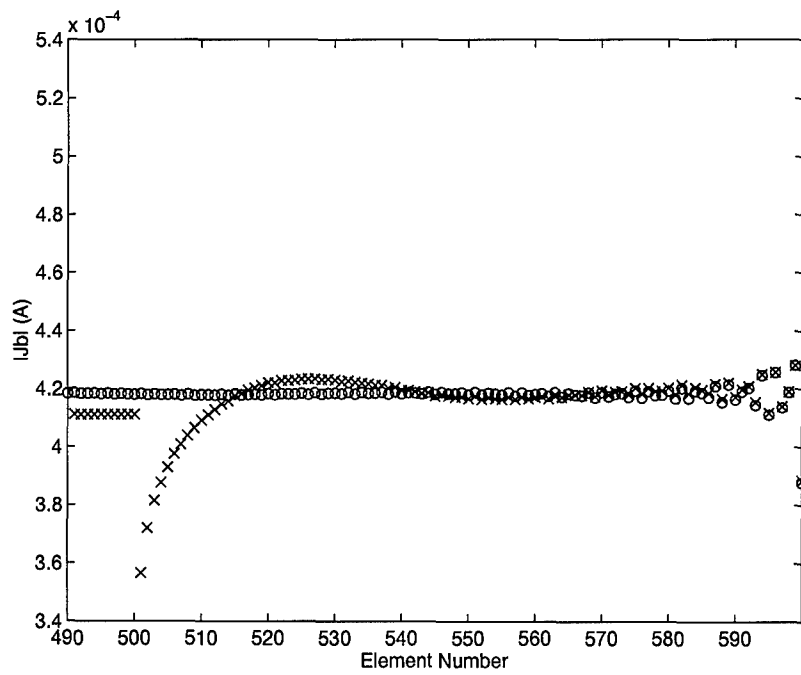


Figure 125. Right 110 Elements Based on Second Formulation (Trailing Edge of Array is Element 600)

## Bibliography

1. Abramowitz, M. and I. A. Stegun. *Handbook of Mathematical Functions*. Number 55 in Applied Mathematics Series, National Bureau of Standards, 1965.
2. Barré, P. R. *Scattering from Finite by Infinite Periodic Arrays with Arbitrary Piecewise-linear Slot Elements*. PhD dissertation, Air Force Institute of Technology, Wright-Patterson AFB, OH, 1995.
3. Bateman, H. *Tables of Integral Transforms, I*. McGraw Hill, Inc., 1954.
4. Bo, Y.M. and W.X. Zhang. "New Algorithm of Scattering From a Finite Periodic Surface-Conjugate Gradient-Circular Convolution (Cg-Cc) Method ." *1991 International Symposium Digest: Antennas and Propagation*. 300-3. New York, NY, USA: IEEE, June 1991.
5. Burnside, W. D. and R. J. Marhefka. "A Technique to Combine the Geometrical Theory of Diffraction and the Moment Method," *IEEE Transactions on Antennas and Propagation*, AP-23:551-8 (July 1975).
6. Caroglanian, A. and K.J. Webb. "Application of the Infinite FSS Spectral Domain Method in Solving Finite Planar FSS Problems with Arbitrary Illumination." *1990 International Symposium Digest: Antennas and Propagation*. 112. New York, NY, USA: IEEE, May 1990.
7. Chan, C.H., et al. "Electromagnetic Scattering From a Two-Layered Frequency Selective Surface of Finite Width." *1988 International Symposium Digest: Antennas and Propagation*. 750-3. New York, NY, USA: IEEE, June 1988.
8. Cwik, T. and R. Mittra. "The Effects of the Truncation And Curvature of Periodic Surfaces: a Strip Grating," *IEEE Transactions on Antennas and Propagation*, 36(5):612-22 (May 1988).
9. English, E. "Perfectly Conducting vs. Lossy Wires." Unpublished notes.
10. Felsen, L. B. and L. Carin. "Time Harmonic and Transient Scattering by Finite Periodic Flat Strip Arrays: Hybrid (Ray)-(Floquet Mode)-(MOM) Algorithm," *IEEE Transactions on Antennas and Propagation*, 41(4):412-21 (April 1993).
11. Felsen, L. B. and N. Marcuvitz. *Radiation and Scattering of Waves*. Prentice-Hall, Inc., 1973.
12. Felson, L. B. and L. Carin. "Diffraction Theory of Frequency- and Time-Domain Scattering by Weakly Aperiodic Truncated Thin-Wire Gratings," *Journal of the Optical Society of America*, 11(4):1291-1306 (April 1994).
13. Goubau, G., et al. "Diakoptic Theory for Multi-element Antennas," *IEEE Transactions on Antennas and Propagation*, AP-30(1):15-26 (January 1982).
14. Grounds, P.W. and K.J. Webb. "Numerical Analysis of Finite Frequency Selective Surfaces with Rectangular Patches of Various Aspect Ratios," *IEEE Transactions on Antennas and Propagation*, 39(5):569-75 (May 1991).
15. Gurel, L. and W.C. Chew. "a Recursive T-Matrix Algorithm For Strips And Patches," *Radio Science*, 27(3):387-401 (June 1992).

16. Hansen, R. C. and D. Gammon. "A Gibbsian Model for Finite Scanned Arrays," *IEEE Transactions on Antennas and Propagation*, 44(2):243–8 (February 1996).
17. Harrington, R. F. *Time-Harmonic Electromagnetic Fields*. McGraw Hill, Inc., 1961.
18. Harrington, R. F. *Field Computation by Moment Methods*. Malabar, Florida: Robert E. Krieger Publishing Company, Inc., 1968.
19. Henderson, L. W. *Introduction to PMM*. Technical 715582-5, ElectroScience Laboratory, The Ohio State University, February 1986. Generated under contract F33615-83-C-1024 for Avionics Laboratory, Air Force Wright Aeronautical Laboratories, Wright-Patterson AFB, OH.
20. Kastner, R. and R. Mittra. "Iterative Analysis of Finite-Sized Planar Frequency Selective Surfaces with Rectangular Patches or Perforations," *IEEE Transactions on Antennas and Propagation*, 35(4):372–7 (April 1987).
21. Kornbau, T. W. *Analysis of Periodic Arrays of Rotated Linear Dipoles, Rotated Crossed Dipoles, and of Biplanar Dipole Arrays in Dielectric*. PhD dissertation, Ohio State University, 1984.
22. Lu, Cai-Cheng and W. C. Chew. "Electromagnetic Scattering of Finite Strip Array on a Dielectric Slab," *IEEE Transactions on Microwave Theory and Techniques*, 41(1):97–100 (January 1993).
23. Mittra, R., et al. "Techniques For Analyzing Frequency Selective surfaces: a review." *Proceedings of the IEEE* 76. 1593–1615. December 1988.
24. Morita, N. "Diffraction by Arbitrary Cross-sectional Semi-infinite Conductor," *IEEE Transactions on Antennas and Propagation*, AP-19:358–65 (May 1971).
25. Moura, L. and R. Kitney. "A Direct Method for Least-Squares Circle Fitting," *Computer Physics Communications*, 64:57–63 (1991).
26. Munk, B. A. *A General Theory of Periodic Surfaces in a Stratified Dielectric Medium*. Technical 715582-4, ElectroScience Laboratory, The Ohio State University, February 1986. Generated under contract F33615-83-C-1013 for Avionics Laboratory, Air Force Wright Aeronautical Laboratories, Wright-Patterson AFB, OH.
27. Munk, B. A. and G. A. Burrell. "Plane-wave Expansion for Arrays of Arbitrary Oriented Piecewise Linear Elements and Its Application in Determining the Impedance of a Single Linear Antenna," *IEEE Transactions on Antennas and Propagation*, 27(5):331–43 (May 1979).
28. Munk, B. A., et al. *A General Theory of Periodic Surfaces in a Stratified Dielectric Medium*. Technical 784346-1, ElectroScience Laboratory, The Ohio State University, November 1977. Generated under contract F33615-76-C-1024 for Avionics Laboratory, Air Force Wright Aeronautical Laboratories, Wright-Patterson AFB, OH.
29. Papoulis, A. *The Fourier Integral and its Applications*. New York, NY, USA: McGraw Hill, Inc., 1962.
30. Shanks, D. "Non-linear transformations of divergent and slowly convergent sequences," *J. Math. Phys.*, 34:1–42 (1955).
31. Singh, S. and R. Singh. "on the Use of the  $\rho$ -Algorithm in Series Acceleration," *IEEE Transactions on Antennas and Propagation*, 39(10):1514–6 (October 1991).

32. Skinner, J. P. "Perturbed Edge Element to Full Edge Element Matrix Conversion." Unpublished notes.
33. Skinner, J. P. *Scattering from a finite collection of transverse dipole and axial slot arrays with edge effects*. PhD dissertation, Ohio State University, 1991.
34. Skinner, J. P. and Munk B. A. "Mutual Coupling Between Parallel Columns of Periodic Slots in a Ground Plane Surrounded By Dielectric Slabs," *IEEE Transactions on Antennas and Propagation*, 40(11):1324-35 (November 1992).
35. Stremmer, F. G. *Introduction to Communication Systems*. Reading, MA: Addison-Wesley, 1977.
36. Stylianou, A. and J.C. Vardaxoglou. "Improved Convergence of Iterative Scheme For Analysing Arrays of Finite Size," *Electronics Letters*, 26(10):641-3 (May 1990).
37. Stylianou, A. and J.C. Vardaxoglou. "Moderate Conjugate Gradient FFT Method For Rapid Convergence in Analysing Finite FSSs (Frequency Selective Surfaces)," *Electronics Letters*, 28(5):506-8 (February 1992).
38. Tew, M. D. and L. L. Tsai. "Use of *a priori* Knowledge in Moment Method Solutions." 1972 *GAP International Symposium*. December 1972.
39. Van Bladel, J. *Electromagnetic Fields*. Hemisphere Publishing Corp., 1985.
40. Wasylkiwskyj, W. "Mutual Coupling Effects in Semi-Infinite Arrays," *IEEE Transactions on Antennas and Propagation*, 21(5):277-85 (May 1973).
41. Wynn, P. "On a device for computing the  $e_m(S_n)$  transformation," *Math Tables and Aids to Comp.*, 10:91-6 (1956).
42. Wynn, P. "On a procrustean technique for the numerical transformation of slowly convergent sequences and series." *Proc. Cambridge Philos. Soc.* 52. 663-71. 1956.

## Vita

Captain Peter J. Collins [REDACTED]. After graduating from Cambridge High School in 1980, he attended Bethel College, St. Paul, Minnesota and the University of Minnesota, Minneapolis, receiving the B.A. and the B.S.E.E. degrees in 1985. Upon graduation, he came on Air Force active duty with the following assignments.

May 86 - May 89	Electro-Optic Signal Processing Engineer Electronic Technology Laboratory, Wright-Patterson AFB, OH
Dec 90	M.S.E.E. Air Force Institute of Technology, Wright-Patterson AFB, OH
Jan 91 - Mar 92	Lead Radar Systems Engineer Radar Target Scatter Division (RATSCAT) 6585th Test Group, Holloman AFB, NM
Mar 92 - Jul 93	Chief, Engineering Branch Radar Target Scatter Division (RATSCAT) 6585th Test Group, Holloman AFB, NM
Jul 93 - present	Doctoral Candidate Air Force Institute of Technology, Wright-Patterson AFB, OH

Captain Collins is the author of the following publications.

1. P. J. Collins and J. P. Skinner, *An Iterative Solution for TM Scattering from Perturbed Circular Dielectric Cylinders*, IEEE Transactions on Antennas and Propagation, Vol. 44, No. 6, June 1996.
2. J. P. Skinner and P. J. Collins, *A One-Sided Version of the Poisson Sum Formula for Semi-Infinite Array Green's Functions*, Accepted for publication in IEEE Transactions on Antennas and Propagation.
3. P. J. Collins, *Investigation of Electromagnetic Wave Interactions with Magneto-Dielectric Thin Films*, Masters Thesis, Air Force Institute of Technology, Dec 90.

He is also a member of IEEE, Eta Kappa Nu, and Tau Beta Pi.

[REDACTED]

# REPORT DOCUMENTATION PAGE

Form Approved  
OMB No. 0704-0188

Public reporting burden for this collection of information is estimated to average 1 hour per response, including the time for reviewing instructions, searching existing data sources, gathering and maintaining the data needed, and completing and reviewing the collection of information. Send comments regarding this burden estimate or any other aspect of this collection of information, including suggestions for reducing this burden, to Washington Headquarters Services, Directorate for Information Operations and Reports, 1215 Jefferson Davis Highway, Suite 1204, Arlington, VA 22202-4302, and to the Office of Management and Budget, Paperwork Reduction Project (0704-0188), Washington, DC 20503.

<b>1. AGENCY USE ONLY (Leave blank)</b>	<b>2. REPORT DATE</b> September, 1996	<b>3. REPORT TYPE AND DATES COVERED</b> Dissertation
---	--	---

<b>4. TITLE AND SUBTITLE</b> Electromagnetic Scattering from Semi-Infinite Planar Arrays	<b>5. FUNDING NUMBERS</b>
---	---------------------------

<b>6. AUTHOR(S)</b> Peter J. Collins	
---	--

<b>7. PERFORMING ORGANIZATION NAME(S) AND ADDRESS(ES)</b> Air Force Institute of Technology, WPAFB OH 45433-6583	<b>8. PERFORMING ORGANIZATION REPORT NUMBER</b> AFIT/DS/ENG/96-06
---	--

<b>9. SPONSORING/MONITORING AGENCY NAME(S) AND ADDRESS(ES)</b> Dr. Brian Kent WL/XPN WPAFB, OH 45433	<b>10. SPONSORING/MONITORING AGENCY REPORT NUMBER</b>
---	---

**11. SUPPLEMENTARY NOTES**

<b>12a. DISTRIBUTION/AVAILABILITY STATEMENT</b> Approved for public release; distribution unlimited	<b>12b. DISTRIBUTION CODE</b>
--	-------------------------------

**13. ABSTRACT (Maximum 200 words)**  
A hybrid method of moments (MM) based numerical model for the electromagnetic scattering from large finite by infinite planar slot arrays is developed. The method incorporates the novel concept of a physical basis function (PBF) to dramatically reduce the number of required unknowns. The model can represent a finite number of slot columns with slots oriented along the infinite axis, surrounded by an arbitrary number of coplanar dielectric slabs. Each slot column can be loaded with a complex impedance, allowing one to tailor the edge currents to provide a desired echo width pattern. The surface equivalence theorem is used to convert the original slotted ground plane geometry to an equivalent unbroken ground plane with magnetic surface currents. An integral equation based on these magnetic scattering currents is solved via the MM. The magnetic currents are approximated by a set of basis functions composed of periodic basis functions representing the edge slot columns and a single PBF representing the interior slot columns. In particular, the PBF captures the behavior of the central portion of the array where the perturbations from the edges have become negligible. Based on Floquet's theorem, the PBF is able to represent an arbitrarily large number of slot columns with just one unknown. The array scanning method (ASM) provides the contributions from the individual edge columns. Finally, a newly developed one-sided Poisson sum formulation provides an efficient means to account for the stratified dielectric media via a spectral domain conversion. The hybrid method is validated using both MM reference codes and measured data. The results clearly demonstrate the method's accuracy as well as its ability to handle array problems too large for traditional MM solutions.

<b>14. SUBJECT TERMS</b> Periodic Array, Frequency Selective Surface, Electromagnetic Scattering, Hybrid Method of Moments	<b>15. NUMBER OF PAGES</b> 182
	<b>16. PRICE CODE</b>

<b>17. SECURITY CLASSIFICATION OF REPORT</b> UNCLASSIFIED	<b>18. SECURITY CLASSIFICATION OF THIS PAGE</b> UNCLASSIFIED	<b>19. SECURITY CLASSIFICATION OF ABSTRACT</b> UNCLASSIFIED	<b>20. LIMITATION OF ABSTRACT</b> UL
--	---	--	---